

DIGITAL ACCESS TO SCHOLARSHIP AT HARVARD
DASH.HARVARD.EDU

HARVARD LIBRARY


From Stars to Galaxies: Unveiling Their Properties, Connection, and Evolution With Next Generation Stellar Models

Link
http://nrs.harvard.edu/urn-3:HUL.InstRepos:40050092

Terms of use
This article was downloaded from Harvard University's DASH repository, and is made available under the terms and conditions applicable to Other Posted Material (LAA), as set forth at
https://harvardwiki.atlassian.net/wiki/external/NGY5NDE4ZjgzNTc5NDQzMGIzZWZhMGFlOWI2M2EwYTg

Accessibility
https://accessibility.huit.harvard.edu/digital-accessibility-policy

Share Your Story
The Harvard community has made this article openly available.
Please share how this access benefits you. Submit a story

From Stars to Galaxies: Unveiling Their Properties, Connection, and Evolution With Next Generation Stellar Models

A DISSERTATION PRESENTED
BY
JIEUN CHOI
TO
THE DEPARTMENT OF ASTRONOMY

IN PARTIAL FULFILLMENT OF THE REQUIREMENTS
FOR THE DEGREE OF
DOCTOR OF PHILOSOPHY
IN THE SUBJECT OF
ASTRONOMY AND ASTROPHYSICS

HARVARD UNIVERSITY
CAMBRIDGE, MASSACHUSETTS
APRIL 2018

©2018 – JIEUN CHOI
ALL RIGHTS RESERVED.

From Stars to Galaxies: Unveiling Their Properties, Connection, and Evolution With Next Generation Stellar Models

ABSTRACT

Many areas of astrophysics spanning orders of magnitudes in physical scales—from exoplanets to high-redshift galaxies—are deeply rooted in our interpretation of light emitted by stars. Thus the importance of a well-tested and comprehensive set of stellar models extends well beyond the realm of stellar astrophysics. In this thesis, I use a new set of stellar evolution models to study the physical properties and the evolution of stars both as individual astrophysical objects and the constituents of stellar populations.

In the first half of this thesis, I describe the construction of the new stellar evolution models and explore the implications of several model uncertainties. I begin by introducing the MESA Isochrones and Stellar Tracks (MIST) project, a single, self-consistent database of stellar evolutionary tracks and isochrones computed over a wide range of masses, ages, metallicities, and evolutionary states. The models are compared extensively with other models in the literature and a variety of observations. Next, I investigate one of the key model ingredients, the surface boundary condition, in the stellar evolution calculations. In particular, I critically evaluate its influence on the effective temperatures of red giant stars and assess the ramifications for inferring stellar ages from isochrones and placing constraints on the mixing length parameter, which describes convection in 1D stellar models. I find that even though the models I consider can reproduce the properties of the Sun, both the type of boundary condition and the location at which it is applied to the interior model yield ≈ 100 K, metallicity- and $\log g$-dependent changes to the effective temperature distribution along the red giant branch. I close the first half by exploring the prospects for inferring the stellar ages of star clusters in the *Gaia* era and studying the effects of model uncertainties, for example the efficiency of mass loss, on the typical observations of star clusters, such the main sequence turn off

colors. Case studies of three well-studied open clusters—NGC6819, M67, NGC6791—demonstrate that more precise data than are currently available are required for firmer constraints on these model parameters. With a combination of exquisite photometry, parallax distances, and cluster memberships from *Gaia* at the end of its mission, we expect to be able to differentiate between the subtle yet qualitatively distinct color-magnitude diagram morphologies induced by the model parameters, and to measure precise and accurate ages for these nearby open clusters.

In the second half, I showcase two examples that highlight the star-galaxy connection. First, I infer the assembly histories of quiescent galaxies using their stellar populations as tracers. I present stellar ages and elemental abundances from modeling the optical spectra of a large sample of quiescent galaxies between $0.1 < z < 0.7$. I find negligible evolution in the elemental abundances at fixed galaxy stellar mass over roughly 7 Gyr of cosmic time, and that the increase in stellar ages with time for massive galaxies is consistent with passive evolution since $z = 0.7$. Taken together, these results favor a scenario in which the inner regions ($\sim$ 0.3–3 $R_{\rm e}$) of massive quiescent galaxies have been passively evolving over the last half of cosmic time. Finally, I examine the role of stellar rotation on the ionizing photon production of young, massive stellar populations. I find that even in low-metallicity environments where rotation has a significant effect on the evolution of massive stars, stellar population models require substantial contribution from fast-rotating (initial speed $> 40\%$ of breakup speed) stars in order to sustain the production of ionizing photons beyond a few Myr following a starburst. These results have important implications for cosmic reionization by massive stars and the interpretation of nebular emission lines in high-redshift star-forming galaxies.

CONTENTS

1 INTRODUCTION **1**
1.1 Stars as "1D Spheres" of Gas . . . 1
1.2 Stars as Stellar Populations . . . 8
1.3 Thesis Outline . . . 11

2 MESA ISOCHRONES AND STELLAR TRACKS (MIST): SOLAR-SCALED MODELS **13**
2.1 Introduction . . . 14
2.2 The MESA Code . . . 16
2.3 Adopted Physics . . . 18
2.4 Solar Model . . . 41
2.5 Model Outputs and Bolometric Corrections . . . 47
2.6 Overview and Basic Properties of the Models . . . 56
2.7 Comparisons with Existing Databases . . . 65
2.8 Comparisons with Data I: Low Mass Stars . . . 72
2.9 Comparisons with Data II: High Mass Stars . . . 96
2.10 Interesting Features in the MIST Models and Resolution Tests . . . 108
2.11 Summary . . . 115

3 ON THE RED GIANT BRANCH: AMBIGUITY IN THE SURFACE BOUNDARY CONDITION LEADS TO $\approx$ 100 K UNCERTAINTY IN MODEL EFFECTIVE TEMPERATURES **118**
3.1 Introduction . . . 119
3.2 Stellar Models . . . 121
3.3 Models vs. Data . . . 126
3.4 Discussion . . . 129
3.5 Summary . . . 132

4 PROSPECTS FOR AGE-DATING STAR CLUSTERS IN THE *Gaia* ERA **134**
4.1 Introduction . . . 135
4.2 Observations: What Can They Tell Us? . . . 136
4.3 Models: Where is the Information Content? . . . 144
4.4 Open Clusters: Case Studies . . . 159
4.5 What We Can Expect From Gaia . . . 169
4.6 Summary . . . 171

5 THE ASSEMBLY HISTORIES OF QUIESCENT GALAXIES SINCE $z = 0.7$ FROM ABSORPTION LINE SPECTROSCOPY **173**
5.1 Introduction . . . 174
5.2 Data . . . 178
5.3 Model Fitting . . . 186
5.4 Results . . . 189
5.5 Discussion . . . 200
5.6 Quantifying Systematic Uncertainties . . . 211
5.7 Summary . . . 217

6 THE EVOLUTION AND PROPERTIES OF ROTATING MASSIVE STAR POPULATIONS **221**
6.1 Introduction . . . 222
6.2 MIST Models . . . 225
6.3 Stellar Population Synthesis Models . . . 232
6.4 Stellar Population Properties . . . 236
6.5 Discussion . . . 252
6.6 Summary . . . 254

7 CONCLUSIONS **256**
7.1 Summary . . . 256
7.2 Future Work . . . 258
7.3 The *Gaia* Era and Beyond . . . 260

REFERENCES **262**

LIST OF PUBLICATIONS

Chapter 2 originally appeared in the literature as

Choi, J., Dotter, A., Conroy, C., Cantiello, M., Paxton, B., and Johnson, B. D., 2016, The Astrophysical Journal, 823, 102

Chapter 3 originally appeared in the literature as

Choi, J., Dotter, A., Conroy, C., and Ting, Y.-S., in press, The Astrophysical Journal.

Chapter 4 originally appeared in the literature as

Choi, J., Conroy, C., Ting, Y.-S., Cargile, P., and Dotter, A., submitted to The Astrophysical Journal.

Chapter 5 originally appeared in the literature as

Choi, J., Conroy, C., Moustakas, J., Graves, G. J., Holden, B. P., Brodwin, M., Brown, M. J. I., and van Dokkum, P. G., 2014, The Astrophysical Journal, 792, 95

Chapter 6 originally appeared in the literature as

Choi, J., Conroy, C., and Byler, N., 2017, The Astrophysical Journal, 838, 159

TO *appa*, *umma*, SANGEUN, AND C.

ACKNOWLEDGMENTS

First, I would like to thank Charlie Conroy, who has been a wonderful advisor, teacher, mentor, and role model over the last six years. I am grateful for his encouragement, kindness, and patience.* I would also like to thank Dimitar Sasselov, Andrea Dupree, and Daniel Eisenstein—who served on both my research exam and thesis defense committees—for their support and guidance, and my external examiner and mentor, Dan Weisz, for encouraging my scientific pursuits over the years.

I could not have completed this thesis without the members of the Conroy group, the best research group that ever existed. In particular, I am sincerely grateful to Aaron Dotter, who has been my collaborator from day one. Without his patience and wisdom, the MIST project would not exist.† I also wish to thank Ben Johnson, Phill Cargile, Ana Bonaca, Joel Leja, and Phil Rosenfield for sharing their amazing postdoc wisdom over the years. I also thank the rest of the group—Meng Gu, Ben Cook, Shany Danieli, Yuan-Sen Ting, Alexa Villaume, Harshil Kamdar, Seth Gossage, Josh Speagle, Rohan Naidu, Lindsay Oldham, Ivan Cabrera-Ziri, and Sandro Tacchella—for fostering a collaborative, intellectual environment.

My thesis would not exist without Bill Paxton, the architect of MESA, and the contributions from the hundreds of members of the MESA community around the world. MESA has revolutionized the field of stellar astrophysics and I am excited to have been a part of it.

I would also like to warmly thank the department administrators, Peg Herlihy, Robb Scholten, and Lisa Catella for making my transition to Harvard seamless and for going through my all too frequent and confusing reimbursement requests.

I wish to thank the wonderful graduate students I met here at Harvard for their friendship and support, especially the members of the 2nd floor P country club, 3rd floor P, coffee club, lunch group, climbing

*And for reassuring me that there is light at the end of the seemingly infinite solar-calibration tunnel!

†Alternatively, I might still be stuck on solar calibrations.

group, and movie club. Special-est thanks to the friends from my earliest days here—Luke Kelley, Jenny Bergner, Ryan Loomis, Laura Schaefer (and Zavi Dogic), Lehman Garrison, Ben Cook, Dawn Graninger, and Ben Montet—who helped me feel like I belong here.

I am immensely grateful for my UC Santa Cruz friends. There are too many wonderful humans to name individually here, but here are special shoutouts to Phil Macias and Zach Jennings, my fellow first years and housemates for two years. I will never forget Apt 227.*

I want to thank my fantastic friends from Berkeley, especially Allison Merritt, Jessamyn Allen, Joel Leja, and Michelle Kislak. Together we survived that unbelievably hot summer in Tucson, the dark depths of Pine River Pond, and the icy slopes on the Catskill Mountains. Next on the list—Devil's Path?

I am also very grateful for my dear Beech Street family—Amanda Gross, Sarina Tracy, Tori Frank, Ari Mannan, Alex Mankovich, and Gabe Mankovich. Thank you for creating a home away from home.

I have had many wonderful teachers throughout the last 20+ years, but I want to specially thank two educators, my high school physics teacher Sean Fottrell and my first astronomy professor Alex Filippenko. I attended a summer program on cosmology at LBL following Mr. Fottrell's suggestion, and I enjoyed it so much that I enrolled in Alex's intro to astronomy course at Berkeley later that fall. And the rest is history.

I want to thank my loving parents, JungAe Joo and Munho Choi, and my younger sister SangEun. My parents took us on a journey around the world, from one hemisphere to another, so that my sister and I would have better opportunities in life. And I thank them from the bottom of my heart for always encouraging me to pursue what interests and excites me the most. My sister was there with me from the beginning—I still remember our nerve-wracking first day of school together 17 years ago! Even though we did not know anybody nor speak the language, it was fine because we had each other. Finally, I thank my partner and best friend in life, Chris Mankovich, for being by my side, at my strongest and weakest moments, night and day, all around the world. I owe everything to their unrelenting love and support.

*A small, twisted part of me even misses our late-night problem sessions in the living room.

1

INTRODUCTION

Stars have been described as the fundamental particles of the Universe. Individually, they are both hosts to rich planetary systems and progenitors of some of the most spectacular transients in the distant Universe. As an ensemble, they are both cosmic engines that transformed the state of the early Universe and fossils bearing clues to galaxy formation and evolution. The interpretation of these systems and phenomena hinges on our understanding of stellar physics and well-calibrated stellar evolution models across a wide range of masses, metallicities, and evolutionary states.

1.1 STARS AS "1D SPHERES" OF GAS

Stellar evolution models, in the simplest terms, are a time series of solutions to the four differential equations of stellar structure and composition under the assumption of spherical symmetry. They are the equations of hydrostatic equilibrium, energy transport, conservation of energy, and conservation of mass:

$$\frac{\partial P}{\partial m} = \frac{-Gm}{4\pi r^4} \tag{1.1}$$

$$\frac{\partial T}{\partial m} = \frac{-GmT}{4\pi r^4 P}\nabla, \qquad \nabla = \frac{\partial \ln T}{\partial \ln P} \tag{1.2}$$

$$\frac{\partial L}{\partial m} = \varepsilon_{\rm nuc} + \varepsilon_{\rm grav} - \varepsilon_{\nu} \tag{1.3}$$

$$\frac{\partial r}{\partial m} = \frac{1}{4\pi r^2 \rho}\ , \tag{1.4}$$

where P, T, L, ρ, and r are local pressure, temperature, luminosity, mass density, and radius. The local temperature gradient, ∇, in Equation 2 determines the mode of energy transport in the stellar interior. If it is shallower (steeper) than the adiabatic temperature gradient, energy is carried by photons (convection). In Equation 3, the three ε terms correspond to the specific energy generation rate due to gravitational expansion/contraction and nuclear reactions, and the specific energy loss rate due to neutrinos.

There are four equations and four unknowns (P, T, L, and r), which require four boundary conditions: two in the center and two at the surface. In the center, L and r are trivially zero. Setting the two surface boundary conditions requires more careful thought, and one must appeal to either analytic relations or atmosphere models in order to specify P and T. This subject is discussed extensively in Chapter 3.

In addition to the four structure equations, there are N equations tracking the composition, one for each species i:

$$\frac{\partial X_i}{\partial t} = \frac{\partial X_{i,\,\mathrm{nuc}}}{\partial t} + \frac{\partial F_i}{\partial m} \ , \tag{1.5}$$

where F_i is the mass flux of species i. The first and second terms account for the changes due to nuclear reactions and various mixing processes, e.g., convection and diffusion. Finally, there are several auxiliary equations of microphysics, such as $\kappa(\rho, T, \mathbf{X})$ and $P(\rho, T)$, that specify the opacity and the state of matter (i.e., the equation of state), respectively.

Modules for Experiments in Stellar Astrophysics (MESA; Paxton et al. 2011, 2013, 2015, 2018), the 1D stellar evolution software primarily used in this work, simultaneously solves these $4 + N$ differential equations. In practice, this is a complicated multi-step procedure since the code must also make calls to various modules that supply additional pieces of information, such as the equations of state, opacity, and nuclear reaction rates, not to mention prescriptions for mixing, mass loss, and other processes that cannot be modeled from first principles. Differences between the numerous stellar evolution models that are in

use today largely stem from the differences in their choices of these input physics.

1.1.1 The Need for New Stellar Models

Decades since the golden era of stellar astrophysics (e.g., Burbidge et al. 1957; Böhm-Vitense 1958; Schwarzschild 1958; Kippenhahn 1963; Henyey et al. 1964; Paczyński 1970), the field has enjoyed a renaissance in recent years, largely due to technological advances in both computing and observational astronomy. According to Kippenhahn et al. 2012, M. Schwarzschild remarked in his 1958 book that "a person can perform more than twenty integration steps per day," such that "for a typical single integration consisting of, say, forty steps, less than two days are needed" (Schwarzschild 1958). Since then, improvements in computers and numerical algorithms have resulted in a tremendous speedup in solving the nonlinear, coupled differential equations of stellar structure and evolution. Another important contribution to the modern progress in stellar astrophysics has been the availability of increasingly precise and complete set of tabulated opacities, nuclear reaction rates, and equations of state. Accordingly, a large number of stellar evolution models have been published to tackle a wide variety of problems in astrophysics. For historical and practical reasons, stellar evolution models were generally computed over a limited range in mass, evolutionary phases, and abundances to address problems in specific areas of astrophysics. Studies of old, low-mass stellar populations in globular clusters and quiescent galaxies have relied on models such as BaSTI (Pietrinferni et al. 2004), DSEP/Dartmouth (Dotter et al. 2008), GARSTEC (Weiss & Schlattl 2008), Lyon (Baraffe et al. 1998, 2003, 2015), Padova/PARSEC (Girardi et al. 2002; Marigo et al. 2008; Bressan et al. 2012), Yale-Yonsei/Y^2 (Yi et al. 2001; Kim et al. 2002; Yi et al. 2003; Demarque et al. 2004), Victoria-Regina (VandenBerg et al. 2006), and more. On the other hand, studies of young, massive stellar populations in clusters and star-forming environments have made use of e.g., Geneva (Ekström et al. 2012; Georgy et al. 2013), STARS (Eggleton 1971; Pols et al. 1995; Eldridge & Tout 2004), and STERN (Brott et al. 2011a; Köhler et al. 2015) stellar evolution models.

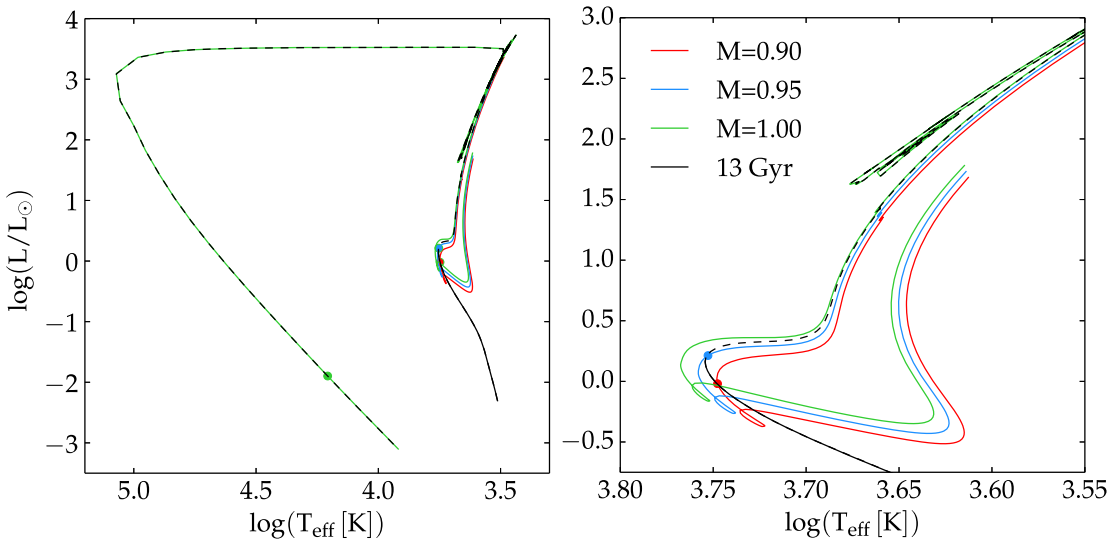


Figure 1.1: Example stellar evolutionary tracks with an isochrone in the Hertzsprung-Russell diagram. The red, blue, and green curves correspond to 0.9, 0.95, and 1.0$M_{\odot}$ evolutionary tracks and the black curve represents a 13 Gyr isochrone constructed from a grid of tracks, including the three shown here. The circles denote where each star is in its evolutionary path at 13 Gyr. The left panel shows all of the phases, while the right panel is zoomed in on the main sequence turnoff and the red giant branch. From Dotter 2016.

Many astrophysical applications of stellar evolution actually make use of isochrones instead of evolutionary tracks. An isochrone represents a stellar population of a single age and composition, and it is constructed from individual stellar evolutionary tracks through a non-trivial interpolation scheme. As an illustrative example, Figure 1.1, from Dotter (2016), shows evolutionary tracks of three stars and a 13 Gyr isochrone constructed from a grid of models, including the three that are shown, in a Hertzsprung-Russell (HR) diagram. The circles denote where each star is in its evolution at 13 Gyr, and necessarily lie exactly on the black curve. A naive approach that performs a simple interpolation as a function of time over the grid of evolutionary tracks is not suitable here,* as this method would fail to capture the complex morphologies of the post-main sequence (MS) evolution (note the relative locations of the three circles). This is because the timescales for these advanced evolutionary phases are very short compared to the main sequence lifetimes. I refer the reader to Dotter 2016 for an extended discussion on this topic.

Once theoretical isochrones (e.g., $\log L$, $T_{\rm eff}$) are constructed, they can be transformed to magnitudes

*This mass sampling is typical of, or even finer than, most stellar evolution databases.

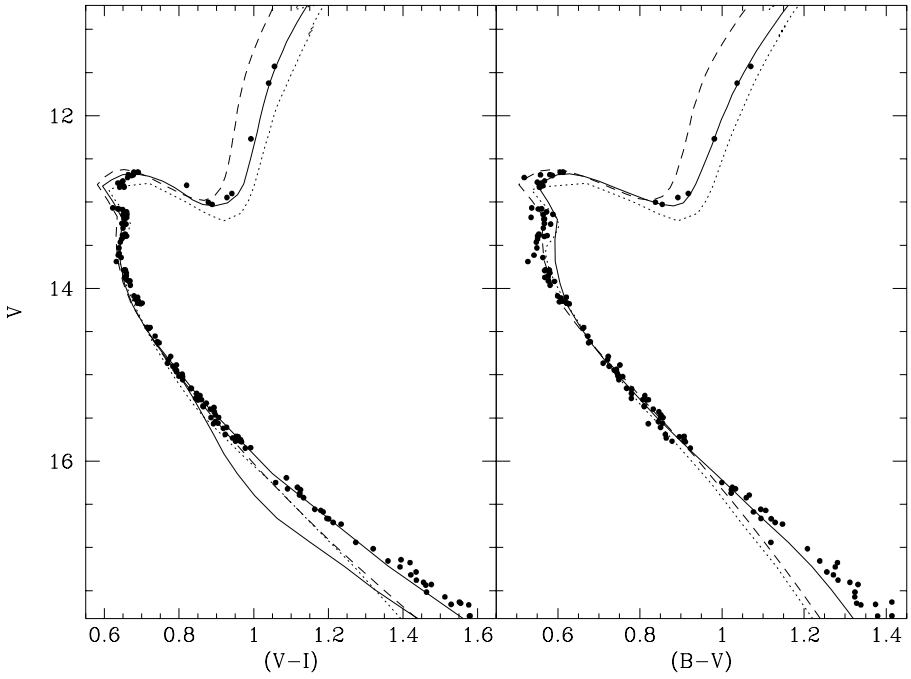


Figure 1.2: Color-magnitude diagrams of M67, a solar-metallicity, $\sim$ 4 Gyr galactic open cluster. The three lines correspond to three isochrones from the literature. From Sandquist 2004.

and colors from either empirical relations (e.g., Flower 1996; Alonso et al. 1996; Ramírez & Meléndez 2005; Casagrande et al. 2008) or bolometric correction tables constructed from synthetic spectra (e.g., PHOENIX, Allard et al. 2012; ATLAS9, Castelli & Kurucz 2004). Figure 1.2 shows two color-magnitude diagrams (CMDs) of a galactic open cluster M67 with three isochrones from the Yale-Yonsei, Padova, and Lyon databases. This type of fitting or comparison—with varying degrees of sophistication—is the main method by which ages and star formation histories are determined for star clusters and some types of dwarf galaxies (e.g., Jørgensen & Lindegren 2005; Marín-Franch et al. 2009; Weisz et al. 2011; Brown et al. 2014).

Furthermore, isochrones form the backbone of stellar population synthesis (SPS) models (discussed in more detail in Section 1.2), which have numerous astrophysical applications, e.g., as inputs to galaxy simulations (e.g., Illustris, Genel et al. 2014; FIRE, Hopkins et al. 2014). One of the challenges of building robust and accurate SPS models is ensuring that the grid of isochrones is complete (in the sense of

masses, ages, and compositions considered) and finely sampled in age and metallicity. However, as noted earlier, most stellar evolution models thus far have been computed over a limited range in mass, evolutionary phases, and/or abundances. For example, the Dartmouth models cover a wide range in metallicities and abundances but stop the evolution at the tip of the red giant branch after core helium ignites, and the Geneva models (Ekström et al. 2012; Georgy et al. 2013) adopt relatively coarse mass sampling below 10 $M_\odot$ and are limited to two metallicities. In order to circumvent this problem, some SPS models resorted to stitching heterogeneous sets of stellar evolution models together (see Figure 1 of Conroy & van Dokkum 2012 for one such example, where three separate sets of isochrones are used). This is suboptimal given that each set of models has its own set of input physics and assumptions. Thus there was an evident need for a new generation of stellar evolutionary tracks and isochrones that are self-consistent and cover a wide range of masses/ages, metallicities, and evolutionary phases. In Chapter 2, I present a new set of such models that were computed as part of the MESA Stellar Tracks and Isochrones (MIST) project using MESA.*† The framework I have constructed for the MIST project will reappear throughout the chapters, as stellar evolution models form the foundation of the work herein.

1.1.2 Uncertainties in the Stellar Models

Many of the essential ingredients in the standard 1D stellar evolution models, including MIST, cannot be modeled from first principles and instead rely on physically-motivated prescriptions, which are uncertain. For example, convection is usually implemented according to the mixing length formalism in which the mixing efficiency, and as a result the stellar structure, depend sensitively on $\alpha_{\rm MLT}$, a free parameter of order unity (Böhm-Vitense 1958). There are ongoing complementary efforts to determine $\alpha_{\rm MLT}$ using sophisticated 3D hydrodynamic simulations (e.g., Trampedach et al. 2014; Magic et al. 2015) and detailed

*Since I began the project, other groups have also produced updated and more complete sets of models, e.g., PARSEC (Bressan et al. 2012; Tang et al. 2014)

†I emphasize that MESA's open-source philosophy has tremendous significance not only in terms of its availability to the broader community but also for the transparency of model assumptions and numerical methods.

constraints and calibrations from a variety of observations (e.g., Bonaca et al. 2012; Wu et al. 2015; Tayar et al. 2017; Joyce & Chaboyer 2017; Chun et al. 2018; Li et al. 2018).

One source of uncertainty that is both better understood in, and particularly relevant to, the realm of low mass stars is the surface boundary condition. As discussed in Section 1.1, surface boundary conditions are essential inputs to any stellar model as they, along with the two trivial boundary conditions at the center, are required to close the four equations of stellar structure. A common treatment of the surface boundary conditions involves the integration of the hydrostatic balance equation with a T–τ relation, a simple analytic equation relating temperature and optical depth (e.g., "gray" atmosphere, Eddington 1926; empirical solar atmosphere, Krishna Swamy 1966). A less common but physically better motivated and more accurate approach is the use of model atmospheres (e.g., ATLAS, Kurucz 1970, 1993; PHOENIX, Hauschildt et al. 1999a,b; MARCS, Gustafsson et al. 2008), which tabulate thermodynamic and other microphysical quantities as a function of optical depth over a grid of metallicities, surface gravities, and effective temperatures. The choice of surface boundary condition and other associated ambiguities, e.g., where the boundary condition is set, can lead to large differences in model effective temperatures, particularly in red giants and low-mass dwarfs (e.g., Chabrier & Baraffe 1997; Salaris et al. 2002; VandenBerg et al. 2008). In Chapter 3, I compute a series of MESA models to explore the sensitivity of the effective temperatures of red giant stars to the treatment of the surface boundary condition. I also discuss the results in the context of recent papers that find evidence for a metallicity-dependent $\alpha_{\rm MLT}$ as a way to resolve discrepancies between model and observed effective temperatures.

It is crucial to continue investigating ways to both better understand the underlying physics *and* better constrain uncertain model parameters. Indeed, if $\alpha_{\rm MLT}$ does vary with stellar parameters such as $\log g$, $T_{\rm eff}$, and metallicity, this has profound implications reaching far beyond stellar physics. For example, in the case of a solar metallicity, $\log g \sim 2$ star, an increase in $\alpha_{\rm MLT}$ by ~ 0.1 can make the red giant branch hotter by ~ 50 K, which will shift the isochrone-based mass and age estimates upward by ~ 0.25 $M_\odot$ and down-

ward by a factor of ~ 2, respectively. This is an uncomfortable margin of error when considering e.g., red giant branch-based star formation histories of the Milky Way and nearby resolved galaxies. In this case, it is also worth pursuing complementary methods to infer stellar ages (e.g., C and N abundances, Masseron & Gilmore 2015; Salaris & Cassisi 2015; Martig et al. 2016; Ness et al. 2016) that are less sensitive to some model parameters.

Looking toward the very near future, the *Gaia* mission, which promises to deliver microarcsecond astrometry and proper motions for a billion Milky Way stars, will also obtain high-precision photometry consisting of both broadband G and blue/red spectrophotometry (B and R) (Jordi et al. 2010). Together, this unprecedented data set will yield homogeneous, proper motion-cleaned photometry for star clusters with accurate and precise distance measurements. In Chapter 4, I use the MIST framework to compute a series of isochrones and assess the advantages of various observational data sets for jointly constraining stellar model parameters and stellar ages. I also explore the possibility of disentangling the subtle effects induced by model parameters on the CMDs in the *Gaia* era. I will return to *Gaia* in the Conclusions (Section 7).

1.2 Stars as Stellar Populations

In the simplest terms, the light we observe from an unresolved star cluster or a galaxy can be thought of as the sum of light from the individual constituent stars.* Consider a simple stellar population, a group of stars born from a single, instantaneous burst of star formation in a well-mixed birth cloud. An SPS model for this simplified case only requires three ingredients: a library of stellar isochrones, a library of stellar spectra, and an initial mass function (IMF). The isochrone tabulates the surface properties of the constituent stars—such as the elemental abundances, effective temperatures, and surface gravities—and together they specify a unique spectrum for each star. Next, empirical (e.g., MILES; Sánchez-Blázquez et al. 2006b) or theoretical (e.g., C3K; Conroy et al., submitted) spectra are summed along the isochrone

*Ignoring for now other sources such as ionized gas and active galactic nuclei.

with weights provided by an IMF to produce a spectral energy distribution (SED) of the stellar population. This simple framework can be extended to include other ingredients such as dust, a metallicity distribution, a star formation history (SFH), and nebular emission lines to yield a model of a complex stellar population, e.g., a star-forming galaxy such as the Milky Way. An SED represents a fundamental prediction from any SPS model (e.g., Starburst99, Leitherer et al. 1999, 2014; FSPS, Conroy et al. 2009, 2010), and it can be compared directly to an observed spectrum or convolved with a filter response function to compare to photometry.

1.2.1 The Role of Stellar Population Models in Galactic Archaeology

The SED of a galaxy contains vital clues about its unresolved stellar population, including its SFH, IMF, and elemental abundances. This concept is at the core of galactic archaeology, which extracts and interprets the properties of present day stellar populations to trace the formation and assembly histories of galaxies. In the ΛCDM framework, structures in our Universe formed through a "bottom-up" process: in the early Universe, small overdense regions collapsed first, which then clumped together to form the large-scale structures that we see today. This implies that low-mass galaxies were the building blocks of more massive galaxies, and the naive expectation from this is that stellar populations in low-mass galaxies are generally older than those found in massive galaxies. However, stellar population studies indicate an anti-hierarchical growth in the Universe: massive galaxies are quiescent, consisting mostly of old stars, whereas low-mass galaxies appear to be either actively forming stars or harboring younger populations (e.g., Trager et al. 1998; Thomas et al. 2005; Jimenez et al. 2007; Conroy et al. 2014). Exactly how galaxies formed and assembled over time is one of the key unanswered questions in astrophysics today.

In this paragraph, let us focus exclusively on quiescent, i.e., no longer actively star-forming, galaxies containing old stellar populations. The SPS analysis of massive quiescent galaxies has revealed that their stellar populations are old, enhanced in α-capture elements such as Mg, and generally more metal-

rich compared to the lower mass counterparts and Milky Way disk stars (e.g., Worthey et al. 1994). The total metallicity is an important diagnostic for the formation history of the galaxy because it is sensitive to the depth of the potential well in which its stars were formed (e.g., supernovae-driven winds can efficiently remove metals from shallow potential wells; Larson 1974). On the other hand, [α/Fe] is akin to a star formation clock: massive stars expel α elements into their interstellar environments on million-year timescales, while type Ia supernovae enrich the star-forming gas with iron-peak elements on billion-year timescales (e.g., Tinsley 1979). Thus the ratio of the abundances of α elements and iron is sensitive to the timescale of star formation (e.g., Thomas et al. 1999). In Chapter 5, I present the results from modeling the optical spectra of a large sample of $z \sim 0.1$ to $z \sim 0.7$ quiescent galaxies from the AGN and Galaxy Evolution Survey (Kochanek et al. 2012). I derive stellar ages and abundances of several elements including Mg and Ca, and discuss the constraints they place on the assembly histories of quiescent galaxies over the last ~ 7 Gyr of cosmic time.

1.2.2 Importance of Stellar Feedback on Galaxy Evolution

An important aspect of galaxy evolution theory is the self-regulation of star formation through stellar feedback (e.g., Murray et al. 2010; Hopkins et al. 2011). Broadly speaking, stellar feedback refers to the deposition of energy, momentum, mass, and nuclear-burning products via channels that include type I and type II supernovae, stellar radiation, and winds. These processes influence the state of the interstellar medium (e.g., McKee & Ostriker 1977), thereby regulating star formation (e.g., Williams & McKee 1997; Mac Low & Klessen 2004; McKee & Ostriker 2007) and driving both turbulence and galactic-scale outflows (e.g., Dekel & Silk 1986; Martin 1999; de Avillez & Breitschwerdt 2004; Joung & Mac Low 2006; Oppenheimer & Davé 2006; Agertz et al. 2009; Tamburro et al. 2009; Hopkins et al. 2012; Creasey et al. 2013).

Massive stars, though rare in number, are energetically dominant across a wide range of environ-

ments from star cluster to extragalactic scales. Observations of star-forming giant molecular clouds suggest that early feedback from these young, massive stars disperse the dense gas well before the first supernovae explode, which may increase the overall efficiency of feedback and reduce the star formation efficiency (e.g., Evans et al. 2009; Krumholz et al. 2012). The complex interplay between the properties of young stellar populations and the dissolution of their birth gas has significant implications for the number of photons that are able to leak out of the host galaxies (e.g., Dove & Shull 1994; Gnedin 2000; Ma et al. 2015) and drive cosmic reionization (e.g., Haardt & Madau 1996).

Galaxy simulations that attempt to include the effects of stellar feedback must appeal to SPS models that tabulate the energy and momentum output as a function of time and metallicity. Although there is a general consensus that stellar feedback plays an important role in shaping the physical conditions of their immediate surroundings, the evolution of the host galaxy, and its extragalactic environment, there are still substantial uncertainties due to unresolved questions in massive star evolution. In particular, the relative importance of stellar rotation and multiplicity (e.g., binary, triplet systems) in stellar feedback is still an active area of research (e.g., Levesque et al. 2012; Ma et al. 2016b). These two phenomena are both ubiquitous in nature and critical for setting the evolutionary lifetimes and physical properties of massive stars, but the multiplicity and rotation rate distributions as a function of metallicity, mass, etc., are still relatively uncertain (e.g., de Mink et al. 2014; Kobulnicky et al. 2014). In Chapter 6, I explore the importance of rotation in the evolution of young, massive stellar populations within the MIST and FSPS framework, and examine the implications for cosmic reionization.

1.3 Thesis Outline

This thesis is broadly divided into two themes: 1. the construction of stellar evolution models and the assessment of model uncertainties, and 2. the exploration of the star-galaxy connection.

In the first chapter, I discuss the MIST project and present extensive comparisons with observations

and some of the most widely used existing models in the literature. In the second chapter, I critically examine one of the sources of uncertainties in stellar models—surface boundary conditions—on the effective temperatures of red giant stars. In the third chapter, I explore the relationship between uncertain model parameters and stellar age constraints for star clusters during the *Gaia* era.

In the latter half of this work, I turn to two examples that highlight the star-galaxy connection. In the fourth chapter, I present a method to unveil the assembly histories of galaxies using their stellar population properties as tracers. I derive stellar population parameters of a large population of quiescent galaxies and examine their evolution over the last 7 Gyr of cosmic history. In the fifth chapter, I demonstrate one of the ways in which stellar populations influence the evolution of host galaxies and the extragalactic neighborhoods. I investigate the role of stellar rotation in the ionizing photon production of young, massive stellar population and the implications for cosmic reionization.

Finally, I conclude with a summary and a brief discussion of future directions.

2

MESA Isochrones and Stellar Tracks (MIST): Solar-Scaled Models

This is the first of a series of papers presenting the MESA Isochrones and Stellar Tracks (MIST) project, a new comprehensive set of stellar evolutionary tracks and isochrones computed using Modules for Experiments in Stellar Astrophysics (MESA), a state-of-the-art open-source 1D stellar evolution package. In this work, we present models with solar-scaled abundance ratios covering a wide range of ages ($5 \leq \log(\mathrm{Age})\ [\mathrm{yr}] \leq 10.3$*), masses (*$0.1 \leq M/M_{\odot} \leq 300$*), and metallicities (*$-2.0 \leq [\mathrm{Z/H}] \leq 0.5$*). The models are self-consistently and continuously evolved from the pre-main sequence to the end of hydrogen burning, the white dwarf cooling sequence, or the end of carbon burning, depending on the initial mass. We also provide a grid of models evolved from the pre-main sequence to the end of core helium burning for* $-4.0 \leq [\mathrm{Z/H}] < -2.0$*. We showcase extensive comparisons with observational constraints as well as with some of the most widely-used existing models in the literature. The evolutionary tracks and isochrones can be downloaded from the project website at http://waps.cfa.harvard.edu/MIST.*

2.1 Introduction

Decades since the golden era of stellar astrophysics (e.g., Burbidge et al. 1957; Böhm-Vitense 1958; Schwarzschild 1958; Henyey et al. 1964; Paczyński 1970), the field has enjoyed a renaissance in recent years, largely due to technological advances in both computing and observational astronomy. Improvements in computers and numerical algorithms have resulted in a tremendous speedup in solving the non-linear, coupled differential equations of stellar structure and evolution. Another important factor was the availability of increasingly precise tabulated opacities, nuclear reaction rates, and equations of state. Accordingly, a large number of stellar evolution models have been published to tackle a wide variety of problems in astrophysics. Studies of old, low-mass stellar populations in globular clusters and quiescent galaxies have relied on models such as BaSTI (Pietrinferni et al. 2004), DSEP (Dartmouth; Dotter et al. 2008), GARSTEC (Weiss & Schlattl 2008), Lyon (Baraffe et al. 1998, 2003, 2015), Padova/PARSEC (Girardi et al. 2002; Marigo et al. 2008; Bressan et al. 2012), Y^2 (Yi et al. 2001; Kim et al. 2002; Yi et al. 2003; Demarque et al. 2004), Victoria-Regina (VandenBerg et al. 2006), and more. On the other hand, studies of young, massive stellar populations in clusters and star-forming environments have made use of e.g., Geneva (Ekström et al. 2012; Georgy et al. 2013), STARS (Eggleton 1971; Pols et al. 1995; Eldridge & Tout 2004), and STERN (Brott et al. 2011a; Köhler et al. 2015) stellar evolution models.

On the observational front, large quantities of precise data from recent and ongoing space- and ground-based programs have initiated an explosive growth in fields such as asteroseismology (e.g., *CoRoT*; Baglin et al. 2006, *Kepler*; Gilliland et al. 2010), time-domain astronomy (e.g., *Palomar Transient Factory*; Law et al. 2009, *Pan-STARRS*; Kaiser et al. 2010), galactic archaeology (e.g., *APOGEE*; Zasowski et al. 2013, *GALAH*; De Silva et al. 2015), and resolved stellar populations (e.g., the *Hubble Space Telescope* program *PHAT*; Dalcanton et al. 2012). Moreover, future surveys, e.g., *LSST* (Ivezic et al. 2008), and next-generation observatories such as *JWST* and *Gaia* will provide an unprecedented volume of high-quality

data whose analysis demands uniform models covering all relevant phases of stellar evolution.

In order to fully exploit these new and upcoming datasets, we have set out to construct stellar evolution models within a single, self-consistent framework using Modules for Experiments in Stellar Astrophysics (MESA; Paxton et al. 2011, 2013, 2015), a popular open-source 1D stellar evolution package.* MESA is well-suited for this purpose due to its flexible architecture and its capability to self-consistently model the evolution of different types of stars to advanced evolutionary stages in a single continuous calculation. Furthermore, its thread-safe design enables parallel computing, which greatly reduces the computation time and makes the large-scale production of models feasible.

This is the first of a series of papers presenting MESA Isochrones and Stellar Tracks (MIST), a new set of stellar evolutionary tracks and isochrones. In this paper, we present models with solar-scaled abundances covering a wide range of ages, masses, phases, and metallicities computed within a single framework. We will subsequently present models with non-scaled-solar abundances, including e.g., alpha-enhanced, carbon-enhanced metal-poor, and CNONa-enhanced for modeling globular clusters, in Paper II.

The paper is organized as follows. Section 2.2 gives an overview of MESA, focusing on the high-level architecture of the code and its time step and spatial mesh controls. Section 2.3 reviews the treatment of the relevant physical processes as implemented in a 1D framework, all of which is summarized in Table 2.2. Calibration of the model against the properties of the Sun is discussed in Section 2.4, and a short overview of the model outputs, the method for constructing isochrones, and the treatment of bolometric corrections is presented in Section 2.5. Section 2.6 presents an overview of the properties of the models, and Section 2.7 features comparisons with some of the most widely-used existing databases. Sections 2.8 and 2.9 separately present comparisons with data for low-mass ($\lesssim 10\ M_\odot$) and high-mass stars ($\gtrsim 10\ M_\odot$). Finally, Section 2.11 concludes the paper with a discussion of caveats and future work.

We define some conventions and assumptions adopted in the paper. We use M_i throughout to refer

*There exists another database of isochrones computed also using MESA. See Zhang et al. (2013) for more details.

to the initial stellar mass of a model. Both Z and [Z/H] are used to refer to metallicities, where Z is the metal mass fraction. For the models presented in this paper, [Z/H] = [Fe/H] since we adopt solar-scaled abundances. The [Z/H] notation assumes the Asplund et al. (2009) protosolar birth cloud bulk metallicity, not the current photospheric metallicity, as the reference value (see 2.3.1 for more details). Magnitudes are quoted in the Vega system unless noted otherwise. Where necessary, we adopt a Kroupa IMF (Kroupa 2001). Lastly, in accordance with the XXIXth IAU resolutions B2 and B3,* we adopt the following two conventions. First, we use the following nominal values to express stellar properties in solar units: $M_{\odot} = 1.988 \times 10^{33}$ g, $L_{\odot} = 3.828 \times 10^{33}$ erg s^{-1}, $R_{\odot} = 6.957 \times 10^{10}$ cm, and $T_{\text{eff},\odot} = 5772$ K. Formally, the IAU published these values in SI units, but we report them in cgs units here to be consistent with the convention adopted in this work. Second, the zero point of the absolute bolometric magnitude scale is set by enforcing that $M_{\text{bol}} = 0$, which corresponds exactly to $L_{\circ} = 3.0128 \times 10^{35}$ erg s^{-1}. This zero point was chosen such that the nominal solar luminosity $L_{\odot}$ has an $M_{\text{bol},\odot} = 4.74$ mag, a value commonly adopted in the literature.

2.2 The MESA Code

Modules for Experiments in Stellar Astrophysics (MESA)† is an open-source stellar evolution package that is undergoing active development with a large user base worldwide (Paxton et al. 2011, 2013, 2015). Its 1D stellar evolution module, MESAstar, has been thoroughly tested against existing stellar evolution codes and databases, including BaSTI/FRANEC (Pietrinferni et al. 2004), DSEP (Dartmouth; Dotter et al. 2008), EVOL (Blöcker 1995; Herwig 2004; Herwig & Austin 2004), GARSTEC (Weiss & Schlattl 2008), Lyon (Baraffe et al. 1998, 2003, 2015), KEPLER (Heger et al. 2005), and STERN (Petrovic et al. 2005; Yoon & Langer 2005; Brott et al. 2011a). Its highly modular and therefore flexible infrastructure combined with its robust numerical methods enable its application to a wide range of problems in compu-

*http://astronomy2015.org/sites/default/files/IAU_XXIX_GA_Final_Resolutions_B1-B4.pdf
†http://mesa.sourceforge.net/

tational stellar astrophysics, from asteroseismology to helium core flash in low-mass stars, as well as the evolution of giant planets, accreting white dwarfs (WD), and binary stars.

MESAstar simultaneously solves the fully coupled Lagrangian structure and composition equations using a Newton-Raphson solver. The required numerics (e.g., matrix algebra, interpolation) and input physics (e.g., opacity, mass loss) are organized into individual thread-safe "modules," each of which is an independently functional unit that generates, tests, and exports a library to the general MESA libraries directory. This modular structure is unique among stellar evolution programs. One of its main advantages is that experimentation with different available physics or even implementation of new physics is easy and straightforward. The user input is given at runtime via the `inlist` file, which contains the user's choice for parameters for input physics, time step, mesh, and output options. The `run_star_extras.f` file, a Fortran module that is compiled at runtime, allows the user to introduce new routines that hook into the source codes in order to adapt MESA to the problem of interest. Examples include the introduction of new physics routines, modification of model outputs, and customization of time step adjustments.

Here we provide an overview of some of the features in MESAstar, namely its time step controls, adaptive mesh refinement, and parallelization. We refer the reader to Paxton et al. (2011, 2013, 2015) for more detailed information.

Choosing an appropriate time step throughout various stages of stellar evolution is critical to the accurate evolution of a model. It must be both sufficiently small to allow convergence and sufficiently large to carry out evolution calculations in a reasonable amount of time. In MESA, a new time step is first proposed using a scheme based on digital control theory (Söderlind & Wang 2006). Next, the proposed time step undergoes a series of tests to check if the hypothetical changes to various properties of the model (e.g., nuclear burning rate, luminosity, central density) in a single time step are adequately small, as excessively large changes can lead to convergence or accuracy issues in subsequent evolution.

At the beginning of each evolution step, MESAstar checks whether or not a spatial mesh adjustment

is necessary. Similar to time step controls, there is a trade-off between having sufficiently small cells to properly resolve physical processes locally while avoiding an unnecessarily fine grid that is computationally expensive. Remeshing involves the splitting and merging of cells, and each remesh plan aims to minimize the number of cells affected in order to reduce numerical diffusion and improve convergence. At the same time, the remesh plan must meet the criteria for the tolerated cell-to-cell changes in relevant variables, which are specifiable by the user in addition to the basic variables, e.g., mass, radius, and pressure. For instance, cells near a convective boundary might be split in order to better resolve its location, while cells well within the convective zone might be merged if they are sufficiently similar in, e.g., composition and temperature. We refer the reader to Section 2.10 for temporal and spatial convergence tests.

MESA is optimized for parallelization and uses OpenMP* to carry out computations in parallel. Since Paxton et al. (2011), MESA's performance has been greatly improved mainly due to the implementation of a new linear algebra solver—the single-most computationally expensive component—that is compatible with multicore processing. As demonstrated in Figure 48 of Paxton et al. (2013), many key components of MESAstar, such as the linear algebra solver and the evaluation of the nuclear reaction network, closely obey the ideal scaling law.

For this work, we use MESA version v7503 compiled with GNU Fortran version 4.9.3 installed as part of the MESA SDK version 245.†

2.3 Adopted Physics

In this section we review the relevant physics adopted in the models and their implementation in MESA. Readers who are interested in the most salient points can skip to Table 2.2, which presents a summary of the adopted physics. For the effects of varying some key physics ingredients, see Section 2.6.2.

*http://openmp.org/wp/

†http://www.astro.wisc.edu/ townsend/static.php?ref=mesasdk

Table 2.1: Summary of the Adopted Physics.

Ingredient	Adopted prescriptions & parameters	Section	Reference
Solar Abundance Scale	$X_\odot = 0.7154$, $Y_\odot = 0.2703$, $Z_\odot = 0.0142$	2.3.1	Asplund et al. (2009)
Equation of State	OPAL+SCVH+MacDonald+HELM+PC	2.3.2.1	Rogers & Nayfonov (2002); Saumon et al. (1995); MacDonald & Mullan (2012)
Opacity	OPAL Type I for $\log T \gtrsim 4$; Ferguson for $\log T \lesssim 4$; Type I $\rightarrow$ Type II at the end of H burning	2.3.2.2	Iglesias & Rogers (1993, 1996); Ferguson et al. (2005)
Reaction Rates	JINA REACLIB	2.3.2.3	Cyburt et al. (2010)
Boundary Conditions	ATLAS12; $\tau = 100$ tables + photosphere tables + gray atmosphere	2.3.3	Kurucz (1970, 1993)
Diffusion	Track five "classes" of species; MS only	2.3.4	Thoul et al. (1994); Paquette et al. (1986)
Radiation Turbulence	$D_{\rm RT} = 1$	2.3.4	Morel & Thévenin (2002)
Rotation	solid-body rotation at ZAMS with $v_{\rm ZAMS}/v_{\rm crit} = \Omega_{\rm ZAMS}/\Omega_{\rm crit} = 0.4$	2.3.5	Paxton et al. (2013)
Convection: Ledoux + MLT	$\alpha_{\rm MLT} = 1.82$, $\nu = 1/3$, $y = 8$	2.3.6.1	Henyey et al. (1965)
Overshoot	time-dependent, diffusive, $f_{\rm ov,\,core} = 0.0160$, $f_{\rm ov,\,env} = f_{\rm ov,\,sh} = 0.0174$	2.3.6.2	Herwig (2000)
Semiconvection	$\alpha_{\rm sc} = 0.1$	2.3.6.3	Langer et al. (1983)
Thermohaline	$\alpha_{\rm th} = 666$	2.3.6.3	Ulrich (1972); Kippenhahn et al. (1980)
Rotational Mixing	Include SH, ES, GSF, SSI, and DSI with $f_\mu = 0.05$ and $f_c = 1/30$	2.3.6.4	Heger et al. (2000)
Magnetic Effects	Not currently implemented	2.3.6.5	
Mass Loss: Low Mass Stars	$\eta_{\rm R} = 0.1$ for the RGB $\eta_{\rm B} = 0.2$ for the AGB	2.3.7.1	Reimers (1975) Blöcker (1995)
Mass Loss: High Mass Stars	$\eta_{\rm Dutch} = 1.0$ a combination of wind prescriptions for hot and cool stars and a separate WR wind prescription	2.3.7.2	Vink et al. (2000, 2001) Nugis & Lamers (2000) de Jager et al. (1988)
Mass Loss: Rotational	$\xi = 0.43$, boost factor capped at 10^4, $\dot{M}_{\rm max} = 10^{-3}\ M_\odot\ {\rm yr}^{-1}$	2.3.7.3	Langer (1998)

2.3.1 ABUNDANCES

The accurate determination of solar abundances has been an ongoing effort for decades. Within the last decade, there has been a systematic downward revision of the solar metallicity from $Z_\odot \sim 0.02$ (e.g., Anders & Grevesse 1989) to $Z_\odot \lesssim 0.015$ (e.g., Lodders et al. 2009; Asplund et al. 2009; Caffau et al. 2011). Recently, the abundances of C, N, O, and Ne have experienced dramatic revisions as a collective result of improved atomic and molecular linelists and the introduction of 3D non-local thermodynamic equilibrium (NLTE) hydrodynamical modeling techniques (see Asplund et al. 2009 for a review). In this paper, we adopt the *protosolar* abundances recommended by Asplund et al. (2009) as the reference scale for all metallicities, unless noted otherwise. In other words, [Z/H] is computed with respect to $Z = Z_{\odot,\,\rm protosolar} = 0.0142$, not $Z = Z_{\odot,\,\rm photosphere} = 0.0134$. The difference between the two is a consequence of diffusion of heavy elements out of the photosphere over time. We emphasize that this is not an attempt to redefine $Z_{\odot,\,\rm photosphere}$—the current photospheric abundances are determined by spectroscopy—

but rather to clarify what a "solar metallicity model" entails.

To compute X and Y for an arbitrary Z, we use the following formulae:

$$Y_{\rm p} = 0.249 \tag{2.1}$$

$$Y = Y_{\rm p} + \left(\frac{Y_{\odot,\,\rm protosolar} - Y_{\rm p}}{Z_{\odot,\,\rm protosolar}} \right) Z \tag{2.2}$$

$$X = 1 - Y - Z \ . \tag{2.3}$$

This approach adopts a primordial helium abundance $Y_{\rm p} = 0.249$ (Planck Collaboration et al. 2015) determined by combining the *Planck* power spectra, *Planck* lensing, and a number of "external data" such as baryonic acoustic oscillations. In the above equations, we assume a linear enrichment law to the protosolar helium abundance, $Y_{\odot,\,\rm protosolar} = 0.2703$ (Asplund et al. 2009), such that $\Delta Y/\Delta Z = 1.5$. Once Y is computed for a desired value of Z, X is trivial to compute. We assume the isotopic ratios ${}^2{\rm H}/{}^1{\rm H} = 2 \times 10^{-5}$ and ${}^3{\rm He}/{}^4{\rm He} = 1.66 \times 10^{-4}$ from Asplund et al. (2009).

2.3.2 Microphysics

2.3.2.1 Equation of State

The equation of state (EOS) tables in MESA are based on the OPAL EOS tables (Rogers & Nayfonov 2002), which smoothly transition to the SCVH tables (Saumon et al. 1995) at lower temperatures and densities. The extended MESA EOS tables cover $X = 0.0, 0.2, 0.4, 0.6, 0.8$, and 1.0, and $Z = 0.0, 0.02$, and 0.04. At higher metallicities, MESA switches to the MacDonald EOS tables (MacDonald & Mullan 2012) for $Z = 0.2$ and 1.0, which, unlike the HELM EOS tables (Timmes & Swesty 2000) used in the earlier versions of MESA, allow for partially ionized species. The HELM and PC tables (Potekhin & Chabrier 2010) are used at temperatures and densities outside the range covered by the OPAL + SCVH + MacDonald tables, and assume full ionization. The EOS tables in MESA also cover the late stages of WD

cooling, during which the ions in the core crystallize, although the current MIST models do not reach such conditions. The low-mass models are evolved until Γ, the central plasma interaction parameter or Coulomb coupling parameter, reaches 20 (see Section 2.5.1), and crystallization occurs at $\Gamma \approx 175$ for pure oxygen.

2.3.2.2 OPACITIES

MESA divides the radiative opacity tables into two temperature regimes, high ($\log T \gtrsim 4$) and low ($\log T \lesssim 4$), and treats them separately. This system allows for the user to choose, for the low temperature opacities, between either Ferguson et al. (2005) or Freedman et al. (2008) with updates to ammonia opacity from Yurchenko et al. (2011) and the pressure-induced opacity for molecular hydrogen from Frommhold et al. (2010). The high temperature opacity tables come from either OPAL (Iglesias & Rogers 1993, 1996) or OP (Seaton 2005). The OPAL tables are split into two types, Type I and Type II: Type I tables are used for $0.0 \leq X \leq 1.0 - Z$ and $0.0 \leq Z \leq 0.1$ for a fixed abundance pattern; Type II tables are optionally available which allow for enhanced carbon and oxygen abundances in addition to those already accounted for in Z, covering $0.0 \leq X \leq 0.7$ and $0.0 \leq Z \leq 0.1$. Type II opacities are particularly important for helium burning and beyond. The electron conduction opacity tables are originally based on Cassisi et al. (2007), but they have been extended to cover temperatures up to 10^{10} K and densities up to $10^{11.5}$ g cm^{-3} (Paxton et al. 2013).

We use the Ferguson et al. (2005) low temperature tables and the OPAL Type I tables, then gradually switch to the OPAL Type II opacities starting at the end of hydrogen burning, smoothly interpolating between $X < 10^{-3}$ and $X < 10^{-6}$. Note that we use the Asplund et al. (2009) protosolar mixture where available to be consistent with our choice of the solar abundance scale, but the opacity tables implemented in MESA were computed for the Asplund et al. (2009) photospheric abundances.

2.3.2.3 NUCLEAR NETWORK

We import the nuclear reaction rates directly from the JINA REACLIB database,* a compilation of the latest reaction rates in the literature (Cyburt et al. 2010). For example, the ^{15}N(p,α)^{12}C reaction rate comes from Angulo et al. (1999), while the triple-α reaction rate comes from Fynbo et al. (2005). We use the JINA reaction rates for p-p chains, cold and hot CNO cycles, triple-α process, α-capture up to ^{32}S, Ne-Na and Mg-Al cycles, and C/O burning. We adopt the `mesa_49.net` nuclear network in MESA.

The nuclear network tracks and solves for the abundances of the following 52 species: n, ^{1}H, ^{2}H, ^{3}He, ^{4}He, ^{7}Li, ^{7}Be, ^{9}Be, ^{10}Be, ^{8}B, ^{12}C, ^{13}C, ^{13}N, ^{14}N, ^{15}N, ^{14}O, ^{15}O, ^{16}O, ^{17}O, ^{18}O, ^{17}F, ^{18}F, ^{19}F, ^{18}Ne, ^{19}Ne, ^{20}Ne, ^{21}Ne, ^{22}Ne, ^{21}Na, ^{22}Na, ^{23}Na, ^{24}Na, ^{23}Mg, ^{24}Mg, ^{25}Mg, ^{26}Mg, ^{25}Al, ^{26}Al, ^{27}Al, ^{27}Si, ^{28}Si, ^{29}Si, ^{30}Si, ^{30}P, ^{31}P, ^{31}S, ^{32}S, ^{33}S, ^{34}S, ^{40}Ca, ^{48}Ti, ^{56}Fe. The three heaviest elements ^{40}Ca, ^{48}Ti, and ^{56}Fe are our modifications to the default `mesa_49.net` network and are inert species—they do not participate in any nuclear reactions—that are thus only affected by mixing and diffusion processes.

Electron screening is included for both the weak and strong regimes. We use the default option in MESA which computes the screening factors by extending the classic Graboske et al. (1973) method with that of Alastuey & Jancovici (1978), and adopting plasma parameters from Itoh et al. (1979) for strong screening.†

2.3.3 BOUNDARY CONDITIONS

The pressure and temperature in the outermost cell of a stellar model calculation must be specified as a set of boundary conditions in addition to the trivial boundary conditions at the center of the star. There is a multitude of options that ranges from simple analytic approximations to tables based on full atmospheric structure models.

*10/2015; https://groups.nscl.msu.edu/jina/reaclib/db/

†http://cococubed.asu.edu/code_pages/codes.shtml

The simplest choice, `simple_photosphere`, uses the Eddington $T(\tau)$ relation to obtain T:

$$T^4(\tau) = \frac{3}{4} T_{\rm eff}^4 \left(\tau + \frac{2}{3} \right) \quad , \tag{2.4}$$

where $T_{\rm eff}$ is calculated directly from the MESA interior model. Similarly, P is computed as follows:

$$P = \frac{\tau g}{\kappa} \left[1 + P_0 \frac{\kappa}{\tau} \frac{L}{M} \frac{1}{6\pi c G} \right] \quad . \tag{2.5}$$

The second term in the square brackets accounts for the nonzero radiation pressure (e.g., Cox 1968) which can be significant in high-mass stars. P_0 is a dimensionless factor of order unity used to scale up the radiation pressure in order to help convergence in massive stars and post asymptotic giant branch (post-AGB) stars radiating close to or at super-Eddington luminosities. We adopt $P_0 = 2$ for this work.

In most cases, the `simple_photosphere` option is a poor choice as there is no guarantee that κ and P from the interior model are consistent according to Equation 2.5, assumed to be the correct relation at the stellar surface. For this work, we adopt realistic model atmospheres as the outer boundary conditions for most locations in the Hertzsprung-Russell (HR) diagram. We have computed a new grid of 1D plane-parallel atmosphere models specifically for this project using the ATLAS12 code (Kurucz 1970, 1993). The atmospheres are computed to a Rosseland optical depth of 10^3 with $\alpha_{\rm MLT} = 1.25$ following the implementation of convection as outlined in Castelli et al. (1997).* We employed the latest atomic and molecular line lists from R. Kurucz, including molecules important for cool stars such as TiO and H_2O. Individual models are calculated for $\log(g) = 0$ to 5 and $T_{\rm eff} = 2500$ K to 50000 K for $[{\rm Z/H}] = -7.0$ to $+0.5$ on the Asplund et al. (2009) abundance scale. Beyond these limits the tables have been smoothly extrapolated to encompass all possible locations of the stellar tracks. This is a satisfactory solution since the few phases that fall into these extrapolated regimes (e.g., post-AGB) are typically very short-lived.

*Note that this value of $\alpha_{\rm MLT}$ adopted for the model atmosphere cannot be directly compared to $\alpha_{\rm MLT}$ adopted for the stellar interior in Section 2.3.6.1 due to differences in the details of the implementation of convection.

With model atmosphere tables in hand, one is left to choose where (in terms of Rosseland depth) to use the tables as boundary conditions for the models. The standard convention, which we adopt for most stars, is the photosphere, i.e., where $T = T_{\rm eff}$. However, for cooler dwarfs a more sensible choice is to set the boundary condition deeper in the atmosphere, i.e., $\tau = 100$. This option will result in more realistic models for cool low-mass stars whose atmospheres are heavily influenced by molecules that are not included in the MESA interior model calculations. This issue is less critical for the cool giants because the structure of these stars is overall less sensitive to the boundary condition (i.e., the pressure at the photosphere for giants is much closer to zero than for dwarfs). We refer the reader to Section 2.6.2 for additional discussion on this topic.

For our grid of models, the `tau_100_tables` option is used for 0.1–0.3 $M_\odot$, `photosphere_tables` is used for 0.6–10 $M_\odot$, and `simple_photosphere` is used for 16–300 $M_\odot$. To facilitate a smooth transition between different regimes, we run both `tau_100_tables` and `photosphere_tables` for 0.3–0.6 $M_\odot$ and `photosphere_tables` and `simple_photosphere` for 10–16 $M_\odot$. The tracks in this transition region are then blended (see Section 2.5.2 for more details). At the highest masses, `simple_photosphere` is a sufficient approximation due to the flattening of opacity as a function of temperature for $T_{\rm eff} \gtrsim 10^4$ K.

2.3.4 DIFFUSION

Microscopic diffusion and gravitational settling of elements are essential ingredients in stellar evolution models of low-mass stars, leading to a modification to the surface abundances and main sequence (MS) lifetimes, as well as a shift in the evolutionary tracks toward lower luminosities and temperatures in the HR diagram (e.g., Michaud et al. 1984; Morel & Baglin 1999; Salaris et al. 2000; Chaboyer et al. 2001; Bressan et al. 2012). Calculations of diffusion and gravitational settling are implemented in MESA following Thoul et al. (1994). All species are categorized into one of five "classes" according to their atomic

masses, each of which has a representative member whose properties are used to estimate the diffusion velocities. MESA's default set of representative members for the five classes are ^{1}H, ^{3}He, ^{4}He, ^{16}O, and ^{56}Fe. Atomic diffusion coefficients are calculated according to Paquette et al. (1986): the representative ionic charge for each class is estimated as a function of T, ρ, and free electrons per nucleon, while the diffusion velocity of the representative member is adopted. The diffusion equation is then solved using the total mass fraction within each class.

However, the inclusion of microscopic diffusion alone cannot reproduce observations of surface abundances in the Hyades open cluster and OB associations including the Orion association (e.g., Cunha & Lambert 1994; Varenne & Monier 1999; Daflon et al. 2001). Models with diffusion predict an over-depletion of helium and metals in the outer envelopes of stars with $M_{\rm i} > 1.4\ M_{\odot}$, a problem that appears to worsen with increasing mass due to a disappearing outer convection zone and a concomitant steepening of the temperature and pressure gradients (Morel & Thévenin 2002). The solution to this problem requires additional forces to counteract gravity. Radiative levitation (Vauclair 1983; Hu et al. 2011) can help to reduce the gravitational settling of highly charged elements, such as iron, via radiation pressure. However, it is thought to be mostly important in hot, luminous massive MS stars or helium-burning stars (e.g., hot subdwarf stars; Fontaine et al. 2008), and to have only a modest effect for solar-type stars (e.g., Alecian et al. 1993; Turcotte et al. 1998). We employ radiation turbulence (Morel & Thévenin 2002) to reduce the efficiency of diffusion in hot stars, though there exist other explanations for the observed surface abundances, including turbulent mixing due to differential rotation (e.g., Richard et al. 1996). We adopt the radiative diffusivity parameter $D_{\rm RT} = 1$, which relates the strength of radiative diffusivity (the deposition of photon momentum into the fluid, resulting in radiative mixing) to the kinematic radiative viscosity.

Since the effects of elemental diffusion are most significant in the absence of more efficient mixing processes, such as convection, diffusion is neglected for fully convective MS stars in the MIST models. Additionally, diffusion is expected to play a reduced role in massive stars and during some post-MS phases

(which are also associated with large convective envelopes) for which the evolutionary timescales are comparable to or much shorter than the timescale for diffusion and gravitational settling (e.g., Turcotte et al. 1998). Thus the effects of microscopic diffusion are considered only for the MS evolution. However, it may have a notable impact on both the atmospheres and interiors of cooling WDs by modifying the surface abundances and lengthening cooling times through the release of gravitational energy. The Thoul et al. (1994) formalism, which assumes isolated interactions between two particles at a time, breaks down in the regime of strongly coupled plasmas. This is a particularly relevant issue for the interiors of cooling WDs, and there is ongoing effort in MESA to update the diffusion implementation to account for this. The inclusion of diffusion during the post-MS evolution, especially the WD cooling phase, is one of the priorities for Paper II.

To summarize, the implementation of diffusion is limited to MS stars above the fully-convective limit for which it is most effective in terms of both the relevant timescales and the relative importance compared to other mixing processes.

2.3.5 Rotation

The effect of rotation on stellar models has been studied for decades (e.g., Strittmatter 1969; Fricke & Kippenhahn 1972; Tassoul 1978; Zahn 1983; Pinsonneault 1997; Heger et al. 2000; Maeder & Meynet 2000; Palacios et al. 2003; Talon & Charbonnel 2005; Denissenkov & Pinsonneault 2007; Hunter et al. 2007; Chieffi & Limongi 2013; Cantiello et al. 2014), but it remains as one of the most challenging and uncertain problems in stellar astrophysics. Rotation is particularly important for massive stars, as rotationally induced instabilities, combined with the non-negligible effects of radiation pressure, can significantly alter their evolution (e.g., Heger et al. 2000; Meynet & Maeder 2000; Hirschi et al. 2004; Yoon et al. 2006; Woosley & Heger 2006; de Mink et al. 2010; Georgy et al. 2012; Langer 2012; Köhler et al. 2015). Although the overall importance of rotation in models—lifetimes, surface abundances, evolutionary fates, to

name a few—has been explored, the details are not yet fully understood.

Rotation is inherently a 3D process, but the so-called "shellular approximation" allows stellar structure equations to be solved in 1D (Kippenhahn & Thomas 1970; Endal & Sofia 1976; Meynet & Maeder 1997; Heger et al. 2000; Paxton et al. 2013). This approximation is valid in the regime where strong anisotropic turbulence arises from differential rotation and smears out both chemical composition and velocity gradients along isobars (Zahn 1992; Meynet & Maeder 1997). As a result, the standard stellar structure equations are simply modified by centrifugal acceleration terms in the presence of rotation. More details on the implementation of rotation in MESA can be found in Paxton et al. (2013).

Our models are available in two varieties, with and without rotation. All rotating models are initialized with solid body rotation on the zero age main sequence (ZAMS), which is the standard choice in stellar evolution codes (Pinsonneault et al. 1989; Heger et al. 2000; Eggenberger et al. 2008). As discussed extensively in Heger et al. (2000), pre-main sequence (PMS) stars achieve rigid rotation due to convection, and once they settle onto ZAMS, they establish close-to-rigid rotation mainly via Eddington-Sweet circulation and Goldreich-Schubert-Fricke instability. However, it is worth noting that there are important exceptions. First, this rigid rotation approximation fails in the solar convection zone as inferred from helioseismology observations (e.g., Brown et al. 1989). Second, current detailed evolutionary models (e.g., Bouvier 2008; Gallet & Bouvier 2013) suggest that low-mass stars ($\lesssim 1.2\ M_\odot$), particularly those with slow and moderate rotation rates, have strong differential rotation profiles at ZAMS.

Currently, surface magnetic fields are not included in MESA calculations, which can couple to mass loss and give rise to magnetic braking (e.g., Weber & Davis 1967; Mestel 1968; ud-Doula & Owocki 2002; Meynet et al. 2011), a mechanism for winding down surface rotation over time in stars with appreciable convective envelopes (Kraft 1967; see also Section 2.3.6.5).

Since magnetic braking is not presently modeled in MIST, we do not include rotation for stars with $M_\mathrm{i} \leq 1.2\ M_\odot$ in order to reproduce the slow rotation rate observed in the Sun and in other low-mass stars.

Over the mass range 1.2 to 1.8 $M_\odot$, the rotation rate is gradually ramped up from 0 to the maximum value of $v_{\rm ZAMS}/v_{\rm crit} = \Omega_{\rm ZAMS}/\Omega_{\rm crit} = 0.4$, where $v_{\rm crit}$ and $\Omega_{\rm crit}$ are critical surface linear and angular velocities, respectively (See Equation 2.22). This rotation rate, also adopted in the Geneva models (Ekström et al. 2012),* is motivated by both recent observations of young B stars (Huang et al. 2010) and theoretical work on rotation rates in massive stars (Rosen et al. 2012). A comparison with observed rotation rates of both MS and evolved stars in the mass range 1.2–1.5 $M_\odot$ (Wolff & Simon 1997; Canto Martins et al. 2011) reveals that our ramping scheme produces velocities that are reasonable ($\sim$ 10–25 km s^{-1} during the main sequence for 1.3–1.35 $M_\odot$) even in the absence of magnetic braking.

Chemical mixing and angular momentum transport due to rotationally-induced instabilities are discussed in Section 2.3.6.4, and rotationally-enhanced mass loss is discussed in Section 2.3.7.3.

2.3.6 Mixing Processes

2.3.6.1 Convection

Mixing Length Theory (MLT), whose modern implementation in stellar evolution codes was pioneered by Böhm-Vitense (1958), describes the convective transport of energy in the stellar interior. There is a vexing yet crucial free parameter of order unity, $\alpha_{\rm MLT}$, that determines how far a fluid parcel travels before it dissolves into the background, $l_{\rm MLT}$, in units of the local pressure scale height, $H_{\rm P}$ ($l_{\rm MLT} = \alpha_{\rm MLT} H_{\rm P}$). In other words, it parametrizes how efficient convection is, because a large $\alpha_{\rm MLT}$ means that the parcel travels a large distance before it deposits its energy into the ambient medium.

Convective mixing of elements is treated as a time-dependent diffusive process with a diffusion coefficient computed within the MLT formalism, which may later be modified by overshoot mixing across convection boundaries (see Section 2.3.6.2). Convective heat flux is computed by solving the MLT cubic

*Note that $v_{\rm crit}$ and $\Omega_{\rm crit}$ are defined differently in MESA and in the Geneva models. In the Geneva models, the equatorial radius is 1.5 times larger than the polar radius when $\Omega = \Omega_{\rm crit}$ but this distinction is not made in MESA. See Section 2.1 in Georgy et al. (2013) for more details.

equations to obtain the temperature gradients (e.g., Equation 42 in Henyey et al. 1965). We adopt the modified version of MLT from Henyey et al. (1965) instead of the standard MLT prescription (Cox 1968), as the latter assumes no radiative losses from fluid elements and is therefore applicable only at high optical depth.* In addition to $\alpha_{\rm MLT}$, there are two free parameters, ν and y, which are multiplicative factors to the mixing length velocity and the temperature gradient in the convective element. The latter two parameters are set to 8 and 1/3, respectively (Henyey et al. 1965). This particular framework allows for convective efficiency to vary with the opacity of the convective element, an important effect to take into account in the layers near the stellar surface. The empirical calibration of $\alpha_{\rm MLT}$ is discussed in Section 2.4.1

Classically, the location of the convective region is determined using the Schwarzschild criterion, which implies that a region is convectively stable if

$$\nabla_T < \nabla_{\rm ad} \ , \tag{2.6}$$

where ∇_T is the local background temperature gradient (in practice, it is set to the radiative temperature gradient $\nabla_{\rm rad}$) and $\nabla_{\rm ad}$ is the adiabatic temperature gradient. Alternatively, the Schwarzschild criterion can be replaced by the Ledoux criterion, which also takes into account the composition gradient, ∇_μ. In this case, a region is convectively stable if

$$\nabla_T < \nabla_{\rm L} \tag{2.7}$$

$$\nabla_{\rm L} \equiv \nabla_{\rm ad} - \frac{\chi_\mu}{\chi_T}\nabla_\mu \tag{2.8}$$

$$\chi_\mu \equiv \left[\frac{\partial \ln(P)}{\partial \ln(\mu)}\right]_{\rho,T} \tag{2.9}$$

$$\chi_T \equiv \left[\frac{\partial \ln(P)}{\partial \ln(T)}\right]_{\rho,\mu} \ , \tag{2.10}$$

*We note that neither prescription is adequate for treating the radiation dominated envelopes of very massive stars, for which 1D stellar evolution calculations must be considered uncertain. See Jiang et al. (2015) for more details.

where the thermodynamic derivatives χ_μ and χ_T are equal to -1 and 1 for an ideal gas, respectively. We adopt the Ledoux criterion for convection in our models to account for the composition effects in the stellar interiors.

2.3.6.2 Overshoot Mixing

Rather unsurprisingly, the MLT framework, which relies on a 1D diffusive model in place of a full 3D hydrodynamical treatment, offers an incomplete description of convection. To model the mixing occurring at convective boundaries, also known as overshoot mixing, one must turn to yet another set of parameterizations. Typically, a convective region is extended beyond the fiducial boundary determined by either the Schwarzschild or Ledoux criterion in order to account for the nonzero momentum of the fluid element approaching the edge of the convective zone as well as its subsequent penetration into the non-convective region (e.g., Böhm 1963; Shaviv & Salpeter 1973; Maeder 1975; Roxburgh 1978; Bressan et al. 1981). This overshoot action leads to enhanced mixing and it can account for both the observed properties of asymptotic giant branch (AGB) and post-AGB stars (Herwig 2000), the observed MS width (e.g, Schaller et al. 1992), and the main sequence turn off (MSTO) morphology in clusters such as M67 (e.g., Magic et al. 2010).

There are two prescriptions for convective overshoot available in MESA. The first method, which we call step overshoot, is to simply extend the fiducial convective boundary by a fraction, usually ~ 0.2, of the local pressure scale height. This instantaneous treatment is often calibrated to fit the observed MSTO of stellar clusters and associations, and is a commonly adopted scheme in many stellar evolution codes (e.g., Pietrinferni et al. 2004; Demarque et al. 2004; Dotter et al. 2008; Brott et al. 2011a; Bressan et al. 2012; Ekström et al. 2012).

The second method, adopted in the present work, was motivated by the plume-like nature of convective elements seen in 2D and 3D radiation hydrodynamic simulations, where coherent downward and

upward flows were observed rather than a hierarchy of blob-like eddies (e.g., Freytag et al. 1996). This led to a picture in which the turbulent velocity field decays exponentially away from the fiducial convective boundary and the convective element eventually disintegrates in the overshoot region through a diffusion process. Following the parametrization discussed in Herwig (2000), the resulting diffusion coefficient in the overshoot region is given by

$$D_{\rm OV} = D_0 \exp\left(\frac{-2z}{H_{\rm v}}\right) \;;\; H_{\rm v} = f_{\rm ov} H_{\rm P} \;, \tag{2.11}$$

where $H_{\rm v}$ is the velocity scale height of the overshooting convective elements at the convective boundary, $f_{\rm ov}$ is a free parameter that essentially determines the efficiency of overshoot mixing, $H_{\rm P}$ is the local pressure scale height, and D_0 is the diffusion coefficient in the unstable region "near" the convective boundary (more specifically at a depth of $f_{0,\,\rm ov} H_{\rm P}$ from the convective boundary). For simplicity, we adopt two sets of ($f_{\rm ov}$, $f_{0,\,\rm ov}$) values, one for the core and another for shell/envelope, irrespective of the type of burning taking place in the overshoot region. For further simplicity, $f_{0,\,\rm ov}$ is set to $0.5 f_{\rm ov}$. The temperature gradient in the overshoot region is assumed to be equal to the radiative gradient as in the step overshoot approach.

Other models in the literature make use of an additional parameterization to both avoid a physically unrealistic size of the overshoot region outside a small convective core as well as to account for the possibility that convective overshoot efficiency is smaller in lower mass stars (Pietrinferni et al. 2004; Demarque et al. 2004; Dotter et al. 2008; Bressan et al. 2012). In the step overshoot formalism where the size of the convective core is extended by a fraction $f_{\rm ov,\,step}$ of $H_{\rm P}$, one could end up with a physically unrealistic situation where the size of the overshoot region exceeds the size of the convective core itself. This can occur when the convective core is very small, e.g., for the critical mass around 1.1–1.2 $M_\odot$ when the CNO cycle begins to dominate over the pp-chain and the hydrogen-burning core becomes convective instead of radiative. Since the convective core boundary is not far from the center and $H_{\rm P}$ formally diverges as $r \to 0$,

the size of the overshoot region, $f_{\mathrm{ov,\,step}} H_{\mathrm{P}}$, also diverges. Thus, to avoid the excessive growth of the convective core for low-mass MS stars, the common solution is to gradually ramp up the overshoot efficiency from $M_1 \sim 1\ M_\odot$ to $M_2 \sim 1.7\ M_\odot$, with no convective overshoot below M_1 and maximum efficiency above M_2. These boundary masses vary with metallicity due to opacity effects (Demarque et al. 2004; Bressan et al. 2012). In the exponential overshoot formalism adopted in this work, we bypass this issue, and thus do not require a secondary parameterization involving M_1 and M_2.

We adopt a modest overshoot efficiency $f_{\mathrm{ov,\,core}} = 0.016$ for the core which is roughly equivalent to $f_{\mathrm{ov,\,step}} = 0.2$ in the step overshoot scheme (Magic et al. 2010). This value is calibrated to reproduce the shape of the MSTO in the open cluster M67 (Section 2.8.3.1). However, it is worth noting that the strength of core convective overshoot depends on numerous other factors as well. For instance, Stothers & Chin (1991) explored the role of opacities in models with core overshoot and found that the overall increase in radiative opacities from the OPAL group (Iglesias & Rogers 1991) compared to the older values from the Los Alamos groups (e.g., Cox & Stewart 1965, 1970) reduced the overshoot efficiency required to reproduce observations of intermediate- and high-mass stars. Magic et al. (2010) studied how variations in the solar abundances (Asplund et al. 2005 vs. Grevesse & Sauval 1998), element diffusion, overshooting, and nuclear reaction rates influence the MSTO morphology in M67. The authors concluded that the appearance of the characteristic MSTO hook (also known as the "Henyey hook") depends sensitively on the choice of the input solar abundances and that the effects of uncertain input physics on the Henyey hook morphology are degenerate.

We emphasize that the strength of convective overshoot is calibrated purely empirically: the overshoot efficiency in the core is constrained by matching the MSTO in M67, and the overshoot efficiency in the envelope, $f_{\mathrm{ov,\,env}}$, is chosen along with α_{MLT} during solar calibration (Section 2.4.1). As noted in Bressan et al. (2012), envelope overshoot has a negligible effect on the evolution, e.g., the MS lifetime, though it is believed to affect the surface abundances of light elements, the location of the red giant branch

(RGB) bump, and the extension of the blue loops. We also remind the reader that the overshoot efficiency in shells, e.g., hydrogen-burning shells during the RGB, is set to $f_{\mathrm{ov,\,env}}$ for simplicity.

2.3.6.3 Semiconvection and Thermohaline Mixing

As noted in Section 2.3.6.1, we adopt the Ledoux criterion for convection in our models. Due to the additional composition gradient term, a region that is formally convectively unstable to Schwarzschild criterion may be stable according to the Ledoux criterion (i.e., a thermally unstable medium with a stabilizing, positive composition gradient), which leads to a type of mixing called semiconvection. The importance of semiconvection on the evolution of massive stars has been studied for many decades, e.g., during the core helium burning phase (Stothers & Chin 1975; Langer et al. 1985; Grossman & Taam 1996). The fraction of a star's core helium burning lifetime spent on the Hayashi line relative to that in the blue part of the HR diagram, in other words the ratio of red supergiants to blue supergiants, is found to depend sensitively on the inclusion of semiconvection in the model. Additionally, the resulting core mass has significant implications for the supernova progenitors, from their ability to undergo a successful explosion (e.g., Sukhbold & Woosley 2014) to the actual nucleosynthetic yields (e.g., Langer et al. 1989; Heger & Woosley 2002; Rauscher et al. 2002). Semiconvection also operates in lower-mass stars with convective cores on the MS and it can have an important effect on the actual size and appearance of the core (e.g., Faulkner & Cannon 1973; Silva Aguirre et al. 2011; Paxton et al. 2013).

Alternately, a thermally stable medium may have a negative, destabilizing composition gradient, which triggers a different type of instability called thermohaline mixing. An inverted chemical composition gradient is rare in stars, since fusion usually occurs inside out and synthesizes lighter elements into heavier products. This phenomenon can occur due to mass-transfer in binaries (Stothers & Simon 1969; Stancliffe et al. 2007), off-center ignition in semi-degenerate cores (Siess 2009), or the ^{3}He(^{3}He,2p)^{4}He reaction taking place just beyond the hydrogen-burning shell during the RGB, horizontal branch (HB),

and AGB (Eggleton et al. 2006; Charbonnel & Zahn 2007; Charbonnel & Lagarde 2010; Stancliffe 2010; Cantiello & Langer 2010). Thermohaline mixing is thought to be responsible for the modification of surface abundances of RGB stars near the luminosity bump that otherwise cannot be explained using standard models. However, more recent work suggests that thermohaline mixing alone cannot account for the observed surface abundance anomalies (Denissenkov 2010; Traxler et al. 2011; Wachlin et al. 2011, 2014).

In MESA, semiconvection and thermohaline mixing are both implemented as time-dependent diffusive processes. The diffusion coefficient for semiconvection is computed following Langer et al. (1983):

$$D_{\rm sc} = \alpha_{\rm sc} \left(\frac{K}{6 C_P \rho} \right) \frac{\nabla_T - \nabla_{\rm ad}}{\nabla_{\rm L} - \nabla_T} \ , \tag{2.12}$$

where K is the radiative conductivity, C_P is the specific heat at constant pressure, and $\alpha_{\rm sc}$ is a dimensionless free-parameter. Similarly, the diffusion coefficient for thermohaline mixing is computed following Ulrich (1972) and Kippenhahn et al. (1980):

$$D_{\rm th} = \alpha_{\rm th} \left(\frac{3K}{2 C_P \rho} \right) \frac{-\frac{\chi_\mu}{\chi_T} \nabla_\mu}{\nabla_T - \nabla_{\rm ad}} \ , \tag{2.13}$$

where $\alpha_{\rm th}$ is a dimensionless number that describes the aspect ratio of the mixing blobs or "fingers" (a large $\alpha_{\rm th}$ corresponds to slender fingers).

As summarized in Paxton et al. (2013), the range of $\alpha_{\rm sc}$ and $\alpha_{\rm th}$ adopted by various authors spans several orders of magnitude, partially due to differences in the implementation in various codes. We adopt $\alpha_{\rm sc} = 0.1$ though values as small as 0.001 or as large as 1 can be found in the literature (Langer 1991; Yoon et al. 2006). For thermohaline mixing we adopt $\alpha_{\rm th} = 666$, as this value has been shown to reproduce the surface abundances anomalies in RGB stars past the luminosity bump (Charbonnel & Zahn 2007; Cantiello & Langer 2010). Note however that in the literature $\alpha_{\rm th}$ spans the range 1 to 1000 (Kippenhahn et al. 1980; Charbonnel & Zahn 2007; Cantiello & Langer 2010; Stancliffe 2010; Wachlin et al. 2011). There are on-

going theoretical efforts aimed at eliminating these free parameters with full 3D simulations (e.g., Traxler et al. 2011; Wood et al. 2013; Spruit 2013; Brown et al. 2013).

2.3.6.4 Rotationally-Induced Instabilities

In MESA, the transport of both chemicals and angular momentum arising from rotationally-induced instabilities are treated in a diffusion approximation (Endal & Sofia 1978; Zahn 1983; Pinsonneault et al. 1989; Heger et al. 2000; Yoon & Langer 2005) in place of the alternative diffusion-advection approach (Maeder & Meynet 2000; Meynet & Maeder 2000; Eggenberger et al. 2008; Potter et al. 2012). The five rotationally-induced instabilities included in our models are: dynamical shear instability, secular shear instability, Solberg-Høiland (SH) instability, Eddington-Sweet (ES) circulation, and Goldreich-Schubert-Fricke (GSF) instability (Heger et al. 2000; Paxton et al. 2013). Of these, ES circulation and shear instabilities have the largest impact on the evolution of a rotating star. We refer the reader to Heger et al. (2000) and Maeder & Meynet (2000) for excellent overviews of these phenomena.

Once the diffusion coefficients for these rotational mixing processes are computed, they are combined with the diffusion coefficients for convection, semiconvection, and thermohaline. This grand sum enters the angular momentum and abundance diffusion equations solved at each time step. There are two free parameters in this implementation, first introduced by Pinsonneault et al. (1989) to model the Sun: f_c, a number between 0 and 1 that represents the ratio of the diffusion coefficient to the turbulent viscosity, which scales the efficiency of composition mixing to that of angular momentum transport; and f_μ, a factor that encodes the sensitivity of rotational mixing to the mean molecular weight gradient, ∇_μ. A small f_c corresponds to a process that transports angular momentum more efficiently than it can mix material, and a small f_μ means that rotational mixing is efficient even in the presence of a stabilizing ∇_μ. We adopt $f_c = 1/30$ and $f_\mu = 0.05$ following Pinsonneault et al. (1989), Chaboyer & Zahn (1992), and Heger et al. (2000). As we demonstrate in Section 2.9.4, these parameters produce surface nitrogen enhancements that

are in reasonable agreement with the observations.

2.3.6.5 MAGNETIC EFFECTS

There is a growing body of evidence that our understanding of internal angular momentum transport in stars is not complete. For example, the observed spin rates of WDs and neutron stars (Heger et al. 2005; Suijs et al. 2008) and the angular velocity profiles inferred from asteroseismic observations of red giants (Eggenberger et al. 2012; Cantiello et al. 2014) cannot be reproduced with models that only include rotational mixing from hydrodynamic instabilities and circulations.

Spruit-Tayler (ST) dynamo is a mechanism for the amplification of seed magnetic fields in radiative stellar interiors in the presence of differential rotation (Spruit 2002). Stellar models including torques from ST dynamo fields can reproduce the flat rotation profile in the solar interior (Mestel & Weiss 1987; Charbonneau & MacGregor 1993; Eggenberger et al. 2005) and the observed spin rates of WDs and neutron stars (Heger et al. 2005; Suijs et al. 2008), although they still cannot explain the slow rotation rates of cores in red giants (Cantiello et al. 2014). The chemical mixing and the transport of angular momentum due to internal magnetic fields are not included in our models, though this is implemented in MESA following KEPLER (Heger et al. 2005) and STERN (Petrovic et al. 2005). We note that the very existence of the ST-dynamo loop is still under debate (Braithwaite 2006; Zahn et al. 2007), and there are ongoing efforts to understand the role of angular momentum transport via magnetic fields in radiative stellar regions (e.g. Rüdiger et al. 2015; Wheeler et al. 2015).

Magnetic fields are also observed near the stellar surface, which are thought to be either of fossil origin (e.g., Braithwaite & Spruit 2004) or generated through dynamo operating in convective zones in the outer layers of low-mass stars (e.g., Brandenburg & Subramanian 2005). However, as discussed in Section 2.3.5, magnetic braking due to the coupling between winds and surface magnetic fields is not yet included in MESA.

2.3.7 Mass Loss

The implementation of mass loss in stellar evolution calculations is based on a number of observationally- and theoretically-motivated prescriptions. It is frequently cited as one of the most uncertain ingredients in stellar evolution, and is thought to play a crucial role in the advanced stages of stellar evolution for low-mass stars and in all phases of evolution for massive stars (see Smith 2014 for a recent review on this topic). In this section we review our treatment of mass loss across the HR diagram. We note that the total mass loss rate is capped at $10^{-3}\ M_{\odot}\ \mathrm{yr}^{-1}$ in all models to prevent convergence problems.

2.3.7.1 Low Mass Stars

Mass loss for stars with masses below $10\ M_{\odot}$ is treated via a combination of the Reimers (1975) prescription for the RGB and Blöcker (1995) for the AGB. Both mass loss schemes are based on global stellar properties such as the bolometric luminosity, radius, and mass:

$$\dot{M}_{\mathrm{R}} = 4\times10^{-13}\eta_{\mathrm{R}}\frac{(L/L_{\odot})(R/R_{\odot})}{(M/M_{\odot})}\ \mathrm{M}_{\odot}\ \mathrm{yr}^{-1}\ , \tag{2.14}$$

$$\dot{M}_{\mathrm{B}} = 4.83\times10^{-9}\eta_{\mathrm{B}}\frac{(L/L_{\odot})^{2.7}}{(M/M_{\odot})^{2.1}}\frac{\dot{M}_{\mathrm{R}}}{\eta_{\mathrm{R}}}\ \mathrm{M}_{\odot}\ \mathrm{yr}^{-1}\ , \tag{2.15}$$

where η_{R} and η_{B} are factors of order unity. These free parameters have been tuned to match numerous observational constraints, including the initial-final mass relation (Section 2.8.2; see also Kalirai et al. 2009), AGB luminosity function (Section 2.8.5.1; see also Rosenfield et al. 2014), and asteroseismic constraints from open cluster members in the *Kepler* fields (Miglio et al. 2012). The Blöcker (1995) mass loss scheme was proposed as an alternative to the classic Reimers (1975) prescription to account for the onset of the superwind phase found in dynamical simulations of atmospheres of Mira-like variables. However, we emphasize that these are still empirically-motivated recipes and therefore remain agnostic on the subject of the actual mechanism driving the winds (see a review by Willson 2000 for a discussion on, e.g., dust-driven

winds).

For simplicity, we turn on Reimers mass loss at the beginning of the evolution, but a negligible amount of mass loss occurs throughout the MS ($\sim 10^{-13}\ M_\odot\ \mathrm{yr}^{-1}$ for a solar metallicity 1 $M_\odot$ star). Once core helium is depleted, the mass loss rate is chosen to be $\max[\dot{M}_\mathrm{R}, \dot{M}_\mathrm{B}]$ at any given time. We adopt $\eta_\mathrm{R} = 0.1$ and $\eta_\mathrm{B} = 0.2$ in order to reproduce the initial-final mass relation (Section 2.8.2) and the AGB luminosity functions in the Magellanic Clouds (Section 2.8.5.1).

2.3.7.2 High Mass Stars

For hot and luminous massive stars, mass loss is thought to arise from the absorption of ultraviolet photons by metal ions in the atmosphere, resulting in a preferentially outward momentum transfer from the absorbed photons to the plasma (line-driven winds; Lucy & Solomon 1970; Castor et al. 1975). For our models, mass loss for stars above 10 $M_\odot$ uses a combination of radiative wind prescriptions, collectively called the `Dutch` mass loss scheme in MESA, inspired by Glebbeek et al. (2009). There is an option for an overall scaling factor η_Dutch analogous to η_R and η_B for the low-mass stars, but we adopt $\eta_\mathrm{Dutch} = 1.0$. For prescriptions that include metallicity-scaling, we retain the reference $Z_\odot$ adopted by each author. We expect this difference to have a negligible effect relative to the large overall uncertainties in mass loss prescriptions.

We now describe our mass-loss scheme for high-mass stars in each region of the HR diagram:

1. For $T_\mathrm{eff} > 1.1 \times 10^4$ K and X_surf (surface hydrogen mass fraction) > 0.4, the mass loss prescription from Vink et al. (2000, 2001) is used, which is appropriate for the early phases of the evolution prior to the stripping of the hydrogen-rich envelope. The authors computed mass loss rates using a Monte Carlo radiative transfer code, taking into account multiple scatterings and assuming that the loss of photon energy is coupled to the momentum gain of the wind. The Vink mass loss rate is specified by five parameters; M, L, T_eff, v_∞/v_esc, and Z_surf.

For $2.75 \times 10^4 < T_{\rm eff} < 5 \times 10^4$ K,

$$\begin{aligned} \dot{M}_{\rm V,\,hot} = 10^{-6.697} \times (L/10^5 L_\odot)^{2.194} \times \\ (M/30\,M_\odot)^{-1.313} \times \left(\frac{v_\infty/v_{\rm esc}}{2.0}\right)^{-1.226} \times \\ (T_{\rm eff}/4 \times 10^4\ {\rm K})^{0.933} \times \\ 10^{-10.92[\log(T_{\rm eff}/4\times10^4\ {\rm K})]^2} \times (Z_{\rm surf}/Z_\odot)^{0.85} \quad . \end{aligned} \tag{2.16}$$

The ratio of terminal flow velocity to the escape velocity increases with metallicity according to $v_\infty/v_{\rm esc} = 2.6(Z_{\rm surf}/Z_\odot)^{0.13}$.

For $1.1 \times 10^4 < T_{\rm eff} < 2.25 \times 10^4$ K,*

$$\begin{aligned} \dot{M}_{\rm V,\,cool} = 10^{-6.688} \times (L/10^5 L_\odot)^{2.210} \times \\ (M/30\,M_\odot)^{-1.339} \times \left(\frac{v_\infty/v_{\rm esc}}{2.0}\right)^{-1.601} \times \\ (T_{\rm eff}/4 \times 10^4\ {\rm K})^{1.07} \times (Z_{\rm surf}/Z_\odot)^{0.85} \quad , \end{aligned} \tag{2.17}$$

where $v_\infty/v_{\rm esc} = 1.3(Z_{\rm surf}/Z_\odot)^{0.13}$.

For $2.25 \times 10^4 \leq T_{\rm eff} \leq 2.75 \times 10^4$ K, either $\dot{M}_{\rm V,\,hot}$ or $\dot{M}_{\rm V,\,cool}$ is adopted depending on the exact position of the so-called bi-stability jump, a phenomenon in which $\dot{M}$ increases with decreasing $T_{\rm eff}$ due to the recombination of metal lines:

$$T_{\rm eff,\,jump} = 61.2 + 2.59 \log\langle\rho\rangle \quad , \tag{2.18}$$

where $\langle\rho\rangle$ corresponds to the characteristic wind density at 50% of the terminal velocity of the wind. The successful predictions of the mass loss rates and the bi-stability jump near $T_{\rm eff} \sim 2.5 \times 10^4$ K for the Galactic and SMC O-type stars have made the Vink prescription a popular choice among massive star modelers (but see the discussion below).

2. Once the star reaches $T_{\rm eff} > 10^4$ K and $X_{\rm surf} < 0.4$, it is formally identified as a Wolf-Rayet (WR) star and we switch over to the Nugis & Lamers (2000) empirical mass loss prescription which depends strongly on luminosity and chemical composition:

$$\dot{M}_{\rm NL} = 10^{-11} (L/L_\odot)^{1.29} X_{\rm surf}^{1.7} Z_{\rm surf}^{0.5}\ {\rm M}_\odot\ {\rm yr}^{-1} \quad . \tag{2.19}$$

This formula has been shown to reproduce the properties of a large sample of Galactic WR stars (WN, WC, and WO subtypes) that have well-constrained stellar and wind parameters (Nugis & Lamers 2000). With Equation 2.19, we are able to reproduce the observed ratio of WC to WN subtypes as a function of metallicity (see Section 2.9.3).

*In Vink et al. (2001), mass loss rates were computed for $T_{\rm eff} \geq 1.25 \times 10^4$ K, but the prescription is extended down to $T_{\rm eff} = 1.1 \times 10^4$ K in MESA.

3. For all stars with $T_{\rm eff} < 10^4$ K,* including stars in the red supergiant (RSG) phase, we utilize the de Jager et al. (1988) empirically-derived wind prescription:

$$\dot{M}_{\rm dJ} = 10^{-8.158}(L/L_\odot)^{1.769}T_{\rm eff}^{-1.676}\ {\rm M}_\odot\ {\rm yr}^{-1}\ . \tag{2.20}$$

Although a quantitative model of mass loss in RSGs does not exist yet, it is believed that the main mechanism is dust-driven outflows. The low temperatures and pulsations in the outer layers lead to the condensation of dust at large radii, which is then driven out due to radiation pressure on grains (Mauron & Josselin 2011). In a recent work comparing different wind prescriptions with mass loss rates estimated from a sample of RSGs in the Galaxy and in the Magellanic Clouds, Mauron & Josselin (2011) found that the de Jager rates agree to within a factor of 4 with most estimates derived from the 60 μm flux. Furthermore, the authors concluded that the de Jager wind recipe performs better overall compared to more recent prescriptions, though they recommended an additional metallicity scaling $(Z_{\rm surf}/Z_\odot)^{0.7}$. For simplicity, we adopt the original de Jager prescription available in MESA.

A recent review by Smith (2014) explores some of the shortcomings of these prescriptions, one of which is that they fail to account for the clumpiness and inhomogeneity in outflows.† For instance, mass loss inferred from Hα emission or free-free continuum excess that assumes a homogeneous wind (e.g., de Jager et al. 1988; Nieuwenhuijzen & de Jager 1990) is believed to overestimate the true rate by a factor of 2 to 3. However, the reduced mass loss rate corrected for clumpiness may be problematic for the formation of WR stars, which requires the removal of their hydrogen-rich envelopes. Eruptive episodic mass loss episodes and/or binaries are likely to play a role (e.g., Smith & Owocki 2006; Yoon & Cantiello 2010; Sana et al. 2012), but neither phenomenon can be realistically captured in a simple recipe for implementation in a 1D stellar evolution code. Other forms of enhanced mass loss rates include super-Eddington winds when the stellar luminosity exceeds Eddington luminosity (Gräfener et al. 2011; Vink et al. 2011).

*In MESA, mass loss rate for $10^4 < T_{\rm eff} < 1.1 \times 10^4$ is computed by smoothly transitioning between the low temperature prescription (de Jager) and high temperature prescription (Vink or Nugis & Lamers).

†An exception is the Nugis & Lamers (2000) prescription which does take clumping effects into account.

2.3.7.3 Rotationally-Enhanced Mass Loss

Observations of O and B type stars have long argued for rotationally-enhanced mass loss rates (Gathier et al. 1981; Vardya 1985; Nieuwenhuijzen & de Jager 1988). It is now a standard ingredient in modern stellar evolution models with rotation (e.g., Heger et al. 2000; Brott et al. 2011a; Potter et al. 2012). In MESA, mass loss rates are enhanced in models as a function of surface angular velocity Ω as follows:

$$\dot{M}(\Omega) = \dot{M}(0) \left(\frac{1}{1 - \Omega/\Omega_{\rm crit}} \right)^{\xi} , \tag{2.21}$$

where $\dot{M}(0)$ is the standard mass loss rate (Reimers, Blöcker, or "Dutch"), ξ is assumed to be 0.43 (Friend & Abbott 1986; Bjorkman & Cassinelli 1993; Langer 1998), and $\Omega_{\rm crit}$ is the critical angular velocity at the surface:

$$\Omega_{\rm crit}^2 = \left(1 - \frac{L}{L_{\rm Edd}} \right) \frac{GM}{R^3} . \tag{2.22}$$

The Eddington luminosity, $L_{\rm Edd}$, is a mass-weighted average over the optical depth τ between 1 and 100. For stars close to the Eddington limit, $\Omega_{\rm crit}$ approaches 0 and therefore even a small Ω will result in a dramatic boost according to Equation 2.21. To prevent the mass loss from becoming too catastrophic, we cap the rotational boost to 10^4.

2.4 Solar Model

2.4.1 Solar Calibration

As mentioned in Section 2.3.6.1, it is customary to calibrate the mixing length parameter, $\alpha_{\rm MLT}$, using helioseismic data and surface properties of the Sun. We utilize the MESA test suite `solar_calibration` which conducts an extensive parameter search using the simplex method to obtain a set of input parameters that reproduces the solar observations. We vary the initial composition of the Sun, $\alpha_{\rm MLT}$, and convective

Table 2.3: Solar calibration results.

Parameter	Target	Model Value	Fractional Error (%)
$L_\odot (10^{33}$ erg s$^{-1})$	3.828 (XXIXth IAU resolutions B2 and B3)	3.828	4.1×10^{-3}
$R_\odot (10^{10}$ cm)	6.957 (IAU)	6.957	1.2×10^{-3}
$T_{\text{eff},\odot}$ (K)	5772 (IAU)	5772	2.4×10^{-3}
X_{surf}	0.7381(Asplund et al. 2009)	0.7514	1.8
Y_{surf}	0.2485 (Basu & Antia 2004)	0.2351	5.4
Z_{surf}	0.0134(Asplund et al. 2009)	0.0134	0.3
R_{cz}	0.7133 (Basu & Antia 2004)	0.7321	2.6
α_{MLT}	-	1.82	-
$f_{\text{ov, env}}$	-	0.0174	-
$\text{X}_{\text{initial}}$	-	0.7238	-
$\text{Y}_{\text{initial}}$	-	0.2612	-
$\text{Z}_{\text{initial}}$	-	0.0150	-

overshoot in the envelope. For each iteration, a new set of parameters is drawn and the star is evolved from the PMS to 4.57 Gyr.* A global χ^2 value is computed by summing over the $\log L$, $\log R$, surface composition, R_{cz} (the location of the base of the convection zone), and δc_{s} (model $-$ observed sound speed) terms with non-uniform user-defined weights. This process is repeated until χ^2 ceases to change considerably and the tolerance parameters are met. For simplicity and consistency, the target solar values we adopt are the same nominal values recommended by the IAU.

Table 2.4 summarizes the solar calibration results and Figure 2.1 shows $\delta c_{\text{s}}/c_{\text{s}}$, the fractional error in sound speed compared to that from helioseismic observations (Rhodes et al. 1997), as a function of radius. The best-fit MIST solar-calibrated model is shown in black and two Serenelli et al. (2009) models adopting Grevesse & Sauval 1998 (GS98) and Asplund et al. 2009 (AGSS09) protosolar abundances are shown in red and blue, respectively.

Although the model $\log L$ and $\log T_{\text{eff}}$ are in excellent agreement with the observed values, there are noticeable discrepancies in the surface helium abundance, the location of the base of the convection zone, and the sound speed profile. Although many initial guesses and different weighting schemes were

*As noted by Bahcall et al. (2006), there is some ambiguity in the exact definition of the "age of the Sun" as the PMS contraction is estimated to last approximately 0.04 Gyr. For simplicity, we adopt the commonly assumed age of 4.57 Gyr.

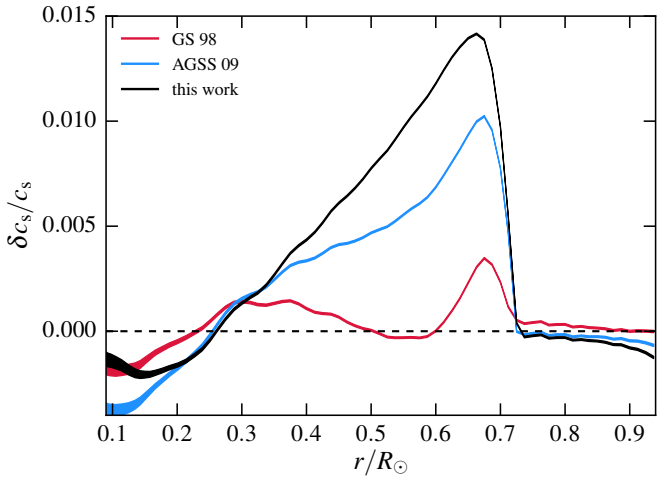


Figure 2.1: The fractional error in sound speed compared to helioseismology observations from Rhodes et al. (1997) for the present model (black) and two Serenelli et al. (2009) models each with Grevesse & Sauval 1998 (GS98; red) and Asplund et al. 2009 (AGSS09; blue) meteoritic abundances.

explored, we were unable to obtain a solar model that satisfies all available observational constraints. This is a well-known problem for solar models that adopt the AGSS09 abundances (e.g., Asplund et al. 2009; Serenelli et al. 2009).

The helium surface abundance at 4.57 Gyr in the best solar model is much lower compared to the helioseismologically inferred value of 0.2485 ± 0.0034 (Basu & Antia 2004). While most elemental abundances are determined through 3D spectroscopic modeling, the helium abundance is inferred indirectly from helioseismology, relying on the change in the adiabatic index in the He II ionization zone near the surface (Asplund et al. 2009). The tension between the helioseismic value and the inferred abundance from interior modeling was noted in Asplund et al. (2009), and remains an unsolved problem to this day.

The sound speed profile comparison shows that the GS98 model is in good agreement while the models adopting the AGSS09 abundances show a large deviation at $\sim 0.6\ R_\odot$. This is partly due to the discrepancy between the predicted and observed locations of the convective boundary. In particular, the lower oxygen and neon abundances in AGSS09 relative to the older models like GS98 (or an even newer model like Caffau et al. 2011) imply a smaller mean opacity below the convective zone, which shifts the inner

convective boundary further out in radius. The abundance of oxygen, one of the most abundant and important elements, has undergone a striking overall downward revision over the past few decades. Still, there are likely lingering uncertainties in the surface abundance determinations due to the challenges associated with spectroscopic modeling, such as non-LTE effects, line blending, and uncertainties in the atomic and molecular data (Asplund et al. 2009).

The Serenelli et al. (2009) AGSS09 sound speed profile is in better agreement with the observed profile, likely because their model matches the location of the base of the convection zone more closely than the MIST model predicts. However, their model prefers an even lower surface helium abundance compared to the best-fit helium abundance in our model, and the present-day luminosity, radius, and effective temperature are not included as part of their fit.

Several explanations have been offered to reconcile the mismatch between the standard AGSS09 solar model and helioseismology results. One resolution invokes increased opacity, an idea that has been quantitatively explored by several authors (e.g., Bahcall et al. 2005a; Christensen-Dalsgaard et al. 2009; Serenelli et al. 2009). These authors concluded that a $\sim 10\%$ increase is required to match the observations, but that current atomic physics calculations do not leave room for such substantial change in opacities. However, there was a recent upward revision of iron opacities, based on new experimental data, that might account for roughly half the increase in the total mean opacity required to resolve this problem (Bailey et al. 2015). Other possible resolutions include more efficient diffusion processes in the radiative zone (e.g., Asplund et al. 2004), increased neon abundance to compensate for decreased oxygen abundance (e.g., Antia & Basu 2005; Bahcall et al. 2005b; Drake & Testa 2005), the introduction of new physics currently missing from stellar evolution calculations (e.g., convectively induced mixing in radiative zone; Young & Arnett 2005), and improved implementations of the current input physics (e.g., a replacement for mixing length theory; Arnett et al. 2015).

Although the widely adopted practice is to fix the solar-calibrated $\alpha_{\rm MLT}$ across all masses, evolution-

ary phases, and abundances, there has been a recent effort to map out $\alpha_{\rm MLT}$ as a function of $\log g$ and $T_{\rm eff}$ (Trampedach 2007; Trampedach et al. 2014) as well as metallicity (Magic et al. 2015) from full 3D radiative hydrodynamic calculations of convection in stellar atmospheres. Recently, Salaris & Cassisi (2015) included variable $\alpha_{\rm MLT}$ and $T(\tau)$ boundary condition from Trampedach et al. (2014) in their stellar evolution calculations and found that varying $\alpha_{\rm MLT}$ has a small effect on the evolution and surface properties. We adopt a constant value of $\alpha_{\rm MLT} = 1.82$ for the present work, but discuss the implications of this assumption in more detail in Section 2.8.3.1

In summary, we adopt solar-calibrated $\alpha_{\rm MLT}$ and convective overshoot efficiency in the envelope $f_{\rm ov,\,env}$ ($f_{0,\,\rm ov,\,env}$ is fixed to $0.5 f_{\rm ov,\,env}$). As noted earlier in the Introduction, we adopt the Asplund et al. (2009) abundance mixture and "solar metallicity" in this paper refers to the initial bulk $Z = Z_{\odot,\,\rm protosolar} = 0.0142$.

2.4.2 Lithium Depletion

Lithium is a very fragile element that is burned via proton capture at temperatures as low as 2.5×10^6 K. Mixing processes such as convection that transport lithium from the outer layers to the interior where the temperature is sufficiently high lead to the depletion of surface lithium on very short timescales. The time evolution of surface lithium abundance therefore depends very sensitively on the initial stellar mass (proxy for temperature) and mixing physics.

Standard stellar evolution models so far have not been able to successfully reproduce the solar surface lithium abundance, indicating the need to include extra physical mechanisms. One way to account for missing physics in the models is to vary $\alpha_{\rm MLT}$ (see e.g., Lyon models; Baraffe et al. 1998, 2003, 2015). Alternatively, models that incorporate the effects of rotation and internal gravity waves (e.g., Charbonnel & Talon 2005) are able to reproduce both the solar interior rotation profile and surface lithium abundances for the Sun and other galactic cluster stars. Relatedly, Somers & Pinsonneault (2014) found that radius dis-

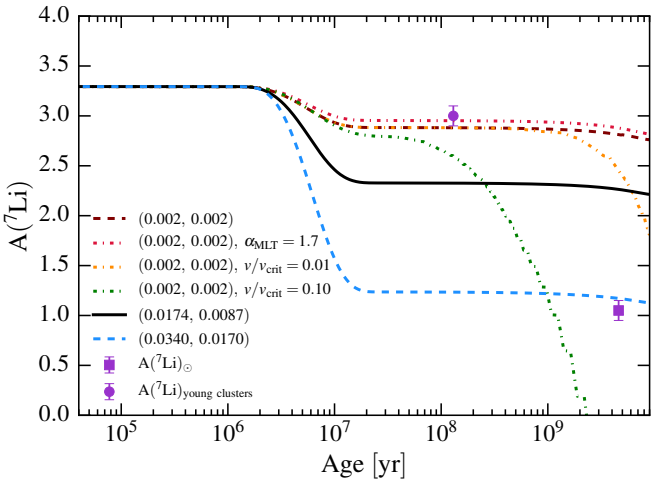


Figure 2.2: The evolution of surface lithium abundance relative to hydrogen, $\mathrm{A}(^7\mathrm{Li}) = \log(N_{^7\mathrm{Li}}/N_{^1\mathrm{H}}) + 12$, as a function of time for several 1 $M_\odot$ models. Each pair of numbers in parentheses corresponds to the two envelope overshoot efficiency parameters $f_{\mathrm{ov,\,env}}$ and $f_{\mathrm{ov,\,env,\,0}}$, respectively. The solid black line represents the fiducial model that adopts the solar-calibrated envelope overshoot parameters (0.0174, 0.0087) and $\alpha_{\mathrm{MLT}} = 1.82$. The two dashed maroon and blue lines are models with less and more efficient overshoot, resulting in reduced and enhanced lithium depletion, respectively. The three dot-dashed lines show additional variations in input physics: the red line correspond to $\alpha_{\mathrm{MLT}} = 1.7$, while the orange and green lines are models that include PMS rotation with $v/v_{\mathrm{crit}} = 0.01$ and 0.10, respectively. The purple square and circle are surface lithium abundance for the present-day Sun (Asplund et al. 2009) and the typical surface lithium abundance for nearby solar-metallicity, young clusters (e.g., Jeffries & Oliveira 2005; Sestito & Randich 2005; Juarez et al. 2014). The current models cannot simultaneously reproduce both observed lithium abundances.

persion on the PMS (correlated with rotation and chromospheric activity) can explain the spread in lithium abundances in young clusters such as the Pleiades.

In Figure 2.2 we show the evolution of surface lithium abundance relative to hydrogen, $\mathrm{A}(^7\mathrm{Li}) = \log(N_{^7\mathrm{Li}}/N_{^1\mathrm{H}}) + 12$, as a function of time for several 1 $M_\odot$ models. The purple square and circle are surface lithium abundance for the present-day Sun (Asplund et al. 2009) and the typical surface lithium abundance for nearby solar-metallicity, young clusters (e.g., Jeffries & Oliveira 2005; Sestito & Randich 2005; Juarez et al. 2014). Each pair of numbers in parentheses corresponds to the two envelope overshoot efficiency parameters $f_{\mathrm{ov,\,env}}$ and $f_{0,\,\mathrm{ov,\,env}}$, respectively. The surface lithium abundance decreases over time in all of the displayed models due to the inclusion of diffusion. The solid black line represents the fiducial model that adopts the solar-calibrated envelope overshoot parameters (0.0174, 0.0087) and $\alpha_{\mathrm{MLT}} = 1.82$. The fiducial model burns too much lithium early on and then does not deplete lithium efficiently on the

MS. The two dashed maroon and blue lines are models with less and more efficient overshoot, resulting in reduced and enhanced lithium depletion, respectively. The three dot-dashed lines show additional variations in input physics: the red line correspond to $\alpha_{\rm MLT} = 1.7$, while the orange and green lines are models that include PMS rotation with $v/v_{\rm crit} = 0.01$ and 0.10, respectively. As expected, a lower $\alpha_{\rm MLT}$ produces a puffier, cooler star, resulting in less lithium depletion. The inclusion of rotation during the PMS produces very different, potentially more promising behavior, though the current absence of magnetic braking (see Sections 2.3.6.5 and 2.3.5) in MESA results in an unrealistically high rotation speed ($v/v_{\rm crit}$ between 0.1 and 1) on the MS. The models presented here fail to simultaneously match both the young and present-day solar surface lithium abundances. The inclusion of rotation on the PMS, the implementation of magnetic braking, as well as the exploration of a variable $\alpha_{\rm MLT}$ to mimic the effects of non-standard physics are planned for follow-up investigations in the near future.

2.5 Model Outputs and Bolometric Corrections

In this section, we provide an overview of the two principal model outputs: evolutionary tracks and isochrones, which can be downloaded from http://waps.cfa.harvard.edu/MIST. There are both theoretical and observational isochrones available. We offer both packaged models for download and a web interpolator that generates models with user-specified parameters.

2.5.1 Ages, Masses, Phases, Metallicities

One of the main goals of the MIST project is to produce extensive grids of stellar evolutionary tracks and isochrones that cover a wide range in stellar masses, ages, evolutionary phases, and metallicities. The stellar mass of evolutionary tracks ranges from 0.1 $M_\odot$ to 300 $M_\odot$ for a total of $\gtrsim$ 100 models, and the ages of isochrones cover $\log \mathrm{Age} = 5$ to $\log \mathrm{Age} = 10.3$ in 0.05 dex steps. For $M_{\rm i} \leq 0.7\ M_\odot$, the models are terminated at TAMS, i.e., central ^{1}H abundance drops to 10^{-4}. For a 0.7 $M_\odot$ star at $Z_\odot$, this limit is

typically reached at an age > 35 Gyr. For $M_i > 0.7\ M_\odot$, the models are either evolved through the WD cooling phase ("low-mass" type) or the end of carbon burning ("high-mass" type), depending on which criterion is satisfied first. We adopt this flexible approach to take into account the blurry boundary—further complicated by its metallicity dependence—between low- and intermediate-mass stars that end their lives as WDs and high-mass stars that continue to advanced stages of burning. In particular, the "low-mass" type models are terminated when Γ, the central plasma interaction parameter, also known as the Coulomb coupling parameter, exceeds 20. Γ is defined to be $\bar{Z}^2 e^2 / a_i k_b T$, where $\bar{Z}$ is the average ion charge, e is the electron charge, a_i is the mean ion spacing, k_b is the Boltzmann constant, and T is the temperature. A large Γ corresponds to a departure from the ideal gas limit toward solidification (crystallization of a pure oxygen WD occurs at $\Gamma \approx 175$; Paxton et al. 2011). The "high-mass" type models—stars that are sufficiently massive to burn carbon—are stopped when the central ^{12}C abundance drops to 10^{-2}. The metallicity ranges from $[\mathrm{Fe/H}] = -2.0$ to $+0.5$, with 0.25 dex spacing. We also provide an additional set of models evolved from the pre-main sequence to the end of core helium burning for $-4.0 \leq [\mathrm{Z/H}] < -2.0$ for modeling ancient, metal-poor populations. We provide a limited set at low metallicities at this time due to computational difficulties we have encountered. In particular, mixing between convective boundaries during the thermally-pulsating AGB phase results in the ingestion of protons into a burning region, resulting in dramatically higher nuclear burning luminosities (e.g., Lau et al. 2009; Stancliffe et al. 2011; Woodward et al. 2015). Non-solar-scaled abundance grids will be presented in Dotter et al., in prep.

We note that in any grid, there is a subset of models that does not run to completion due to convergence issues. This is not generally problematic because the mass sampling is sufficiently fine such that there are enough models to smoothly interpolate a new EEP track and/or construct isochrones. We also note that there are interesting features in the tracks and isochrones that may appear to be numerical issues at first glance, but in fact a number of them are real phenomena captured in the MESA calculations. We refer the reader to Section 2.10 for a discussion of these features. Of these, an example feature that may be

Table 2.5: Primary EEPs and corresponding evolutionary phases.

Primary EEP	Phase
1	pre-main sequence (PMS)
2	zero age main sequence (ZAMS)
3	intermediate age main sequence (IAMS)
4	terminal age main sequence (TAMS)
5	tip of the red giant branch (RGBTip)
6	zero age core helium burning (ZACHeB)*
7	terminal age core helium burning (TACHeB)†
Low Mass Type	
8	thermally pulsating asymptotic giant branch (TPAGB)
9	post asymptotic giant branch (post-AGB)
10	white dwarf cooling sequence (WDCS)
High Mass Type	
8	carbon burning (C-burn)

a numerical artifact is an extremely short-lived glitch that appears during the early post-AGB phase for a subset of the models. Since it has zero bearing on the evolution of the star, we post-process this feature out of the final evolutionary tracks in order to facilitate the construction of smooth isochrones.

2.5.2 Isochrone Construction

We briefly describe the isochrone construction process and defer a detailed discussion of this topic to Dotter (2016). In each evolutionary track, we identify a set of the so-called primary equivalent evolutionary points (primary EEPs). These correspond to specific stages of evolution defined by a set of physical conditions, such as the terminal age main sequence (TAMS; central hydrogen exhaustion), and the tip of the RGB (RGBTip; a combination of lower limits on the central helium abundance and luminosity). Next, each segment between adjacent primary EEPs is further divided into so-called "secondary-EEPs" according to a distance metric that evenly samples the tracks in certain relevant variables, such as $T_{\rm eff}$ and L. Put another way, primary EEPs serve as physically meaningful reference locations along the evolutionary track and secondary EEPs finely sample the track between primary EEPs. This method maps a set of evolutionary tracks from ordinary time coordinates onto uniform EEP coordinates. The primary EEPs and corre-

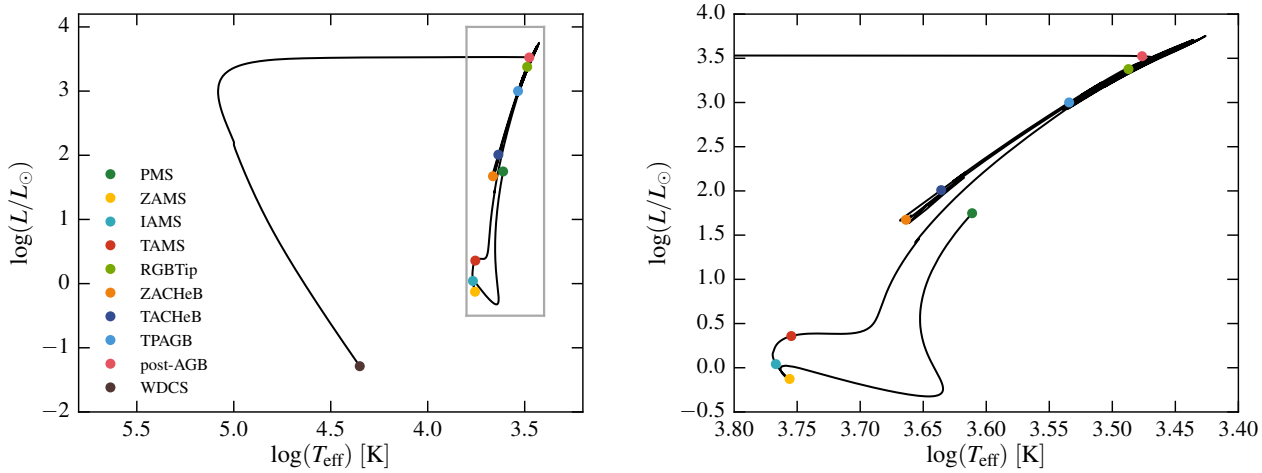


Figure 2.3: *Left*: An example 1 $M_\odot$ evolutionary track in the equivalent evolutionary point (EEP) format, with the locations of the primary EEP points marked by colored circles. The gray box marks the zoomed-in region shown in the right panel. *Right*: A zoomed-in view of the track.

sponding evolutionary phases are listed in Table 2.6. In Figures 2.3 and 2.4, we show example 1 $M_\odot$ and 30 $M_\odot$ evolutionary tracks in the EEP format, with colored dots marking the locations of the primary EEPs. Note that we require both IAMS and TAMS points in order to properly resolve the MSTO for stars that burn hydrogen convectively in their cores during the MS, i.e., the Henyey hook. Also note that although "RGBTip" does not have the same morphological significance in high-mass stars as in low-mass stars since high-mass stars ignite helium under non-degenerate conditions, we retain this terminology for consistency reasons.

As described in Section 2.3.3, we use three different boundary conditions depending on the initial mass of the model ($\tau = 100$ tables for 0.1–0.3 $M_\odot$, photosphere tables for 0.6–10 $M_\odot$, and simple photosphere for 16–300 $M_\odot$). To facilitate a smooth transition from one regime to another, we run both $\tau = 100$ and photosphere tables for 0.3–0.6 $M_\odot$ and photosphere tables and simple photosphere for 10–16 $M_\odot$. For every mass in the transition regime, the two EEP tracks are blended with a smooth weighting function to

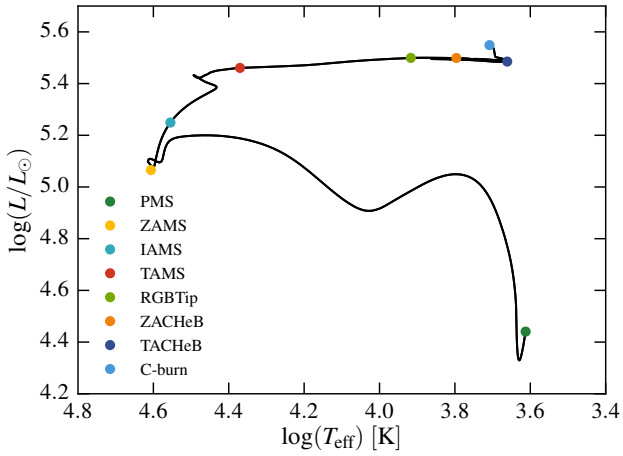


Figure 2.4: Same as Figure 2.3 but now for a 30 $M_\odot$ evolutionary track. Note the different primary EEP point following the core helium burning phase. Although "RGBTip" does not have the same morphological significance in high-mass stars as in low-mass stars since high-mass stars ignite helium under non-degenerate conditions, we retain this terminology for consistency reasons.

create a hybrid EEP track:

$$w = 0.5 \left[1 - \cos \left(\pi \frac{M_* - M_1}{M_2 - M_1} \right) \right] \quad , \tag{2.23}$$

where M_1 and M_2 are the transition masses (e.g., $M_1 = 0.3\ M_\odot$ and $M_2 = 0.6\ M_\odot$ for the transition from $\tau = 100$ to photosphere tables).

To generate an isochrone at age t_0 with all of the EEP tracks now in hand, we first cycle through all masses and construct a piecewise monotonic function between M_i and t for each EEP point.* Next, we interpolate to obtain $M_\mathrm{i}(t_0)$. Once we have $M_\mathrm{i}(t_0)$ for every EEP, we can now construct an isochrone for any parameter, e.g., L, by interpolating that parameter as a function of M_i, e.g., $L(M_\mathrm{i}(t_0))$, at every EEP. The EEP framework is superior to a direct interpolation scheme in time coordinates as it can properly treat evolutionary phases with short timescales (e.g., post-AGB) or complex trajectories (e.g., thermally pulsating AGB; TPAGB).

A sensible approach is to construct a monotonic relationship between mass and age assuming that

*Note that we no longer distinguish between primary and secondary EEPs for the purposes of isochrone construction.

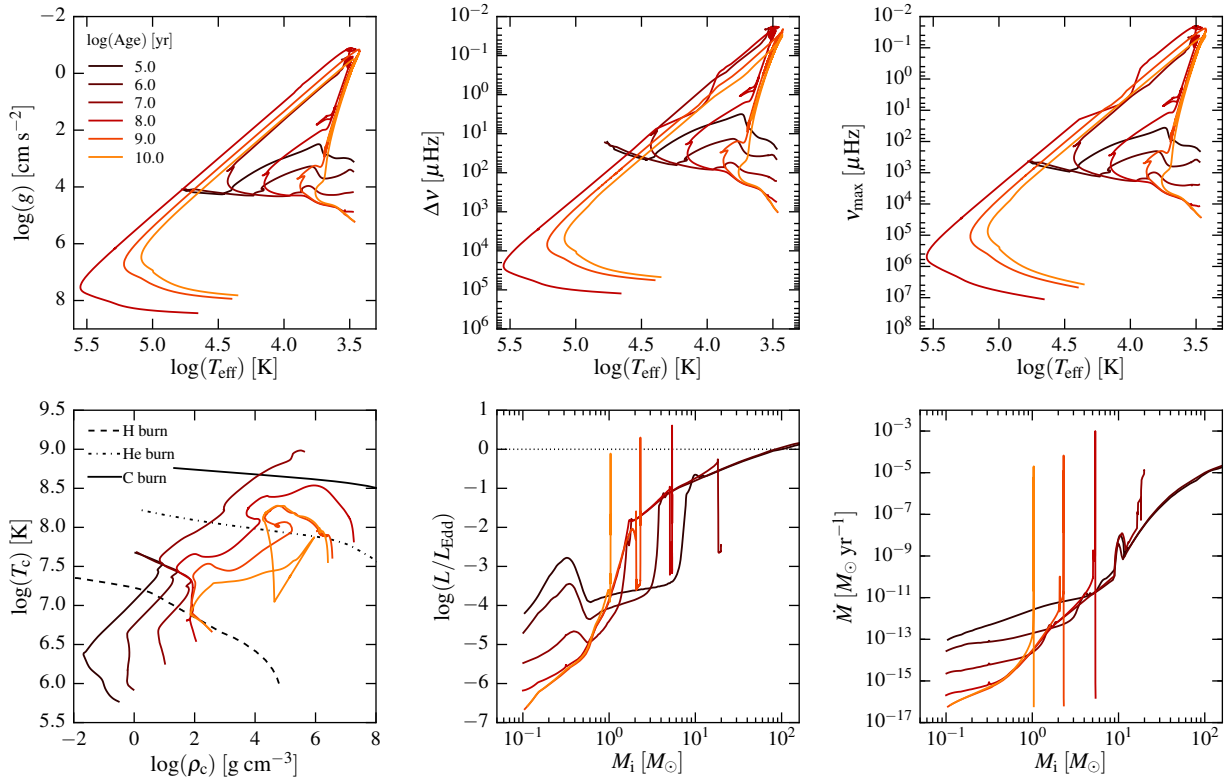


Figure 2.5: Isochrones from log(Age) [yr] $= 5$ to 10 in various physical quantities. *Top left*: Isochrones in the $\log(g) - \log(T_{\rm eff})$ plane. *Top middle*: Asteroseismic isochrones in the $\Delta\nu - \log(T_{\rm eff})$ plane, where $\Delta\nu$ corresponds to the large frequency separation for p-modes. Note that $\Delta\nu$ is computed from the scaling relations. *Top right*: Asteroseismic isochrones in the $\nu_{\rm max} - \log(T_{\rm eff})$ plane, where $\nu_{\rm max}$ corresponds to the frequency of maximum power. Note that $\nu_{\rm max}$ is computed from the scaling relations. *Bottom left*: Isochrones in the $\log(T_c)$-$\log(\rho_c)$ plane with the dashed, dot-dashed, and solid lines showing thresholds for hydrogen, helium, and carbon ignition. The discontinuous feature at log(Age) [yr] ≥ 10 is due to the ignition of helium in a degenerate core, i.e, helium core flash at the tip of the RGB. *Bottom middle*: Isochrones in the $\log(L/L_{\rm Edd})$-$M_{\rm i}$ plane, where $L_{\rm Edd}$ is the Eddington luminosity. *Bottom right*: Isochrones in the $\dot{M}$-$M_{\rm i}$ plane, where $\dot{M}$ is the mass loss rate. In the last two figures, isochrones become steadily truncated at the high-mass end as more stars evolve and die.

"increasing mass = decreasing phase lifetime" is always true. However, interesting non-monotonic behaviors begin to appear in certain evolutionary phases over a narrow age (or equivalently, mass) interval if the mass resolution is sufficiently high (see Figure 2.13 and also Girardi et al. 2013). Put another way, two stars of different initial masses are at the same evolutionary stage in terms of their EEPs over a special narrow age interval. This effect will be explored in future work but for this work, we enforce monotonicity in the age-mass relationship.

2.5.3 Available Model Outputs

The published tracks and isochrones include a wealth of information, ranging from basic parameters such as $\log(L)$, $\log(T_{\rm eff})$, $\log(g)$, and surface abundances of 19 elements to more detailed quantities such as $\beta \equiv P_{\rm gas}/P_{\rm total}$ and asteroseismic parameters (the full list of available parameters is available on the project website). To highlight this fact, we show examples of isochrones in several different projections in Figure 2.5. From left to right, the top three panels feature isochrones in the $\log(g) - \log(T_{\rm eff})$, $\Delta\nu - \log(T_{\rm eff})$, and $\nu_{\rm max} - \log(T_{\rm eff})$ planes. $\Delta\nu$ and $\nu_{\rm max}$ are asteroseismic quantities that correspond to the large frequency separation for p-modes and the frequency of maximum power, respectively, which can be readily obtained from power spectra of e.g., *Kepler* light curves. We clarify that $\Delta\nu$ and $\nu_{\rm max}$ in the MIST models are computed from simple scaling relations (e.g., Ulrich 1986; Brown et al. 1991; Kjeldsen & Bedding 1995) and not from full pulsation analysis, though the pulsation code GYRE (Townsend & Teitler 2013) is integrated into MESA. The bottom left panel shows isochrones in the $\log(T_c)$–$\log(\rho_c)$ plane, where the dashed, dot-dashed, and solid lines show thresholds for hydrogen, helium, and carbon ignition. The 10 Myr isochrone contains massive stars that are able to ignite carbon whereas at the older ages, the isochrones cannot reach sufficiently high central densities and temperatures. At 10 Gyr, only the low-mass stars remain and helium core flash at RGBTip shows up as a discontinuous sharp feature. The bottom middle and right panels show $\log(L/L_{\rm Edd})$, the ratio of total luminosity to Eddington luminosity, and $\dot{M}$, the mass loss rate, as a function of initial mass. As expected, both quantities generally increase as the initial mass increases. A very prominent increase immediately followed by a sharp decrease at intermediate ages (0.1 and 1 Gyr) in both panels is due to the TPAGB phase, followed by the post-AGB and WD cooling phases.

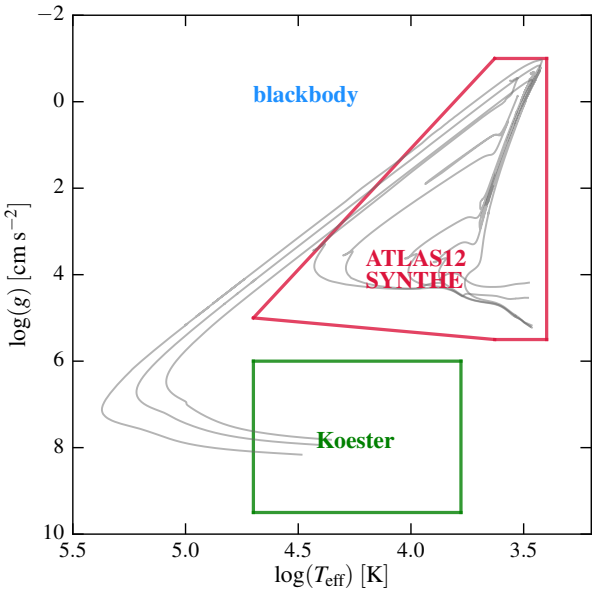


Figure 2.6: Coverage of the synthetic spectra grids used to derive bolometric corrections. Example isochrones at log(Age) [yr] = 7.0, 7.5, 8.5, 9.0, and 10.0 are overplotted in gray for reference. The coverage in $\log g$ and $\log T_{\rm eff}$ is the same for all metallicities.

2.5.4 Bolometric Corrections

Bolometric corrections are necessary to transform theoretical isochrones into magnitudes that allow for direct comparisons with observations. The bolometric corrections are largely based on a new grid of stellar atmosphere and synthetic spectra created with the ATLAS12 and SYNTHE codes (Conroy et al. in preparation). These same models are used for the surface boundary conditions discussed in Section 2.3.3. They include the latest atomic line list from R. Kurucz (including both laboratory and predicted lines) and many molecules including CH, CN, TiO, H_2, H_2O, SiO, C_2, SiH, MgH, CrH, CaH, FeH, CO, NH, VO, and OH. We have also computed model atmosphere and spectra for carbon stars with C/O = 1.05 over the range $2400 < T_{\rm eff} < 4700$ K and $-1.0 < \log g$ [g cm^{-3}] < 0.5. Our carbon star spectra agree well with the models of Aringer et al. (2009). The primary differences arise at > 2 μm as our models do not currently include the important molecules C_3, HCN, and C_2H_2. We chose to create our own carbon star spectra in order to have models covering the full wavelength range and at the same resolution as our main

Table 2.7: Current list of photometric systems.

System	Reference
UBVRI + JHK	Bessell & Murphy (2012); Bessell & Brett (1988)
Strömgren	Bessell (2011)
Washington	Bessell (2001)
DDO51	www.noao.edu/kpno/mosaic/filters/
SDSS	classic.sdss.org/dr7/instruments/imager/index.html
CFHT/MegaCam	www.cfht.hawaii.edu/Instruments/Imaging/Megacam/specsinformation.html
PanSTARRS	Tonry et al. (2012)
DECam	www.ctio.noao.edu/noao/sites/default/files/DECam/DECam_filters.xlsx
SkyMapper	Bessell et al. (2011)
Kepler	keplergo.arc.nasa.gov/CalibrationResponse.shtml
HST/ACS	www.stsci.edu/hst/acs/analysis/throughputs
HST/WFPC2	Holtzman et al. (1995)
HST/WFC3	www.stsci.edu/hst/wfc3/ins_performance/filters/
2MASS	Cohen et al. (2003)
UKIDSS	Hewett et al. (2006)
Spitzer/IRAC	Fazio et al. (2004)
WISE	Wright et al. (2010)
GALEX	http://asd.gsfc.nasa.gov/archive/galex/Documents/PostLaunchResponseCurveData.html

spectral library. The ATLAS12/SYNTHE spectra are combined with synthetic spectra for H-rich WDs with $6,000 \leq T_{\rm eff} \leq 50,000$ K from Koester (2010). These are supplemented by a set of blackbody spectra with $200,000 \leq T_{\rm eff} \leq 1$ million K. The coverage of the different synthetic libraries is shown in Figure 2.6. Example isochrones at $\log(\text{Age})$ [yr] $= 7.0$, 7.5, 8.5, 9.0, and 10.0 are overplotted for reference.

Bolometric corrections are computed from the synthetic spectra following Equation 1 of Girardi et al. (2008). As noted in the Introduction, we adopt as a zeropoint $L_\circ = 3.0128 \times 10^{35}$ erg s^{-1} to define $M_{\rm bol} = 0$. This is equivalent to adopting solar values of $M_{\rm bol,\odot} = 4.74$ and $L_\odot = 3.828 \times 10^{33}$ erg s^{-1}. The bolometric corrections include a range of extinction values, as characterized by both A_V and R_V, following the extinction curve of Cardelli et al. (1989). We provide $A_V = 0$ to 6 with $R_V = 3.1$, though other R_V values can be made upon request. We emphasize that Z of the bolometric correction is matched to the surface Z (and surface C/O ratio where relevant) for each star along the isochrone.

The photometric systems included in the initial MIST release are summarized in Table 2.8. This is only an initial set and will expand over time. Photometric systems define their magnitude scales according to a flux standard.

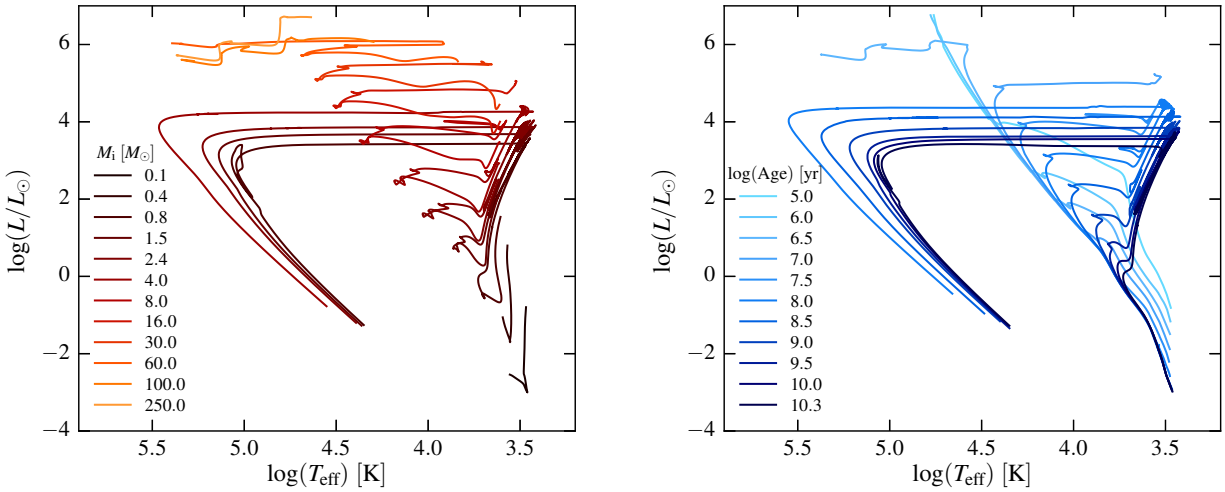


Figure 2.7: An example solar metallicity grid of stellar evolutionary tracks (*left*) and isochrones (*right*) covering a wide range of stellar masses, ages, and evolutionary phases.

2.6 Overview and Basic Properties of the Models

2.6.1 Tracks and Isochrones

As described in detail in Section 2.5.1, the MIST models cover a wide range in stellar masses, ages, metallicities, and evolutionary phases. The stellar mass of evolutionary tracks ranges from 0.1 $M_\odot$ to 300 $M_\odot$, the ages of isochrones cover $\log \mathrm{Age} = 5$ to $\log \mathrm{Age} = 10.3$, and the metallicity ranges from $[\mathrm{Fe/H}] = -4.0$ to $+0.5$. The evolution is continuously computed from the PMS phase to the end of hydrogen burning, WD cooling phase, or the end of carbon burning, depending on the initial stellar mass and metallicity.

Figure 2.7 illustrates the range of stellar masses, ages, and evolutionary phases, showing the evolutionary tracks and isochrones in the left and right panels, respectively. As noted in Section 2.3, the models include rotation with $v/v_{\rm crit} = 0.4$ by default. Figure 2.8 shows the effect of rotation on both the evolutionary tracks and isochrones, where the rotating and non-rotating models are shown in solid and dashed lines, respectively. For display purposes, we omit the post-AGB phase where relevant. Rotation makes stars more luminous during the MS because rotational mixing (see Section 2.3.6.4) promotes core growth.

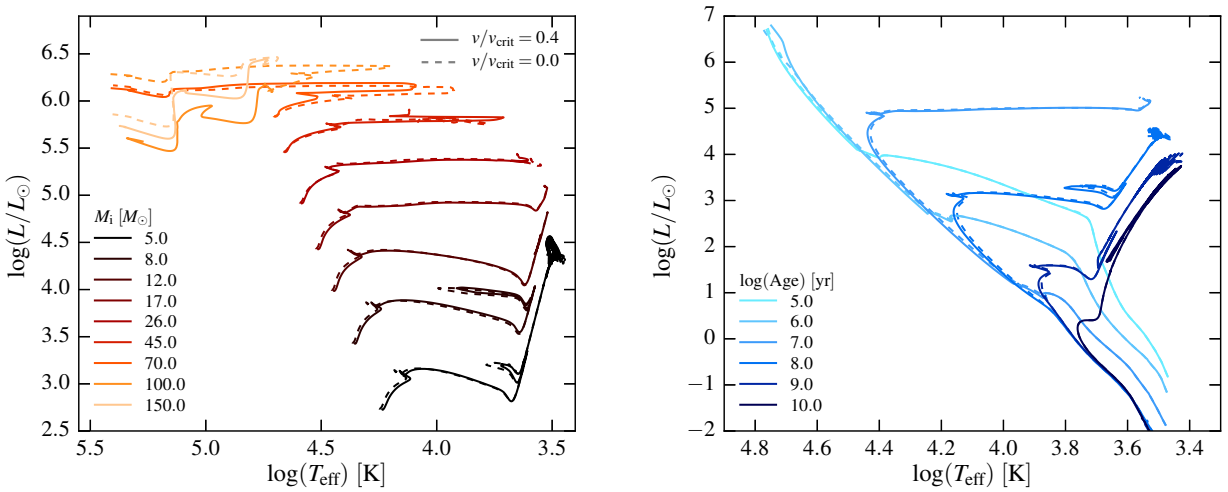


Figure 2.8: Similar to Figure 2.7 but now showing the effect of rotation on both the evolutionary tracks (*left*) and isochrones (*right*). Models with and without rotation are shown in solid and dashed lines, respectively. For rotating models, solid-body rotation with $v_{\rm ZAMS}/v_{\rm crit} = \Omega_{\rm ZAMS}/\Omega_{\rm crit} = 0.4$ is initialized at ZAMS. The PMS phase is not shown in the left panel for display purposes.

It makes the star appear hotter or cooler depending on the efficiency of rotational mixing in the envelope: if rotational mixing introduces a sufficient amount of helium into the envelope and increases the mean molecular weight, the star becomes more compact and hotter. However, in the absence of efficient rotational mixing, the centrifugal effect dominates, making the star appear cooler and more extended. This is because in a rotating system, ordinary gravitational acceleration g is replaced by $g_{\rm eff}$ that includes both the gravitational and centrifugal terms. Since $T_{\rm eff} \propto g_{\rm eff}^{1/4}$ for a star with a radiative envelope and $|g_{\rm eff}| < |g|$, $T_{\rm eff}$ is thus lower in a rotating system. Generally speaking, rotation increases $T_{\rm eff}$ in massive stars where rotational mixing operates efficiently, and it decreases $T_{\rm eff}$ in low-mass stars as well as at all ZAMS locations where the centrifugal effect dominates.

The top two panels of Figure 2.9 show a series of 2.2 $M_\odot$ (left) and 6.4 $M_\odot$ (right) evolutionary tracks for three metallicities. A portion of the PMS phase in both panels and the evolution following the core helium burning phase (CHeB) in the right panel are omitted for display purposes. The tracks become hotter and more luminous with decreasing metal content due to a lower Rosseland mean opacity. In the bottom panels, we zoom in on the TPAGB and CHeB to further highlight the effects of metallicity on these

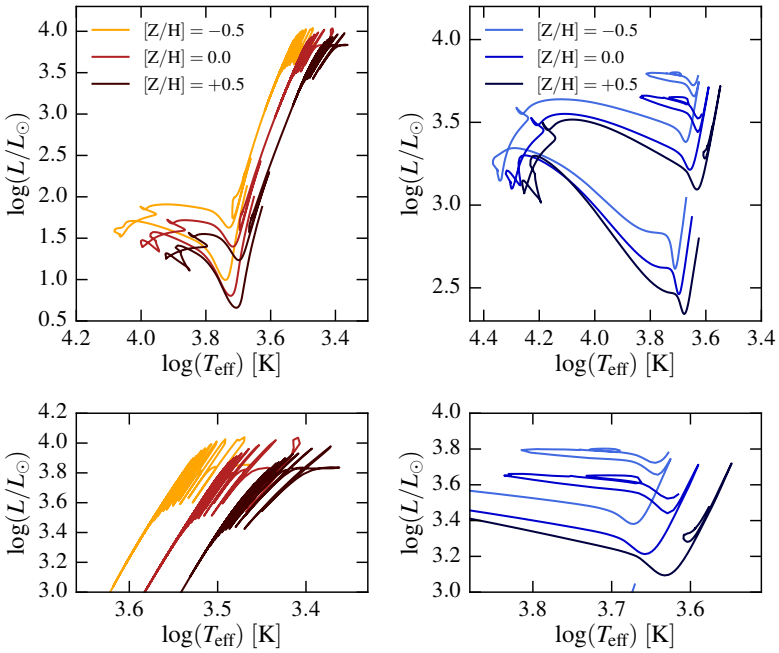


Figure 2.9: A series of 2.2 $M_\odot$ (*left*) and 6.4 $M_\odot$ (*right*) evolutionary tracks for three metallicities. The tracks become hotter and more luminous with decreasing metallicity due to a lower Rosseland mean opacity. In the bottom panels, we zoom in on the TPAGB (*left*) and CHeB (*right*) to further highlight the effects of metallicity on these evolutionary phases.

evolutionary phases. The blue loops become hotter and more prominent with decreasing metallicity and the entire TPAGB phase also shifts to hotter temperatures as metallicity decreases. To scrutinize the effect of metallicity on the TPAGB phase in more detail, we plot the number of TPs executed by each model as a function of mass at a number of metallicities in Figure 2.10. There are two notable features: the maximum number occurs at around 2 $M_\odot$ independent of metallicity; and the number of thermal pulses increases with [Z/H] from -1.0 to 0.0, and there is a hint that the trend reverses for [Z/H] > 0. We leave a more detailed discussion of the number of TPs as a function of uncertain physical parameters (e.g., mixing, mass loss) and comparisons to other databases for future work.

In order to illustrate the range of metallicities available in the current MIST models, we show 10 Gyr isochrones at [Z/H] $= -4$, -3, -2, -1, 0, and 0.5 in Figure 2.11. For clarity, we only show phases up to the RGBTip. As the metallicity decreases, the MSTO becomes hotter and more luminous (and the MSTO mass decreases) and the RGBTip becomes fainter due to the helium ignition occurring at lower

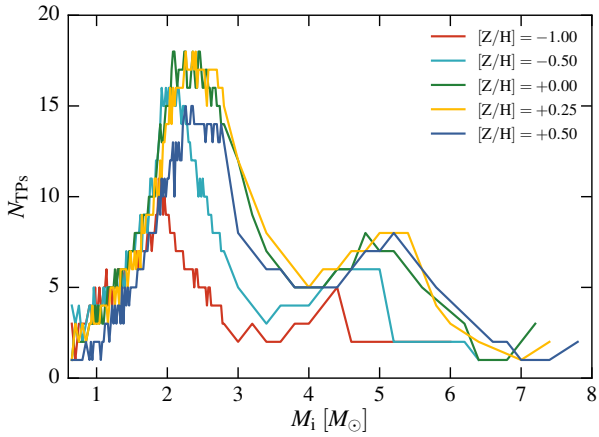


Figure 2.10: The number of thermal pulses (TPs) executed by each model as a function of mass at a number of metallicities. There are two notable features: first, the maximum occurs at around 2 $M_\odot$ independent of metallicity, and two, the number of thermal pulses increases with [Z/H] from -1.0 to 0.0, and there is a hint that the trend reverses for [Z/H] > 0.

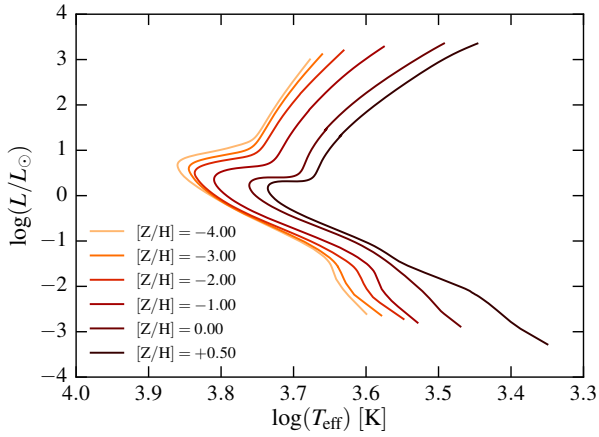


Figure 2.11: Isochrones at 10 Gyr over a wide range of metallicities. For display purposes, we omit the phases beyond RGBTip. As the metallicity decreases, the MSTO becomes hotter and more luminous (and the MSTO mass decreases) and the RGBTip becomes fainter due to the helium ignition occurring at lower core masses. Note that the isochrone changes more subtly with metallicity in the very metal-poor regime, i.e., [Z/H] $\lesssim -2$.

core masses. Note that the isochrone changes more subtly with metallicity in the very metal-poor regime, i.e., [Z/H] $\lesssim -2$.

In the top panel of Figure 2.12 we show phase lifetimes as a function of initial mass for [Z/H] $= -0.25$, 0.0 and $+0.25$ in solid, dot-dashed, and dotted lines, respectively. The bottom panel shows the ratio of phase lifetimes to the MS lifetime. Note that the "RGB" label refers to the phase between TAMS and helium ignition, which includes the short subgiant branch (SGB) evolution, and "post-AGB" includes

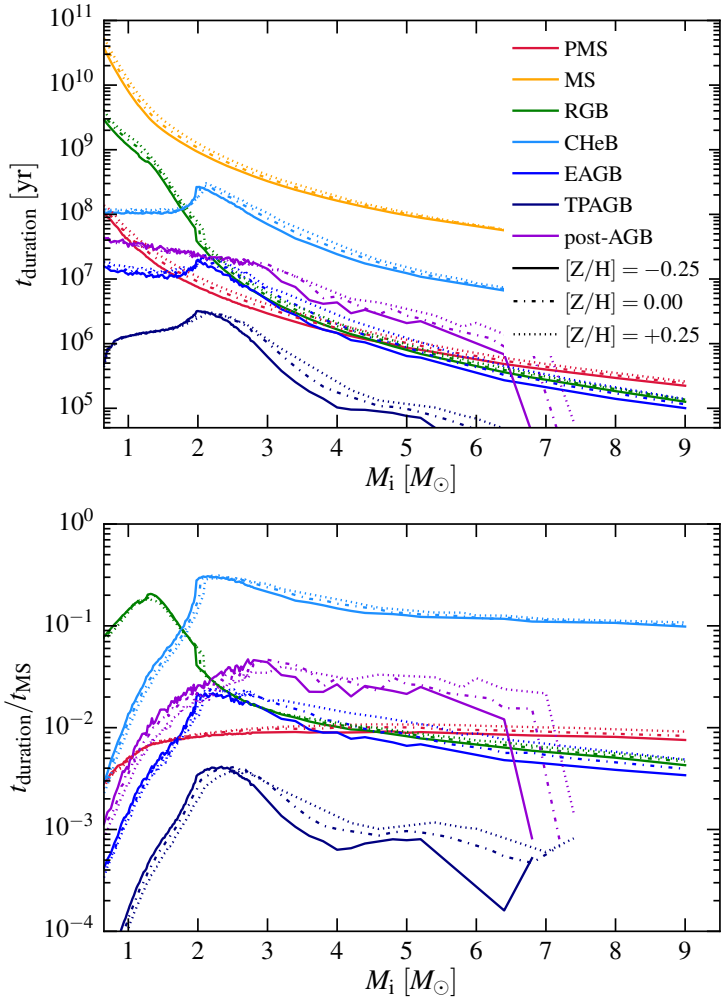


Figure 2.12: *Top*: Phase lifetimes as a function of initial mass for [Z/H] $= -0.25$, 0.0 and $+0.25$. High mass stars are not included because they do not go through the same set of evolutionary phases featured here. Note that the "RGB" label refers to the phase between TAMS and helium ignition, which includes the short subgiant branch (SGB) evolution, and "post-AGB" includes the white dwarf cooling phase up to $\Gamma = 20$. *Bottom*: Same as above but now showing the ratio of phase lifetimes to the MS lifetime instead.

the white dwarf cooling phase up to $\Gamma = 20$. The post-AGB timescales in the MIST models (adopting the definition from Miller Bertolami 2016) are consistent with those reported by Miller Bertolami (2016) and Weiss & Ferguson (2009), which are a factor of 3–10 shorter compared to the older post-AGB stellar evolution models (Vassiliadis & Wood 1994; Blöcker 1995). High mass stars are not included because they do not go through the same set of evolutionary phases featured here. The TPAGB and post-AGB phases are not shown for a subset of the models that do not completely evolve through those evolutionary stages.

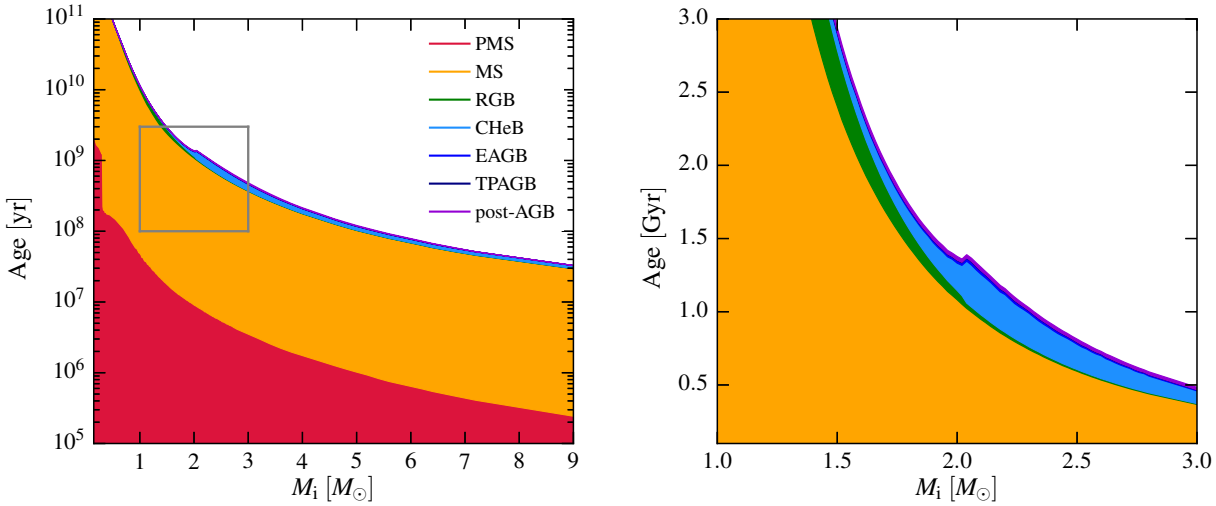


Figure 2.13: *Left*: Similar to Figure 2.12 but now showing the cumulative age as a function of mass for $[Z/H] = 0.0$. The gray box marks the zoomed-in region shown in the right panel. *Right*: Zooming in on a mass range that shows a critical transition from degenerate helium ignition to quiescent helium ignition. This produce a non-monotonic mass-age relationship for these phase. Note the linear scale in y. This figure is adapted from Figure 1 of Girardi et al. (2013).

Unsurprisingly, the lifetimes generally decrease with increasing mass, though there are some notable exceptions including the peak in CHeB and AGB lifetimes at $\sim 2\ M_\odot$ (see the discussion below).

The left panel of Figure 2.13 is a slight variation of the previous plot, where we now show the cumulative age as a function of mass for $[Z/H] = 0.0$. In the right panel, we zoom in on a particularly interesting mass range around $2\ M_\odot$, where there a noticeable increase in the CHeB lifetime. This effect, explored in detail in Girardi et al. (2013), is due to the transition from the explosive ignition of helium in degenerate cores of low-mass stars, i.e., helium core flash at RGBTip, to quiescent ignition of helium in more massive stars. This is because more massive stars start burning helium at lower core masses and therefore have smaller initial helium-burning luminosities compared to those that undergo the helium core flash (see also Girardi 1999). Note that this non-monotonicity in the CHeB lifetime is present even in models computed without RGB mass loss. Thus, the simple "increasing mass = decreasing MS lifetime" rule of thumb is violated over a very narrow mass range. In other words, there is a special age at which two stars of different masses are at the same evolutionary stage in terms of their EEPs. This notion of "double EEPs" is

discussed in more detail in Paper 0 (Dotter 2016) and will be explored in a future paper.

2.6.2 NON-STANDARD MODELS

To explore the effects of uncertain input physics and choices of free parameters on the resulting tracks and isochrones, we ran several sets of models varying one ingredient at a time. In Figure 2.14 we present four such variations. The black solid lines represent solar metallicity models with fiducial parameters listed in Table 2.2. We note that several of these parameters affect the lifetimes of different evolutionary phases, though this is not explicitly shown in the figures.

In the top left panel, we show two sets of isochrones which are identical except for their surface boundary conditions. The three sets of ages correspond to $\log(\mathrm{Age})\ [\mathrm{yr}] = 9.0, 9.6$, and 10.2. The solid lines are isochrones with our default implementation of boundary conditions; $\tau = 100$ and photosphere tables from the ATLAS12/SYNTHE atmosphere models plus the simple Eddington gray $T(\tau)$ approximation for the hottest stars. The dashed lines are models with the Eddington gray $T(\tau)$ relation applied across the entire mass range. For clarity, we only plot the isochrones up to the RGBTip. As expected, the choice of boundary conditions has the largest effect on the lower MS populated by cool, compact dwarfs. The shift in T_{eff} on the RGB is smaller but important, amounting $\sim$ 50–60 K. Differences both on the SGB and RGB and on the lower MS are larger at non-solar metallicities. In particular, the isochrones become more discrepant on the SGB and RGB at $[\mathrm{Z/H}] = -1$ and on the lower MS at $[\mathrm{Z/H}] = +0.3$.

In the top right panel, we show three sets of isochrones at $\log(\mathrm{Age})\ [\mathrm{yr}] = 6.7, 7.4$, and 9.0 to illustrate the impact mass loss has on various stages of evolution. The solid lines correspond to isochrones with $\eta_{\mathrm{R}} = 0.1,\ \eta_{\mathrm{B}} = 0.2$, and $\eta_{\mathrm{Dutch}} = 1.0$, whereas the dashed lines and dotted lines represent mass loss rates that are twice and half as efficient, respectively. For display purposes, we omit the PMS and post-AGB phases. The temperature evolution is especially sensitive to the mass loss rates at the youngest ages because massive star evolution is strongly affected by the choice of input physics. The morphology of the

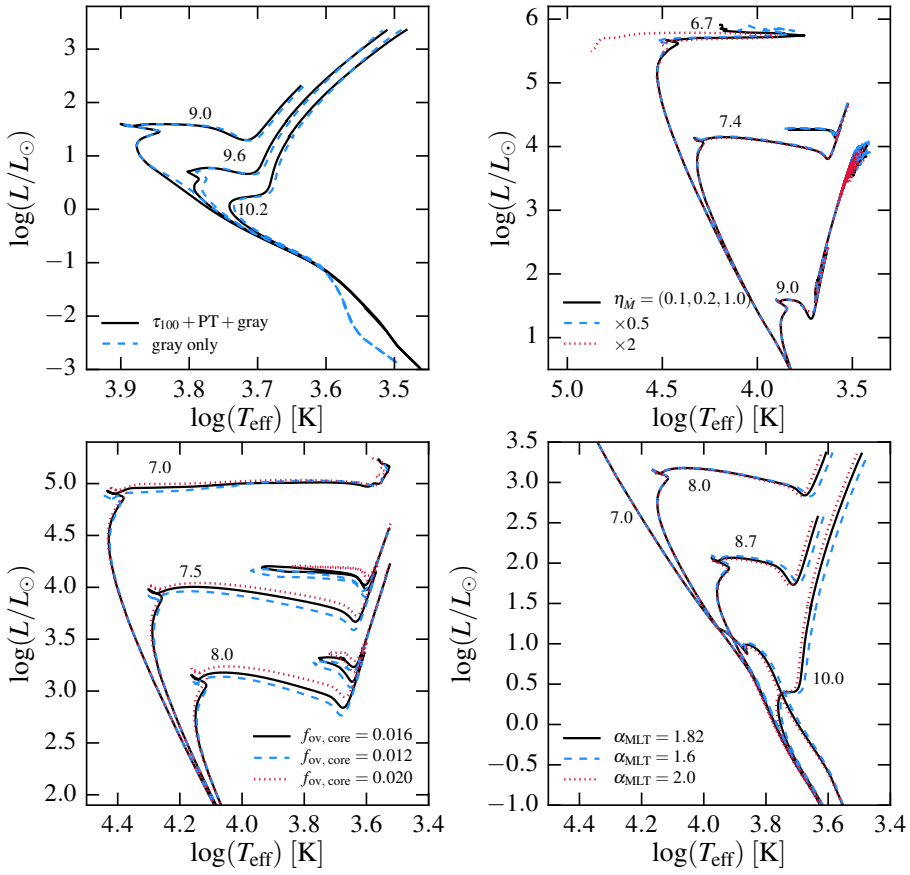


Figure 2.14: Solar metallicity isochrones at a number of ages showing the effects of varying input physics. The fiducial model is shown in black solid lines in all four panels. Note different x and y axes in each panel. *Top left*: Variations in the adopted boundary conditions for $\log(\text{Age})$ [yr] $= 9.0, 9.6$, and 10.2. *Top right*: Variations in the efficiency of mass loss for $\log(\text{Age})$ [yr] $= 6.7, 7.4$, and 9.0. The set of three numbers corresponds to $\eta_{\rm R}$, $\eta_{\rm B}$, and $\eta_{\rm Dutch}$. *Bottom left*: Variations in the efficiency of overshoot in the core parameterized by $f_{\rm ov,\,core}$ for $\log(\text{Age})$ [yr] $=$ $7.0, 7.5$, and 8.0. *Bottom right*: Variations in the efficiency of convection parameterized by $\alpha_{\rm MLT}$ for $\log(\text{Age})$ [yr] $=$ $7.0, 8.0, 8.7$, and 10.0.

CHeB is also directly influenced by mass loss rates: lower and higher $\dot{M}$ values yield hotter and cooler CHeB, respectively. The morphology and lifetime of the notorious TPAGB phase are also affected mass loss rates, with more efficient winds resulting in fainter and fewer TPs as expected. The mass loss efficiency, parameterized by the η parameter, is calibrated empirically to match various observational constraints, including the number ratios of different stellar types for the high-mass stars (Section 2.9.3) and the AGB luminosity functions for the low-mass stars (Section 2.8.5.1).

In the bottom left panel, we highlight the importance of core convective overshoot. The three sets of ages shown are $\log(\text{Age})\ [\text{yr}] = 7.0, 7.5$, and 8.0. The solid lines are isochrones with the default core overshoot parameter $f_{\text{ov, core}} = 0.016$ in the exponential diffusive overshoot formalism. The dashed and dotted lines represent decreased and increased ($f_{\text{ov, core}} = 0.012,\ 0.020$) overshoot efficiency, respectively. For clarity, we plot the evolution up through helium burning only. Since convective overshoot enhances the mixing of fresh fuel into the core, a higher overshoot efficiency results in longer MS lifetimes and systematically higher MSTO masses and luminosities. Likewise, SGB and CHeB luminosities are higher for more efficient overshoot due to the larger resulting core masses. Note that the overshoot efficiency in the core is constrained by matching the MSTO in M67, and the overshoot efficiency in the envelope is determined during solar calibration.

In the bottom right panel, we show isochrones with different values of the mixing length parameter α_{MLT}. The four ages shown are $\log(\text{Age})\ [\text{yr}] = 7.0, 8.0, 8.7$, and 10.0. The solid lines are isochrones with the solar-calibrated value $\alpha_{\text{MLT}} = 1.82$. The dashed and dotted lines correspond to isochrones with $\alpha_{\text{MLT}} = 1.6$ and $\alpha_{\text{MLT}} = 2.0$, respectively. For display purposes, we only show the evolution up through the RGBTip. The physical interpretation of a small value of α_{MLT} is a fluid parcel traveling a short radial distance (in units of H_{P}) before it deposits its internal energy and blends into the surrounding medium. The net effect is reduced convective efficiency, thus cooler temperatures and more inflated radii. For this reason, α_{MLT} is used to mimic the effects of physical ingredients, e.g., the inhibition of convection by a magnetic field, that are missing from the majority of current stellar evolution models (but see Feiden & Chaboyer 2013). For example, α_{MLT} that is smaller compared to the solar-calibrated value is commonly used to bring models into agreement with observations of inflated radii in low-mass stars (see Section 2.8.1).

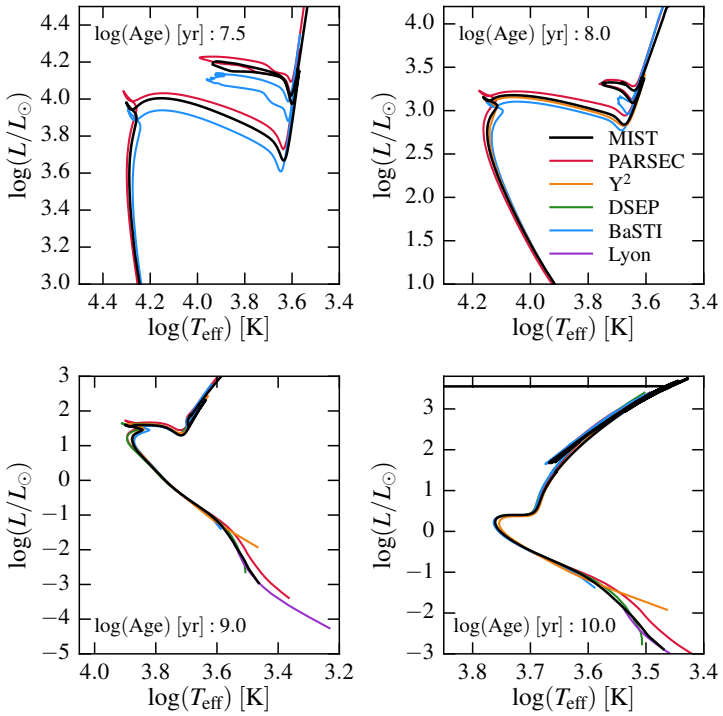


Figure 2.15: A comparison between MIST (black; this work), PARSEC v1.2S (red; Bressan et al. 2012; Chen et al. 2014; Tang et al. 2014), Y^2 (orange; Demarque et al. 2004), DSEP (green; Dotter et al. 2008), BaSTI "non-canonical" (turquoise; Pietrinferni et al. 2004), and Lyon (navy; Baraffe et al. 1998, 2003, 2015) isochrones at $Z = Z_{\odot}$ as defined by each model.

2.7 Comparisons with Existing Databases

In this section we compare the MIST models to several popular stellar evolution databases in the literature. Due to differences in the choice of input physics and their implementations in the codes, an apples-to-apples comparison is challenging. We stress that this is neither a comprehensive review of all published models in the literature nor a thorough and detailed comparison between different databases. Instead, we aim to provide the reader with a general impression of how the new MIST models compare to several widely-used models. We refer the reader to the MESA instrument papers (Paxton et al. 2011, 2013, 2015) for closer comparisons at the level of the codes themselves and their evolutionary track outputs. Our goal here is to compare at the level of databases, which reflects the net effect of many different choices for input physics.

2.7.1 Evolutionary Tracks and Isochrones

We first compare isochrones at $Z_\odot$ adopted by each model. In Figure 2.15, we compare MIST (black; this work), PARSEC v1.2S (red; Bressan et al. 2012; Chen et al. 2014; Tang et al. 2014), Y^2 (orange; Demarque et al. 2004), DSEP (green; Dotter et al. 2008), BaSTI "non-canonical" with $\eta = 0.4$ (turquoise; Pietrinferni et al. 2004), and Lyon (navy; Baraffe et al. 1998, 2003, 2015) for $\log(\text{Age})$ [yr] $= 7.5$, 8.0, 9.0, and 10.0. The DSEP and Lyon models are not included in the top two panels because they are not available at young ages. Note that of the models featured here, only the MIST models include the effects of rotation.* We choose MIST models with rotation instead of those without to make the comparison because the fiducial models include rotation and all calibrations are performed on this set. Overall, the MIST isochrones are in broad agreement with other isochrones. Although the absolute metal contents differ by as much as 30% between various models due to differences in the preferred definition of $Z_\odot$, the isochrones are less discrepant than one might imagine because they have been calibrated to match the properties of the Sun. There is more noticeable discrepancy at the young ages due to the complex and uncertain physics—such as core convective overshoot—governing the evolution of massive stars. In particular, the CHeB phase (e.g., the development of the blue loop) is notoriously sensitive to the details of input physics (e.g., McQuinn et al. 2011) though there are ongoing efforts to address this issue (e.g., Tang et al. 2016). Moreover, the PARSEC isochrones depart notably from the rest of the models on the lower MS due to their recent implementation of $T - \tau$ boundary conditions that have been empirically calibrated to match the observed mass-radius relations for cool dwarfs (Chen et al. 2014).

In Figure 2.16, we now compare isochrones at fixed Z. Note that although Z is the same, there are still element-to-element variations due to the different solar abundance scales adopted by each group. We plot $\log(\text{Age})$ [yr] $= 10.0$ isochrones at $Z = 0.0001$ and $Z = 0.03$ for PARSEC, Y^2, DSEP, BaSTI, and MIST. Note that only the MIST models follow the evolution continuously from the helium ignition in the

*There is a version of Y^2 models with rotation for $M < 1.25\ M_\odot$. See Spada et al. (2013).

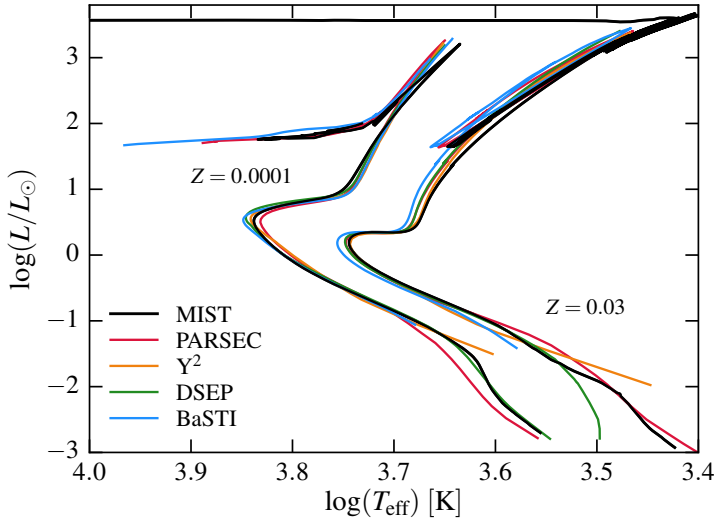


Figure 2.16: The same as Fig 2.15, except now at $Z = 0.0001$ and $Z = 0.03$ for $\log \mathrm{Age} = 10.0$.

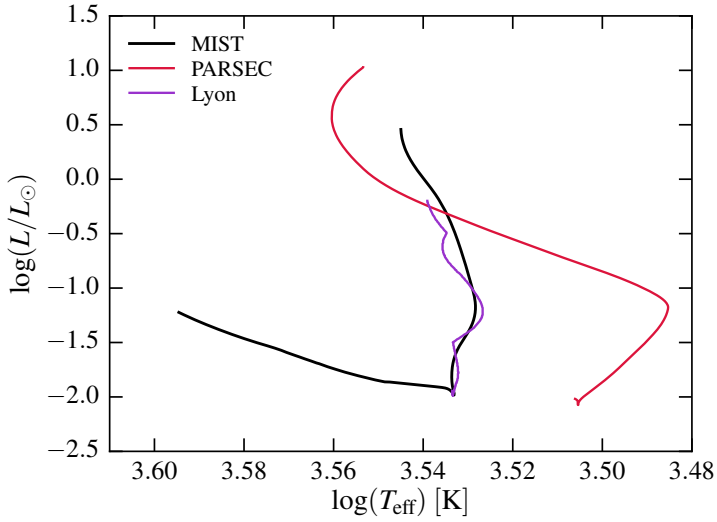


Figure 2.17: The evolutionary tracks for a 0.3 $M_\odot$ star from MIST, PARSEC, and Lyon models at $Z = Z_\odot$.

degenerate core (RGBTip) to the CHeB through a series of helium flashes (see also Section 2.10.1). The models are broadly in agreement, though there are some differences in the lower MS and the extent of the CHeB. The former is likely mostly due to differences in the adopted boundary conditions in the models, and the latter is possibly due to differences in the adopted Reimers mass loss efficiency (BaSTI, PARSEC, and MIST adopt $\eta_\mathrm{R} = 0.4$, 0.2, and 0.1, respectively, while Y^2 does not include mass loss).

Figure 2.17 presents a comparison between the MIST, PARSEC, and Lyon models for a 0.3 $M_\odot$ evo-

lutionary track. As noted above, the PARSEC models now adopt a modified $T - \tau$ relation for low-mass stars, which likely explains the relatively large difference between that model and the others. The Lyon and MIST models largely agree, although several sharp features are noticeable in the Lyon models during the PMS phase that do not appear in the MIST models. The origin of these small differences is unclear to us.

2.7.2 Simple Stellar Population Colors

In Figure 2.18 we show the evolution of integrated colors of a simple stellar population for MIST (black), PARSEC/COLIBRI (red; Bressan et al. 2012; Marigo et al. 2013; Rosenfield et al. 2014), and BaSTI (blue; Pietrinferni et al. 2004) isochrones at solar metallicity. The colors are computed by integrating along the isochrone at a given age with weights provided by the Kroupa IMF (Kroupa 2001). They are calculated using the Python bindings* to the Flexible Stellar Population Synthesis code (FSPS, v2.5; Conroy et al. 2009, 2010). We turn the AGB circumstellar dust option off to enable a more direct comparison between the three models. There are no predictions from the BaSTI models at $\log(\mathrm{Age})\ [\mathrm{yr}] < 7.5$ because they only go up to 10 $M_{\odot}$ in mass. Note that we used the same bolometric corrections for all three cases so any variation in color is purely due to differences in the isochrones.

Overall, the models are in good agreement with each other, especially in $B - V$, though there are some noticeable differences between the models in other colors. At $\log(\mathrm{Age})\ [\mathrm{yr}] \gtrsim 9$ in $FUV - V$, the MIST prediction turns over toward bluer colors while the PARSEC/COLIBRI and BaSTI predictions continue to get redder. This qualitative difference is due to the inclusion of the post-AGB and WD phases in the MIST models. In $V - K$ and $J - K$, the large spikes at young ages ($\log(\mathrm{Age})\ [\mathrm{yr}] \sim 7$) are due to the onset of the RSG phase from massive stars. This feature appears at a slightly later time in MIST compared to in PARSEC/COLIBRl, which points to the differences in the lifetimes of massive stars in the two databases. The inclusion of rotational mixing in the MIST models may explain the longer MS lifetimes.

*https://github.com/dfm/python-fsps

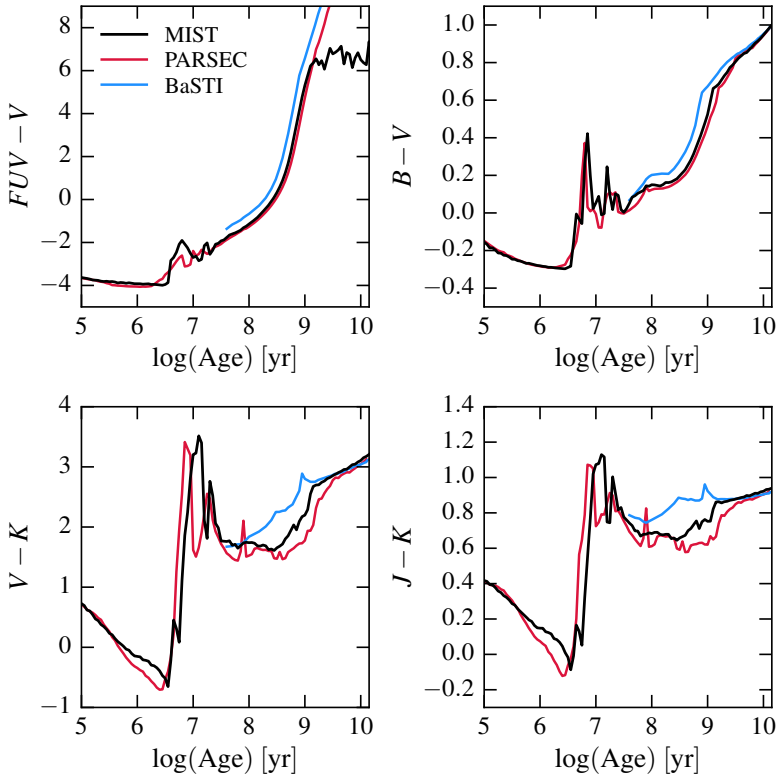


Figure 2.18: The evolution of integrated colors of a simple stellar population for MIST (black), PARSEC/COLIBRI (red), and BaSTI (blue) isochrones at solar metallicity. The colors were computed with the Flexible Stellar Population Synthesis code (FSPS, v2.5; Conroy et al. 2009, 2010) assuming a Kroupa (2001) IMF and AGB circumstellar dust turned off. Note that we used the same bolometric corrections for all three cases so any variation in color is purely due to differences in the isochrones.

Finally, significant differences between the three models occur at intermediate ages in redder colors, where TPAGB stars are expected to contribute a significant fraction of the total luminosity. The MIST color predictions fall between the BaSTI and PARSEC predictions. We note that the full luminosity and temperature variations—the actual thermal pulses—are included in the MIST isochrones.

2.7.3 The Effects of Rotation

We compare MIST and Geneva (Ekström et al. 2012) evolutionary tracks for a wide range of masses in Figure 2.19. The Geneva models, shown in pink, also include rotation with $v/v_{\rm crit} = 0.4$ and adopt a similarly low-metallicity solar abundance scale—$Z_\odot = 0.014$ to be exact—with the elemental mixture from Asplund et al. (2005) combined with the Ne abundance from Cunha et al. (2006). At fixed stellar

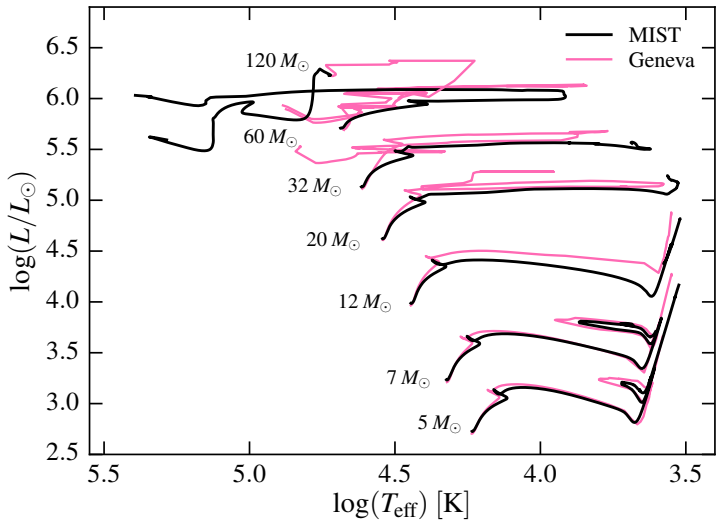


Figure 2.19: A comparison of MIST and Geneva (Ekström et al. 2012) evolutionary tracks with rotation in black and pink, respectively.

mass, the Geneva models are hotter and more luminous at TAMS, which implies that rotational mixing is more efficient in their models compared to that in the MIST models. As discussed in Section 2.6.1, efficient rotational mixing gives rise to hotter temperatures and higher luminosities due to larger core sizes and increased μ in the envelope.

Some MIST models, such as the 120 $M_\odot$ star in Figure 2.19, lose their hydrogen-rich envelope very promptly as they reach the so-called $\Omega\Gamma$-limit (Maeder & Meynet 2000). As evident from Equations 2.21 and 2.22, massive stars with $\Gamma = L/L_{\rm Edd} \rightarrow 1$ only require the smallest amount of rotation Ω to receive a large boost in mass loss rates. As the star evolves, its surface metallicity increases due to a combination of mixing processes and mass loss, and as a result, its surface Rosseland mean opacity increases. This in turn decreases $L_{\rm Edd}$, which makes it easier for a star to experience a large rotational boost. The star then may enter a positive feedback loop where mass loss leads to even more efficient mass loss until it removes all of its envelope and becomes a very compact star almost completely devoid of angular momentum. At the moment, it is not clear whether nature produces such stars, perhaps because of more complex behavior not included in the current 1D models.

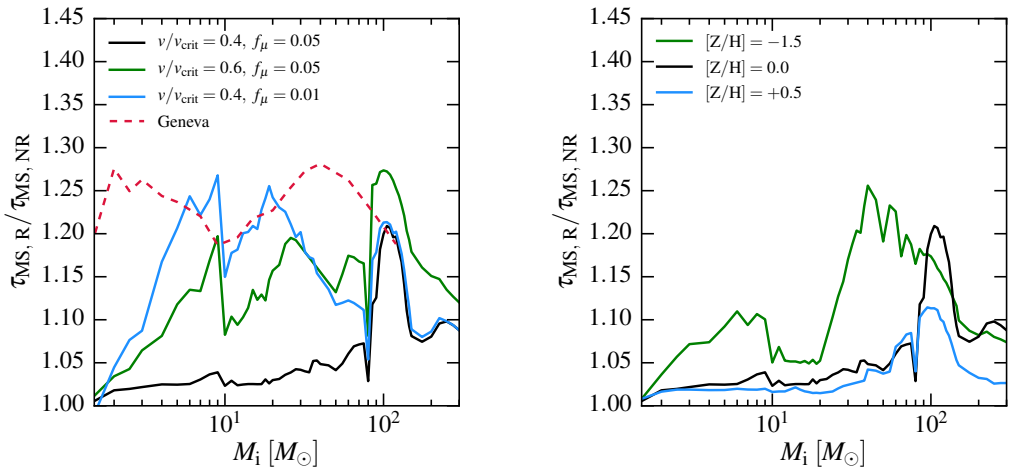


Figure 2.20: The ratio of MS lifetimes for rotating and non-rotating models as a function of initial mass. *Left*: Comparison at $Z_\odot$. The solid black, green, blue, and dashed pink lines correspond to the default model with $v/v_{\rm crit} = 0.4$ and $f_\mu = 0.05$, model with $v/v_{\rm crit} = 0.6$, model with $f_\mu = 0.01$, and the Geneva model, respectively. The default MIST model shows a modest $\sim 5\%$ enhancement in the MS lifetime due to rotational mixing, whereas the Geneva model experiences a $\sim 20\%$ increase due to more efficient rotational mixing. *Right*: Comparison among MIST models at [Z/H] $= -1.0$, 0.0, and $+0.5$ with default parameters $v/v_{\rm crit} = 0.4$ and $f_\mu = 0.05$. The efficiency of rotational mixing is larger in more metal-poor stars because line-driven mass loss—thus angular momentum loss efficiency—is lower.

Differences in the efficiency of rotational mixing between the MIST and Geneva models is further explored in the left panel of Figure 2.20, which shows the ratio of MS lifetimes for rotating and non-rotating models as a function of initial mass. This ratio is expected to be greater than unity since rotational mixing channels additional fuel into the core. The solid black, green, blue, and dashed pink lines correspond to the default model at solar metallicity with $v/v_{\rm crit} = 0.4$ and $f_\mu = 0.05$, solar metallicity model with $v/v_{\rm crit} = 0.6$ and $f_\mu = 0.05$, solar metallicity model with $v/v_{\rm crit} = 0.4$ and $f_\mu = 0.01$, and the Geneva model, respectively. Recall that f_μ is the parameter that captures the sensitivity of rotational mixing to the mean molecular weight gradient, such that a small f_μ corresponds to efficient mixing even in the presence of a stabilizing composition gradient.* The default MIST model experiences only a modest enhancement in the MS lifetime. In contrast, the Geneva model experiences an overall $\sim 25\%$ increase in the MS lifetime for stars more massive than 2 $M_\odot$ (Ekström et al. 2012; Georgy et al. 2013).

*This is at a fixed value of f_c, the ratio of the diffusion coefficient and the turbulent viscosity. See Section 3 of Heger et al. (2000) for more details.

Although the MIST and Geneva models experience quantitively different amounts of MS lifetime boost, this is not entirely surprising given their different implementations of rotational mixing. Moreover, massive star evolution, regardless of the inclusion of rotation, is highly uncertain and very sensitive to small changes in the input physics. At fixed $v/v_{\rm crit}$, the efficiency of rotational mixing depends sensitively on f_μ. As expected, MS lifetime boost in the MIST models is increased for a higher rotational mixing efficiency via increased rotation velocity or decreased f_μ. The default values $f_c = 1/30$ and $f_\mu = 0.05$ are adopted from Heger et al. (2000). This combination, though not unique, is able to reproduce many of the observational constraints such as the high-mass star ratios (see Section 2.9.3) and observed surface nitrogen enrichment (see Section 2.9.4). The fact that both MIST and Geneva models broadly reproduce observational constraints in spite of the different lifetime enhancements implies that current observations are not uniquely constraining. For reference, we note that the MS lifetimes for the rotating models in Geneva and MIST agree to within 10–15% at solar metallicity: for low-mass stars ($\lesssim 1.5\ M_\odot$), the MS lifetime is shorter in the Geneva models, whereas for higher mass stars, the MIST models have MS lifetimes that fall between those of non-rotating and rotating Geneva models.

In the right panel, we compare the ratio of MS lifetimes among MIST models with different metallicities. Since the primary mass loss mechanism for massive stars is strongly metallicity-dependent line-driven winds, rotational mixing becomes more important at low metallicities due to the lowered efficiency of angular momentum loss, as expected.

2.8 Comparisons with Data I: Low Mass Stars

2.8.1 Luminosity-Mass-Radius-Temperature Relations

Relations between mass, radius, luminosity, and temperature provide powerful and fundamental tests of stellar evolution models. In the past two decades, there have been enormous improvements in measuring

these quantities to high precision from a variety of techniques, including eclipsing binaries and interferometry (see Torres et al. 2010 for a recent review on this topic).

In Figure 2.21, we plot $\log(R)$, $\log(L)$, and $\log(T_{\rm eff})$ as a function of stellar mass for the DEBCat* sample, an online catalog of DEBs with well-measured parameters compiled from the literature (Southworth 2015), and a sample of DEBs selected from the literature that was homogeneously reanalyzed by Torres et al. (2010). Note that the Torres et al. (2010) sample appears to show smaller scatter, especially around $\sim 1\ M_{\odot}$. We applied a $\log(g)$ cut—$\log(g) > 4.1$ cm s^{-2} and 3.4 cm s^{-2} for $M_{\rm i} > 1.2\ M_{\odot}$ and $< 1.2\ M_{\odot}$, respectively, as estimated from our model isochrones—to remove evolved stars from the sample of likely MS stars. Furthermore, we removed from the final sample a few conspicuous outliers identified as PMS or RGB stars in the literature. The predicted ZAMS relations for solar metallicity are shown as black solid lines in each of the panels. Since the ages of the stars are unknown, we also show the full range of possible MS values as the gray shaded region. The vertical dashed, dotted, and dot-dashed lines demarcate the initial masses for which $t_{\rm MS} \sim t_{\rm Hubble}$ for [Z/H] $= -1.0$, 0.0, and $+0.5$. Below these masses, we do not expect stars to have evolved off the ZAMS relations. Overall, the observed points fall comfortably within the region bounded by the ZAMS and TAMS relations. However, the observed stars start to deviate from the predicted relations below $M_{\rm i} \lesssim 0.7\ M_{\odot}$. In the insets, we zoom in on the low-mass range to show that the models systematically underpredict radii by ~ 0.03 dex and overpredict temperatures by ~ 0.05 dex, for a total deficit of ~ 0.2 dex for the predicted luminosity.

There is a well-known discrepancy between observed and predicted effective temperature, radius, and luminosity relations for stars with appreciable convective layers, most notably M dwarfs (e.g., Casagrande et al. 2008; Torres et al. 2010; Kraus et al. 2011; Feiden & Chaboyer 2013; Spada et al. 2013; Torres 2013; Chen et al. 2014). At fixed stellar mass, models tend to predict stars that are 5–10% hotter and 10–20% smaller in radius compared to observations. This disagreement is present in both field stars and detached

*http://www.astro.keele.ac.uk/jkt/debcat/

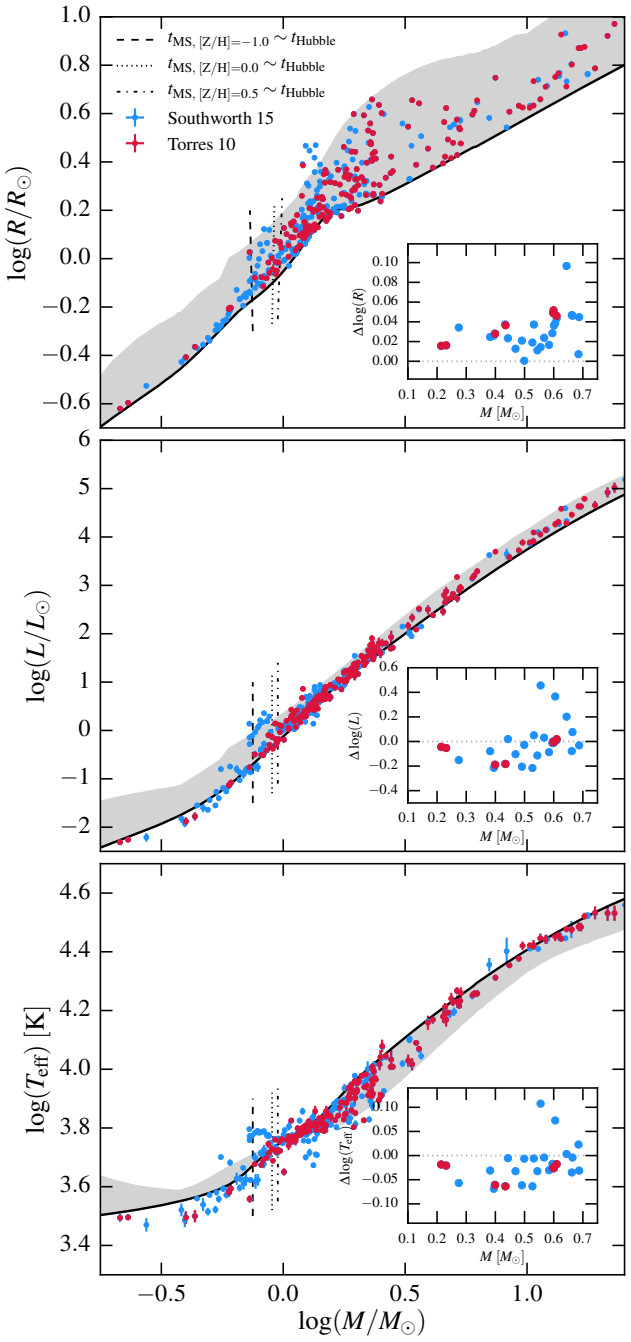


Figure 2.21: $\log(R)$, $\log(L)$, and $\log(T_{\rm eff})$ as a function of stellar mass measured for MS stars in detached eclipsing binaries (DEB). The Southworth (2015) sample in blue comes from DEBCat, an online catalog of DEBs with well-measured parameters gathered from the literature. The red points correspond to a sample of DEBs selected from the literature that was homogeneously reanalyzed by (Torres et al. 2010). Note that the Torres et al. (2010) sample appears to show smaller scatter, especially around $\sim 1\ M_\odot$. The predicted ZAMS relations for solar metallicity are shown as black solid lines in each of the panels. Since the ages of the stars are unknown, we also show the full range of possible MS values as the gray shaded region. The vertical dashed, dotted, and dot-dashed lines demarcate the initial masses for which $t_{\rm MS} \sim t_{\rm Hubble}$ for $[{\rm Z/H}] = -1.0$, 0.0, and $+0.5$, respectively. The insets highlight the well-known discrepancy for the low-mass stars ($< 0.7\ M_\odot$).

eclipsing binaries (DEBs), suggesting that this is an effect intrinsic to dwarfs (Boyajian et al. 2012b; Spada et al. 2013). However, there are systematic errors of a few percent expected from DEB light curve analysis due to variations in the spot size and coverage (Morales et al. 2010). A proposed explanation for this mismatch invokes magnetic activity and rotation effects that are not currently modeled accurately (Spruit & Weiss 1986; Morales et al. 2008, 2010; Kraus et al. 2011; Irwin et al. 2011; Feiden & Chaboyer 2012; MacDonald & Mullan 2014; Jackson & Jeffries 2014). Large-scale magnetic fields are thought to both inhibit the upwelling of hot convective bubbles and generate more starspots on the surface (e.g., Feiden & Chaboyer 2012). In order to conserve flux, the stellar radius is inflated, causing a subsequent decrease in the surface temperature. Rotation may play a role since it is believed to generate a dynamo and has been linked to magnetic activity (see Section 2.3.6.5). Furthermore, the choice of surface boundary conditions in stellar models has a non-trivial effect on the mass-radius relation and the optical CMDs at the lowest masses (e.g., Baraffe et al. 1995; Chabrier et al. 1996; Baraffe et al. 1997; Spada et al. 2013; Chen et al. 2014). When it comes to modeling cool dwarfs, it is especially important to use accurate boundary conditions—such as those computed from atmosphere models, e.g., PHOENIX (Hauschildt et al. 1999a) and ATLAS12/SYNTHE (Kurucz 1970, 1993)—in place of simple models that assume gray atmospheres (see Section 2.3.3).

2.8.2 Initial-Final Mass Relation

Low- and intermediate-mass stars shed a nontrivial fraction of their mass via winds during the course of their lifetime, eventually terminating their lives as WDs. Total mass loss integrated over the lifetime directly connects the initial mass to the remnant mass through the initial-final mass relation (IFMR; e.g., Reimers 1975; Weidemann 1977; Renzini & Fusi Pecci 1988; Weidemann 2000). It is an important diagnostic for the cumulative effect of mass loss occurring at various stages of evolution. The expectation is that stars with higher initial masses produce more massive WD remnants (e.g., Claver et al. 2001; Dobbie

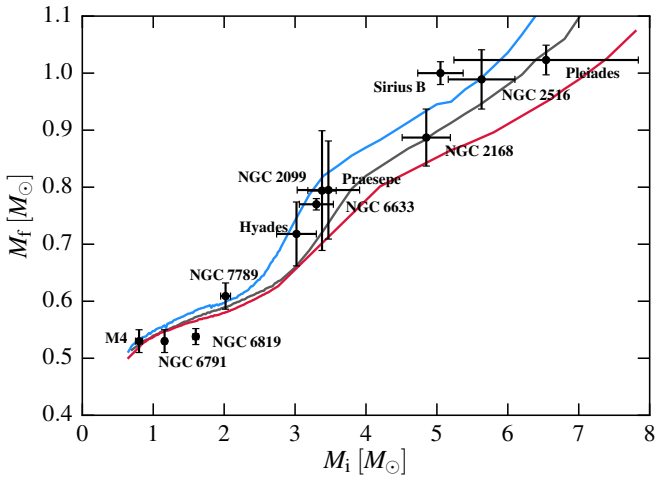


Figure 2.22: The initial-final mass relation constructed using binned cluster data and Sirius B from Ferrario et al. (2005) (see references therein) and Kalirai et al. (2008). The predicted relations for $[\mathrm{Z/H}] = -0.5$, 0.0, and $+0.5$ are shown in blue, gray, and red. These metallicities roughly bracket the metallicity range of the systems in the sample.

et al. 2004; Williams & Bolte 2007; Catalán et al. 2008b; Kalirai et al. 2008; Williams et al. 2009; Zhao et al. 2012).

We compare the predicted IFMR to a sample of eight young open clusters, three older open clusters with ages $>$ 1 Gyr, and Sirius B (see Ferrario et al. (2005) and Kalirai et al. (2008) for references therein). It is useful to study clusters of a variety of ages because it allows us to probe a large range of initial masses. Observed initial and final masses for each WD in a cluster are inferred using the following method (see e.g., Kalirai et al. 2008 for details). A combination of WD spectral analysis and modeling yields both the WD mass (final mass) and cooling age (age since the end of shell helium burning on the TPAGB). The WD progenitor age up to the end of the TPAGB is simply the difference between the total age of the system as estimated from the cluster turn-off and the WD cooling age from the previous step. Finally, stellar evolution models provide the progenitor mass (initial mass) corresponding to the WD progenitor age. Note that initial and final masses are not directly observed but instead are inferred from modeling: the final mass comes from the spectral analysis while the initial mass depends on stellar evolution theory and CMD analysis.

In Figure 2.22 we plot the predicted IFMRs for three values of [Z/H] that altogether encompass the metallicities of the systems represented here. Individual measurements within a single cluster have been binned to represent a weighted mean. Overall, the models are in excellent agreement with the data, though there are some notable outliers like NGC 6819 and Sirius B. The low-mass plateau at $M_{\rm i} \lesssim 2\ M_{\odot}$ ($M_{\rm f} \sim 0.6\ M_{\odot}$) is marginally consistent with the peak of the galactic disk WD mass function near $\sim 0.6\ M_{\odot}$ (Liebert et al. 2005; Kleinman et al. 2013; Kepler et al. 2015), although a full model that folds in the age and metallicity distributions as well as the initial mass function (IMF) weights will be required for a robust comparison against the observed mass function (see also Catalán et al. 2008a).

Furthermore, the steep slope predicted around $M_{\rm i} \sim 3\ M_{\odot}$ to $4\ M_{\odot}$ (slope ~ 0.16) is consistent with the empirical estimate from Cummings et al. (2015), who found a slope of $M_{\rm f} = (0.163 \pm 0.022) M_{\rm i} + (0.238 \pm 0.071)\ M_{\odot}$ from a combined sample of newly identified WDs in NGC 2099 and the WDs in the Hyades and Praesepe from Kalirai et al. (2014). Interestingly, in agreement with Romero et al. (2015) but in contrast with Marigo & Girardi (2007), our theoretical relations show a clear systematic trend with metallicity above $3\ M_{\odot}$. As discussed in Marigo & Girardi (2007), the core can grow/erode through shell-burning/third dredge-up during the TPAGB, while mass loss more or less determines when the TPAGB phase terminates. Metallicity is predicted to affect all these processes: at low metallicities, third dredge-up and hot bottom burning efficiencies, as well as the core mass at the onset of the first thermal pulse, increase, but mass loss efficiency is believed to decrease. The measurement of the IFMR as a function of metallicity therefore has great potential for constraining these uncertain evolutionary phases.

It is worth noting that calculations of $M_{\rm i}$ and $M_{\rm f}$ which rely on, e.g., WD spectral analysis and isochrone fitting, and the quality of the data vary between cluster to cluster. As noted in Kalirai et al. (2008), the sample is likely affected by small systematic offsets and nonzero field contamination. In particular, precision measurements of ages with the MSTO method in young systems is particularly challenging due to the vertical placement of the MSTO in an optical CMD (note the larger error bars toward younger ages and higher

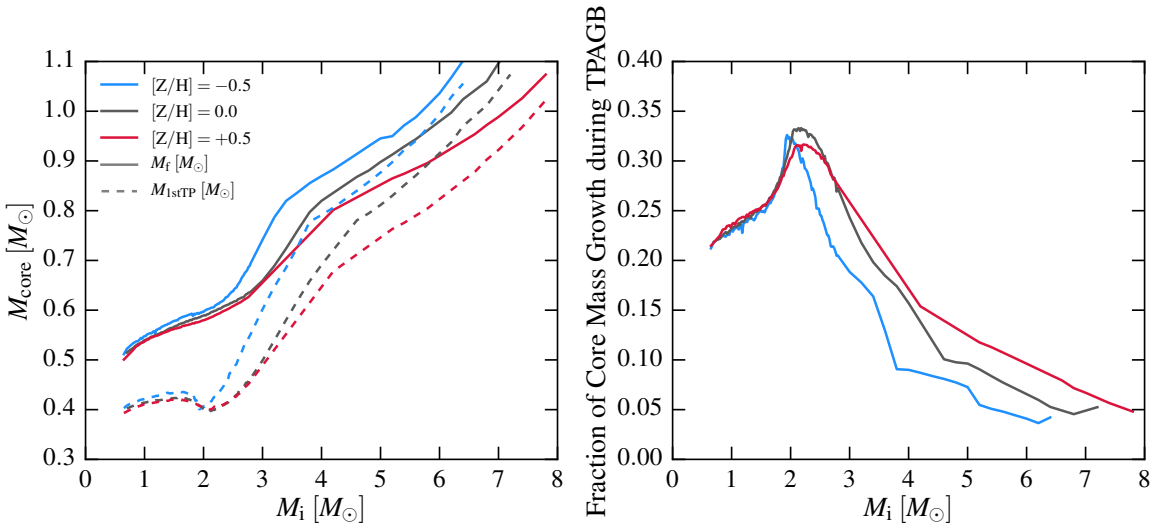


Figure 2.23: *Left*: A comparison highlighting the difference between the final mass (solid) from Figure 2.22 and the core mass at first thermal pulse (dashed) as a function of initial mass for three metallicities. The latter is devoid of large uncertainties in mass loss, third dredge-up, and hot bottom burning that strongly influence the TPAGB evolution, and consequently, the final remnant mass. *Right*: Fractional growth in core mass during the TPAGB phase for the same three metallicities.

$M_{\rm i}$). Moreover, the thickness of the hydrogen and helium layer assumed in the WD spectral model can also have a non-negligible effect on the inferred cooling age and thus the initial mass (Prada Moroni & Straniero 2002; Catalán et al. 2008a). Catalán et al. (2008a) found that reasonable variations in the envelope thickness can lead to differences as large as 1 $M_\odot$ for progenitors with $M_{\rm i} \gtrsim 5\ M_\odot$ but a more modest $\sim 0.1\ M_\odot$ difference for the lower masses. Other model uncertainties include the assumed core composition. A stringent test of the IFMR should be entirely self-consistent; a single set of isochrones should be used to estimate the "observed" masses $M_{\rm i}$ and $M_{\rm f}$.

We conclude this section with a comparison between the final mass and the core mass at the first thermal pulse in Figure 2.23. It is useful to consider the core mass before the star experiences significant core growth from the subsequent thermal pulses, because this comparison is devoid of large uncertainties in mass loss, third dredge-up, and hot bottom burning that strongly influence the TPAGB phase (e.g., Wagenhuber & Groenewegen 1998; Weidemann 2000). In the left panel, we show the predicted IFMR from Figure 2.22 and the core mass at the beginning of the TPAGB phase as a function of initial mass in solid

and dashed lines, respectively. The right panel shows the fractional growth in core mass during the TPAGB phase ($M_{\rm f} - M_{\rm 1stTP}/M_{\rm f}$) as a function of initial mass. Overall, there is considerable growth in core mass occurring during this phase, with a broad peak over 2–3 $M_{\odot}$. The location of maximum growth coincides with the peak in TPAGB lifetime as shown in Figure 2.13. This result is in good agreement with what Bird & Pinsonneault (2011) and Kalirai et al. (2014) found using the Pietrinferni et al. (2004) and PARSEC/COLIBRI (Bressan et al. 2012; Marigo et al. 2013) models, respectively.

2.8.3 Optical and NIR Color Magnitude Diagrams of Clusters

2.8.3.1 Star Clusters

In this section we present comparisons with observed color magnitude diagrams of star clusters. Models shown here include a reddening correction according to the standard $R_{\rm V} \equiv A_{\rm V}/E(B-V) = 3.1$ reddening law from Cardelli et al. (1989). The majority of the systems presented here are metal-rich and we will provide comparisons with metal-poor clusters with non-solar-scaled abundance patterns in Dotter et al., in prep. The CMD comparisons here are by-eye fits to check that the models yield a reasonable agreement. We plan to perform more robust CMD fitting with MATCH (Dolphin 2002) in future work.

M67 (NGC 2682), an intermediate-age (4 Gyr) solar metallicity open cluster at a distance of $\sim$800 pc, is a benchmark system for stellar evolution models (Taylor 2007; Sarajedini et al. 2009). In particular, its well-developed Henyey hook on the MSTO is used to calibrate core convective overshoot in low- and intermediate-mass stars (e.g., Michaud et al. 2004; VandenBerg et al. 2006; Magic et al. 2010; Bressan et al. 2012).

Figure 2.24 shows optical and near-infrared (NIR) color magnitude diagrams (CMDs) and $\log({\rm Age})$ [yr] = 9.58 (3.80 Gyr) isochrones with [Z/H] = 0.0, $A_V = 0.2$, and $\mu = 9.7$, where μ is the distance modulus. The Sandquist (2004) *BV* sample (blue points) was carefully selected using proper motion, radial velocity, variability, and CMD-location information to yield cluster members that are most likely to be single stars. The

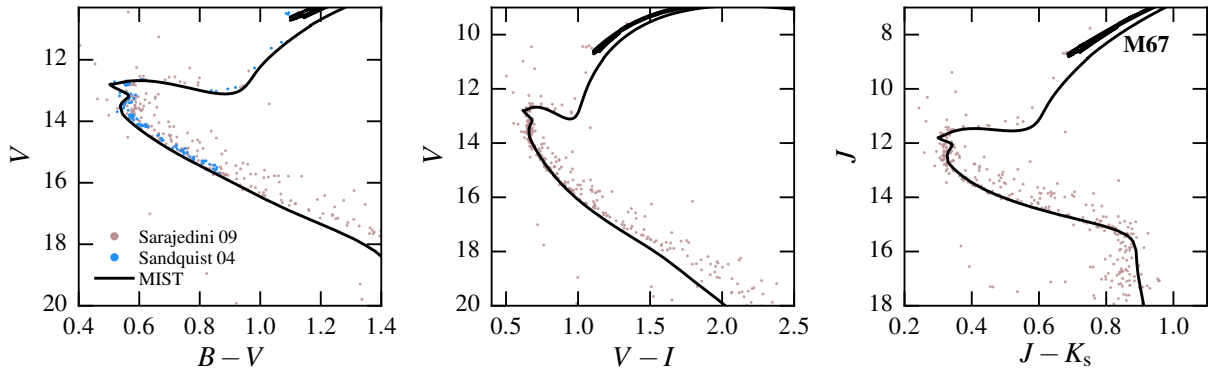


Figure 2.24: CMDs for M67 from *2MASS* and *BVI* photometry (Sandquist 2004; Sarajedini et al. 2009). The Sandquist (2004) *BVI* sample (blue points) was carefully selected to exclude likely binaries, and the Sarajedini et al. (2009) sample (mauve points) reflects a membership probability cut of $> 20\%$. MIST isochrones with $[\mathrm{Z/H}] = 0.0$, $\log(\mathrm{Age})$ [yr] $= 9.58$ (3.80 Gyr), $A_V = 0.2$, and $\mu = 9.7$ are shown in black.

Sarajedini et al. (2009) *2MASS* sample (mauve points) reflects a membership probability cut of $> 20\%$.

The MS, MSTO morphology, as well as the RC luminosity are well-matched in all three colors. However, the isochrone begins to peel away from the MS ridge line at fainter than $V \sim 17$ which corresponds to $M_{\mathrm{i}} \sim 0.7\ M_{\odot}$. This is a well-known issue: models that successfully reproduce the NIR colors (e.g., Sarajedini et al. 2009) predict MS colors that are too blue in the optical (e.g., An et al. 2009; Chen et al. 2014). One of the goals of future work is to revisit and address this problem.

Praesepe (M44; NGC 2632) is a young ($\sim$ 757 Myr) and moderately super-solar cluster at a distance of 180 pc, making it one of the nearest open clusters to the Sun (Taylor 2006; Gáspár et al. 2009; Carrera & Pancino 2011). A combination of its rich cluster membership ($N \gtrsim 1000$; Kraus & Hillenbrand 2007), large proper motion, and proximity makes Praesepe a favorable target for stellar population studies.

In Figure 2.25, we show *2MASS* (mauve points) and *UKIDSS* Galactic Clusters Survey photometry data (blue points) from Wang et al. (2014) and Boudreault et al. (2012), respectively. The Wang et al. (2014) sample consists of proper-motion-selected cluster members that are likely to be single stars and includes stars with masses as low as $\sim 0.15\ M_{\odot}$. The Boudreault et al. (2012) sample was obtained using astrometric and five-band photometric selection criteria and consists mostly of low-mass stars with

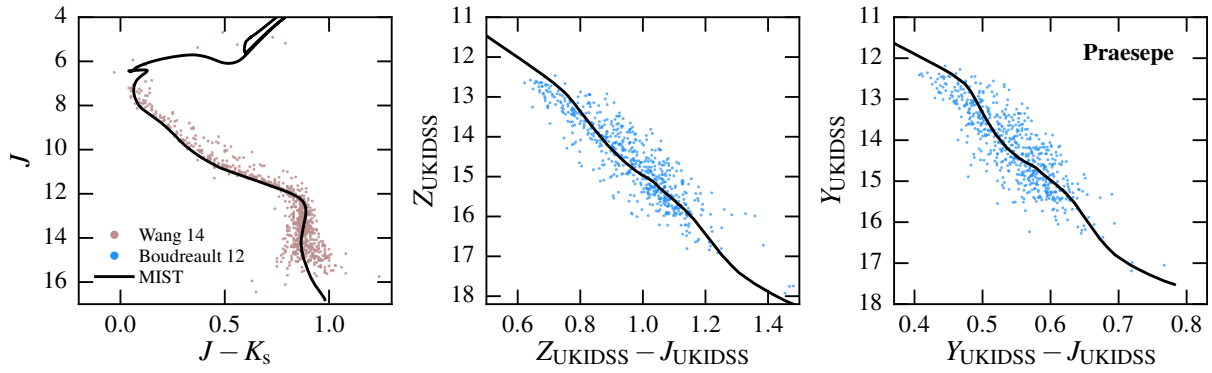


Figure 2.25: CMDs for Praesepe from *2MASS* (Wang et al. 2014) and *UKIDSS* Galactic Clusters Survey photometry (Boudreault et al. 2012). The Wang et al. (2014) sample (mauve points) consists of proper-motion-selected cluster members that are likely to be single stars and the Boudreault et al. (2012) sample (blue points) was identified with an astrometric and five-band photometric cut. MIST isochrones with [Z/H] $= +0.15$, log(Age) [yr] $= 8.80$ (630 Myr), $A_V = 0.08$ and $\mu = 6.26$ are shown in black.

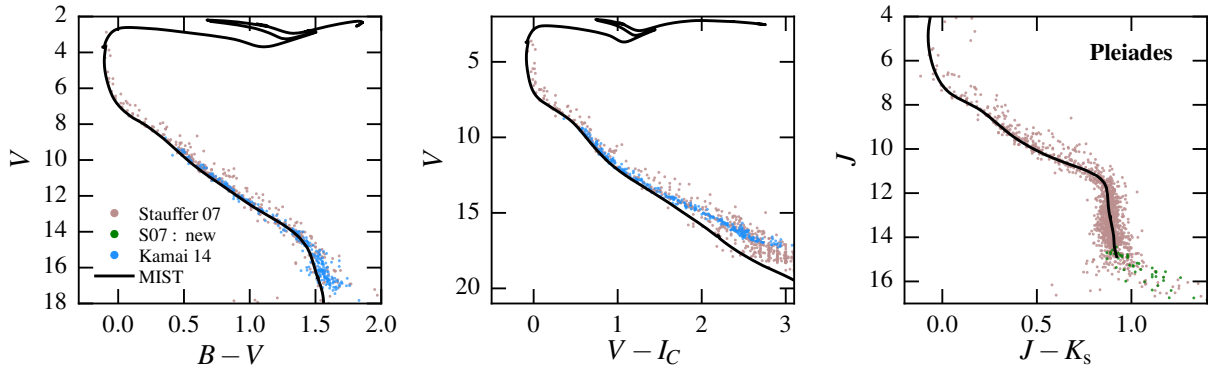


Figure 2.26: CMDs for Pleiades from *2MASS* and BVI_C photometry Stauffer et al. (2007); Kamai et al. (2014). The mauve points represent the Stauffer et al. (2007) compilation of *2MASS* and BVI_C photometry from the literature, the green points correspond to a sample of newly identified *2MASS* candidates by Stauffer et al. (2007), and the blue points are the Kamai et al. (2014) sample of proper motion members from the Stauffer catalog with updated BVI_C photometry. MIST isochrones with [Z/H] $= 0.0$, log(Age) [yr] $= 8.0$ (100 Myr), $A_V = 0.1$, and $\mu = 5.62$ are shown in black. We omit the TPAGB and post-AGB phases for display purposes.

$M_{\rm i} \lesssim 0.8\ M_{\odot}$. We applied an additional cut to remove objects that were flagged as variable stars and/or had $< 50\%$ membership probability. We overplot $\log(\mathrm{Age})$ [yr] $= 8.8$ (630 Myr) isochrones with $[\mathrm{Z/H}] = +0.15$, $A_V = 0.08$, and $\mu = 6.26$. Overall, the MIST isochrones provide good fits in all three colors.

Pleiades (M45) is a young ($\sim$ 100 Myr) solar metallicity open cluster at a distance of only 133 pc (Soderblom et al. 2005, 2009; Melis et al. 2014). Like Praesepe, its richness ($N \sim 1400$) and proximity make it a popular choice for testing stellar evolution models. In fact, the tension between observed and predicted CMD locations of K and M dwarfs dates back to Herbig (1962) who proposed non-coeval evolution, i.e., age spread, as a solution to the discrepancy. Theoretical isochrones were systematically offset toward higher luminosities and cooler temperatures in $B-V$ but predicted fainter and hotter stars in redder colors such as $V-I$ (Stauffer et al. 2003; Kamai et al. 2014). A more recent proposed explanation attributes this discrepancy to magnetic activity (e.g., spots) and/or rotation (e.g., Stauffer et al. 2003).

In Figure 2.26, we show optical and NIR CMDs constructed from the Stauffer et al. (2007) compilation of *2MASS* and BVI_C photometry from the literature (mauve points), a sample of newly identified *2MASS* candidates by Stauffer et al. (2007) (green points), and the Kamai et al. (2014) sample of proper motion members from the Stauffer catalog with updated BVI_C photometry (blue points). We overplot $\log(\mathrm{Age})$ [yr] $= 8.0$ (100 Myr) isochrones with $[\mathrm{Z/H}] = 0.0$, $A_V = 0.1$, and $\mu = 5.62$. Overall, the isochrones are well-matched to the observed CMDs in all filters. However, as seen in M67, the isochrones depart blueward from the MS ridge line in $V-I_C$ and $B-V$ at fainter than $V \sim 14$, corresponding to $M_{\rm i} \sim 0.6\ M_{\odot}$.

NGC 6791 is one of the most well-known and well-studied open clusters in the Milky Way. Its unusually old age ($\sim$ 8 Gyr) and high metallicity ($[\mathrm{Fe/H}] \sim 0.3$–0.5) combined with its rich membership make it a unique system for studying extreme stellar populations and their chemical evolution (e.g., Carney et al. 2005; Bedin et al. 2005; Origlia et al. 2006; Kalirai et al. 2007; Brogaard et al. 2012). NGC 6791 is particularly suitable for testing the present MIST models given its solar-scaled $[\alpha/\mathrm{Fe}]$ abundances.

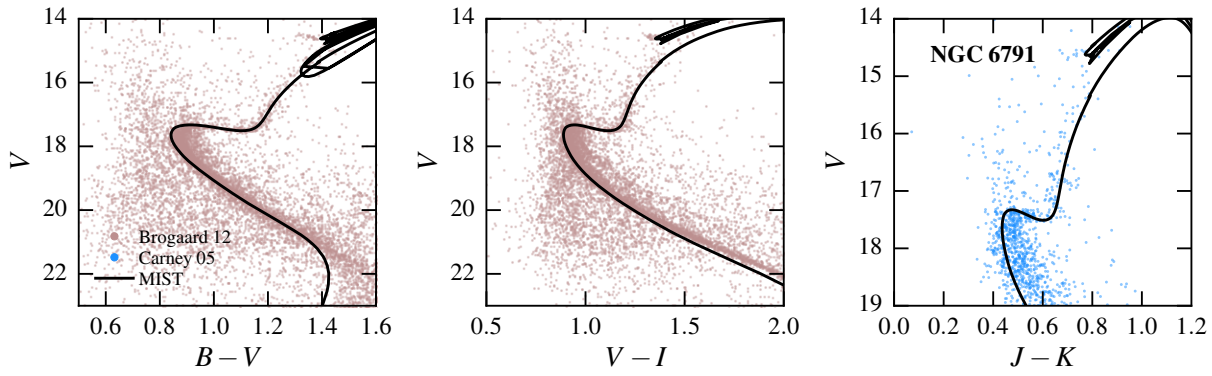


Figure 2.27: CMDs for NGC 6791 in *B*–*V* and *V*–*I* (mauve points; Brogaard et al. 2012) and in *J*–*K* (blue points; Carney et al. 2005). The Brogaard et al. (2012) sample consists of photometry from Stetson et al. (2003) that has been empirically corrected for differential reddening effects. MIST isochrones with [Z/H] = +0.47, log(Age) [yr] = 9.93 (8.5 Gyr), $A_V = 0.32$ and $\mu = 13.1$ are shown in black.

In Figure 4.10, we show optical and NIR CMDs in *B*–*V* and *V*–*I* (mauve points; Brogaard et al. 2012) and in *J*–*K* (blue points; Carney et al. 2005). The Brogaard et al. (2012) sample consists of photometry from Stetson et al. (2003) that has been empirically corrected for differential reddening effects. We overplot log(Age) [yr] = 9.93 (8.5 Gyr) isochrones with [Z/H] = +0.47, $A_V = 0.32$ and $\mu = 13.1$.

The agreement between data and MIST isochrones is generally good, in particular the MSTO and SGB morphologies and the CHeB (red clump) luminosity in all three colors. However, we see the same issue in $B-V$ and $V-I$ as in Figures 2.24 and 2.26: MIST isochrones predict colors that are too blue for stars fainter than $V \sim 21$. We return to this point at the end of this section.

Ruprecht 106 is a relatively low-mass ($M \sim 10^{4.8}\ M_\odot$) globular cluster with a metallicity of [Fe/H] ~ -1.5 (Kaluzny et al. 1995; Francois et al. 1997; Brown et al. 1997; Dotter et al. 2011; Villanova et al. 2013). Its peculiar properties include the lack of α-enhancement and the absence of abundance spread in light elements, e.g., Na-O anti-correlation, both of which are typical of globular clusters (Carretta et al. 2009). The spread in abundances found in globular clusters has been proposed to be a signature of self-enrichment through multiple generations of stellar populations (Kraft 1994; Gratton et al. 2004; D'Antona & Caloi 2008; Piotto et al. 2012; Gratton et al. 2012). Thus the modest mass of Ruprecht 106 combined

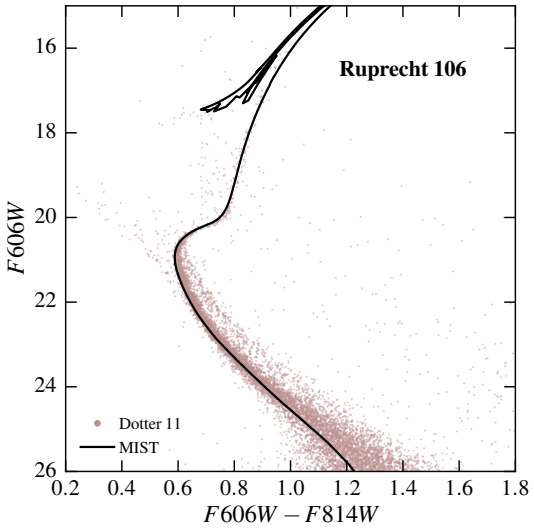


Figure 2.28: CMD from the *HST* ACS observations in the $F606W$ and $F814$ broadband filters Dotter et al. (2011). We overplot a $[\mathrm{Z/H}] = -1.50$, $\log(\mathrm{Age})$ [yr] $= 10.08$ (12.0 Gyr) isochrone with $\mu = 16.7$ and $A_V = 0.55$.

with its "stubby" HB morphology (consistent with the lack of helium variation via self-pollution) suggest that it is an archetypical single-population globular cluster (Caloi & D'Antona 2011; Villanova et al. 2013). It is an excellent choice for testing our low-metallicity models because we can bypass the issue of α-enhancement. We plan to perform many more tests against a large sample of globular clusters with our α-enhanced models in Paper II.

Figure 2.28 shows the optical CMD from the *HST* ACS observations in the $F606W$ and $F814$ broadband filters (Dotter et al. 2011). We plot a $\log(\mathrm{Age})$ [yr] $= 10.08$ (12.0 Gyr) isochrone with $\mu = 16.7$, $A_V = 0.55$, and $[\mathrm{Z/H}] = -1.50$ in black. The lower MS, SGB, and RGB are very well-matched though the model fails to accurately predict the extreme blue extent of the HB.

We conclude this section by addressing a recurring issue raised from the CMD comparisons. Our models predict $V - I$ and $B - V$ colors that are too blue for stars below $\lesssim 0.6$–$0.7\ M_\odot$. These discrepancies are due to missing and/or inaccurate atomic and molecular line opacity data used in our bolometric corrections. Efforts are ongoing to address these shortcomings.

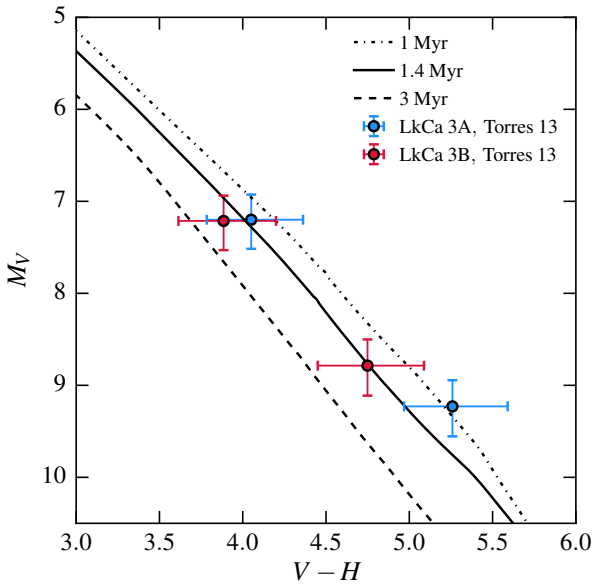


Figure 2.29: LkCa 3, a quadruple system of PMS stars in the Taurus-Auriga star-forming region (Torres et al. 2013) is compared to 1, 1.4, and 3 Myr isochrones at solar metallicity.

2.8.3.2 The Quadruple System LkCa 3

LkCa 3, a quadruple system of PMS stars in the Taurus-Auriga star-forming region (Torres et al. 2013), offers an excellent opportunity to test PMS evolution models. Operating under the assumption that the system is coeval, we expect all four objects to fall on a single-age isochrone. However, there is evidence that early accretion episodes affect the location and evolution of PMS stars on the HR diagram (e.g., Baraffe et al. 2009; Hosokawa et al. 2011), possibly complicating the comparison to PMS at these young ages. Torres et al. (2013) concluded that the predicted CMD locations of the four components in the Dartmouth models (Dotter et al. 2008) are better matched than those from the Lyon models (Baraffe et al. 2003), though their recently updated models (Baraffe et al. 2015) show good agreement with the observations as well. Their updates include a new solar abundance scale (a combination of Asplund et al. 2009 and Caffau et al. 2011), improved linelists, and recalibrated mixing length parameter for the treatment of convection.

In Figure 2.29, we show the observed LkCa 3 stars from Torres et al. (2013) with our 1, 1.4, and

3 Myr solar metallicity isochrones in the $V-H$ vs. M_V plane. The observations as reported by Torres et al. (2013) were already corrected for interstellar extinction assuming $A_V = 0.31$. The best-fitting isochrone shown in solid black line indicates that the age of the LkCa 3 system is ~ 1.4 Myr, consistent with previous estimates.

2.8.4 The Age Discrepancy in Upper Scorpius

Upper Scorpius (Upper Sco) is one of three subgroups (Upper Centaurus Lupus and Lower Centaurus Crux) in Scorpius-Centaurus (Sco-Cen), the nearest OB association from the Sun with $d \sim 145$ pc (de Zeeuw et al. 1999; Preibisch et al. 2002). The three subgroups altogether constitute a rich environment to study the formation and evolution of massive stars, circumstellar disks, low-mass stars, and brown dwarfs (e.g., Preibisch et al. 2002; Chen et al. 2011; Lodieu 2013). There has been some recent tension in the literature over the ages of these subgroups (Song et al. 2012). In particular, the age of Upper Sco is quoted to be either ~ 5 or ~ 11 Myr depending on the analysis method and the spectral types of stars used to estimate the age (de Geus et al. 1989; Preibisch et al. 2002; Slesnick et al. 2008; Lodieu et al. 2008; Pecaut et al. 2012; Herczeg & Hillenbrand 2015). This discrepancy poses a problem for other studies that rely on accurate age measurements, e.g., inferred mass functions (Preibisch et al. 2002; Lafrenière et al. 2008; Lodieu 2013).

Pecaut et al. (2012) used isochrones to determine the age of Upper Sco from a kinematic sample of PMS F-type stars. The authors compared luminosities and temperatures derived from *Hipparcos* and *2MASS* photometry to four different sets of models (D'Antona & Mazzitelli 1997; Siess et al. 2000; Demarque et al. 2004; Dotter et al. 2008). They inferred an age of ~ 13 Myr—much older than the previous estimates of ~ 5 Myr—regardless of the model used in the analysis. This intriguing result prompted the authors to repeat their analysis using a number of other datasets from the literature, namely the MSTO B-type stars, M supergiant Antares (α Sco), MS A-type stars, and PMS G-type stars. The resulting ages were

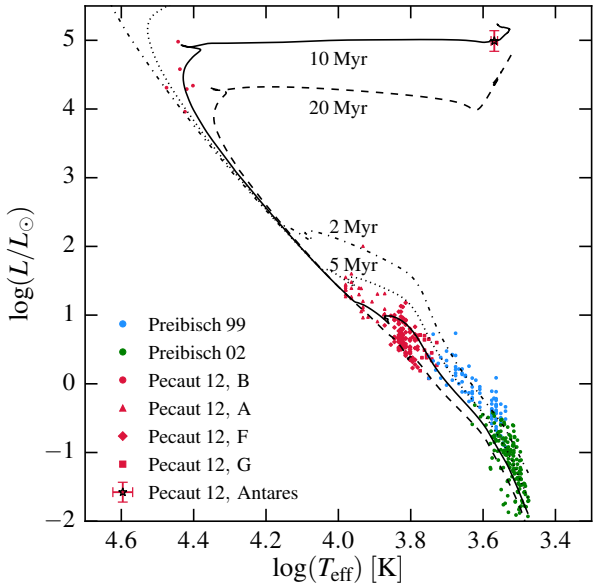


Figure 2.30: HR diagram of Upper Sco stars from Preibisch & Zinnecker (1999), Preibisch et al. (2002), and Pecaut et al. (2012), in blue, green, and red symbols, respectively. Solar metallicity isochrones with ages of 2, 5, 10, and 20 Myr are shown in black. There is a well-known discrepancy in the ages inferred from stars with spectral types earlier than G-type versus those later than G-type (with the exception of Antares which has evolved off the MS).

all consistently older than 5 Myr albeit with a large scatter, and the authors concluded that Upper Sco has a median age of $11 \pm 1 \pm 2$ (statistical, systematic) Myr.

Figure 2.30 compares 2, 5, 10, and 20 Myr MIST isochrones at solar metallicity with observations from Preibisch & Zinnecker (1999), Preibisch et al. (2002), and Pecaut et al. (2012), in blue, green, and red symbols, respectively. For spectral types later than G (with the exception of Antares, a RSG), the models yield an age of $\lesssim 5$ Myr which is consistent with the earlier results (e.g., de Geus et al. 1989; Preibisch et al. 2002). For the hotter stars, however, the best-fit model has an older age of ~ 10 Myr, consistent with the conclusion from Pecaut et al. (2012).

Recent work by Kraus et al. (2015) on UScoCTIO 5, a low-mass spectroscopic binary consisting of nearly identical stars that was recently observed by *Kepler* as part of the K2 mission (Howell et al. 2014), offered yet another perspective on this issue. Thanks to direct mass and radius measurements, the authors were able to avoid making a comparison in $T_{\rm eff}$ and therefore exclude potential problems with temperature

scales as the culprit of this discrepancy. They found that none of the considered models—Lyon (Baraffe et al. 2015), Dartmouth (Dotter et al. 2008), Pisa (Tognelli et al. 2011), Siess (Siess et al. 2000), and PARSEC (Chen et al. 2014)—predicted an age around $\sim$ 11 Myr given the system's stellar properties.* A simple exercise where they horizontally shifted the evolutionary tracks in the $\log L$–$\log T_{\rm eff}$ plane to bring the predicted $T_{\rm eff}$ into agreement with the observations yielded an age of $\sim$ 11 Myr, consistent with the age derived from hotter stars. As a result, the authors concluded that the low age predicted from low-mass stars is likely problematic and recommended $\sim$ 11 Myr instead of $\sim$ 5 Myr as the probable correct age for Upper Sco. This again emphasizes the imperative need for more robust and detailed modeling of the PMS and low MS stars, which we plan to explore in future work.

2.8.5 Asymptotic Giant Branch Stars

Low- and intermediate-mass stars ($1\ M_\odot \lesssim M_{\rm i} \lesssim 8\ M_\odot$, depending on metallicity) ascend the Hayashi track for the second time and enter the AGB phase after they exhaust their central helium supply. During the first part of the AGB phase (the Early AGB; EAGB), the star contains at its center a degenerate carbon and oxygen core surrounded by helium-burning and hydrogen-burning shells. As the star ascends the AGB, the helium-burning shell moves outward until it reaches the hydrogen-rich zone and shuts off. Meanwhile, a thin helium-rich shell starts to grow in mass due to the helium ash raining down from the hydrogen-burning shell, which now dominates the total energy output of the star. The TPAGB phase begins when the helium shell reaches a critical mass and ignites in a thermonuclear runaway as a consequence of thin shell instability (Schwarzschild & Härm 1965). The resulting expansion of the overlying material quenches the hydrogen-burning shell while the helium-burning shell settles into a period of quiescent burning. Next, the outer envelope begins to contract, causing the bottom of the hydrogen-rich shell to heat up and ignite. The

*The Lyon, Dartmouth, Pisa, and Siess models underpredict the radius, which is a well-known problem (see Section 2.8.1). On the other hand, the PARSEC model overpredicts the radius, which Kraus et al. (2015) attributes to a likely overcorrection in their new boundary conditions.

helium-burning shell moves outward in mass until it eventually becomes extinguished. The entire cycle repeats as a series of thermal pulses until the star sheds its envelope and becomes a post-AGB star (observationally, a planetary nebula). The entire TPAGB phase lasts approximately 10^5 to 10^6 years depending on mass and metallicity (see Figure 2.12), and the majority of that time is spent in the quiescent "interpulse" state.

The AGB phase plays a significant role in the chemical evolution of galaxies due to its rich nucleosynthetic processes coupled with its high typical mass loss rate, which can be as large as $\sim 10^{-3}\ M_\odot$ year^{-1} during the "superwind" phase (Willson 2000; Herwig 2005). In particular, mixing through repeated dredge-up episodes can enrich the surfaces of AGB stars with heavy elements formed from the slow neutron capture process (*s*-process). In massive ($M_\mathrm{i} \gtrsim 4 - 8\ M_\odot$) super-AGB stars, products of hot bottom burning through the CNO, NeNa, and MgAl cycles are transported up to the surfaces as well. Super-AGB stars are interesting in their own right because they occupy the blurry mass boundary within which ONe and ONeMg WDs can form as a consequence of advanced burning in the core (e.g., Doherty et al. 2015). From a stellar population synthesis perspective, the combination of high luminosities and relatively long lifetimes of AGB stars implies that stars in the AGB phase contribute a large fraction to the integrated light in intermediate-age (a few Gyr) galaxies (Frogel et al. 1990; Maraston 2005; Henriques et al. 2011; Melbourne et al. 2012; Conroy 2013; Noël et al. 2013).

Given its importance, it is therefore disconcerting that the AGB phase is still one of the most poorly understood stellar evolutionary stages. This is because a number of very uncertain and complex physical processes such as mixing and mass loss operate simultaneously and contribute significantly to the evolution (see Lattanzio 2007 for an excellent short overview of these issues). As succinctly summarized in Cassisi & Salaris (2013), "AGB stars are fascinating objects, where a complicated interplay between physical and chemical processes takes place; an occurrence that still makes computing reliable stellar models for this evolutionary phase a challenge." Nevertheless, there has been steady progress toward improving

our understanding of AGB stars by calibrating the models against optical and NIR photometry and spectroscopy of the AGB population in nearby galaxies, including the Magnellanic Clouds, dwarf spheroidals, and spirals (e.g., Marigo & Girardi 2001; Girardi & Marigo 2007; Marigo & Girardi 2007; Girardi et al. 2010; Boyer et al. 2011; Rosenfield et al. 2014). Since the duration of this phase strongly influences the time evolution of the rest-frame optical and NIR integrated light in intermediate-age stellar populations, it is important to carefully calibrate the models against observations in the local Universe so that integrated light from unresolved systems, e.g., high redshift galaxies, can be accurately interpreted.

2.8.5.1 AGB Luminosity Functions

We calibrate the AGB phase in our models via Carbon star (C star) and total AGB luminosity functions (LFs) in the Magellanic Clouds. C stars, the most evolved subset of AGB stars, are formed when the atmosphere becomes carbon-rich ($C/O > 1$) as a consequence of recurrent third dredge-up (TDU) episodes (Iben 1983). The observed C star LF is a popular diagnostic used to calibrate the TDU efficiency (Groenewegen & de Jong 1993; Marigo et al. 1999; Marigo & Girardi 2007). The faint cutoff contains information about the minimum initial mass that experiences TDU, the maximum near $M_{\rm bol} \sim -5.0$ is sensitive to the efficiency of mass loss as well as TDU, and the bright end reflects the decreasing numbers both due to mass loss leading to the termination of the TPAGB phase and hot bottom burning that converts carbon to nitrogen in intermediate-mass AGB stars (Cassisi & Salaris 2013).

The observed LFs are constructed using photometric catalogs of cool, evolved stars in the Magellanic Clouds from the Surveying the Agents of Galaxy Evolution (SAGE)-SMC and LMC surveys (private communication, M. Boyer; see also Meixner et al. 2006; Gordon et al. 2011; Boyer et al. 2011 for more details). The very wide baseline in wavelength—optical $UBVI$ from the Magellanic Clouds Photometric Survey (MCPS; Zaritsky et al. 2002) all the way out to 160 μm from *Spitzer*/MIPS—allows for accurate photometric classification of AGB subtypes and identification of contaminants such as unresolved back-

ground galaxies, compact HII regions, and young stellar objects. From the entire catalog, we select only those located within the MCPS footprint to ensure consistency with the model prediction which folds in star formation histories derived from the MCPS observations. Next, we select AGB (x-, O-, C-, aO-AGB according to the scheme introduced in Boyer et al. 2011) and C stars (x-, C-AGB) to construct cumulative LFs.

To create the predicted LFs, we utilize the Flexible Stellar Population Synthesis code (FSPS, v2.5; Conroy et al. 2009, 2010). We first convolve the isochrones with star formation and metallicity histories (SMC; Harris & Zaritsky 2004, LMC; Harris & Zaritsky 2009) to generate composite CMDs in various filters, including the effects of circumstellar dust around AGB stars that can strongly influence the flux at longer wavelengths (Villaume et al. 2015). Next, we select the AGB and C stars using the same CMD cuts that were applied to the SAGE observed sample and construct the LFs assuming a Kroupa IMF. As a consistency check, we ensured that the convolution of the adopted star formation histories with the integrated luminosities and stellar masses reproduces the observed integrated light in the NIR and total stellar mass quoted in Harris & Zaritsky (2004) and Harris & Zaritsky (2009) to within a factor of two.

In Figures 2.31 and 2.32, we plot the observed cumulative AGB and C star LFs in four different bands for the SMC and LMC, respectively, in thick black lines and the associated Poisson uncertainties in gray bands. We overplot in red the MIST prediction assuming the same CMD cuts as applied to the data. Overall, the MIST models do a reasonably good job, but the models slightly overpredict and underpredict the numbers for the SMC and LMC, respectively. Originally, our goal was to use these LF comparisons as a means of calibrating various input parameters, e,g., mass loss and TDU efficiencies, that influence AGB star lifetimes, luminosities, and the formation of C-stars. Along the way, we encountered several factors that have rendered this task more challenging than initially expected.

First, there are uncertainties in the adopted star formation and metallicity histories from Harris & Zaritsky (2004) and Harris & Zaritsky (2009). These were derived using a different set of isochrones

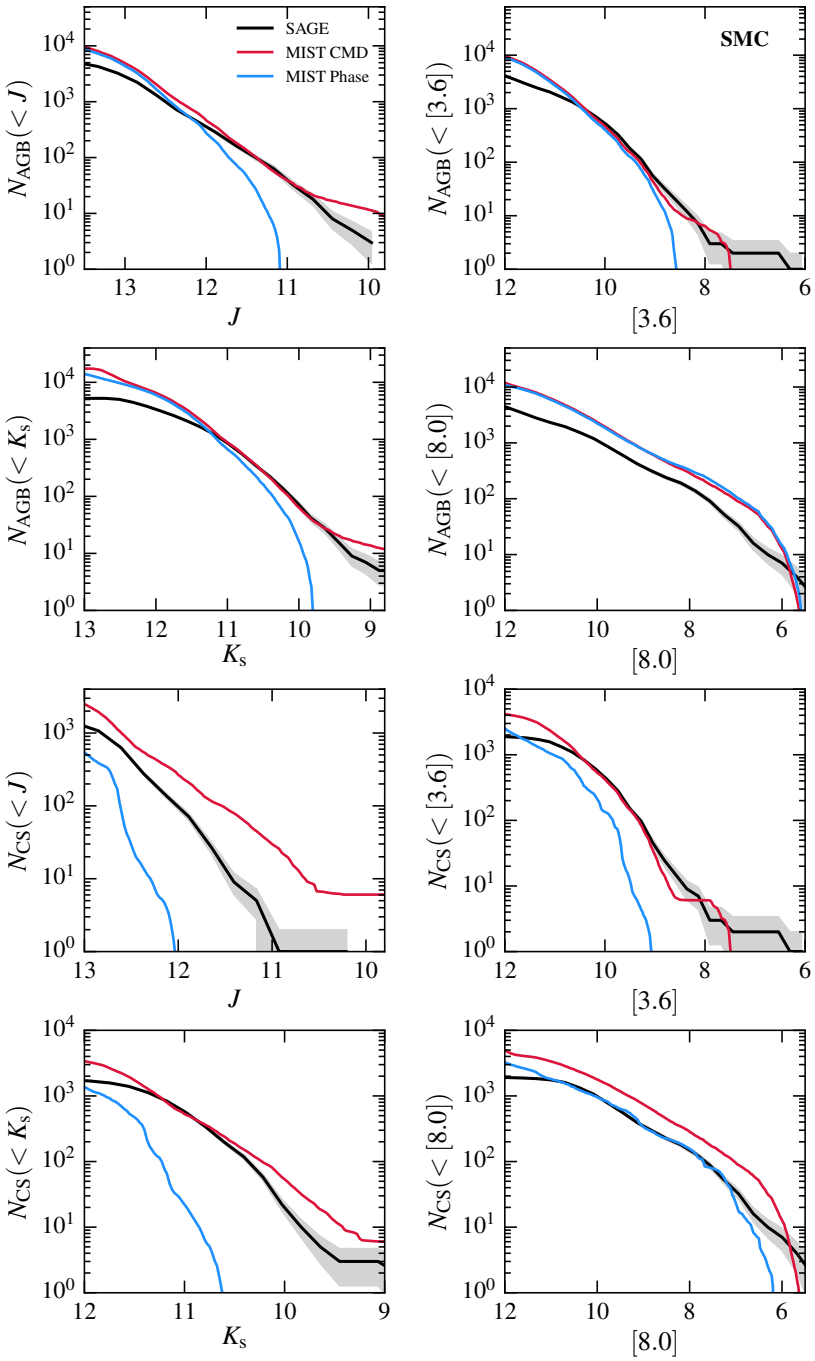


Figure 2.31: Cumulative luminosity functions of AGB and C stars in the SMC. The observed LFs in black lines are constructed from the SAGE-SMC survey photometric catalogs (private communication, M. Boyer; see also Gordon et al. 2011; Boyer et al. 2011 for more details) and the gray bands reflect Poisson uncertainties. The predicted LFs are computed by convolving the isochrones with star formation and metallicity histories from Harris & Zaritsky (2004) to create composite CMDs in different filters. The stars are then selected using two methods: "CMD cut" uses the same CMD-based criteria that were applied to the SAGE observed sample and "phase cut" selects all stars that are phase-tagged as "TPAGB" stars in the isochrones. The differences between the two methods emphasize the need for a careful analysis when comparing populations in the CMD.

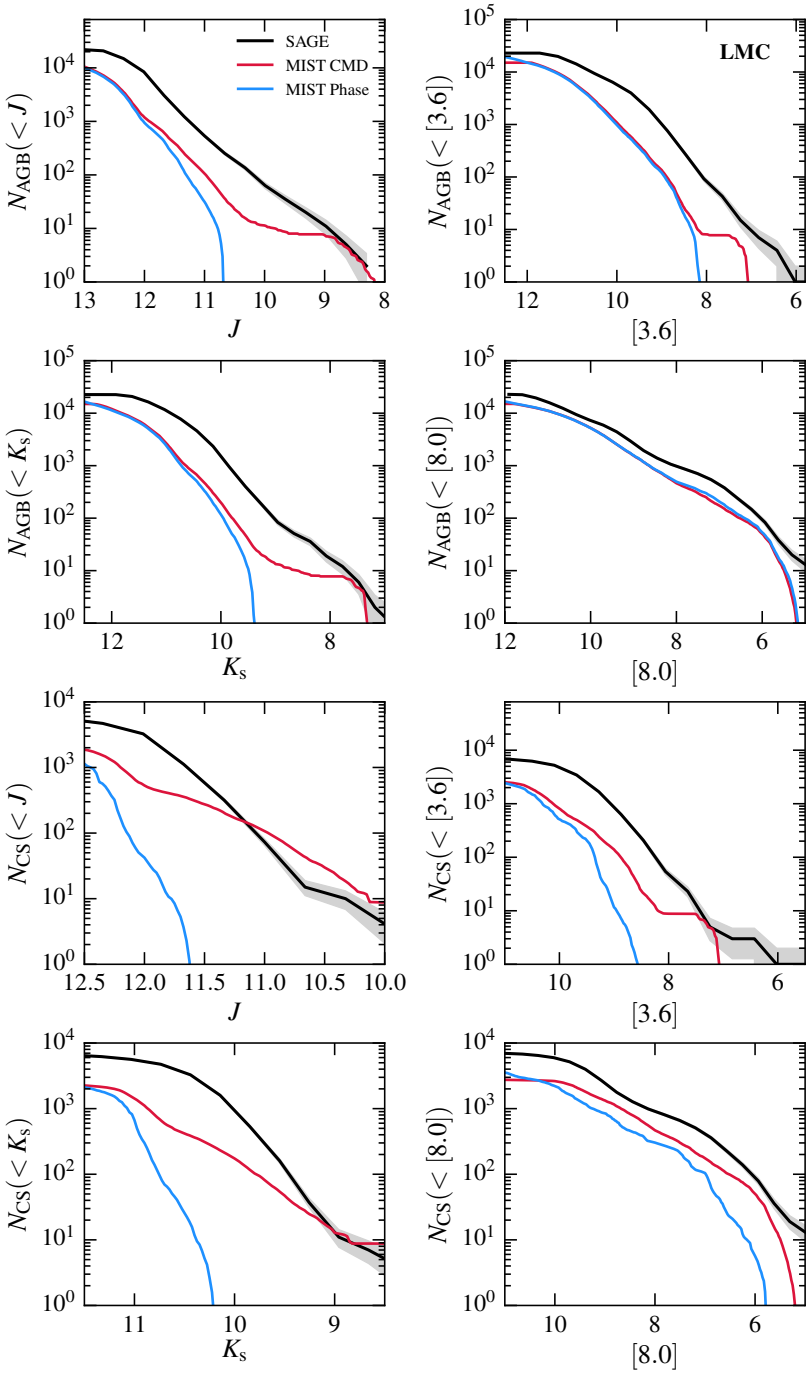


Figure 2.32: The same as Figure 2.31, now for the LMC. The data come from the SAGE-LMC survey (private communication, M. Boyer; see also Meixner et al. 2006 for more details) and the star formation and metallicity histories are from Harris & Zaritsky (2009).

(Padova 2002; Girardi et al. 2002, to be exact) compared to the MIST isochrones used for the AGB LF predictions. There is thus a fundamental inconsistency that can be addressed by reconstructing the LMC and SMC SFHs with MIST isochrones. Moreover, the recovered star formation histories are sensitive to the adopted dust attenuation model and to crowding, which affect the completeness in high density areas like 30 Doradus. Also important is the recovered metallicity history, which is far more imprecise than the star formation history itself, since the predicted AGB colors and evolution are extremely metallicity sensitive.

Second, since predicted AGB and C stars are selected using the observed CMD cuts, a small mismatch in the locations of the isochrones, especially in color, may strongly influence the comparison with the data, e.g., separation of C-stars from O-stars ($C/O < 1$). Undertaking the comparison in multiple bands makes this a particularly demanding task because obtaining good agreement across all wavelengths leaves little room for error in each component: star formation and metallicity histories, stellar evolutionary models, bolometric corrections, and AGB circumstellar dust models. A perhaps more straightforward test is to compare the predicted and observed CMDs directly, though the same uncertainties will make this a challenging task as well.

Finally, although Boyer et al. (2011) took great care to ensure a high-fidelity sample, there is most likely a nonzero amount of contamination in the final sample of AGB stars by e.g., RSGs. By adopting the observed CMD cuts as the selection criteria, we can, to some degree, account for the possibility of contamination from RSGs in the AGB sample and O stars in the C star sample.

To illustrate the challenges of comparing samples based on CMD cuts, we have also computed LFs by identifying AGB and C stars directly in the isochrone according to their evolutionary stages. It is trivial to tag the phase of every star in the predicted CMD because we have all of the necessary evolutionary information, e.g., stellar mass and surface C/O abundance. The MIST model predictions are shown in blue in Figures 2.31 and 2.32. There are a few interesting and revealing differences. Interestingly, objects at the bright end of the J- and K_s-band LFs are absent in the phase-selected MIST models, which suggests that

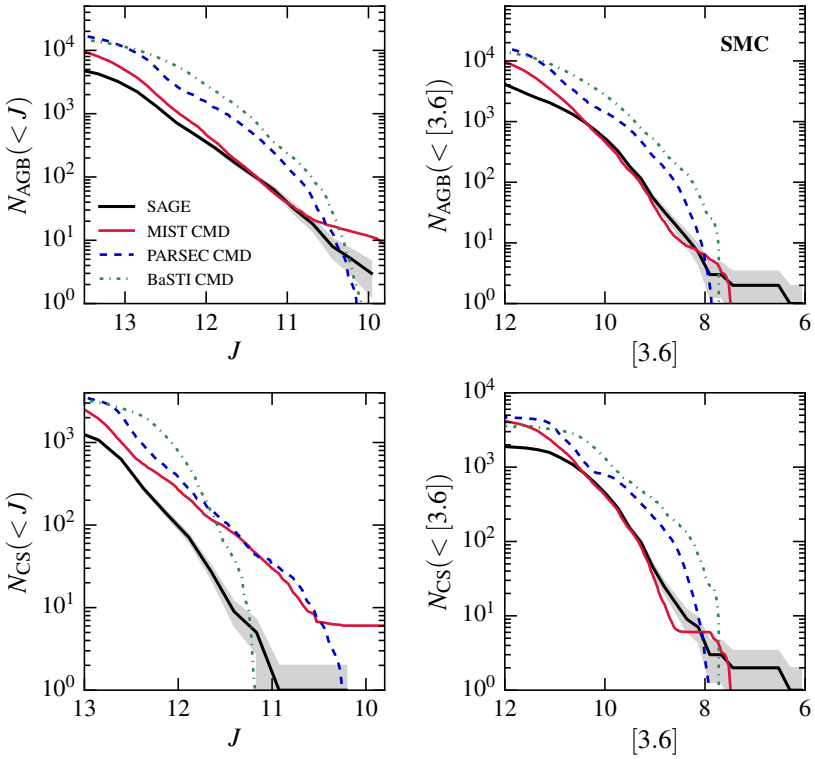


Figure 2.33: The same as Figure 2.31, but now comparing MIST predictions to the PARSEC/COLIBRI (Bressan et al. 2012; Marigo et al. 2013; Rosenfield et al. 2014) and BaSTI (Pietrinferni et al. 2004) predictions in J and [3.6]. The predicted composite CMDs used to generate the LFs displayed here were selected with a CMD cut.

RSG contamination may be important for the bright end of the AGB LFs. The C star LFs show a more dramatic difference. Possible reasons for the discrepancy include inaccurate modeling of surface abundance enrichment through TDU and winds, the current lack of C/O-variable molecular opacities in the envelope in the models, as well as any deficiencies in the AGB circumstellar dust models. The implementation of low temperature molecular opacities in MESA, which have been shown to play an important role in AGB evolution (Marigo 2002; Marigo et al. 2003), is a high priority for the MIST project.

We conclude this section by comparing the predicted LFs from the MIST isochrones to those from other widely used isochrones. In Figures 2.33 and 2.34, we plot MIST, PARSEC/COLIBRI (Bressan et al. 2012; Marigo et al. 2013; Rosenfield et al. 2014), and BaSTI (Pietrinferni et al. 2004) predictions in red, dark blue, and green, respectively, for J and [3.6]. The LFs were computed with stars selected from CMD cuts. The $\dot{M}$ required for the computation of AGB circumstellar dust effects came directly from the

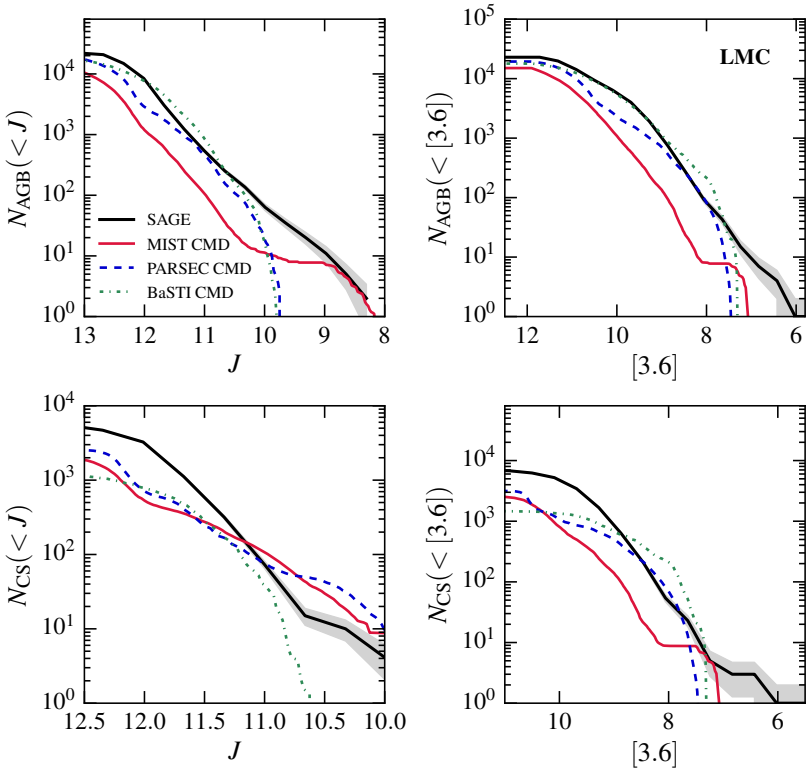


Figure 2.34: The same as Figure 2.33, now for the LMC.

isochrone files for MIST and PARSEC/COLIBRI, while for BaSTI $\dot{M}$ was computed using the Vassiliadis & Wood (1993) AGB mass loss prescription. We emphasize that all the rest of the input ingredients for constructing the LFs, including the bolometric corrections in FSPS, are identical for the three isochrones showcased here in order to isolate the effects of varying the isochrones alone. Overall, the models are in broad agreement with each other and the observations.

2.9 Comparisons with Data II: High Mass Stars

2.9.1 Width of the MS

In Section 2.8.3.1 we used the MSTO morphology of M67 to calibrate the efficiency of core overshoot. Another popular calibration option is to match the observed width of the MS (e.g., Ekström et al. 2012). We check to see if the MSTO-calibrated overshoot efficiency predicts MS width that is consistent

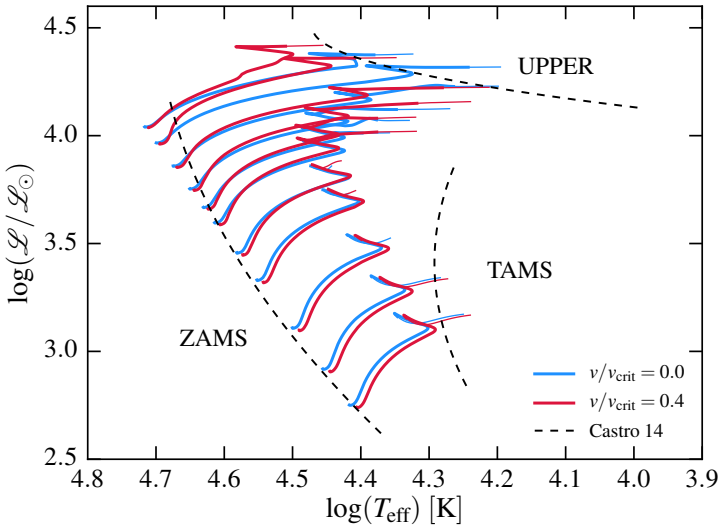


Figure 2.35: Spectroscopic HR diagram, with $\log T_{\rm eff}$ on the x-axis and the quantity $\mathscr{L} \equiv T_{\rm eff}^4/g$ on the y-axis. Black dashed lines correspond to empirical fits to the probability density distribution constructed from a sample of more than 600 stars (Castro et al. 2014). The red and blue tracks show the MS in the solar metallicity MIST evolutionary tracks with and without rotation, respectively.

with the observed MS width reported by Castro et al. (2014). Following Langer & Kudritzki (2014), the authors performed their analysis on a so-called "spectroscopic HR diagram." It differs from an ordinary HR diagram in that it still has $\log(T_{\rm eff})$ on the x-axis but a new quantity $\mathscr{L} \equiv T_{\rm eff}^4/g$ on the y-axis. The main advantage of a spectroscopic HR diagram is that all of the relevant quantities can be obtained from spectroscopic analysis without having to worry about ambiguities in distance or extinction.

In Figure 2.35, we plot three lines demarcating the MS region (ZAMS, TAMS, UPPER) from Castro et al. (2014), which are empirical fits to the probability density distribution constructed from a sample of more than 600 stars. The top portion of the TAMS line is missing because there is no clean break from the MS to cooler temperatures in the observed distribution of stars for $\log \mathscr{L}/\mathscr{L}_\odot \gtrsim 4$. This continuous distribution could be explained by the inflation of stars approaching the Eddington limit or the presence of helium burning stars. Castro et al. (2014) compared evolutionary tracks from Ekström et al. (2012) and Brott et al. (2011a) both with and without rotation and found that the ZAMS loci are generally well-reproduced by all models except at the highest masses. However, these massive objects could be missing from the ob-

served sample simply due to their rarity or obscuration by their birth clouds. The authors concluded that no model can reproduce the broad MS width at high $\mathscr{L}$ and suggested that core overshoot efficiency may be mass-dependent.

We overplot a series of solar-metallicity MIST evolutionary tracks with masses ranging from 10 to 80 $M_{\odot}$ with (solid red) and without (solid blue) rotation in Figure 2.35. The MIST models also correctly predict the ZAMS line but fail to reproduce the broad MS width at the highest masses. These models suggest that rotation alone cannot explain the full extent of the MS width. A mass-dependent core overshoot efficiency is a topic we plan to explore in future work.

2.9.2 Locations of Red Supergiants on the HR Diagram

When a high-mass star runs out of hydrogen in its core, it may migrate towards the Hayashi track and become a RSG. For a long time, the observed RSGs were found to be too luminous and cool compared to the predicted RSGs (Massey & Olsen 2003), which was problematic as the region redward of the theoretical Hayashi track represents a "forbidden zone." At fixed metallicity, each point along the Hayashi line corresponds to the coolest possible model in hydrostatic equilibrium.

Levesque et al. (2005) resolved this problem for Galactic stars, demonstrating that the new effective temperature scale computed from improved MARCS atmospheric models yielded much better agreement between the Geneva evolutionary tracks and the observed HR diagram locations. Shortly after, Levesque et al. (2006) utilized these new models to analyze a sample of RSGs in the Magellanic Clouds and confirmed previous results from Elias et al. (1985) that these RSGs belong to earlier spectral subtypes compared to their galactic counterparts. This is also consistent with the theoretical expectation that the Hayashi line should shift toward warmer temperatures at lower metallicities. Levesque et al. (2006) also found that RSGs in the SMC span a wide range of $T_{\rm eff}$ for a given $M_{\rm bol}$, possibly due to the increased importance of rotational mixing at lower metallicities (see Section 2.7.3 for more details).

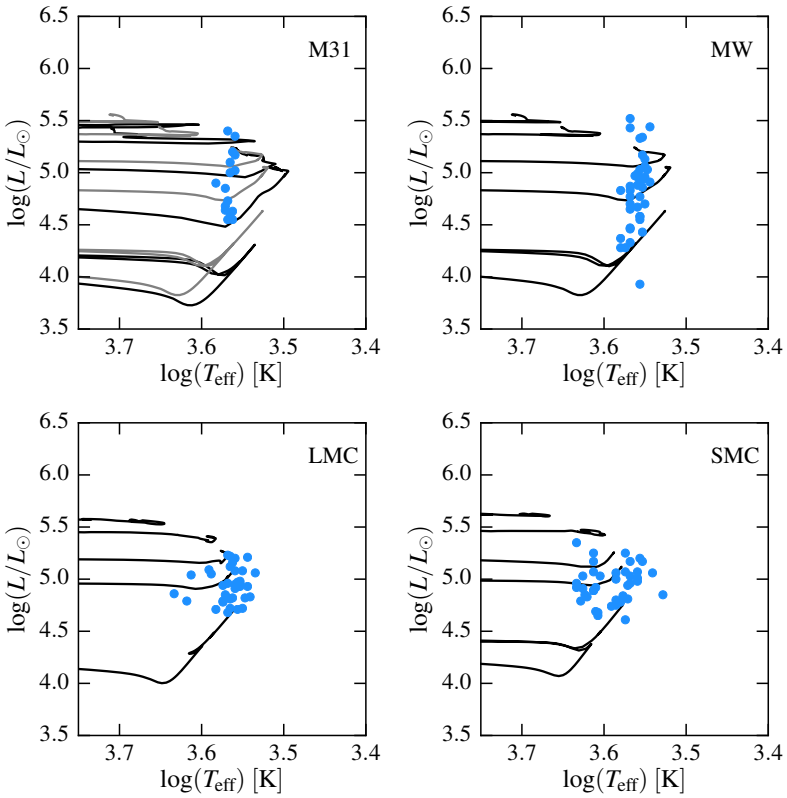


Figure 2.36: A comparison between the MIST evolutionary tracks with rotation and observed RSGs (Levesque et al. 2005, 2006; Massey et al. 2009). The masses of the tracks displayed are 10, 16, 20, 26, and 30 $M_{\odot}$. The observed $L_{\rm bol}$ is calculated from K-band photometry. *Top left*: M31 ([Z/H] $= +0.3$ in black; [Z/H] $= 0.0$ in gray). *Top right*: Milky Way ([Z/H] $= 0.0$). *Bottom left*: LMC ([Z/H] $= -0.5$). *Bottom right*: SMC ([Z/H] $= -0.75$).

In Figure 2.36, we compare the MIST evolutionary tracks in black and the sample of observed RSGs from Massey et al. (2009). Only for the top left panel (M31), we show additional tracks at [Z/H] $= 0.0$ in gray since the metallicity of M31 is still under debate (Venn et al. 2000; Trundle et al. 2002; Sanders et al. 2012; Zurita & Bresolin 2012). The observed $L_{\rm bol}$ shown here is derived from M_K rather than M_V since the former is less sensitive to extinction. The typical measurement uncertainty in $T_{\rm eff}$ ranges from ~ 100 K for the warmest stars to ~ 20 K for the coolest stars, and the uncertainty in $\log(L)$ is negligible (~ 0.05 dex). We expect the high density of observed stars to coincide with the location of the Hayashi line (Drout et al. 2012). For the LMC and the SMC, $T_{\rm eff}$ and maximum luminosity are both reproduced by the models. For M31 and the MW, the predicted slopes of the RGB tracks are too shallow compared to the observations, but it is still encouraging that no observed RSGs fall in the forbidden zone. We plan to investigate this

further in the future.

2.9.3 Relative Lifetimes

One of the most popular tests of massive star models is to compare the observed and predicted ratios of stars belonging to different evolutionary stages as a function of metallicity. The ratio of the IMF-weighted sums of phase A and B lifetimes serves as a proxy for the observed number ratio of stars in phases A and B, $N_{\mathrm{obs,\,A}}/N_{\mathrm{obs,\,B}}$:

$$\frac{\int t_{\mathrm{A}}(M)\,\phi(M)\,dM}{\int t_{\mathrm{B}}(M)\,\phi(M)\,dM} = \frac{N_{\mathrm{obs,\,A}}}{N_{\mathrm{obs,\,B}}}\ , \tag{2.24}$$

where t is the phase lifetime and ϕ is the IMF weight. This implicitly assumes that the star formation history is constant over the range of ages considered, which is likely a reasonable approximation for massive stars with $M_{\mathrm{i}} \gtrsim 10\ M_{\odot}$ and MS lifetimes $\lesssim 20$ Myr (but see also e.g., Dohm-Palmer & Skillman 2002 where the authors examined the ratio of blue to red supergiants as a function of age in Sextans A).

Here we present three such tests: the ratio of WR subtypes WC to WN, the ratio of WR to O-type stars, and the ratio of blue supergiants (BSGs) to RSGs. We convert metallicities reported in the literature—$\log(\mathrm{O/H}) + 12$, Z, and [Fe/H]—to a common scale in [Z/H] to enable comparison with the models. There is an estimated ~ 0.1 dex uncertainty in our converted [Z/H] values since there are spatial metallicity gradients within the galaxies and variations in the solar abundances adopted by different groups. Note that these models do not include the effects of binary evolution (see Eldridge et al. 2008).

2.9.3.1 WC/WN

A Wolf-Rayet (WR) star is an evolved massive star with little to no hydrogen in its outer layers. It is formed once the star sheds its hydrogen-rich envelope through mass loss, revealing hydrogen-burning products such as helium and nitrogen (WN subtype) and helium-burning products such as carbon and oxygen (WC subtype). Since the predominant mass loss mechanism in hot massive stars is likely radiative

momentum transfer onto metal ions in the atmosphere, mass loss is predicted to increase with metallicity (Vink & de Koter 2005). As a result, the ratio of WC to WN subtypes is expected to increase with increasing metallicity of the environment (Maeder & Conti 1994), which makes this ratio a useful calibrator for metallicity-dependent mass loss in massive star evolutionary models.

There has been a long-standing mismatch between the predicted and observed WC/WN ratios, especially at high metallicities (Meynet & Maeder 2005; Neugent & Massey 2011; Neugent et al. 2012). However, it was unclear whether this disagreement was due to poor models or completeness issues with observations. On the observations front, Neugent et al. (2012) completely revised the WN/WC ratio in M31 by discovering more than 100 new WR stars with an estimated completeness fraction of ~ 0.95. A comparison between the observed WC/WN ratios in M31, M33, SMC, and LMC and the ratios predicted by non-rotating and rotating Geneva models (Meynet & Maeder 2005; Ekström et al. 2012) revealed only a marginal improvement from the new rotating models. Furthermore, they concluded that additional models at different metallicities (full grids of models were only available for two metallicities at that time) were required for a more informative comparison.

We identify WR stars in our models following the classification scheme introduced in Georgy et al. (2012). We group the WNL and WNE stars (late- and early-subtypes of WN) as part of the WN stars, exclude the ambiguous WNC stars (WN to WC transition), and include the WO subtype with the WC stars. We emphasize that this theoretical classification scheme—based on the average surface abundances—is technically not equivalent to the classification scheme used by observers who rely on the spectroscopic detection of emission lines (see e.g., van der Hucht 2001).

First we compute the phase lifetimes for each evolutionary track. For each phase, we sum up the lifetimes for all stellar masses with weights provided by the IMF (Kroupa 2001). The total lifetime for a given phase is a theoretical proxy for the observed number of stars in that phase, which means that we can now take the ratio of WC to WN lifetimes and directly compare to the observations.

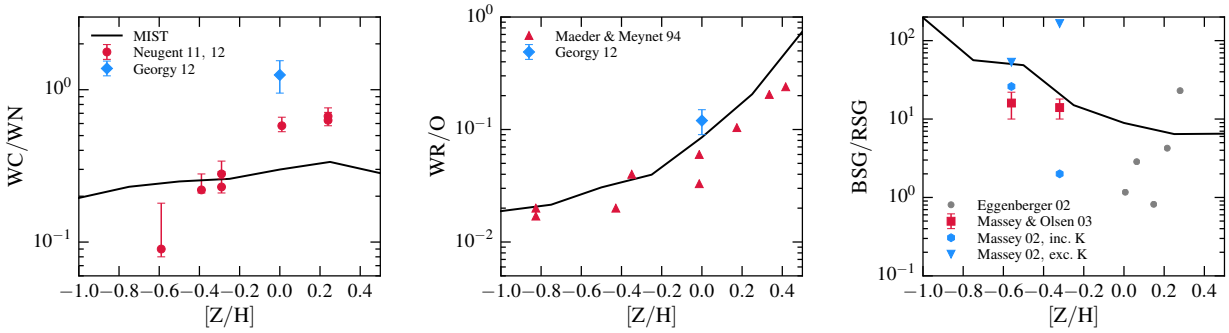


Figure 2.37: *Left*: The predicted WC to WN ratio as a function of metallicity. The red circles are observations from Neugent & Massey (2011) and Neugent et al. (2012), and the blue diamond point is the observed ratio from Georgy et al. (2012), estimated in the 3 kpc radius volume around the solar neighborhood. *Middle*: The same as the left panel except now showing the WR to O ratio. The red triangles are observed number ratios from Table 6 in Maeder & Meynet (1994) and the blue diamond point is the observed ratio from Georgy et al. (2012), estimated in the 2.5 kpc radius volume around the solar neighborhood. *Right*: The same as the left panel except now showing the BSG to RSG ratio. The gray points are observed ratios from young star clusters in the Milky Way and the Magellanic Clouds (Eggenberger et al. 2002). The blue hexagons and triangles are observed ratios computed with and without K-type stars in the RSG category (Massey 2002). The red squares are observed ratios computed from spectroscopically confirmed RSG stars (Massey & Olsen 2003).

In the left panel of Figure 2.37, we plot the predicted WC to WN ratio as a function of metallicity in a solid black line. The red circles are observations from Neugent & Massey (2011) and Neugent et al. (2012), and the blue diamond point is the observed ratio computed by Georgy et al. (2012), estimated in the 3 kpc radius volume around the solar neighborhood (see their Section 4.4 for references therein). Although the MIST model is currently unable to reproduce the observed trend with metallicity, the predicted ratios are in agreement with the observed values to within a factor of 2 to 3. We plan to improve this further in future work.

2.9.3.2 WR/O

The predicted ratio of WR to O-type stars is computed from the models using the method outlined in the previous section and compared to observations. Here, the WR population is the sum of all WR subtypes. O-type MS stars are identified according to the Georgy et al. (2012) classification scheme.

In the middle panel of Figure 2.37, we show the predicted WR to O ratio as a function of metallicity in a solid black line. The red triangles are observed number ratios from Table 6 in Maeder & Meynet

(1994)* and the blue diamond point is the observed ratio computed by Georgy et al. (2012), estimated in the 2.5 kpc radius volume around the solar neighborhood. Again, the model prediction is in qualitative agreement with the observations; WR stars become more abundant in higher metallicity environments. This is to be expected because efficient mass loss at high metallicities readily removes the hydrogen-rich outer layers and promotes the formation of WR stars.

2.9.3.3 BSG/RSG

The number ratio of blue to red supergiants (BSG/RSG) has long been known to decrease with increasing galactocentric radius in the Milky Way, the Magellanic Clouds, and M33 (e.g., Walker 1964; Hartwick 1970; Humphreys 1979; Cowley et al. 1979; Meylan & Maeder 1982). This was explained by invoking radial metallicity gradients in the disks (van den Bergh 1968). The BSG/RSG ratio is an excellent diagnostic tool because whether a star becomes a RSG or a BSG hinges very sensitively on, for example, the details of semiconvection and convective overshoot (e.g, Langer 1991).

Most stellar evolution models have struggled to reproduce this radial/metallicity trend (see Langer & Maeder 1995, for an in-depth discussion of this topic). However, Maeder & Meynet (2001) found that the inclusion of rotation in their models produced more RSGs at low metallicities, which dramatically lowered the predicted BSG/RSG ratio in the SMC and brought the model prediction into better agreement with the observations. Eldridge et al. (2008) computed their model predictions with and without the effects of binarity and concluded that their single-star model underpredicted the BSG/RSG ratio. A mixed population model with a two-thirds binary fraction was required to reproduce the observations.

In the right panel of Figure 2.37, we plot the observed BSG/RSG ratios in the Magellanic Clouds from Massey (2002) and Massey & Olsen (2003). The two Massey (2002) symbols correspond to ratios computed including (blue hexagon) and excluding (blue triangle) K-type stars in the RSG category from

*There are no uncertainties reported by the authors.

their $UBVR$-photometry-selected sample. Their sample was limited to $M_{\rm bol} < -7.5$ (roughly $\log(L/L_{\odot}) > 4.9$) in order to minimize contamination by the AGB stars and improve completeness. There was an estimated $\sim 10\%$ contamination by foreground red dwarfs in their photometric sample, but this was dramatically improved in Massey & Olsen (2003) with spectroscopic radial velocity measurements. The updated ratios from spectroscopically confirmed RSG stars (Massey & Olsen 2003) are shown as red squares.

We also show the observed BSG/RSG ratios computed from spectroscopically identified candidates in a sample of 45 young ($6.8 < \log(\text{Age})\ [\text{yr}] < 7.5$) clusters in the Milky Way and the Magellanic Clouds (gray; Eggenberger et al. 2002). The authors computed the observed BSG/RSG ratios at different metallicities by binning the stars according to their galactocentric distances and assuming a radial metallicity gradient to assign metallicities to each radius bin. Their results showed increasing BSG/RSG ratio with increasing metallicity.

We overplot our prediction as a solid black line. RSGs and BSGs were identified using the selection criteria from Eldridge et al. (2008), which are consistent with observational cuts made by Massey (2002) and Massey & Olsen (2003). The model predictions are bracketed by the two Massey (2002) points and marginally consistent with Massey & Olsen (2003). We do not reproduce the positive trend reported by Eggenberger et al. (2002), but Eldridge et al. (2008) raised the concern that clusters in the Eggenberger et al. (2002) sample generally have an age spread similar to the age of the cluster itself. Additional data over a wider range of environments would be valuable in assessing the quality of the massive star models.

2.9.4 The Effects of Rotation on Surface Abundances

Rotation has been proposed as a viable mechanism for enriching the surfaces of stars (Heger et al. 2000; Meynet & Maeder 2000; see also Sections 2.3.6.4 and 2.3.7.3) by inducing extra mixing and enhancing mass loss.* Models with rotation generally predict a surface enrichment of helium and nitrogen along

*While gravitational settling works against these processes, it is a slow process with a negligible effect in the presence of rapid rotation.

with a concomitant depletion of carbon and oxygen during the MS as the products of the CNO cycle get dredged up to the surface through rotational mixing (Maeder & Meynet 2000; Yoon & Langer 2005). For this reason, observed surface abundances have been used to calibrate the efficiency of rotational mixing in the models (f_μ and f_c; Pinsonneault et al. 1989; Heger et al. 2000; Brott et al. 2011a).

Following Ekström et al. (2012), we check that our rotating models are able to match the range of observed surface nitrogen enrichment in galactic O- and B-type stars. Figure 2.38 shows the predicted surface nitrogen enrichment midway through the MS ($X_c \sim 0.5$; red) and at TAMS (blue) as a function of initial mass. Models with and without rotation are plotted in solid and dashed lines, respectively. The red shaded box corresponds to the mean surface nitrogen excess observed in a sample of galactic MS B-type stars with masses below 20 $M_\odot$ and the blue shaded box on top corresponds to the maximum observed excess. These observed numbers come from Table 2 of Maeder & Meynet (2012), which is a compilation of data from Gies & Lambert (1992), Kilian (1992), Morel et al. (2008), and Hunter et al. (2009). Overall, our models are in excellent agreement with the observed range of nitrogen enrichment on the surfaces of B-type MS stars, and in marginal agreement with the maximum observed excess. They are also broadly in agreement with the predictions from the Geneva models (see Figure 11 of Ekström et al. 2012), though there is a noticeable difference for stars below $\sim 2\ M_\odot$. This is due to the inclusion of magnetic braking effects in the Geneva models; stars with masses below $\sim 1.7\ M_\odot$ experience extra surface nitrogen enrichment due to enhanced mixing induced by large shear in the outer layers, though the authors caution that this effect may be overestimated in their current implementation. In the MIST models, we turn off rotation for stars with $M_\mathrm{i} < 1.2\ M_\odot$ and gradually increase the rotation rate from $v_\mathrm{ZAMS}/v_\mathrm{crit} = 0.0$ to 0.4 over the mass range $M_\mathrm{i} = 1.2$ to $1.8\ M_\odot$. As discussed in Section 2.3.5, the purpose of this ramping scheme is to compensate for the absence of magnetic braking in MESA which is important for low-mass stars with appreciable convective envelopes. At low masses where the MS lifetimes are long and rotational mixing is inefficient or non-existent, the predicted surface nitrogen abundances actually decrease during the MS due

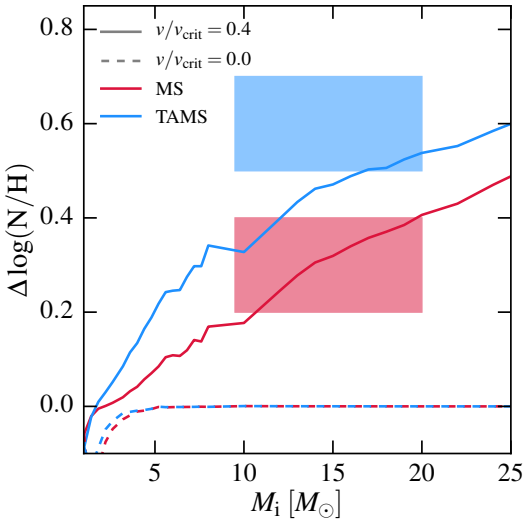


Figure 2.38: Surface nitrogen enrichment midway through the MS ($X_{\mathrm{c}} \sim 0.5$; red) and at TAMS (blue) as a function of initial mass. The red and blue shaded boxes correspond to the average nitrogen excess observed for galactic MS B-type stars with $M_{\mathrm{i}} < 20\ M_{\odot}$ and the maximum observed excess (Gies & Lambert 1992; Kilian 1992; Morel et al. 2008; Hunter et al. 2009). Without rotation, the predicted nitrogen enrichment during the MS at these masses is zero. This figure is adapted from Figure 11 of Ekström et al. (2012).

to diffusion. At higher masses without the inclusion of rotation, the predicted nitrogen enrichment during the MS is zero. Additional nitrogen enhancement measurements in stars with $M_{\mathrm{i}} < 10\ M_{\odot}$ would provide a valuable constraint on the models.

In the left panel of Figure 2.39, we show 7, 16, and 40 $M_{\odot}$ solar metallicity evolutionary tracks with (solid) and without (dashed) rotation in the $\log(g)$–$\log(T_{\mathrm{eff}})$ plane. In the right panel, we show the evolution of surface nitrogen abundance for the same three models. The symbols correspond to O- and B-type galactic dwarfs and supergiants (Takeda & Takada-Hidai 2000; Villamariz et al. 2002; Villamariz & Herrero 2005; Crowther et al. 2006; Morel et al. 2008; Searle et al. 2008; Przybilla et al. 2010). To limit the comparison to O- and B-type stars, we exclude the A-, F-, and Cepheid stars from the Takeda & Takada-Hidai (2000) sample. We adopt the symbol and color scheme from Figure 12 of Ekström et al. (2012) to aid comparison with their figure. As in Ekström et al. (2012), we do not compare surface rotation velocities because only $v \sin i$ is known for most observed stars. The left panel suggests that the observed stars have initial masses ranging roughly between 7 and 40 $M_{\odot}$ and that the observed $\log(g)$ values for

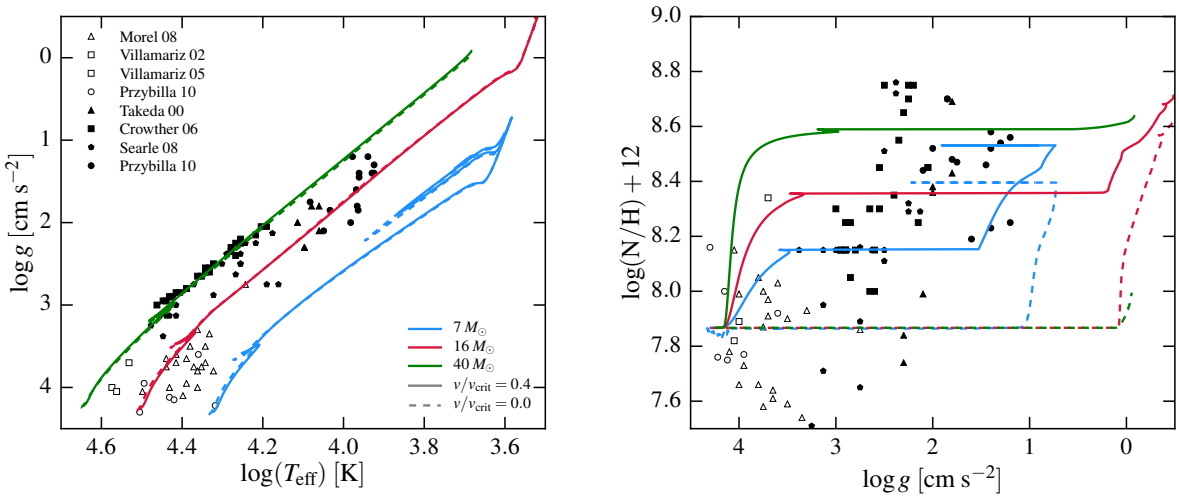


Figure 2.39: *Left*: Evolutionary tracks in the $\log(g) - \log(T_{\rm eff})$ plane for 7, 16, and 40 $M_\odot$ stars at solar metallicity. Solid and dotted lines are models with and without rotation and open and filled symbols correspond to O- and B-type galactic dwarfs and supergiants, respectively. This figure is adapted from Figure 12 of Ekström et al. (2012). *Right*: Surface nitrogen abundance evolution for the same three models.

the dwarfs (open symbols) are in good agreement with the MS location. The right panel demonstrates that models can broadly reproduce the range of observed surface nitrogen abundances. A fair number of observed points fall below the initial N/H ratio in the models, which Ekström et al. (2012) suggest is due to abundance variations in the birth cloud.

We also note that for some samples consisting exclusively of slow rotators (e.g., the Morel et al. (2008) sample of B stars whose $v \sin i$ values range from 10 to 60 km s^{-1}), our default rotating models may be inappropriate for a direct comparison. The observed rotational distribution function is quite broad (Huang et al. 2010) and also the observed stars were most likely born with a range of initial metallicities, which would increase scatter in the observed nitrogen abundances. Moreover, there are physical mechanisms that have not been taken into account in our models, such as mass loss and gain from binary mass transfer (see e.g., Eldridge et al. 2008; de Mink et al. 2009, 2013), and typical measurement uncertainties are quite large: 1000 K for $T_{\rm eff}$, 0.1–0.2 dex for $\log(g)$, and 0.2 dex for the N/H ratio. This is meant to be a coarse-grained comparison to assess whether or not the models can *reasonably* reproduce the range of ob-

served surface nitrogen abundances. Finally, we note that this is still a controversial topic: there are known slow/fast-rotators with/without surface nitrogen enrichment, and some authors even find that de-projected velocities show no statistically significant correlation with surface nitrogen abundances (e.g, Hunter et al. 2008; Brott et al. 2011b; Rivero González et al. 2012; Bouret et al. 2013; Aerts et al. 2014). We defer a more detailed comparison and discussion of these issues to future work.

2.10 Interesting Features in the MIST Models and Resolution Tests

2.10.1 Features in the Evolutionary Tracks and Isochrones

Here we identify and discuss some of the interesting and unusual features in the evolutionary tracks and isochrones. Figure 2.40 shows five such examples. For each row, the left panel shows the evolutionary track in its entirety, and the gray box marks the zoomed-in region shown in the middle panel. The right panel shows a series of relevant physical quantities plotted as a function of time.

The first row displays an example of "born-again" evolution during the post-AGB phase (e.g., Schoenberner 1979; Iben 1982; Iben et al. 1983). Following the end of the TPAGB phase, the star enters the post-AGB phase and rapidly evolves toward hotter temperatures. During this short-lived phase ($\sim 10^3 - 10^4$ years), the luminosity remains roughly constant, powered primarily by hydrogen shell-burning with some contribution from gravitational contraction. In the most uneventful scenario (e.g., the 1 $M_\odot$ model in the left panel, second row), the surface hydrogen envelope mass eventually falls below the critical value and hydrogen burning shuts off as a result. Having lost its nuclear energy source, the star then begins to cool and fade away as a WD. In contrast, more interesting things can happen if the star leaves the TPAGB in the middle of its last TP cycle, in which case it may subsequently undergo a late TP either as a post-AGB star (Late Thermal Pulse; LTP) or as a WD (Very Late Thermal Pulse; VLTP) (Kawaler et al. 1996). In either case, the star loops back around toward cooler temperatures as it puffs up from the sudden injec-

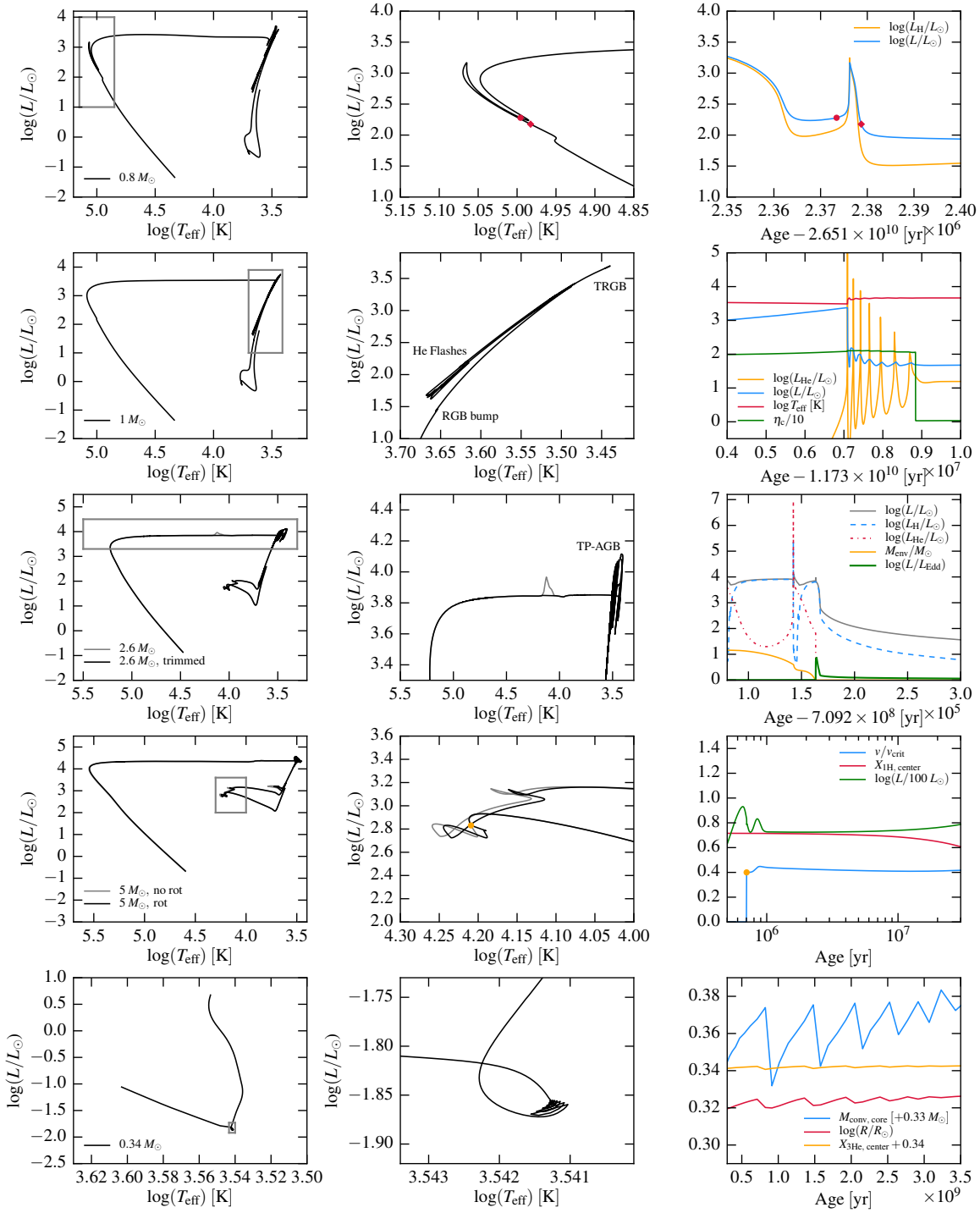


Figure 2.40: An illustration of interesting and unusual features in the evolutionary tracks. For each row, the left panel shows the evolutionary track in its entirety, and the gray box marks the zoomed-in region shown in the middle panel. The right panel shows the relevant physical quantities as a function of time. *First row*: "Born-again" evolution during the post-AGB phase. *Second row*: Helium flashes following helium ignition at the tip of the RGB. *Third row*: TPAGB phase and post-AGB bump. *Fourth row*: A shift in $T_{\rm eff}$ due to the initialization of rotation near ZAMS. *Fifth row*: ^{3}He-driven instability near the transition from fully convective to radiative core during the MS.

tion of energy into the envelope. The middle panel zooms in on the VLPT, where the beginning and the end of this episode are marked by the red circle and diamond, respectively. As the right panel shows, the sudden ignition of hydrogen is what triggers the VLTP in the star just as it enters the WD cooling phase. The stellar bolometric luminosity and hydrogen burning luminosity are shown in blue and orange.

The second row illustrates a series of helium flashes in the degenerate core of a low-mass star as it settles into quiescent helium burning. As the star climbs up the RGB, the inert helium core becomes denser and more degenerate as it undergoes gravitational contraction, continuously growing in mass as the hydrogen-burning shell above rains down freshly-fused helium. For sufficiently large central densities, neutrino cooling becomes significant and the peak in temperature actually shifts away from the center. As a result, helium ignition occurs off-center at the RGBTip (Thomas 1967).* The initial helium flash is followed by a series of weaker helium flashes that move radially inward until helium burning reaches the center. This lifts the degeneracy of the core and the star commences quiescent helium burning. The oscillatory features in the middle panel correspond to these successive helium flashes. The right panel shows the helium burning luminosity, stellar bolometric luminosity, and temperature in orange, blue, and red, respectively. The sharp decline in stellar luminosity in concomitance with a sharp peak in helium burning luminosity marks the location of the RGBTip. The degeneracy parameter $\eta = \varepsilon_F / k_B T$ in the center (shown in green, rescaled for display purposes) plummets to ~ 0 once the helium flash reaches the innermost core.

The third row shows the TPAGB phase followed by a bump in the post-AGB track of a 2.6 $M_\odot$ star. The TPAGB phase is famous both for its namesake thermal pulses triggered by alternating hydrogen and helium burning in shells (see Section 2.8.5 for a more detailed explanation) and high mass loss rates (see Herwig 2005 for an excellent review). The TPAGB phase is terminated once the star sheds almost all of its outer hydrogen-rich envelope to reveal the hot CO core, which launches the star leftward in the HR diagram. In the right panel, the alternating hydrogen and helium burning luminosities for the last $\sim$two TPs

*Schwarzschild & Härm (1962) actually computed the evolution through helium flash prior to this but they did not account for neutrino cooling, so their models ignited helium in the center.

are plotted in blue dashed and red dot-dashed lines. The envelope mass shown in orange decreases rapidly until it reaches 0, marking the end of the TPAGB phase. Since the mass of the envelope is dramatically reduced but the stellar luminosity remains more or less the same, the Eddington ratio $L/L_{\rm Edd}$ goes up and the stellar surface becomes unstable. The star glitches over a very short timescale (< 1 yr) as it attempts to achieve hydrostatic equilibrium, which shows up as a sharp bump at around $\log(T_{\rm eff}) \sim 4.2$ K in the middle panel. We note that this feature only appears sometimes (generally for $> 2.5\ M_\odot$ at solar metallicity). Since it is unclear whether or not this behavior is real or a numerical artifact, and it has zero bearing on the evolution of the star due to its extremely short-lived nature, we post-process this feature out of the final evolutionary tracks in order to facilitate the construction of smooth isochrones. Specifically, we trim out any points with $|d(\log L)/dt| < 0.1$ during the post-AGB phase only. The resulting track is shown in black in the left and middle panels.

The fourth row illustrates the effect of turning on rotation at ZAMS. Once the star reaches ZAMS (defined to be $L_{\rm nuc}/L \geq 0.9$ in MESA) solid-body rotation is established over 10 time steps. In the absence of efficient rotational mixing, rotation simply makes stars cooler (see Section 2.6.1). The middle panel shows that the rotating (black) and non-rotating (gray) tracks overlap up until ZAMS marked by an orange circle. Once rotation is established, the two curves diverge as the rotating model settles to a lower $T_{\rm eff}$. This jump in temperature is extremely short-lived and is purely a feature of our implementation of rotation; a real star is born from a birth cloud with nonzero initial angular momentum. A more realistic model of the PMS phase that includes the effects of rotation will be explored in the future. In the right panel, we plot $v/v_{\rm crit}$, central hydrogen abundance, and $\log L$ as a function of time. The small increase in velocity immediately following velocity initialization is due to the star experiencing additional contraction before it begins to steadily burn hydrogen. During the MS, $v/v_{\rm crit}$ decreases as the stellar radius and luminosity gradually increase.

The fifth and final row demonstrates the presence of a ^{3}He-driven instability in a 0.34 $M_\odot$ star. This

stellar mass represents the transition from stars that are fully-convective (lower mass) on the MS to those with radiative cores and convective envelopes (higher mass). This instability was first reported by van Saders & Pinsonneault (2012) who found that these low-mass stars develop small convective cores—normally characteristic of CNO burning in more massive stars ($\sim 1.1\ M_{\odot}$)—due to non-equilibrium ^{3}He abundances at these low central temperatures. The net production of ^{3}He in the center leads to the development of a small convective core, which steadily grows in extent and eventually makes contact with the bottom of the deep convective envelope. As a result of vigorous convective mixing, the local ^{3}He enhancement in the center is erased as the central ^{3}He abundance dilutes back to the bulk abundance and the cycle resets. This event occurs as the star leaves the Hayashi track, as can be seen in the left and middle panels. As the right panel shows, the sudden drops in central ^{3}He abundance (orange) caused by the convective core coming into contact with the envelope coincides with the shrinking of the convective core (blue) and a drop in the stellar radius (red) and luminosity (not shown for display purposes).

2.10.2 The Effects of Varying Time Step and Mesh Controls in MESA Evolution Calculations

Here we examine the temporal and spatial convergence in our MESA stellar evolution calculations following the methodology in Paxton et al. (2011). In MESA, the sizes of time steps and grid cells are controlled by `varcontrol_target` and `mesh_delta_coeff`, respectively, but there is additional flexibility to adjust the resolution specifically for certain zones or evolutionary phases. `varcontrol_target` is the target value for relative changes in the stellar structure variables, e.g., $\rho(m)$, between two consecutive time steps and `mesh_delta_coeff` is the analogous parameter for differences between adjacent grid cells.

Adopting the notations introduced in Paxton et al. (2011), we vary temporal and spatial resolution in lockstep according to C, a numerical factor by which we multiply the default values for `varcontrol_target`

Table 2.9: Convergence test results.

$1\,M_\odot$											
C: end of H burn	4	2	1	1/2	1/4	C: end of He burn	4	2	1	1/2	1/4
$N_{\rm cells}$	347	486	821	1593	3174	$N_{\rm cells}$	586	1139	2208	3931	6931
$N_{\rm timesteps}$	335	500	818	1432	2726	$N_{\rm timesteps}$	9607	12185	17826	32928	66044
$M/M_\odot$	1.0	1.0	1.0	1.0	1.0	$M/M_\odot$	0.95	0.951	0.951	0.951	0.951
ξ ($\times 10^{-3}$)	0.006	0.009	0.004	0.001	0.0	ξ ($\times 10^{-3}$)	-0.615	-0.148	0.063	0.046	0.0
$\log(L/L_\odot)$	0.261	0.256	0.256	0.256	0.256	$\log(L/L_\odot)$	2.031	2.024	2.008	2.001	2.001
ξ ($\times 10^{-3}$)	10.64	1.151	0.586	1.054	0.0	ξ ($\times 10^{-3}$)	70.953	53.714	14.967	-0.799	0.0
$\log(T_{\rm eff})$ [K]	3.764	3.766	3.767	3.767	3.767	$\log(T_{\rm eff}$ [K])	3.63	3.634	3.636	3.637	3.637
ξ ($\times 10^{-3}$)	-5.652	-1.65	-0.493	-0.159	0.0	ξ ($\times 10^{-3}$)	-14.812	-6.501	-1.779	-0.06	0.0
$\log(t)$	9.94	9.939	9.941	9.942	9.943	$\log(t)$	10.056	10.057	10.059	10.06	10.06
ξ ($\times 10^{-3}$)	-5.617	-8.577	-3.747	-0.836	0.0	ξ ($\times 10^{-3}$)	-10.478	-7.686	-3.576	-1.376	0.0
$\log(T_{\rm c})$ [K]	7.295	7.294	7.294	7.294	7.294	$\log(T_{\rm c})$ [K]	8.282	8.28	8.275	8.273	8.273
ξ ($\times 10^{-3}$)	1.165	-0.103	0.037	0.202	0.0	ξ ($\times 10^{-3}$)	20.975	16.362	4.178	0.649	0.0
$\log(\rho_{\rm c})$ [g cm^{-3}]	2.805	2.788	2.786	2.786	2.784	$\log(\rho_{\rm c})$ [g cm^{-3}]	4.754	4.742	4.733	4.727	4.726
ξ ($\times 10^{-3}$)	48.7	10.331	4.975	4.094	0.0	ξ ($\times 10^{-3}$)	66.899	37.961	15.172	2.266	0.0

$5\,M_\odot$											
C: end of H burn	4	2	1	1/2	1/4	C: end of He burn	4	2	1	1/2	1/4
$N_{\rm cells}$	345	547	1015	2003	3992	$N_{\rm cells}$	603	1248	2148	4582	7283
$N_{\rm timesteps}$	383	584	1019	1919	3699	$N_{\rm timesteps}$	644	1117	2123	4262	8454
$M/M_\odot$	4.997	4.997	4.997	4.997	4.997	$M/M_\odot$	4.984	4.985	4.985	4.985	4.986
ξ ($\times 10^{-3}$)	-0.057	-0.051	-0.02	-0.019	0.0	ξ ($\times 10^{-3}$)	-0.355	-0.124	-0.033	-0.07	0.0
$\log(L/L_\odot)$	3.168	3.154	3.139	3.137	3.136	$\log(L/L_\odot)$	3.294	3.23	3.173	3.175	3.17
ξ ($\times 10^{-3}$)	74.552	40.912	5.28	0.766	0.0	ξ ($\times 10^{-3}$)	330.852	147.317	7.776	12.006	0.0
$\log(T_{\rm eff})$ [K]	4.159	4.16	4.16	4.16	4.164	$\log(T_{\rm eff}$ [K])	3.614	3.624	3.63	3.63	3.631
ξ ($\times 10^{-3}$)	-12.433	-10.03	-7.975	-8.023	0.0	ξ ($\times 10^{-3}$)	-37.609	-15.963	-1.504	-1.559	0.0
$\log(t)$	8.025	8.021	8.01	8.009	8.008	$\log(t)$	8.077	8.076	8.071	8.072	8.071
ξ ($\times 10^{-3}$)	40.171	29.525	5.393	2.926	0.0	ξ ($\times 10^{-3}$)	13.82	12.067	-0.536	2.725	0.0
$\log(T_{\rm c})$ [K]	7.663	7.658	7.657	7.657	7.657	$\log(T_{\rm c})$ [K]	8.379	8.371	8.368	8.371	8.369
ξ ($\times 10^{-3}$)	13.611	2.911	0.973	0.874	0.0	ξ ($\times 10^{-3}$)	21.884	3.362	-2.952	4.452	0.0
$\log(\rho_{\rm c})$ [g cm^{-3}]	2.001	2.001	2.006	2.007	2.007	$\log(\rho_{\rm c})$ [g cm^{-3}]	4.243	4.245	4.246	4.247	4.243
ξ ($\times 10^{-3}$)	-13.275	-14.014	-0.887	0.314	0.0	ξ ($\times 10^{-3}$)	2.19	6.022	7.495	9.271	0.0

$20\,M_\odot$											
C: end of H burn	4	2	1	1/2	1/4	C: end of He burn	4	2	1	1/2	1/4
$N_{\rm cells}$	1467	2683	5024	9912	17655	$N_{\rm cells}$	2325	4598	9133	18303	36666
$N_{\rm timesteps}$	1803	2493	4460	8438	16409	$N_{\rm timesteps}$	2951	3635	6218	11591	22501
$M/M_\odot$	19.279	19.202	19.184	19.188	19.212	$M/M_\odot$	12.156	12.783	13.115	14.655	14.856
ξ ($\times 10^{-3}$)	3.456	-0.532	-1.475	-1.287	0.0	ξ ($\times 10^{-3}$)	-181.746	-139.532	-117.17	-13.479	0.0
$\log(L/L_\odot)$	5.083	5.03	5.02	5.017	5.015	$\log(L/L_\odot)$	5.174	5.131	5.121	5.101	5.099
ξ ($\times 10^{-3}$)	169.241	35.182	11.427	5.929	0.0	ξ ($\times 10^{-3}$)	190.493	77.659	53.169	4.741	0.0
$\log(T_{\rm eff})$ [K]	4.468	4.442	4.437	4.434	4.435	$\log(T_{\rm eff}$ [K])	3.568	3.535	3.532	3.537	3.537
ξ ($\times 10^{-3}$)	78.496	17.202	4.979	-1.602	0.0	ξ ($\times 10^{-3}$)	74.031	-4.799	-10.998	-0.389	0.0
$\log(t)$	6.998	6.961	6.953	6.949	6.947	$\log(t)$	7.034	7.002	6.995	6.993	6.991
ξ ($\times 10^{-3}$)	123.993	31.461	12.596	5.123	0.0	ξ ($\times 10^{-3}$)	103.348	25.481	9.44	4.182	0.0
$\log(T_{\rm c})$ [K]	7.819	7.815	7.815	7.815	7.814	$\log(T_{\rm c})$ [K]	8.511	8.505	8.504	8.503	8.503
ξ ($\times 10^{-3}$)	10.992	2.764	1.188	0.834	0.0	ξ ($\times 10^{-3}$)	17.555	5.504	2.622	0.795	0.0
$\log(\rho_{\rm c})$ [g cm^{-3}]	1.375	1.393	1.396	1.397	1.397	$\log(\rho_{\rm c})$ [g cm^{-3}]	3.525	3.545	3.548	3.55	3.551
ξ ($\times 10^{-3}$)	-48.836	-10.201	-2.678	-0.329	0.0	ξ ($\times 10^{-3}$)	-58.531	-13.623	-6.043	-1.536	0.0

$100\,M_\odot$											
C: end of H burn	4	2	1	1/2	1/4	C: end of He burn	4	2	1	1/2	1/4
$N_{\rm cells}$	1468	2727	5448	10818	-	$N_{\rm cells}$	1569	3152	6486	12465	-
$N_{\rm timesteps}$	275	323	323	328	-	$N_{\rm timesteps}$	696	572	559	584	-
$M/M_\odot$	65.916	25.712	24.583	23.752	-	$M/M_\odot$	33.813	11.914	11.664	11.454	-
ξ ($\times 10^{-3}$)	1775.107	82.495	34.981	0.0	-	ξ ($\times 10^{-3}$)	1952.055	40.126	18.353	0.0	-
$\log(L/L_\odot)$	6.274	5.805	5.774	5.749	-	$\log(L/L_\odot)$	6.162	5.504	5.489	5.475	-
ξ ($\times 10^{-3}$)	2352.624	139.574	58.767	0.0	-	ξ ($\times 10^{-3}$)	3867.197	67.71	31.926	0.0	-
$\log(T_{\rm eff})$ [K]	4.603	4.882	4.877	4.874	-	$\log(T_{\rm eff}$ [K])	5.228	5.2	5.199	5.198	-
ξ ($\times 10^{-3}$)	-463.387	18.996	8.502	0.0	-	ξ ($\times 10^{-3}$)	71.311	4.274	3.703	0.0	-
$\log(t)$	6.476	6.546	6.553	6.56	-	$\log(t)$	6.52	6.595	6.601	6.608	-
ξ ($\times 10^{-3}$)	-174.392	-29.716	-15.581	0.0	-	ξ ($\times 10^{-3}$)	-183.629	-28.855	-14.912	0.0	-
$\log(T_{\rm c})$ [K]	7.894	7.87	7.868	7.867	-	$\log(T_{\rm c})$ [K]	8.56	8.529	8.53	8.528	-
ξ ($\times 10^{-3}$)	65.67	8.314	3.609	0.0	-	ξ ($\times 10^{-3}$)	78.495	3.91	4.801	0.0	-
$\log(\rho_{\rm c})$ [g cm^{-3}]	1.03	1.208	1.216	1.223	-	$\log(\rho_{\rm c})$ [g cm^{-3}]	3.151	3.383	3.392	3.392	-
ξ ($\times 10^{-3}$)	-359.052	-35.601	-15.776	0.0	-	ξ ($\times 10^{-3}$)	-426.172	-19.84	-0.399	0.0	-

and `mesh_delta_coeff` simultaneously. A small C demands small time steps and fine grid cells which increase the numerical accuracy but at the expense of longer computation times. It is thus advantageous to search for the largest C we can afford to use without sacrificing the quality of the models.

Here we consider five values of C: 1/4, 1/2, 1, 2, and 4.* Note that $C = 1$ corresponds to the models computed in this paper. For each value of C, we compute evolutionary tracks for four masses—1, 5, 20, and 100 $M_\odot$—that are representative of the range of stellar types in the MIST models. Each M_i & C combination is computed until the end of hydrogen and helium burning in the core. Convergence of a given model is quantified using the ξ parameter, which is the difference between a variable at a given resolution and at the highest resolution in the study ($C = 1/4$ in this case). For 100 $M_\odot$, however, the highest resolution is $C = 1/2$ because the $C = 1/4$ models did not finish running in a reasonable amount of time. Table 2.10 summarizes the results.

For the low-mass stars, whose early evolution is relatively simple, the result at our default resolution $C = 1$ differs at most by a few percent compared to the model calculations at four times the resolution. We were also able to successfully run $C = 1/8$ and $1/16$ models for 1 and 5 $M_\odot$ models to TAMS. Even compared to model calculations at 16 times the resolution, our default $C = 1$ model is converged to within a few percent. As an additional test, we ran $C = 2$ and $C = 4$ models through to the WDCS to check if the final mass of the WD depends sensitively on the resolution; for example, improperly resolved convective boundaries may influence the growth of the core during the TPAGB phase. We find that decreasing the resolution changes the final mass of the WD by less than a percent, which is highly encouraging.

The behavior is less clear at higher masses (20 and 100 $M_\odot$), but this is not unexpected since massive star evolution is much more complex and sensitive to the choice of input physics. Although the answer can change as much as $\sim 12\%$ between our default resolution and $C = 1/2$, this is not a huge effect given the uncertainties in the evolution calculations of massive stars. We regard agreement at the $\sim 10\%$ level as

*We initially considered additional smaller values of C but many models failed to complete successfully within a reasonable amount of time.

satisfactory because at this level of precision nearly every other detail of the input physics matters, from MLT implementation to mass loss and rotation.

2.11 SUMMARY

In this paper we presented an overview of the MIST models, including a comprehensive discussion of the input physics and comparisons with existing databases and observational constraints. We conclude with a discussion of some of the caveats and plans for future work.

Perhaps the most significant shortcoming common to all stellar evolutionary tracks and isochrones of this generation is that they are computed within a 1D framework despite the inherently 3D nature of stellar astrophysical phenomena, e.g., mass-loss, convective mixing, rotation, and magnetic fields. There has been recent progress in 2D and 3D simulations of stellar interiors and atmospheres, but they are limited to small spatial scales and physical time durations of order only $\sim$ 10 hours (e.g., Woodward et al. 2015). Although full 3D simulations of stellar evolution are much too far beyond grasp today, we are nevertheless taking small steps forward. For example, it is becoming increasingly common to map 3D simulation results to a 1D formulation in order to incorporate the valuable insight we are gaining from these sophisticated simulations into standard 1D stellar evolution models (see e.g., Brown et al. 2013; Trampedach et al. 2014; Magic et al. 2015; Arnett et al. 2015). This is an active area of development in MESA.

Another major caveat is that binary interaction is not taken into account in these models. Multiplicity is extremely common among O- and B-type stars; binary mass exchange is believed to occur for $\gtrsim 70\%$ of O-type stars and about a third of those stars will ultimately form a binary merger product (e.g., Chini et al. 2012; Sana et al. 2012, 2013; de Mink et al. 2014). These numbers have serious implications for the evolution of massive stars and their explosive final fates, including the expected frequency of different types of core-collapse supernovae (see the review by Smartt 2009). Since binarity dramatically expands the size of the parameter space to be explored (e.g., mass ratio, eccentricity, and separation), it is currently com-

putationally infeasible to construct a multi-dimensional grid of binary models from full stellar evolution calculations. In order to make this a tractable problem, the standard approach has been to either couple detailed stellar evolution codes such as MESA to binary population synthesis codes (e.g., Eldridge et al. 2008) or to make use of fitting formulae to approximate models of single stars (e.g., Hurley et al. 2002; Izzard et al. 2006). Although binarity is not included in the current models, some of its evolutionary consequences must be at least partially mimicked through the effects of rotation and ordinary single-star mass loss, given that the models are in broad agreement with a number of observations. Moreover, it is possible to couple MIST to available binary synthesis codes to investigate and model binary effects in detail in the future.

In Paper II, we will present models with non-solar-scaled abundance patterns for the same large range of masses, ages, metallicities, and evolutionary phases, and make extensive comparisons with the observed properties of globular clusters. Most of our intended future directions are also areas of known limitations. Nevertheless, other future projects we hope to pursue include: investigating the effects of varying $\alpha_{\rm MLT}$ across the HR diagram and as a function of metallicity (e.g., Trampedach et al. 2014; Magic et al. 2015), exploring the effects of magnetic fields in low-mass and PMS stars, improving the WD cooling models for joint fitting of entire CMDs of star clusters, implementing low temperature C/O-variable molecular opacities for modeling the envelopes in AGB stars, performing more precise calibration of the AGB phase by jointly modeling the SFHs of the Magellanic Clouds and their AGB LFs, and developing non-standard and innovative isochrone construction methods.

ACKNOWLEDGMENTS

We thank the referee for his/her constructive comments. We thank Martha Boyer, Jason Kalirai, and Guillermo Torres for generously sharing their data with us and Francis Timmes for his assistance with nuclear reaction networks in MESA. We thank Leo Girardi and Dan Weisz for fruitful conversations and

comments on the manuscript. We thank Conny Aerts, Lars Bildsten, Jonathan Bird, Phillip Cargile, Selma de Mink, Falk Herwig, Jessica Lu, Marc Pinsonneault, Philip Rosenfield, and Victor Silva-Aguirre for sharing their expertise. We also thank the entire MESA community for making this work possible, with special thanks to the MESA Council. Finally, we thank the participants of the KITP workshop "Galactic Archaeology and Precision Stellar Astrophysics" for stimulating discussions. This research was supported in part by the National Science Foundation under Grant No. NSF PHY11-25915. J.C. acknowledges support from the National Science Foundation Graduate Research Fellowship Program. A.D. received support from the Australian Research Council under grant FL110100012. C.C. acknowledges support from NASA grant NNX13AI46G, NSF grant AST-1313280, and the Packard Foundation. This work was supported in part by NASA grant NNX15AK14G. The computations in this paper were run on the Odyssey cluster supported by the FAS Division of Science, Research Computing Group at Harvard University.

3

On the Red Giant Branch: Ambiguity in the Surface Boundary Condition Leads to $\approx$ 100 K Uncertainty in Model Effective Temperatures

The effective temperature ($T_{\rm eff}$) distribution of stellar evolution models along the red giant branch (RGB) is sensitive to a number of parameters including the overall metallicity, elemental abundance patterns, the efficiency of convection, and the treatment of the surface boundary condition. Recently there has been interest in using observational estimates of the RGB $T_{\rm eff}$ to place constraints on the mixing length parameter, $\alpha_{\rm MLT}$, and possible variation with metallicity. Here we use 1D `MESA` *stellar evolution models to explore the sensitivity of the RGB $T_{\rm eff}$ to the treatment of the surface boundary condition. We find that different surface boundary conditions can lead to $\pm$100 K metallicity-dependent offsets on the RGB relative to one another in spite of the fact that all models can reproduce the properties of the Sun. Moreover, for a given atmosphere T–τ relation, we find that the RGB $T_{\rm eff}$ is also sensitive to the optical depth at which the surface boundary condition is applied in the stellar model. Nearly all models adopt the photosphere as the location of the surface boundary condition but this choice is somewhat arbitrary. We compare our models to stellar parameters derived from the APOGEE-Kepler sample of first ascent red giants and find that systematic uncertainties in the models due to treatment of the surface boundary condition place a limit of $\approx$ 100 K below which it is not possible to make firm conclusions regarding the fidelity of the current generation of stellar models.*

3.1 Introduction

Models of the red giant branch (RGB) underpin much of our knowledge of nearby resolved dwarf galaxies (e.g., Tolstoy et al. 2009; Weisz et al. 2011), the formation history of various components of the Milky Way (e.g., Freeman & Bland-Hawthorn 2002; Rix & Bovy 2013), photometric metallicities of halo stars in nearby galaxies (e.g., PAndAS, McConnachie et al. 2009; Harris & Harris 2002), and the stellar population properties of distant galaxies (e.g., Walcher et al. 2011; Conroy 2013).

Despite a long history (e.g., Hoyle & Schwarzschild 1955; Demarque & Geisler 1963), accurate modeling of the RGB remains a challenge. The effective temperature ($T_{\rm eff}$) of the RGB is sensitive to changes in chemical composition, stellar mass, and model parameters such as convection efficiency, and there are essentially no "ground truth" observations with which to constrain the models in this evolutionary phase. This is important because 1D stellar evolution models treat various processes including convection in a phenomenological way with one or more free parameters that must be calibrated in some way. The most common framework for convection, the so-called mixing length theory (MLT; Böhm-Vitense 1958), utilizes a free parameter of order unity, $\alpha_{\rm MLT}$, to describe the convection efficiency. Calibration of $\alpha_{\rm MLT}$ in the current generation of stellar evolution models is primarily based upon exquisite knowledge of a single star — the Sun. It is important to test whether the free parameters governing convection that have been calibrated to the Sun are capable of accurately modeling red giants as well.

There have been several lines of evidence, both from a theoretical perspective (e.g., Trampedach et al. 2014; Magic et al. 2015) and from comparing models to observations (e.g., Salaris & Cassisi 1996; Bonaca et al. 2012; Tayar et al. 2017; Joyce & Chaboyer 2017; Chun et al. 2018; Li et al. 2018; Viani et al. 2018), that suggest the properties of convection may vary with stellar parameters, such as $\log g$, $T_{\rm eff}$, and/or metallicity. If true, this would have profound implications extending well beyond the realm of stellar physics. For example, in the case of a solar metallicity, $\log g \approx 2$ star, increasing $\alpha_{\rm MLT}$ by ≈ 0.1 (5 %) would make

the RGB hotter by ≈ 50 K, or equivalently ≈ 0.02 mag in $B-V$ and $J-K$. This seemingly small change shifts the isochrone-based mass and age estimates upward by ≈ 0.25 $M_{\odot}$ and downward by a factor of ≈ 2, respectively. This is an uncomfortable margin of error when they consider e.g., RGB-based star formation histories of the Milky Way and nearby resolved galaxies.

Recently, Tayar et al. (2017, hereafter T17) used the joint APOGEE-*Kepler* catalog of red giants (Pinsonneault et al. 2014) to compare observationally-derived $T_{\rm eff}$ values to YREC (Pinsonneault et al. 1989) and PARSEC (Bressan et al. 2012) stellar evolution models. T17 found that the model $T_{\rm eff}$ values were too hot and cool at low and high metallicities, respectively. They interpreted this metallicity-dependent discrepancy between the YREC and APOGEE $T_{\rm eff}$ as evidence for a metallicity-dependent convection efficiency parameter. Salaris et al. (2018, hereafter S18) revisited the T17 analysis with their own stellar models from the BaSTI collaboration (Pietrinferni et al. 2004). These authors also reported a discrepancy, albeit smaller, between their predicted and APOGEE $T_{\rm eff}$ for the full T17 sample. However, they found that this tension mostly disappears when considering a subsample of metal-rich, solar-scaled stars.

One of the key points from S18 is the importance of the surface boundary condition (BC) in setting the $T_{\rm eff}$ distribution of their model RGB. There have been several studies in the literature on the effect of BCs, both on the $T_{\rm eff}$ and the overall stellar structure (e.g., Chabrier & Baraffe 1997; Montalbán et al. 2001; Salaris et al. 2002; VandenBerg et al. 2008) and on the lithium depletion boundary technique for age-dating clusters (Burke et al. 2003). Given the importance of this issue, we revisit the $T_{\rm eff}$ of the RGB in the context of `MESA` stellar evolution models. In Section 3.2, we introduce the stellar models and discuss the use of different BCs in model computations. This is followed by Section 3.3 where we critically examine the $T_{\rm eff}$ discrepancy as a function of metallicity. We place these results in context in Section 3.4, and we provide a summary in Section 3.5.

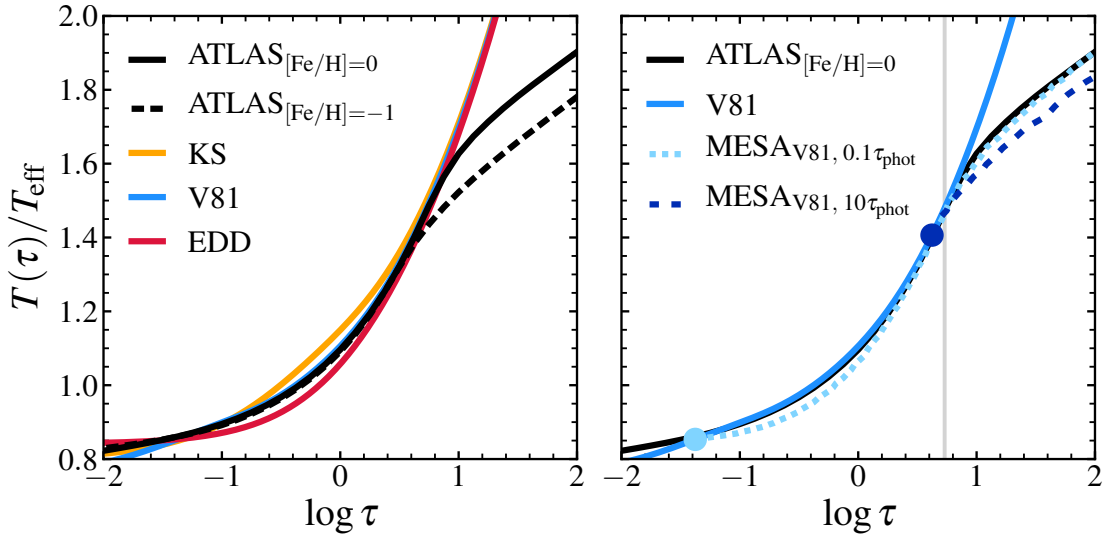


Figure 3.1: Overview of the various atmosphere T–τ profiles considered in this work. Left Panel: The Krishna Swamy (1966), Vernazza et al. (1981), and Eddington (1926) analytic relations are shown in orange, blue, and red lines, respectively. The ATLAS model atmospheres at $\log g = 2$ and $T_{\rm eff} = 4750$ K at both [Fe/H]=−1 and 0 are plotted as black lines. The analytic T–τ relations increase sharply above $\log \tau \approx 1$ while the ATLAS model profiles become shallower due to the onset of convection in the latter. Right Panel: Comparison of the atmosphere T–τ profiles for ATLAS and V81 with the MESA stellar interior profiles computed using the V81 BC. Light and dark blue circles mark the outer edges of the MESA profiles, at optical depths of $0.1\tau_{\rm phot}$ ($\tau_{\rm base} = 0.042$) and and $10\tau_{\rm phot}$ ($\tau_{\rm base} = 4.2$), respectively. The MESA profiles become shallower at large optical depths due to the onset of convection. The gray vertical line marks the optical depth above which the convective flux is greater than the radiative flux.

3.2 Stellar Models

3.2.1 Input Physics

All stellar evolutionary tracks used in this paper are computed using Modules for Experiments in Stellar Astrophysics (MESA; Paxton et al. 2011, 2013, 2015, 2018), revision 9793. The physical assumptions and input data sources are consistent with the MESA Isochrones and Stellar Tracks (Dotter 2016; Choi et al. 2016) project. To summarize, we use opacities from OPAL (Iglesias & Rogers 1996) and AESOPUS (Marigo & Aringer 2009), and equation of state from OPAL (Rogers & Nayfonov 2002), HELM (Timmes & Swesty 2000), and SCvH (Saumon et al. 1995) blended as described by Paxton et al. (2011). We treat atomic diffusion using the formalism of Thoul et al. (1994) with turbulent mixing at the surface as described by Dotter et al. (2017). Nuclear reaction rates are taken from JINA Reaclib v2.2 (Cyburt et al.

2010). Convective boundary mixing is treated in the diffusive approximation with the exponential decay formula (Freytag et al. 1996) and a value of $f_{\rm ov} = 0.016$. We adopt the Asplund et al. (2009) solar abundance pattern throughout.

3.2.2 Surface Boundary Conditions

The surface BC is an essential input to any stellar model as it is required to close the equations of stellar structure. Conceptually, this can be thought of as the point at which the stellar "atmosphere" is attached to the stellar interior. In practice the BC is set by specifying the pressure and temperature at the last grid point in the interior model, or the stellar "surface." The surface is commonly defined as the point at which $T = T_{\rm eff}$; we will refer to this location as the photosphere (with a corresponding Rosseland optical depth of $\tau_{\rm phot}$). However, in some cases the BC is set much deeper in the atmosphere (e.g., at $\tau = 100$; Chabrier & Baraffe 1997; Choi et al. 2016). A more important criterion is that the joining region should be located where the various assumptions and adopted microphysics are in agreement between the atmosphere and the interior.

Most stellar evolution codes approach the treatment of the surface BC in one of two ways: integration of analytic T–τ relations and model stellar atmosphere tables. We consider both approaches in this paper.

The classic means of obtaining the surface BCs for T and P is to adopt an analytic T–τ relation and integrate $dP/d\tau = (g/\kappa) - (a/3)dT^4/d\tau$ from $\tau \approx 0$ to $\tau_{\rm base}$, with $\tau_{\rm base} = \tau_{\rm phot}$ being the most common choice. Here, g and κ are the local surface gravity and Rosseland mean opacity, respectively, and the second term accounts for the radiation pressure where a is the radiation constant. Once $\tau_{\rm base}$ is chosen, $T(\tau_{\rm base})$ is trivially obtained from the T–τ relation, and $P(\tau_{\rm base})$ is obtained from the above integral.

The analytic T–τ relations considered in this paper include: i) EDD: the Eddington (1926) "gray" T–τ relation for which $\tau_{\rm phot} = 2/3$; ii) KS: the fit by Krishna Swamy (1966) for which $\tau_{\rm phot} \approx 0.31$; and iii) V81: an analytical fit to the Vernazza et al. (1981) solar atmosphere from S18 for which $\tau_{\rm phot} \approx$

0.42. These $T-\tau$ relations are shown for a typical red giant star in Figure 3.1. An important (and relatively untested) assumption of analytic $T-\tau$ relations is that they do not depend on chemical composition (metallicity) nor on surface gravity.

Another approach to the surface BC is to use model atmospheres (as in e.g., Lyon, Baraffe et al. 2015; MIST, Choi et al. 2016), which tabulate thermodynamic and other microphysical quantities as a function of optical depth, to determine the pressure at some reference location in the atmosphere. For the purposes of this paper we use model atmosphere BC tables constructed at $\tau = \tau_{\rm phot}$. The model atmosphere surface BC in this work is based on grids of `ATLAS12` (Kurucz 1970, 1993) models. The gas pressures at $\tau_{\rm phot}$ are tabulated as a function of $T_{\rm eff}$, $\log g$, and metallicity, and then interpolated by `MESA` at runtime (see Paxton et al. 2011; Choi et al. 2016 for further details).

Figure 3.1 shows the $T-\tau$ relations extracted from two `ATLAS` models along with the analytic versions. We show an `ATLAS` model with $T_{\rm eff} = 4750$ K, $\log g = 2$, and $[{\rm Fe/H}] = 0$ for which $\tau_{\rm phot} \approx 0.42$ and another `ATLAS` model with $T_{\rm eff} = 4750$ K, $\log g = 2$, and $[{\rm Fe/H}] = -1$ for which $\tau_{\rm phot} \approx 0.44$. Interestingly, $\tau_{\rm phot}$ in both `ATLAS` models are very similar to the V81 relation. Indeed, the similarity with V81 extends from $-1 \leq \log \tau \leq 0.5$. The metallicity-dependence appears to be mild for $\tau < 4$.

In this paper we compute stellar evolutionary tracks for three analytic $T-\tau$ relations and for the `ATLAS` model atmosphere tables. Each surface BC is separately calibrated to reproduce the solar parameters at the solar age as in Choi et al. (2016). The main parameter that changes as one considers different BCs is $\alpha_{\rm MLT}$. Solar calibration as a means to obtain $\alpha_{\rm MLT}$ is standard practice in almost all stellar models (see Ferraro et al. 2006 where the authors calibrate $\alpha_{\rm MLT}$ using globular clusters instead), but there is no guarantee that this is sufficient to accurately model stars in other evolutionary phases or at non-solar abundances and masses.

For the `ATLAS` BC tables we obtain a solar-calibrated $\alpha_{\rm MLT} = 1.848$; for the Eddington $T-\tau$ $\alpha_{\rm MLT} = 1.713$; for the V81 $T-\tau$ $\alpha_{\rm MLT} = 1.908$; and for the Krishna-Swamy $T-\tau$ $\alpha_{\rm MLT} = 2.008$. The solar-calibrated

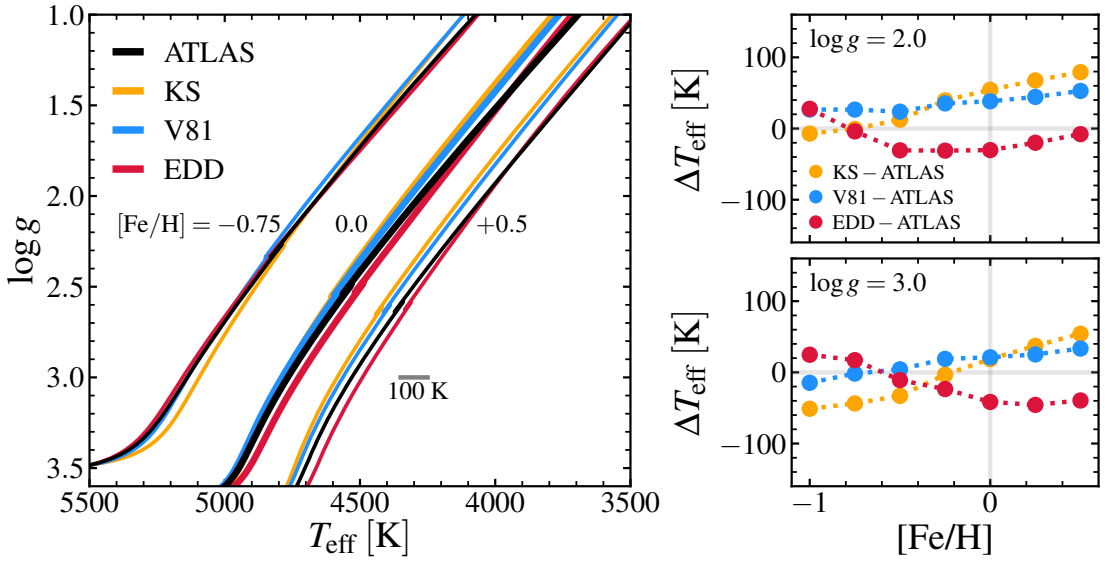


Figure 3.2: Effect of varying boundary conditions in the MESA model calculations on the RGB effective temperatures. Left Panel: RGB sequences in the Kiel diagram for a 1.2 $M_{\odot}$ star at [Fe/H]= -0.75, 0.0, and $+0.5$. The black curves corresponds to the fiducial MESA models computed with ATLAS photosphere tables. Each set of models for a given BC has been independently calibrated to the Sun. Right Panels: $\Delta T_{\rm eff}$ for the RGB models computed with the analytic T–τ models relative to the ATLAS RGB $T_{\rm eff}$ as a function of metallicity at two $\log g$ values.

$\alpha_{\rm MLT}$ values vary by $\approx 15\%$ across the range of surface BCs considered here. As pointed out by S18, the solar-calibrated $\alpha_{\rm MLT}$ values derived from the Vernazza et al. (1981) T–τ relation and model photosphere tables are closer to each other than to either of the other two T–τ relations. As illustrated in Figure 3.1, these two BCs have very similar T–τ profiles.

3.2.3 Influence of the Surface Boundary Condition on the Effective Temperature of the RGB

We compute grids of stellar evolutionary tracks for the four surface BCs and their solar-calibrated $\alpha_{\rm MLT}$ values, for initial masses between 0.7 and 2.5 $M_{\odot}$ in steps of 0.1 $M_{\odot}$ and [Fe/H]= -1 to +0.5 in steps of 0.25 dex, and for [α/Fe]=0, $+0.2$, and $+0.4$. We assume that all of the α-capture elements (O, Ne, Mg, Si, S, Ar, Ca, and Ti) are enhanced by the same amount as denoted by [α/Fe].

The left panel of Figure 3.2 shows RGB tracks computed for the four surface BCs and their solar-

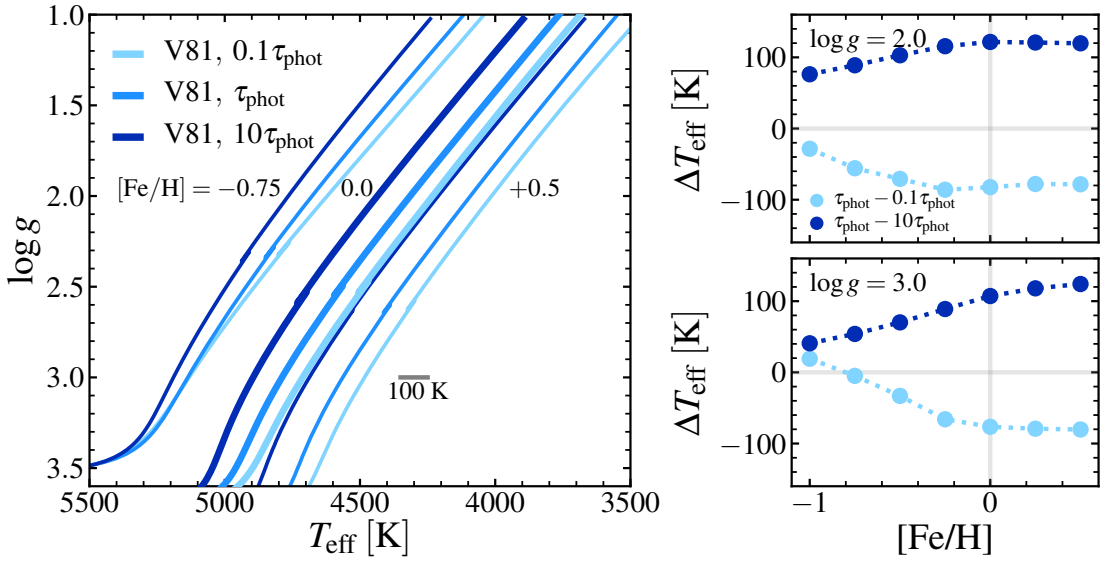


Figure 3.3: Same as Figure 3.2 now varying $\tau_{\rm base}$, the optical depth at which the V81 surface boundary condition is applied in the MESA model. Each set of models has been independently calibrated to the Sun. Depending on one's choice of $\tau_{\rm base}$, there is an approximately 100 K variation in the resulting RGB $T_{\rm eff}$ relative to the nominal $\tau_{\rm base} = \tau_{\rm phot}$ case over the plotted metallicity range.

calibrated $\alpha_{\rm MLT}$ values in the Kiel diagram. The evolutionary tracks correspond to $M_{\rm init} = 1.2\,M_{\odot}$ and [Fe/H]=−0.75, 0, +0.5, all with [α/Fe]=0. The right panels show how $T_{\rm eff}$ varies at fixed $\log g$ over the full range of [Fe/H] relative to the fiducial (ATLAS BC) MESA models. The maximum difference in $T_{\rm eff}$ is about 100 K with the Eddington T–τ BC usually—but not always—producing the coolest RGB and the Krishna-Swamy T–τ BC usually producing the hottest RGB. Aside from these generalities, the $\Delta T_{\rm eff}$ behavior is complex, varying both as a function of [Fe/H] and $\log g$.

In order to explore the implications of changing $\tau_{\rm base}$ within the context of a given surface BC, we have computed a series of models with the V81 T–τ relation but now shifting the fitting point to $\tau_{\rm base} = 0.1\tau_{\rm phot}$ and $10\tau_{\rm phot}$, each with its own solar-calibrated $\alpha_{\rm MLT}$. The V81 models with $\tau_{\rm base} = 0.1\tau_{\rm phot}$ have $\alpha_{\rm MLT} = 1.71$ while those with $\tau_{\rm base} = 10\tau_{\rm phot}$ have $\alpha_{\rm MLT} = 2.106$. We remind the reader that V81 and $\tau_{\rm base} = \tau_{\rm phot}$ has a solar-calibrated $\alpha_{\rm MLT} = 1.908$. We chose the V81 T–τ for this exercise both because it follows the ATLAS model T–τ closely and because MESA provides a convenient option to change the location of $\tau_{\rm base}$ for a given analytic T–τ relation. In contrast, the same test with ATLAS would require the

calculation and implementation of an entirely new set of atmosphere tables. Nevertheless, given their similarities in Figure 3.1, we believe the conclusions drawn from the V81 T–τ relation should be applicable to the ATLAS atmosphere tables.

Figure 3.3 illustrates the effect of changing $\tau_{\rm base}$ on the location of the RGB in the Kiel diagram. The $T_{\rm eff}$ shifts are mainly due to differences in the solar-calibrated $\alpha_{\rm MLT}$ for each assumed $\tau_{\rm base}$. Notice that the $T_{\rm eff}$ shifts are quite large, of order $\pm$100 K at fixed metallicity, with strong variation as a function of $\log g$ and [Fe/H]. This indicates that there is substantial model uncertainty in the effective temperature distribution along the RGB due solely to the ambiguity in where one sets the surface BC.

3.3 Models vs. Data

3.3.1 Observations on the RGB

Now we turn our attention to the comparison between the model-predicted RGB $T_{\rm eff}$ with observational estimates of $T_{\rm eff}$ for real stars. We use the publicly available T17 catalog*, which contains spectroscopic $T_{\rm eff}$, [Fe/H], and [α/Fe], as well as asteroseismic $\log g$ and M. As described in T17, there are approximately 12,000 APOGEE stars with *Kepler* asteroseismic observations (i.e., APOKASC), and of those, 3210 are identified as first ascent red giants. Measurements of two global asteroseimic parameters, $\Delta\nu$ and $\nu_{\rm max}$, can be combined with an external $T_{\rm eff}$ estimate to derive estimates for stellar mass and radius (or $\log g$): $M \propto \nu_{\rm max}^3\,\Delta\nu^{-4}\,T_{\rm eff}^{3/2}$ and $g_{\rm astero} \propto \nu_{\rm max}\,T_{\rm eff}^{1/2}$ (Kjeldsen & Bedding 1995), where the proportionality constants are defined by scaling to the solar values. The $T_{\rm eff}$ values in T17 were corrected for a metallicity-dependent offset that was determined by a comparison to the color-$T_{\rm eff}$ relation from González Hernández & Bonifacio (2009).

Figure 3.4 shows a comparison in the Kiel diagram between the APOKASC RGB stars and the MESA evolutionary tracks. We select stars that have solar-scaled abundances ($[\alpha/{\rm Fe}] < 0.07$) and asteroseismic

*www.astronomy.ohio-state.edu/~tayar/MixingLength.htm

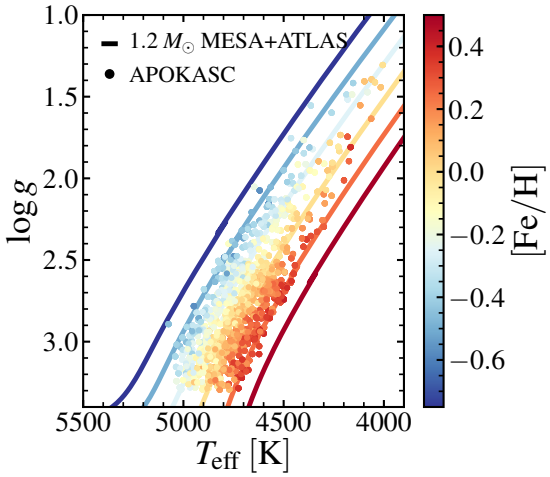


Figure 3.4: Comparison between the observed RGB stars with masses between 1.1 and 1.3$M_\odot$ and MESA evolutionary tracks for a 1.2$M_\odot$ star at a range of metallicities ([Fe/H] $= -0.75$ to 0.50 in steps of 0.25 dex). $T_{\rm eff}$ for the observed sample are derived from the APOGEE spectra and correspond to the post-DR13 values adopted in T17. The $\log g_{\rm astero}$ and $M_{\rm init}$ are obtained using the asteroseismic scaling relations. The stars are selected to have roughly solar-scaled abundances ($[\alpha/{\rm Fe}] < 0.07$) and each star is color-coded by [Fe/H].

masses between 1.1 and 1.3$M_\odot$. Each star is color-coded by its [Fe/H]. The models correspond to a 1.2$M_\odot$ star at a range of metallicities ([Fe/H] $= -0.75$ to 0.50 in steps of 0.25 dex) computed with the ATLAS surface BC. The MESA RGB tracks show a moderate tension with the APOGEE $T_{\rm eff}$, both in terms of the overall $T_{\rm eff}$ shift and in the $T_{\rm eff}$ "stretch" with metallicity. This tension is quantified below.

3.3.2 Effect of Boundary Conditions

In this section we carry out a star-by-star comparison between the APOGEE $T_{\rm eff}$ and the MESA $T_{\rm eff}$ along the RGB. For each star, we interpolate in [Fe/H], [α/Fe], $\log g_{\rm astero}$, and $M_{\rm init}$ from a grid of model evolutionary tracks to obtain $T_{\rm eff}$.* We perform this comparison for each of the surface BCs described in previous sections.

The resulting comparison between APOGEE and model $T_{\rm eff}$ is shown in Figure 3.5. The figure shows the mean difference in $T_{\rm eff}$ as a function of spectroscopic metallicity. The key conclusion of this paper is

*S18 note that [α/Fe] and [Fe/H] reported in the T17 catalog are in fact [α/M] and [M/H] in the in APOGEE DR13 catalog, where M is the total metallicity. The resulting error is small (0.01–0.02 dex). See Figure 7 in S18 for more details.

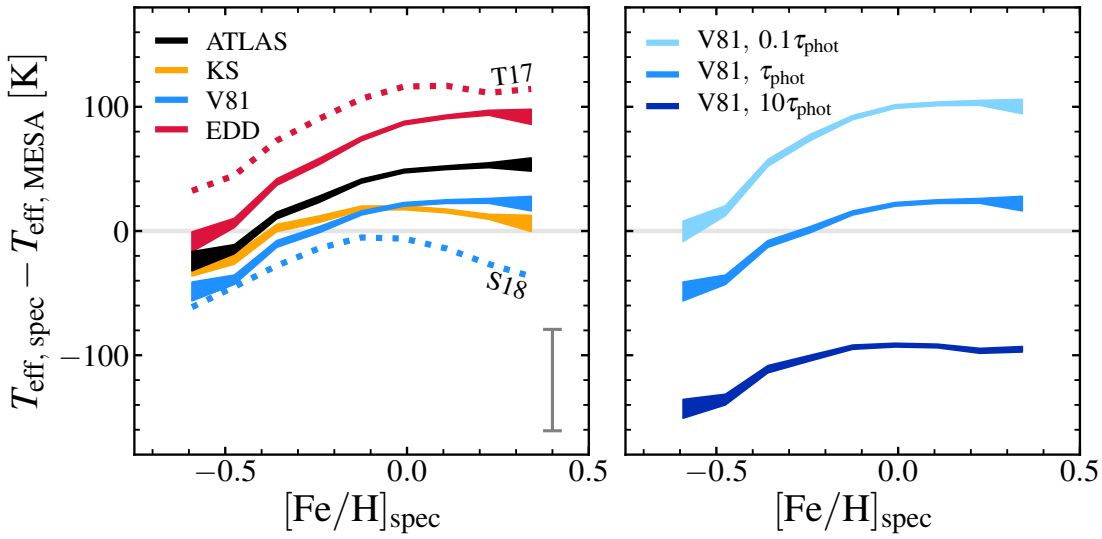


Figure 3.5: Effect of surface boundary condition on model–observation comparisons along the RGB. Curves are mean-binned $\Delta T_{\rm eff}$ for the APOGEE $T_{\rm eff}$ values adopted in T17 and `MESA` models computed with a variety of surface boundary conditions. The line widths correspond to the error on the mean and the gray error bar represents the typical scatter within each bin. *The choice of surface boundary condition and the optical depth at which it is applied in the stellar interior models induces* ≈ 100 K *variation in the resulting RGB effective temperatures.* Left Panel: `MESA` models computed with different types of boundary condition. `ATLAS` is based on realistic model atmosphere computations whereas KS (Krishna Swamy 1966), V81 (Vernazza et al. 1981), and EDD (Eddington 1926) are analytic relations. We include the T17 and S18 $T_{\rm eff}$ trends in dotted lines, color-coded by their adopted model boundary condition (EDD and V81, respectively). Right Panel: Same as the left panel now showing different $\tau_{\rm base}$, the optical depth at which the surface boundary condition is applied in the stellar interior model. All three models were computed with the V81 boundary condition. Note that both the normalization and the slope change in this case.

that the choice of surface BC imparts a $\approx \pm 100$ K systematic uncertainty in the model $T_{\rm eff}$ values, and this uncertainty manifests both as an overall zeropoint shift and a metallicity-dependent offset. This result amplifies and extends the conclusion in S18 that the surface BCs play a pivotal role in the comparison of models and observations.

The left panel shows $\Delta T_{\rm eff}$ resulting from differences in the *types* of BCs employed in stellar models. The black, orange, blue, and red curves represent realistic model atmosphere BC tables from ATLAS, the KS analytic T–τ relation, the analytic fit to the V81 BC tabulation identical to what is used in S18, and the analytic Eddington Gray atmosphere used in T17, respectively. We emphasize that the differences shown here are solely due to the choice of the surface BC, and include the differences in both the T–τ relation and the solar-calibrated $\alpha_{\rm MLT}$. Each curve is mean-binned, the line width corresponds to the standard er-

ror of the mean, and the gray error bar represents the typical scatter within each bin. For comparison, we include the T17 and S18 $T_{\rm eff}$ trends as dotted lines, color-coded by their BC of choice in model computations. Although there are $\approx$ 20 K offsets due to differences in the numerous physical assumptions and input choices among MESA, YREC, and BaSTI, the dotted lines show similar trends compared to the corresponding BC used herein. The Eddington atmosphere results in both the largest overall offset and the strongest trend with metallicity. Notice that the KS BC results in no significant $T_{\rm eff}$ trend with [Fe/H], although we emphasize that there is no physical reason to prefer the KS BC over the others.

The right panel shows $\Delta T_{\rm eff}$ resulting from differences in $\tau_{\rm base}$, the *location* (in terms of the optical depth) at which the surface BC is applied in the stellar interior model. All three models shown here were computed adopting the V81 T–τ relation, each with its own solar-calibrated $\alpha_{\rm MLT}$. The light, medium, and dark blue curves represent $\tau_{\rm base}$ of $0.1\tau_{\rm phot}$, $\tau_{\rm phot}$, and $10\tau_{\rm phot}$, respectively. Recall that $\tau_{\rm phot}$ is defined to be where $T = T_{\rm eff}$ and represents the fiducial location of choice in most stellar evolution codes. Furthermore, since the optical depth increases with increasing depth in the stellar interior, $0.1\tau_{\rm phot}$ means the atmosphere model is "grafted on" farther out in the stellar atmosphere, and vice versa.*

3.4 Discussion

The main result of this paper is that the choice of surface BC in solar-calibrated stellar models imparts a substantial ($\approx$ 100 K) uncertainty in the effective temperature distribution along the RGB. The effect of the surface BC is not a constant shift in $T_{\rm eff}$, but instead results in changes to $T_{\rm eff}$ that vary with $\log g$ and metallicity. Amongst the different models that we have explored, we believe that the model atmosphere-based BCs are the most physically realistic and hence are the most likely to be correct. The

*Unfortunately, many of the $0.1\tau_{\rm phot}$ models suffered from numerical convergence issues and so we adopted a simpler scheme to approximate the full grid. The light blue line in Figure 3.5 was generated by applying a $\Delta T_{\rm eff}$ interpolated as a function of [Fe/H] and $\log g$ at 1.2 $M_{\odot}$ as estimated from Figure 3.3 to the medium blue curve ($\tau_{\rm phot}$). We checked the accuracy of this simple $\Delta T_{\rm eff}$ interpolation by comparing the $10\tau_{\rm phot}$ relation estimated using this method to the relation obtained from actually interpolating evolutionary tracks computed assuming $10\tau_{\rm phot}$ BCs. The difference is negligible, amounting to a few K for the majority of the stars.

analytic T–τ relations suffer from several critical shortcomings. The Eddington model assumes gray opacities, which is well-known to be inadequate for stellar atmospheres (see also the discussion in Chabrier & Baraffe 1997).* The KS and V81 models, both empirical relations derived for the Sun, are meant to be employed in the radiative region, which is why they diverge strongly from the ATLAS models at large τ in Figure 3.1. There is no reason that scaled versions of these relations should adequately describe stars of all metallicities and $\log g$ values.

Self-consistent application of surface BCs requires that the adopted physics in the atmosphere and the interior agree in the joining region. This includes ensuring the same equation of state, sources of opacity, and treatment of convection. We note that ATLAS uses a somewhat different implementation of MLT (Mihalas 1978) compared to the one that we use in MESA (Henyey et al. 1965). Preliminary work (see also Montalbán et al. 2001 and VandenBerg et al. 2008) suggests that the attachment location of the BC does not strongly influence the resulting RGB $T_{\rm eff}$ as long as the treatment of convection and $\alpha_{\rm MLT}$ are self-consistent between the interior and the atmosphere models. In practice, atmosphere models are computed with an internally-calibrated $\alpha_{\rm MLT}$ that is not guaranteed to be consistent with that of an interior model, because this requires iterating the solar-calib rations to converge on a common value of $\alpha_{\rm MLT}$ (VandenBerg et al. 2008). In future work we plan to explore a common treatment of MLT in ATLAS and MESA.

The sensitivity of the RGB $T_{\rm eff}$ to the location of the joining region ($0.1 - 10\tau_{\rm phot}$) in the models presented in this work, as shown in Figure 3.3, is in large part a consequence of the fact that the interiors assume grayness while most of our adopted surface BCs do not. Careful inspection of Figure 3.1 reveals that the Eddington T–τ relation is most similar to the MESA profile extended to $\tau_{\rm base} = 0.1\tau_{\rm phot}$, which is a reflection of the gray assumption in both cases. For the Eddington T–τ we have found that the RGB $T_{\rm eff}$ is in fact *insensitive* to the choice of $\tau_{\rm base}$ up to the point where convection becomes important. This is not surprising — in the limit where the adopted surface BC and the interior model obey the same T–τ relation,

*Note that gray atmospheres are adopted in asteroseismology models because grids of atmosphere tables are generally too coarsely sampled to compute eigenfunctions for pulsation modes.

the resulting model $T_{\rm eff}$ (and L, R, etc.) should be insensitive to the location of the joining region.

These considerations lead us to suggest that the joining region between the atmosphere and the interior should be placed deeper in the atmosphere than is commonly adopted, ideally where the gray opacity assumption is valid and the atmosphere and interior treatments of the opacity and convection are consistent (see Chabrier & Baraffe 1997 who advocate this approach for modeling cool dwarfs).* At sufficiently high values of τ, atmosphere models are convective and follow a simple adiabat, and are thus easy to match seamlessly to an adiabat in the interior model. While there is a physically-motivated preference for $\tau > \tau_{\rm phot}$ to ensure the validity of the diffusion approximation, the surface BC also cannot be applied arbitrarily deep. In the case of analytic T–τ relations considered in this work, their attachment location should not exceed the depth of the onset of convection since they do not model the effects of convection. Moreover, there is the more fundamental concern that a simple solar-scaled or purely analytic description of the stellar atmosphere is woefully insufficient for accurately representing the interior. Similarly, current generation of model atmospheres carry out computationally intensive radiative transfer calculations by simplifying other physics, e.g., assuming an ideal gas, and thus should not replace the detailed interior modeling in significant portions of the outer layers. To summarize, while we propose applying the surface BC deeper than at the photosphere and strongly favor the use of atmosphere models, there is still some ambiguity associated with the appropriate attachment location of the BC. We leave for future work a detailed investigation of this issue.

We now return to the question that originally prompted this investigation — whether or not there is evidence for variation in $\alpha_{\rm MLT}$ with metallicity amongst first ascent giants. T17 found a metallicity-dependent $T_{\rm eff}$ discrepancy when comparing data to models (red dotted line in Figure 3.5), which they

*Note that $T_{\rm eff}$ reported by `MESA` is evaluated using the Stefan-Boltzmann equation along with L and R at $\tau_{\rm base}$, the outermost point in the interior model. We do not solve for the temperature at $\tau_{\rm phot}$ when $\tau_{\rm base} \neq \tau_{\rm phot}$. The resulting error is quite small and, unsurprisingly, depends on the surface gravity. For a 1 $M_\odot$ star at the main sequence turn off, this introduces an error of < 1 K. The error is slightly larger for an RGB star (~ 5 K), but this is still a 0.1% effect.

interpreted as evidence for a metallicity-dependent $\alpha_{\rm MLT}$. Our MESA models show a wide range of behaviors depending on the adopted surface BC, and recover the results of both T17 and S18 as extremes of the theoretical range. The KS T–τ relation shows nearly perfect agreement with the APOGEE data while the Eddington T–τ relation produces a trend of ≈ 100 K dex^{-1}. Other models show behavior in between these two limits. More worrisome from our point of view is the result that varying $\tau_{\rm base}$ for a fixed T–τ relation results in both a different normalization *and* slope in the metallicity-dependent $\Delta T_{\rm eff}$ comparison. Given that the choice of surface BCs imparts a systematic uncertainty at least as large as the model-data tension reported in T17, we conclude that it is premature to appeal to variation of $\alpha_{\rm MLT}$ with metallicity. Indeed, any conclusion that requires model RGB $T_{\rm eff}$ to be more accurate than ≈ 100 K must await a thorough investigation of the proper treatment of surface BCs in stellar evolution models. Moreover, these results demonstrate that solar-calibration alone is insufficient to guarantee accurate models in other parts of the Hertzsprung-Russell diagram, underscoring the need for other "ground truth" observational constraints.

3.5 Summary

In this work we explored the impact of the adopted surface boundary condition on the $T_{\rm eff}$ of red giant stars. We computed 1D stellar evolutionary tracks using MESA with several implementations of surface BCs, including three analytic relations commonly used in the literature (Eddington 1926 "gray", Krishna Swamy 1966, and Vernazza et al. 1981) and one set of realistic model atmosphere BC tables from ATLAS (Kurucz 1970, 1993). We performed solar-calibration for each type of the surface boundary condition to obtain an appropriate $\alpha_{\rm MLT}$. Even though all models line up perfectly around the solar value—by construction—both the type of boundary condition *and* the location at which it is applied to the 1D stellar interior model yield $\approx \pm 100$ K, metallicity- and $\log g$-dependent changes to the $T_{\rm eff}$ distribution along the RGB. This clearly demonstrates that solar-calibration alone is an insufficient check on the accuracy of the stellar models. In light of these results, we caution against attempting to interpret any data-model $T_{\rm eff}$ dis-

crepancies at the $\approx \pm 100$ K level or less until the ambiguity in the surface boundary condition presented herein is resolved.

ACKNOWLEDGMENTS

We thank the anonymous referee, Santi Cassisi, Lars Bildsten, and Jamie Tayar for useful discussions and insightful comments on this manuscript. We would like to thank Bill Paxton and the MESA community for making this work possible. We also wish to acknowledge and thank the Kavli Institute for Theoretical Physics at UC Santa Barbara, where most of this work took place. This research was supported in part by the National Science Foundation under Grant No. NSF PHY-1748958. This paper is based upon work supported by the National Aeronautics and Space Administration (NASA) under Contract No. NNG16PJ26C issued through the WFIRST Science Investigation Teams Program.

4

PROSPECTS FOR AGE-DATING STAR CLUSTERS IN THE *Gaia* ERA

We use the framework developed as part of the MESA Isochrones and Stellar Tracks (MIST) project to assess the efficacy of several types of observables on the joint constraint of age and 1D stellar model parameters in star clusters. First we provide a pedagogical overview summarizing the effects of stellar and model parameters, such as the helium abundance and the mixing length parameter, on observational diagnostics including the color-magnitude diagram (CMD), mass-radius relation, and surface abundances. Next, we investigate three well-studied intermediate-age and old open clusters—NGC6819, M67, NGC6791—as case studies. There are no obvious signs of tension between the MIST models and the existing observations, though more precise data are required for firmer constraints and the detection of potential discrepancies. With a combination of exquisite photometry, parallax distances, and cluster memberships from Gaia, we expect to be able to differentiate between the subtle yet qualitatively distinct CMD morphologies induced by the model parameters, and to measure precise and accurate ages for these nearby open clusters in the next several years.

4.1 Introduction

Over the last decade, improving the state of stellar models has become a critical and necessary step in the quest to understand the properties of thousands of exoplanets that have been discovered (e.g., Torres et al. 2012; Huber et al. 2014; Mathur et al. 2017), probe the formation and evolution histories of galaxies both near and far including our own Milky Way (e.g., Freeman & Bland-Hawthorn 2002; Bovy et al. 2012; Martig et al. 2015), link the diverse set of transient events to their progenitors (e.g., Kochanek et al. 2008; Smartt 2009; Georgy et al. 2012), and interpret the troves of asteroseismology data that have been obtained by the *CoRoT* (Baglin et al. 2006) and *Kepler/K2* missions (Gilliland et al. 2010; Bedding et al. 2010; Huber et al. 2011). Moreover, it has become increasingly clear that the analysis and interpretation of an even larger wealth of data expected from future missions and surveys will require more complete and accurate stellar models.

Many of the essential ingredients in standard 1D stellar evolution models cannot be modeled from first principles and instead rely on physically-motivated prescriptions. For example, turbulent, superadiabatic convection is usually implemented according to the mixing length formalism in which the mixing efficiency and stellar structure depend sensitively on $\alpha_{\rm MLT}$, a free parameter of order unity (Böhm-Vitense 1958). There are ongoing complementary efforts to address this using sophisticated 3D hydrodynamic simulations (e.g., Trampedach et al. 2014; Magic et al. 2015) as well as detailed constraints and calibrations from a variety of observations (e.g., Bonaca et al. 2012; Wu et al. 2015; Tayar et al. 2017). This work adopts the latter approach, in particular using well-studied benchmark star clusters with a comprehensive set of observations to investigate the type of information—both cluster and stellar parameters as well as the input physics parameters—that we can recover and the precision with which we can measure them. Open clusters are uniquely well-suited for this purpose because they are mono-age and mono-metallic, unlike globular clusters, which are known to harbor multiple populations (see Gratton et al. 2012; Bastian &

Lardo 2017 for recent reviews on this topic).

This paper is the first in a series that attempts to measure stellar parameters (e.g., age) and constrain uncertain input physics (e.g., mixing length parameter). The insights gained from this work should guide our intuition to both shape the direction of future observations and forecast what we will be able to learn from future surveys and large data sets. We will explore this more quantitatively in subsequent work. In this first paper, we lay the groundwork for our approach by qualitatively examining the effects of various uncertainties on the observable quantities. We explore uncertainties of both observational (e.g., metallicity of the cluster) and theoretical (e.g., efficiency of mass loss) origins (e.g., Magic et al. 2010; Reese et al. 2016; Lagarde et al. 2017; Angelou et al. 2017). A key aspect of this particular work is that *we consider a diverse set of observables simultaneously*. One of the goals is to explore the separation of the key parameters in the various observed planes and identify a set of suitable observables for each parameter.

The rest of the paper is organized as follows. In Section 4.2, we review the different types of data sets that can be employed to study the properties of star clusters and to improve stellar evolution models. In Section 4.3, we first provide a brief overview of the MIST project that serves as the framework for the evolutionary models explored in this work. Then we explore the information content in these observables using theoretical models, paying particular attention to the observational feasibility as well as degeneracies. Next, in Section 4.4, we present case studies of three well-studied open clusters, NGC6819, M67, and NGC6791. In Section 4.5, we discuss what we can expect to accomplish with the future *Gaia* data, and finally, in Section 5.7, we conclude with a summary. For this work, we adopt a Kroupa (2001) initial mass function (IMF) where necessary.

4.2 Observations: What Can They Tell Us?

Here we provide a broad overview of the different types of data sets and surveys, including those that are ongoing and imminent, that can be used to improve both the characterization of star clusters and the

quality of the stellar models. We also discuss what type of information can be leveraged from different types of observations. We conclude each section with a discussion of the "typical" uncertainties.

4.2.1 PHOTOMETRY

High-precision photometry in multiple filters covering a long wavelength baseline is tremendously useful for measuring the age, metallicity, extinction, and distance. Stellar evolutionary tracks must be paired with bolometric correction tables to transform the theoretical outputs, e.g., $T_{\rm eff}$ and $\log L$, to observed magnitudes. Under the assumption of perfect observational data, any mismatch between the models and observations can be attributed to one or both of the components: interior models and atmosphere models.

In addition to fitting the CMD morphology, photometry can be used for other observational diagnostics such as number counts of different types of stars. Although taking inventory of stars can be a difficult task due to completeness issues as well as low number statistics in some cases, number ratios are still powerful diagnostics because they are sensitive to relative phase lifetimes. We expect to be able to reliably catalog stars in different parts of the CMD with clean membership identification from future surveys (see Section 4.5 for a more in-depth discussion on the improvements due to *Gaia*). A related observable is the luminosity function, e.g., along the red giant branch (RGB), which has been widely adopted in studies of globular clusters (e.g., Renzini & Fusi Pecci 1988).

We also note that multi-band photometry can be used to obtain photometric metallicities (narrow- and medium-band imaging; see e.g., Ross et al. 2014) and temperatures. Temperatures derived from color-temperature relations (e.g., Alonso et al. 1996; Ramírez & Meléndez 2005; González Hernández & Bonifacio 2009; Casagrande et al. 2010) are widely used because they are considered to be reliable and easily measurable en masse. Finally, we note that direct measurements of the stellar angular diameter (and physical diameters if the parallax distance is known) for a sample of nearby stars are available through interfer-

ometry (e.g., Boyajian et al. 2012a,b). In particular, when combined with bolometric flux and multi-band photometry, they provide direct constraints on the empirical color-temperature relations with a few % accuracy (Boyajian et al. 2013).

Ground-based photometry, which is generally limited by seeing due to the Earth's atmosphere, produces typical uncertainties of order ≈ 0.01 mag, while *HST* photometry can routinely yield $\approx$ mmag photometry. One source of uncertainty that impacts both ground- and space-based observations is the photometric zero-point, which is necessary to convert a flux to a magnitude on some standard scale. Although high-quality photometry can produce high relative photometric precision, absolute photometric precision is tied to ≈ 1 % absolute flux uncertainty for flux standards such as Vega (see Bohlin 2014 and also the discussion in Carrasco et al. 2016).

4.2.2 Spectroscopy

4.2.2.1 Basic Stellar Parameters

There are several recent, ongoing, and planned large-scale surveys designed to obtain medium-resolution ($R \simeq 10,000$–$25,000$) spectra of stars in different parts of the Milky Way (e.g., *RAVE*, Steinmetz et al. 2006; *Gaia-ESO*, Gilmore et al. 2012; *APOGEE*, Holtzman et al. 2015; *GALAH*, De Silva et al. 2015; *WEAVE*, Dalton et al. 2012; *Gaia-RVS*, Recio-Blanco et al. 2016; *4MOST*, de Jong et al. 2016). Their principle scientific objective is to shed light on the formation and evolution history of our Galaxy. These spectroscopic surveys yield, at minimum, radial velocity, $\log g$, $T_{\rm eff}$, and metallicity, and in many cases the surface abundances of multiple elements for each star. From the stellar evolution and stellar astrophysics perspective, accurate and precise measurements of these parameters are extremely useful for testing the integrity of the stellar evolution models. With the exception of asteroseismology, surface abundances are some of the only probes of the stellar structure and interior conditions. Since the creation and destruction of different species deep within the star can be imprinted on the surface through various mix-

ing processes, the surface abundances of different elements carry immense diagnostic power. Finally, a Hertzsprung-Russell (HR) diagram constructed from $\log g$ and $T_{\rm eff}$, also known as the "Kiel diagram," is a useful, distance-independent diagnostic that can be compared directly with theoretical isochrones.

There is immense diversity in the analysis techniques and pipelines that are employed to measure stellar parameters for large spectroscopic samples (e.g., Smiljanic et al. 2014; Holtzman et al. 2015)—adopted line lists, optimization for the analysis of different stellar types, equivalent width versus full spectral fitting—and they produce systematically discrepant results. There is ongoing effort to mitigate some of these concerns by carrying out detailed comparisons between different state-of-the-art methods (e.g., *Gaia-ESO* benchmark stars; Smiljanic et al. 2014). There is typically a range of values for the quoted uncertainties (combined systematic and statistical), depending on the adopted methodology and the stellar spectral types; $\log g$, $T_{\rm eff}$ and [Fe/H] uncertainties are generally 0.1–0.2 dex, 50–100 K, and 0.05–0.1 dex,* respectively (e.g., Smiljanic et al. 2014; Holtzman et al. 2015).

4.2.2.2 Carbon and Nitrogen Surface Abundances on the RGB

The surface stellar abundances generally do not reflect the initial or even the bulk interior abundances at any given time. Over the lifetime of a star, physical processes such as diffusion and dredge-up can dramatically modify the surface abundances. The magnitude of these effects vary with the mass and metallicity of the star and the elemental species in question. For this reason, the evolution of surface abundances can be used to trace stellar mass, and thus, stellar ages.

For this work, we focus on the surface abundances of RGB stars because they constitute a significant fraction of the sample in these spectroscopic surveys that require bright beacons in distant parts of the Galaxy (see Dotter et al. 2017 for a discussion of surface versus bulk abundances and their implications on derived stellar ages). One of the parameters that are crucial to galactic archaeology is the stellar age.

*Systematic uncertainties are higher (0.1–0.2) for the other elements.

The classic method of inferring stellar ages using the spectroscopic $\log g$–$T_{\rm eff}$ diagram is notoriously challenging due to small $T_{\rm eff}$ separations between the nearly-vertical RGB tracks of stars with different initial masses. As a result, small uncertainties in $T_{\rm eff}$ yield large uncertainties in the initial mass, and therefore in age.

Recently, an alternative method using the ratio of carbon to nitrogen as an age indicator has gained traction (e.g., Masseron & Gilmore 2015; Salaris & Cassisi 2015; Martig et al. 2016; Ness et al. 2016). When the star leaves the MS, its deepening convective envelope introduces several changes to the surface elemental abundances during what is known as the first dredge-up (FDU). Whereas some species such as iron that were depleted during the MS due to gravitational settling are nearly restored to their initial values, other species such as nitrogen and carbon show a marked change relative to their initial abundances. The latter phenomenon occurs because the convective envelope engulfs the products of hydrogen burning in the deep interior, diluting its original bulk abundances with the CN-processed material. FDU yields an increase in surface ^{14}N and a concordant decrease in surface ^{12}C as dictated by the CNO cycle equilibrium; the $^{14}{\rm N}({\rm p},\gamma)^{15}{\rm O}$ reaction is the bottleneck in the CNO cycle, resulting in the accumulation of nitrogen. Since the maximum fractional depth reached by the convective envelope increases with the initial mass, a larger decrease in the surface [C/N] abundance corresponds to a larger stellar mass, and therefore a younger age (Salaris & Cassisi 2015). This FDU efficiency has also been demonstrated to increase with increasing metallicity (Charbonnel 1994). A caveat of this age inference method is that the initial abundances must be known (e.g., see the discussion in Martig et al. 2016) by disentangling the effects of stellar evolution and galactic chemical evolution. A significant advantage of studying stars in clusters is that we can obtain the abundances for a sample of MS or subgiant branch (SGB) stars in addition to the RGB stars to get a handle on their initial C and N abundances.

The end of the FDU is marked by the convective envelope receding back towards the surface ahead of the hydrogen-burning shell, which is also moving outward. Although canonical models do not show ad-

ditional mixing beyond the FDU, there is solid observational evidence that extra mixing occurs beyond the RGB bump through the tip of the RGB, and possibly during the core helium burning (CHeB) phase (Gratton et al. 2000; Angelou et al. 2015). Several explanations have been put forth, including thermohaline (Charbonnel & Zahn 2007; Charbonnel & Lagarde 2010) and rotational mixing (Sweigart & Mengel 1979; Palacios et al. 2006), though we focus on the former here.

Thermohaline mixing is a double-diffusive instability that occurs in the presence of a destabilizing composition gradient. Although positive mean molecular weight (μ) gradients are rare in the stellar interior (nuclear fusion occurs inside out and it transforms light elements into heavy elements), they do appear in some cases, for example during the ^{3}He(^{3}He, 2p)^{4}He reaction taking place in the external wing of the hydrogen-burning shell (Ulrich 1972; Eggleton et al. 2006). Note that this unusual reaction produces a net increase in the number of particles and thus a decrease in μ. Thermohaline mixing is established only beyond the RGB bump, a brief adjustment period the star undergoes when the hydrogen-burning shell encounters the μ-discontinuity at the base of the chemically homogeneous zone, i.e., maximum depth previously reached by the convective envelope. This instability cannot be triggered at earlier times because the magnitude of the μ gradient inversion is negligible in the presence of the stabilizing composition gradient. Once thermohaline mixing is established in the radiative layer between the hydrogen burning shell and the convective envelope, surface abundances of numerous species, including ^{3}He, ^{12}C, ^{13}C, and ^{14}N, can become modified.

4.2.3 Asteroseismology

Asteroseimology relies on the high-precision monitoring of brightness fluctuations in the light curves originating from stellar oscillations. To date, the *CoRoT* (Baglin et al. 2006) and *Kepler* (Gilliland et al. 2010) missions have detected solar-like acoustic oscillations in well over $\approx 15,000$ red giants (Kallinger et al. 2010b; Stello et al. 2013; Huber et al. 2014). The ongoing repurposed *K2* mission, the upcoming

TESS mission, and next generation surveys such as *WFIRST*, *Euclid*, and *Plato* are expected to increase the sample size dramatically.

The detection of oscillations requires taking the Fourier transforms of the time-series photometry. There are two main techniques for the subsequent analysis and physical interpretation of the data. The first method is called "peakbagging," or "boutique-modeling," which involves the detailed modeling of individual peaks in the frequency spectrum. This is a challenging and time-consuming problem due to the sheer number of detected modes as well as the presence of mixed dipole modes (Corsaro et al. 2015; Handberg et al. 2017).

The second method, which is more widespread given its simplicity, involves reducing the information in the frequency spectrum to two global parameters: the frequency of maximum power, $\nu_{\rm max}$, and the average large frequency separation, $\Delta\nu$. These parameters can be related to stellar parameters via simple scaling relations:

$$\Delta\nu \simeq \sqrt{\frac{M/M_\odot}{(R/R_\odot)^3}}\Delta\nu_\odot \tag{4.1}$$

$$\nu_{\rm max} \simeq \frac{M/M_\odot}{(R/R_\odot)^2\sqrt{T_{\rm eff}/T_{\rm eff,\odot}}}\nu_{\rm max,\odot}\,, \tag{4.2}$$

where $\Delta\nu_\odot = 135.1\ \mu$Hz, $\nu_{\rm max,\odot} = 3100\ \mu$Hz, and $T_{\rm eff,\odot} = 5777$ K correspond to the solar values. As can be gleaned from the equations above, $\Delta\nu$ and $\nu_{\rm max}$ are each sensitive to the average density and surface gravity of the star, respectively. Once they are measured from the observed frequency spectrum, $\Delta\nu$ and $\nu_{\rm max}$ can be combined with an external estimate of $T_{\rm eff}$—either from spectroscopy or a color-$T_{\rm eff}$ relation—to yield masses and radii. Alternative forms of the scaling relations exist for when independent estimates of e.g., bolometric luminosity, are available. These scaling relations are used to derive masses and radii of RGB stars in the field en masse (Stello et al. 2008; Kallinger et al. 2010a; Miglio et al. 2012). Though

extremely useful, these simple scaling relations have been demonstrated to harbor systematics and thus various corrections have been proposed to improve their accuracy (e.g., White et al. 2011; Miglio et al. 2012; Sharma et al. 2016; Viani et al. 2017). There is an ongoing effort to test and validate the accuracy of scaling relations using other independent techniques such as eclipsing binaries (e.g, Gaulme et al. 2016). The general consensus is that the scaling relations provide RGB and RC mass and radius estimates to within $\sim 10\%$ and $\sim 5\%$, respectively (see Viani et al. 2017 and references therein). Estimates of the $\log g$ from the scaling relation are better determined; systematic uncertainties and biases are estimated to be around 0.01 dex (Hekker et al. 2013; Viani et al. 2017).*

4.2.4 Detached Eclipsing Binaries

Eclipsing binary systems yield stellar masses and radii with exquisite precision, routinely below $\sim 3\%$ (Torres et al. 2010). In particular, systems that are well-detached such that both members are effectively undergoing single-star evolution—also known as detached eclipsing binaries (DEBs)—provide a unique opportunity for rigorous tests of stellar evolution models; the masses, radii, and/or luminosities of both binary components must agree within the observational uncertainties at a single age (Andersen 1991). Moreover, DEBs can be used to measure stellar ages without the knowledge of distance and interstellar reddening if they are near the MSTO. DEBs in star clusters are especially useful because they can be combined with CMDs to provide complementary constraints on the models (e.g., Stetson et al. 2003; Brogaard et al. 2012; Yakut et al. 2015; Brewer et al. 2016; Gökay et al. 2013).

Ground-based discoveries and analyses of DEBs trace back well over a century (Russell 1912) and have yielded parameters of many stellar systems (e.g., Popper 1967; Harmanec 1988; Andersen 1991; Torres et al. 2010). The unprecedented, precise monitoring by *Kepler* has observed close to 2000 eclipsing

*Currently there are interesting, unresolved discrepancies between spectroscopic and asteroseismic $\log g$ for red giants with the SDSS APOGEE spectroscopy and *Kepler* asteroseismology (http://www.sdss.org/dr14/irspec/aspcap/#calibration). Not only does there appear to a mild metallicity dependence to this discrepancy, but the size of the offset appears to be different for CHeB and red giant branch stars for reasons that are not well-understood. See also Ting et al. (2018).

binaries, approximately 1400 of which are classified as DEBs (Kirk et al. 2016). Ongoing and future missions such as *Gaia*, *TESS* and *PLATO* are expected to find many more eclipsing binaries.

Accurate and precise masses and orbital parameters require high-quality radial velocities measured from double-lined spectra with high spectral resolution and signal-to-ratio. In a single-lined system, where only the primary component is detected, a full orbital solution generally cannot be obtained. In these systems, the total mass must be combined with the mass ratio inferred from the light curves to obtain estimates of individual masses. Perhaps unsurprisingly, masses obtained using this method are generally less reliable due to correlations and degeneracies among the orbital parameters and their resulting solutions (Kirk et al. 2016). Light curves provide stellar radii and orbital parameters, which can be compared with the spectroscopic determinations as a consistency check. As noted earlier, DEBs generally provide masses and radii measurements to within $\sim 3\%$ (Torres et al. 2010), and even $< 1\%$ in some cases (e.g., Brewer et al. 2016).

4.3 Models: Where is the Information Content?

In this section, we first provide an overview of the MESA Isochrones and Stellar Tracks (MIST) models. Then we present a summary of the effects of various uncertainties on the observable quantities. Next, we evaluate the sensitivity of the observables to each key parameter in order to identify the ideal set of observations with the goal of measuring the cluster parameters (e.g., age) and constraining the uncertain free parameters (e.g., $\alpha_{\rm MLT}$). We will revisit the latter within a more quantitative and rigorous framework in subsequent work.

4.3.1 MESA Isochrones and Stellar Tracks (MIST) Models

The theoretical isochrones for this work are computed within the MIST framework (Dotter 2016; Choi et al. 2016). The main objective of the MIST project* is to build comprehensive grids of well-calibrated stellar evolutionary tracks and isochrones that encompass a wide range of masses, ages, metallicities, and evolutionary phases. The first set of models with solar-scaled abundances both including and excluding the effects of stellar rotation are already available (Choi et al. 2016). The second set of models consisting of non-solar-scaled abundances are currently under development (Dotter et al., in prep.). Stellar evolutionary tracks are computed using Modules for Experiments in Stellar Astrophysics (MESA) (Paxton et al. 2011, 2013, 2015, 2018), an open-source 1D stellar evolution package. Isochrones are constructed from grids of stellar evolutionary tracks following Dotter 2016. For an in-depth overview of the MIST models, including the descriptions of the input physics, we refer the reader to Section 3 and Table 1 of Choi et al. (2016).

4.3.2 Overview: Model Parameters and Observations

In the following sections, we show a series of multi-panel plots (Figures 4.1 through 4.6) illustrating the effect of an individual parameter on the various observables at a given stellar age. Here we describe each panel and the relevant observations in detail.

In each panel, we show a total of nine MIST isochrones projected onto several observed planes. The peach, pink, and purple colors correspond to different parameters (for example, metallicities) and the solid, dot-dashed, and dotted lines correspond to three ages (2, 4, and 10 Gyr). The parameter of interest always increases from peach to purple, and the pink curve corresponds to the fiducial model, unless noted otherwise.

The top row features three CMDs—$B-V$, $V-I$, and $J-Ks$—zoomed in near the main sequence turn off (MSTO), SGB, RGB, and RC. As in the standard MIST models, we use the C3K bolometric correction

*http://waps.cfa.harvard.edu/MIST/

tables (Conroy et al., in prep.) constructed from the ATLAS12/SYNTHE atmosphere models. The ATLAS12/SYNTHE models include the latest atomic line list from R. Kurucz (including both laboratory and predicted lines) and many molecules whose contributions are important especially at longer wavelengths. There are no extinction and distance modulus applied to these CMDs.

In the first panel of the middle row, we show the theoretical mass-radius relations, which can be compared to high-precision measurements from DEBs. The second panel shows a slight variation on the classic HR diagram with $\log g$ instead of $\log L$ on the y-axis (Kiel diagram), zoomed in on the RGB and the RC where most of the asteroseismic targets are located. For these evolutionary phases, the predicted $\log g$ can be compared with the asteroseismic surface gravity, $\log g_{\rm astero}$, inferred from the $\nu_{\rm max}$ asteroseismic scaling relation (Equation 1). Note that the $\nu_{\rm max}$ measurement must be combined with a spectroscopic or photometric $T_{\rm eff}$ to infer $\log g$. For display purposes, we omit the transition from the core helium flash (the tip of the RGB) to the RC and mark the start of quiescent core helium burning using an open circle.

The next row shows surface abundance ratios of carbon to nitrogen (left) and ^{12}C to ^{13}C (right) along the RGB and RC (shown as an open circle for clarity) as a function of surface gravity. Surface abundances are powerful indirect probes of the stellar interior because various mixing processes lead to changes in the surface abundances of different species at different stages of the evolution.

Finally, the bottom row features two panels that each shows an integrated or averaged quantity as a function of the age of the cluster. The first panel shows the ratio of MSTO to RC stars. In this context, the MSTO stars are defined to be those that fall within 0.5 magnitude below the hottest point of the MS in the V band. For an isochrone with a Henyey hook, instead of the tip of the hook (the actual hottest point), we use the inflection point at which the blueward excursion begins. This is because the actual hook corresponds to a fast phase of expansion and contraction, and thus it is observationally unlikely to find many stars there. The RC stars are selected based on the MIST phase label (CHeB phase). The predicted number ratio of MSTO and RC stars is simply the ratio of the sum of the IMF weights of stars of each type. This

quantity represents the relative phase lifetimes averaged over the IMF. In the right panel, we show the average mass difference between the RGB and the RC stars. Note that this is currently observable stellar mass instead of the initial mass, and that this is a simple average without the IMF weights. We can safely ignore the IMF weights in this case due to the negligible dynamic range in mass. RGB stars are first identified using the phase label in the MIST isochrones, then we apply further selection cuts using the criteria adopted by Miglio et al. (2012); we discard stars that are brighter than the RC magnitude to reduce possible confusion with asymptotic giant branch (AGB) stars, and fainter than 1.5 mag below the RC in the V band to avoid possible blending and low signal-to-noise issues. RC stars are simply selected by their MIST phase label. The resulting prediction can be compared to the "observed" mass difference inferred from asteroseismic masses (e.g., Miglio et al. 2012).

In each panel we also include reddening vectors to illustrate how the positions of the CMDs can be shifted due to dust. We adopt the standard $R_V = A_V/E(B-V) = 3.1$ reddening law from Cardelli et al. (1989) and assume $A_V = 0.4$ evaluated at $[\mathrm{Fe/H}] = 0$, $\log g = 4$, and $T_{\mathrm{eff}} = 5500$. Reddening may appear to be degenerate with metallicity especially at the MSTO, SGB and RGB. But there are subtle differences in the CMD morphology, e.g., the lower MS , especially when multiple CMDs covering a wide wavelength baseline are considered simultaneously (e.g., the "kink" in the lower MS in infrared CMDs; see Pulone et al. 1998; Milone et al. 2014; Correnti et al. 2016). Given exquisite photometry (e.g., *Hubble Space Telescope* or *Gaia*) and sophisticated fitting techniques, we should be able to distinguish the two effects.

4.3.3 Effect of Metallicity

Figure 4.1 shows the effect of varying [Fe/H], more specifically Z/X, the ratio of metal to hydrogen mass fractions. Note that we assume solar-scaled abundances for the models considered here, i.e., initial [C/N] is held constant. The initial helium mass fraction Y is computed assuming a linear enrichment law, a

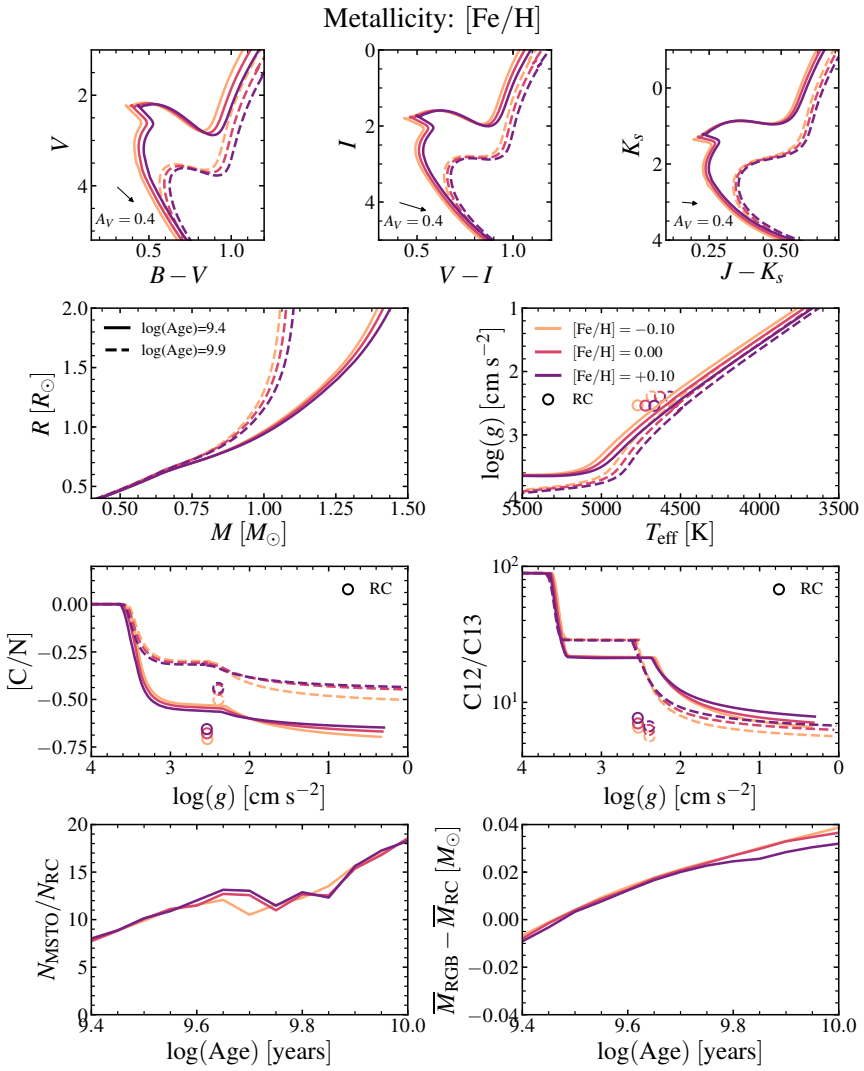


Figure 4.1: The effect of metallicity and age on a variety of observable parameters. There are a total of six MIST models shown, where the peach, pink, and purple colors correspond to different metallicities and the solid and dashed lines correspond to two different ages (2.5 and 8 Gyr). First row: CMDs ranging from optical to near-infrared wavelengths. There are no extinction and distance modulus applied to these CMDs, but we include reddening vectors to illustrate how the positions of the CMDs can shift. We adopt the standard $R_V = A_V/E(B-V) = 3.1$ reddening law from Cardelli et al. (1989) and assume $A_V = 0.4$ evaluated at $[\mathrm{Fe/H}] = 0$, $\log g = 4$, and $T_{\mathrm{eff}} = 5500$ K. Second row: mass-radius and Kiel diagrams, which can be compared with DEB data and asteroseismic $\log g$, respectively. For display purposes, we omit the transition from the core He flash (RGB tip) to the RC and mark the start of quiescent core helium burning using an open circle. Third row: the surface abundance evolution as the star ascends the RGB and undergoes helium flash before settling into a quiescent, helium-burning RC phase. The first large decrease at $\log g \sim 3.5$ marks the onset of first dredge-up, and the second large decrease at $2.5 \gtrsim \log g \gtrsim 2.0$ after the RGB bump is due to thermohaline mixing. Fourth row: the number ratio of MSTO to RC stars and the difference in the average mass of the RGB and RC stars, both shown as a function of the cluster age. MSTO stars are defined to be those that fall within 0.5 magnitude below the hottest point of the MS in the V-band. Asteroseismology can be used to both distinguish RC from RGBs and provide average masses for both types of stars. The first two rows clearly demonstrate that higher metallicity corresponds to cooler T_{eff} (redder colors) and longer MS lifetimes. The third row shows that FDU and thermohaline operate more and less efficiently, respectively, as the metallicity is increased. Finally, the last row shows that metallicity does not appear to have a strong effect on the relative numbers of MSTO to RC stars and the difference in the average mass of RGB and RC stars.

common approach also adopted in MIST.* As expected, the CMDs show that increasing metallicity leads to redder colors. The mass-radius panel clearly shows that there is little separation in radius until the stars evolve away from the MS, which suggests that the sensitivity of the models to variations in the age and metallicity is concentrated in the post-MS stars. At a fixed initial mass, metal-rich stars are cooler and have longer MS lifetimes—the Kiel diagram show a clear sequence in temperature with metallicity.

Both of the surface abundances panels show a large dip between the first two plateaus ($\log g \sim 3.5$ to $\log g \sim 3$), corresponding to the FDU (see Section 4.2.2.2) and the subsequent decrease is due to thermohaline mixing that is established beyond the RGB bump. Interestingly, the net change in [C/N] and $^{12}C/^{13}C$ during the two stages of mixing (FDU and thermohaline) show opposite trends with metallicity: FDU and thermohaline mixing appear to operate more efficiently in high and low metallicity systems, respectively. FDU is more efficient at higher metallicities and higher stellar masses because the convective envelope reaches deeper into the CN-processed region and is thus able to dredge up more material to the surface (e.g., Charbonnel 1994; Salaris & Cassisi 2015; Lagarde et al. 2017). Thermohaline is more efficient at lower metallicities and lower stellar masses (e.g., Charbonnel & Zahn 2007; Eggleton et al. 2008; Charbonnel & Lagarde 2010; Lagarde et al. 2017) due to the compactness of the thermohaline-mixing region and the resulting steeper temperature gradient.

The bottom panels show relatively large variation with stellar age but little variation with metallicity, suggesting that these integrated quantities are more sensitive diagnostics of the stellar age than the metallicity. The number ratio is sensitive to the age because the MS lifetime increases dramatically with decreasing initial mass but the CHeB lifetime is roughly constant for stars $\lesssim 2\ M_\odot$. The CHeB lifetime is relatively insensitive to the initial mass for these stars because they have roughly equal-sized degenerate helium cores that ignite once a critical temperature (corresponding to a critical mass of $\sim 0.45\ M_\odot$) is

*The helium abundance is tied to the metallicity assuming a linear relationship, i.e., $Y = Y_\mathrm{p} + \left(\frac{Y_{\odot,\,\mathrm{protosolar}} - Y_\mathrm{p}}{Z_{\odot,\,\mathrm{protosolar}}}\right) Z$, where Y_p is the primordial, Big Bang nucleosynthesis value. The enrichment slope in MIST is $\frac{\Delta Y}{\Delta Z} = \frac{Y_{\odot,\,\mathrm{protosolar}} - Y_\mathrm{p}}{Z_{\odot,\,\mathrm{protosolar}}} = 1.5$.

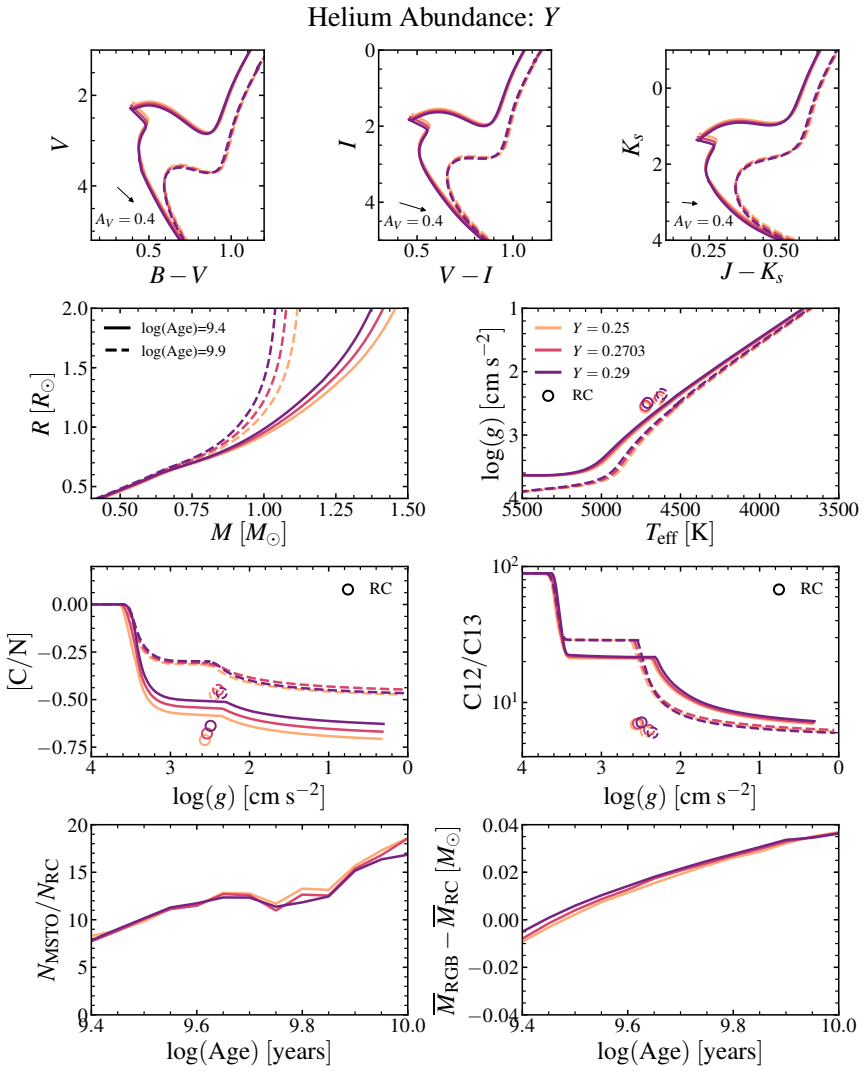


Figure 4.2: Same as Figure 4.1 except now varying the helium abundance at a fixed metal mass fraction Z. The fiducial value of $Y = 0.2703$ comes from the protosolar helium abundance in Asplund et al. (2009). At a fixed stellar age, higher helium content leads to hotter stars and shorter MS lifetimes.

reached.

4.3.4 Effect of Helium

Figure 4.2 shows the effects of varying the initial bulk helium mass fraction, Y, on the various observables. We hold Z fixed at the protosolar value $Z_{\odot,\,\mathrm{protosolar}} = 0.0142$ and vary Y and the hydrogen abundance X. Helium abundance cannot be inferred spectroscopically because there are no photospheric helium lines due to their high excitation potential (Asplund et al. 2009 but see Dupree & Avrett 2013). However,

helioseismology provides an indirect probe of the helium abundance in the Sun, relying on the fact that the adiabatic index changes in the He II ionization zone. This technique has yielded a highly precise estimate of the solar helium abundance (0.2485 ± 0.0034; Basu & Antia 2004), which is at an apparent tension with the helium abundance required to reproduce the correct solar luminosity and temperature at the solar age for an interior model (Asplund et al. 2009).

The CMDs in the first row demonstrate a systematic trend with Y as they did with metallicity in Figure 4.1. The mass-radius relation and the $\log g$–$T_{\rm eff}$ panels also show a sequence in Y; at a fixed age, higher helium content leads to hotter stars and lower MSTO masses. The hotter temperature is due to helium's low opacity and the decreased MSTO mass (equivalent to a shorter lifetime) is due to the reduced hydrogen abundance. It is interesting to note that these optical/near-infrared CMDs do not show a clearly separated sequence in Y*; the effect of helium variation moves "along" the isochrone, such that the effect on the CMD is not drastic. On the other hand, the change in the surface abundances, in particular [C/N], during the FDU is less pronounced at high Y. This is because a smaller fraction of the star becomes engulfed, or dredged up, as the stellar mass is decreased. Interestingly, the efficiency of thermohaline mixing appears to be largely unaffected by initial Y. Finally, the number ratio of MSTO to RC stars does not show a clear sequence in Y, and the mass difference between RGB and *RC* shows marginal separation in Y. However, the difference is much smaller than the current observational uncertainties ($\sim 0.01\ M_{\odot}$) and is unlikely to be detectable in the near future.

4.3.5 Effect of Mixing Length Parameter

In Figure 4.3, we show the effects of varying the mixing length parameter $\alpha_{\rm MLT}$, a free parameter of order unity that is frequently calibrated to match the observations of the Sun (in MIST, $\alpha_{\rm MLT} = 1.82$; Choi et al. 2016). The physical interpretation of $\alpha_{\rm MLT}$ is the distance, in units of the pressure scale height, that

*This is more readily seen in the UV; see e.g., Milone et al. 2013

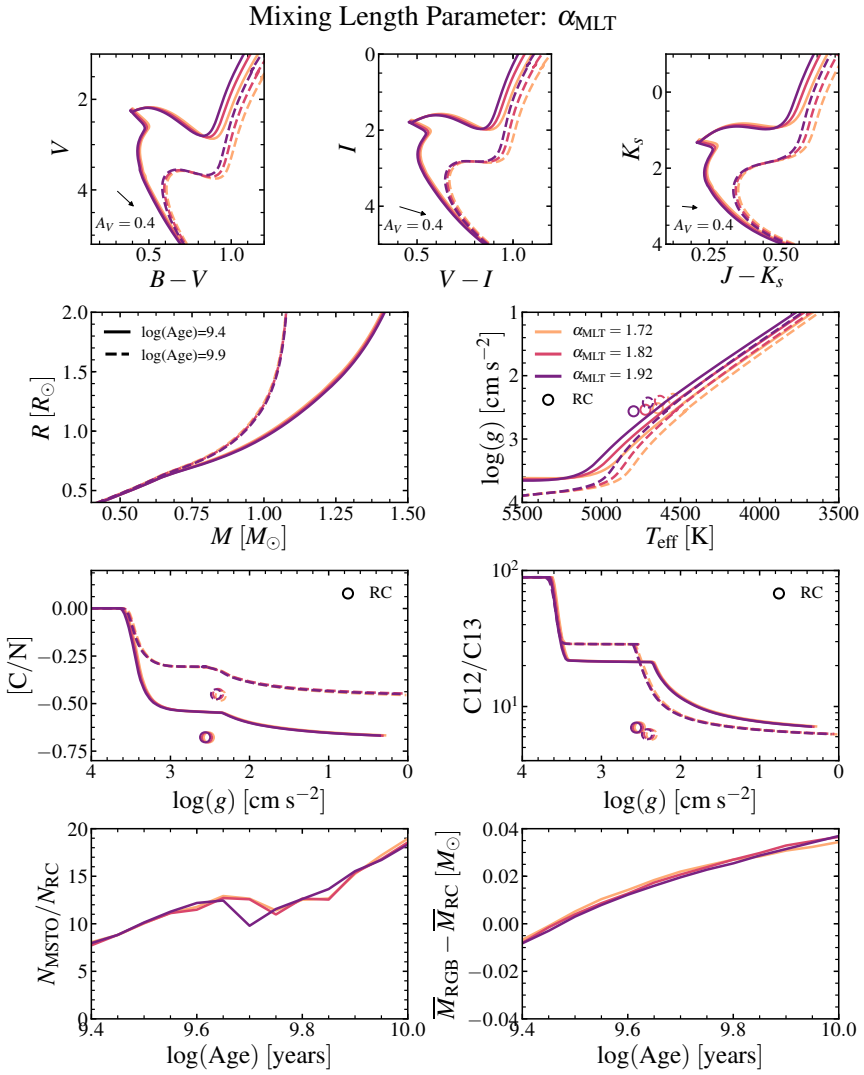


Figure 4.3: Same as Figure 4.1 except now varying the mixing length $\alpha_{\rm MLT}$, which parameterizes the efficiency of convective mixing. The fiducial value of $\alpha_{\rm MLT} = 1.82$ was chosen by calibrating to the observations of the Sun (see Section 4.1 in Choi et al. 2016 for more details). The choice of $\alpha_{\rm MLT}$ has the largest effect on the temperature and therefore the color of the RGB.

a fluid parcel travels before depositing its energy and disintegrating into the background. Thus it parameterizes the efficiency of convective mixing and affects the stellar structure: a small $\alpha_{\rm MLT}$ is associated with cooler $T_{\rm eff}$ and inflated radius. This is clearly illustrated in the CMDs, mass-radius relation, and the Kiel diagram, particularly for the RGB stars which have large convective envelopes. Interestingly, the separation between the models with different values of $\alpha_{\rm MLT}$ is larger in the colors than in $T_{\rm eff}$, especially on the upper RGB. Given the typical observational uncertainties of $\sim$ 50–100 K in $T_{\rm eff}$ (e.g., Holtzman et al. 2015) and

tens of mmag in color* this suggests that CMDs may be preferable to HR diagrams for constraining $\alpha_{\rm MLT}$. However, the CMD approach requires a reddening correction, though a joint fitting of multiple CMDs may help alleviate the issues with degeneracies. Finally, $\alpha_{\rm MLT}$ appears to have a negligible effect on the RGB surface abundances, the number ratio of MSTO to RC stars, and the average mass difference between the RGB and RC phases.

4.3.6 Effect of Convective Overshoot Mixing

The MLT framework on its own offers an incomplete description of convection and requires a separate prescription for extra mixing that occurs at the convective boundaries. This process, also known as convective overshoot, is meant to capture the nonzero momentum of the fluid parcel approaching the boundary of the convection zone and its subsequent penetration into the radiative region (Unno 1957; Böhm 1963; Shaviv & Salpeter 1973). Overshoot implies enhanced mixing and thus has several observable consequences, including the properties of AGB and post-AGB stars (e.g., Herwig 2000; Herwig et al. 2011), the MS width (Schaller et al. 1992), and the MSTO morphology in open clusters (e.g., Magic et al. 2010).

We adopt the "exponential diffusive overshoot" framework introduced by Freytag et al. (1996) and implemented in MESA following Herwig (2000). This prescription is meant to capture both the exponential decay of the convective velocity field and the dissolution of the fluid parcel as a diffusive process. There are two sets of free parameters available for every convective boundary in MESA: $f_{\rm ov}$ and $f_{0,\rm ov}$. The first parameter, $f_{\rm ov}$, determines the efficiency of overshoot mixing and describes the velocity scale height in terms of the local pressure scale height. The second parameter, $f_{0,\rm ov}$, determines the location inside the convection zone at which the diffusion coefficient is calculated. For simplicity, we fix the latter to $f_{0,\rm ov} = 0.008$ (half of the fiducial value for $f_{\rm ov}$) as we vary $f_{\rm ov}$ to investigate the role of the efficiency of

**Hubble Space Telescope*, which nominally represents the best-case scenario today, routinely achieves $\lesssim 1$ mmag photometry.

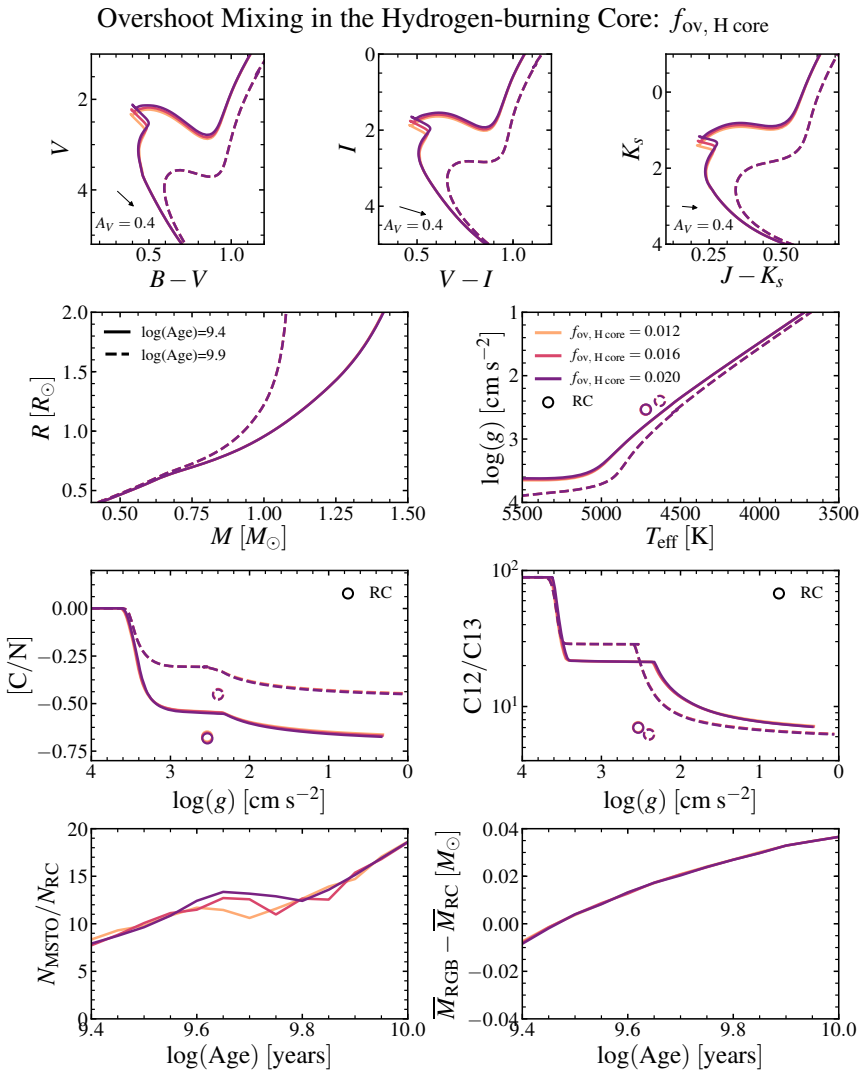


Figure 4.4: Same as Figure 4.1 except now varying the efficiency of convective overshoot mixing in the hydrogen-burning core, $f_{\rm ov,\,H\,core}$. The fiducial value of $f_{\rm ov,\,H\,core} = 0.016$ was chosen to reproduce the MSTO morphology of the open cluster M67. Independent constraints from DEBs (Claret & Torres 2016) also lend support for this calibrated value. The choice of $f_{\rm ov,\,H\,core}$ most noticeably affects the MSTO morphology and the luminosity of the SGB because the enhanced mixing during the MS leads to longer MS lifetimes (thus a larger MSTO mass at a fixed age) and a larger core. However, note that this has no effect on an old population because the MSTO stars are low in mass and thus harbor radiative cores.

overshoot mixing.

Figure 4.4 shows the effect of varying $f_{\rm ov}$ in the hydrogen-burning core. Increasing the efficiency of overshoot mixing in the hydrogen core leads to a more prominent MSTO morphology and a brighter SGB due to an enhanced MS lifetime and a larger core. Note that this parameter has no effect on old populations because their MSTO stars are sufficiently low in mass such that they do not harbor convective cores during

the MS.

We also tested the effect of varying f_{ov} in the helium-burning core. Somewhat surprisingly, changing this parameter seems to have little to no effect on any of the observables, therefore the corresponding figure is not shown. Montalbán et al. (2013) computed a series of stellar models and adiabatic frequencies and found a correlation between the average value of the asymptotic period spacing (ΔP) and the size of the helium-burning core. In a more recent work, Arentoft et al. (2017) analyzed a sample of red giants in the open cluster NGC6811 and found that overshoot mixing in the helium-burning core does not appear to have a noticeable effect on the resulting $\Delta\nu$ and ν_{max} as long as overshoot mixing is included during the MS. However, the authors also found that $\Delta\nu$ and ΔP together has the potential to constrain the efficiency of overshoot mixing in the helium core and shed light on the still-debated presence of breathing pulses (Castellani et al. 1985). Asteroseismic modeling that probes the detailed interior stellar structure may be required to constrain the efficiency of overshoot in the helium-burning core.

4.3.7 Effect of Thermohaline Mixing

In Figure 4.5, we show the effects of varying α_{th}, the efficiency of thermohaline mixing. As described in Section 4.2.2.2, thermohaline is a type of mixing that occurs in a thermally stable medium that has a destabilizing composition gradient. Standard models do not predict any further changes to the surface abundances along the RGB at the conclusion of the FDU, but abundance evolution beyond the RGB bump is indeed observed (e.g., Gratton et al. 2000). Thermohaline mixing is a viable mechanism for explaining this phenomenon (but see also e.g., Denissenkov 2010; Traxler et al. 2011; Wachlin et al. 2014), wherein an unstable composition gradient is established by the ^{3}He reaction taking place in the external wing of the hydrogen burning shell. In the framework of Ulrich (1972) and Kippenhahn et al. (1980), α_{th} has a geometric interpretation—a large value corresponds to a slender fluid element—which is also directly linked to the mixing timescale and thus, the mixing efficiency. The fiducial value of α_{th} in the MIST

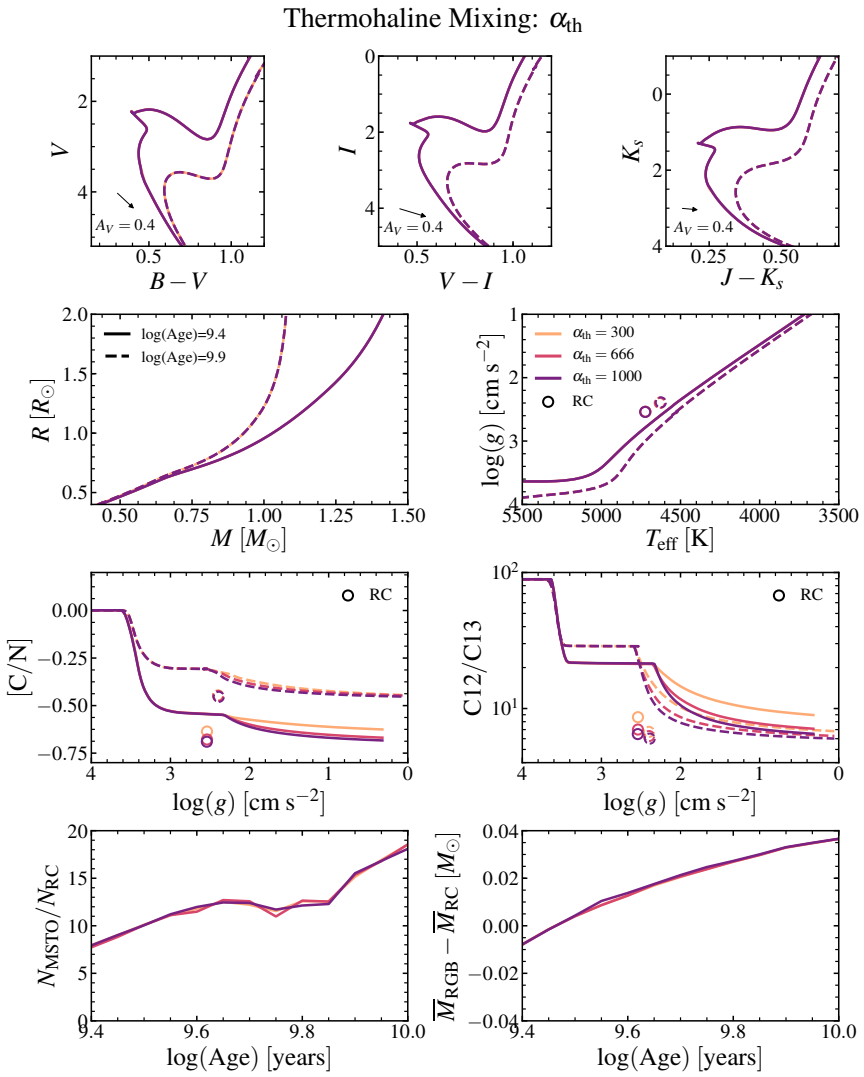


Figure 4.5: Same as Figure 4.1 except now varying the efficiency of thermohaline mixing $\alpha_{\rm th}$. The fiducial value of $\alpha_{\rm th}$ was recommended by Charbonnel & Zahn (2007) to reproduce the observed surface abundances of stars brighter than the RGB bump. The choice of $\alpha_{\rm th}$ has essentially no distinguishable effect on any of the observables except for the surface abundances of RGB stars brighter than the bump.

models was recommended by Charbonnel & Zahn (2007) to reproduce the observed surface abundances of stars brighter than the RGB bump.

Perhaps unsurprisingly, changing the efficiency of thermohaline mixing has almost no observable influence except in the surface abundances beyond the RGB bump (see also Lagarde et al. 2017). Note that this effect saturates beyond some critical value of $\alpha_{\rm th}$ (pink and purple curves), suggesting that there is a maximum efficiency with which thermohaline mixing operates. Given the very minor influence of

thermohaline mixing on the overall evolution, we do not expect noticeable differences among the models in the bottom left panel showing the number ratio of MSTO and RC stars. The small variations are largely due to the presence of very weak breathing pulses occurring at the end of the CHeB phase* and thus the size of these variations nominally represents the minimum theoretical uncertainty on this quantity.

4.3.8 Effect of Mass Loss Efficiency

Figure 4.6 illustrates the effects of varying the wind efficiency, η. In particular, since we are focusing on the evolutionary phases preceding the AGB, the relevant mass loss scheme is the Reimers (1975) prescription, where $\dot{M} \propto LR/M$ with a prefactor η of order unity. For the fiducial MIST models, we adopt $\eta = 0.1$ which is smaller than the value traditionally adopted in stellar models (e.g., Girardi et al. 2000; Pietrinferni et al. 2004; Ekström et al. 2012). This choice was motivated by the results from Miglio et al. (2012) and more recently Handberg et al. (2017), who demonstrated that the asteroseismic masses prefer only a modest amount of mass loss on the RGB. The mass loss rate rises steadily as the star ascends the RGB, eventually reaching values as high as $10^{-8}\ M_{\odot}\ \mathrm{yr}^{-1}$ at the tip of the RGB. Unsurprisingly, variations in the mass loss efficiency parameter have almost no observable effect except in the average mass difference between the RGB and the RC. If there is no mass loss on the RGB, this mass difference is always less than zero because the current stellar mass is exactly equal to the initial mass and MS lifetime decreases with increasing stellar mass. On the other hand, if there is significant mass loss between the RGB and the RC, this quantity will be positive. The mass difference is negative-valued at almost all stellar ages for the model with very little mass loss (peach curve), which suggests that evolutionary timescale is the dominant effect in this case.

*As with most modern stellar evolution codes, breathing pulses are suppressed given their uncertain nature and the potential to strongly affect the CHeB lifetimes. Although the presence of breathing pulses and the particular suppression method can impact the final C and O abundance profiles, these details have little consequence for this work since we only consider the evolution up to the end of the CHeB phase.

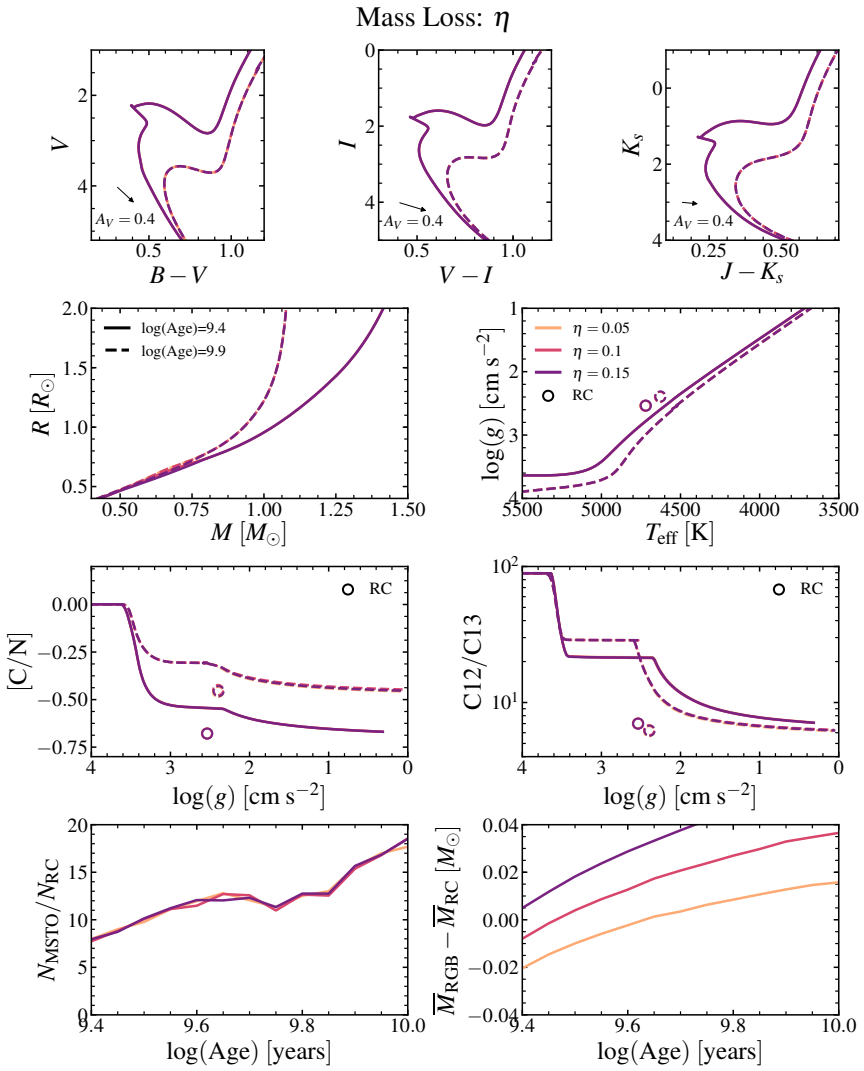


Figure 4.6: Same as Figure 4.1 except now varying the Reimers mass loss parameter η. The fiducial value of $\eta = 0.1$ was recommended by the *Kepler* asteroseismic constraints from open clusters (Miglio et al. 2012; Handberg et al. 2017). It also reproduce the initial-final mass relation (see Section 8.2 in Choi et al. 2016 for more details). The choice of η has almost no discernible effect on any of the observables shown here except for the masses of RGB and RC stars.

4.3.9 Other Parameters to Consider

We have thus far explored the effects of several parameters on the various observables. In addition to these "internal" sources of uncertainties, there are also "external" sources of uncertainties due to difficulties in measuring abundances, distances, and extinction. In general, we can assume metallicity* to

*But not helium!

be a well-determined quantity from spectroscopy, though different methods yield systematically different measurements at the ~ 0.1 dex level (Smiljanic et al. 2014). In the next few years, the *Gaia* mission will effectively eliminate distance and membership uncertainties for open clusters provided that they are sufficiently nearby.* For reference, the three open clusters considered for this work in Section 4.4 are at distances of ~ 800 pc to ~ 4 kpc. Line-of-sight extinction (particularly differential extinction) remains a problem, though the systems considered in this work, i.e., open clusters, are sufficiently nearby and have only a relatively small amount of extinction. In cases where extinction is unavoidable, a joint fitting of CMDs spanning a long wavelength baseline will ameliorate this problem by breaking the metallicity-dust degeneracy.

4.3.10 Separation of Information

The goal of this section is to provide a succinct summary of the information presented in the previous sections. In particular, we focus on identifying the ideal set of observables for disentangling these effects with currently and soon-to-be available data.

For each parameter of interest, we identified a set of observables that most cleanly separate its effect from the age effect, though this was not always possible in every case, e.g., convective overshoot mixing efficiency in the helium core. Each panel of Figure 4.7 illustrates the diagnostic sensitivity of a pair of observables to a parameter of interest and the stellar age. The blue error bar represents a typical observational uncertainty.

4.4 Open Clusters: Case Studies

Now that we have qualitatively explored the effects of key uncertain parameters on several observables, we evaluate the current state of the available data and assess whether they can be used to disentan-

*The expected end-of-mission parallax uncertainty for a solar spectral type is 24μas and 540μas for $V = 15$ and $V = 20$, respectively. See https://www.cosmos.esa.int/web/gaia/science-performance.

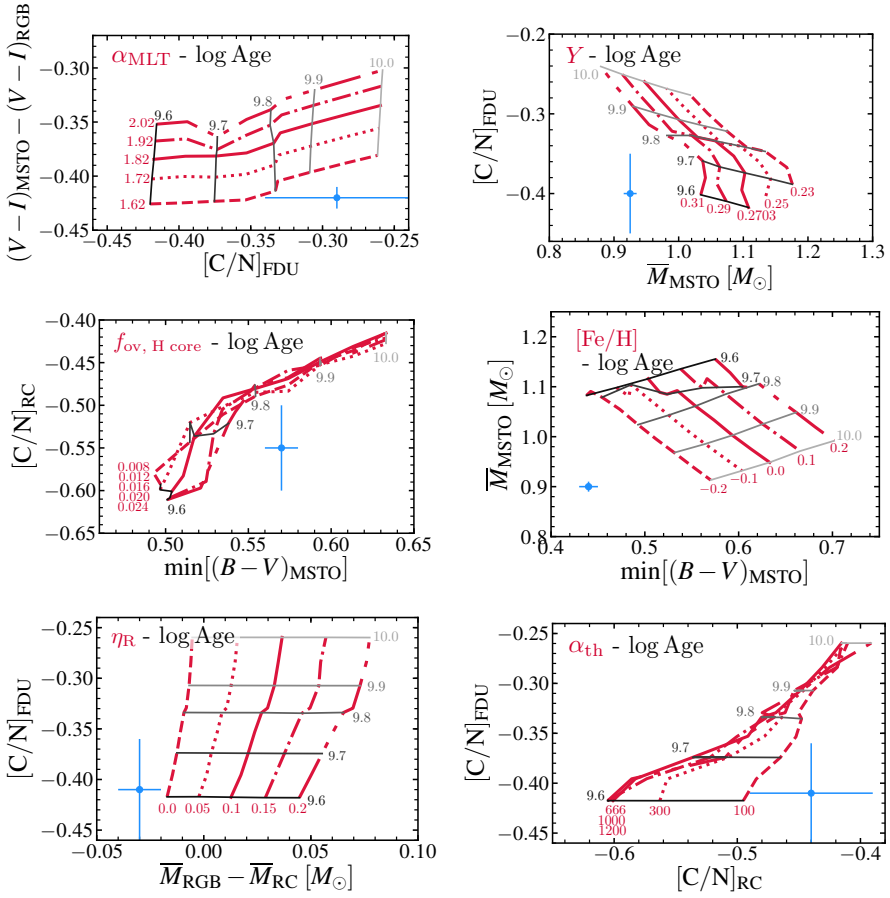


Figure 4.7: Diagnostic sensitivity of a pair of observables to a parameter of interest and the stellar age. For each parameter of interest, we identify a set of observables that most cleanly separate in log(Age) (gray lines) and the parameter in question (red lines), though this was not always possible in every case. Top left: mixing length parameter; $V-I$ color difference between the MSTO and the RGB (measured at $V=1.5$) vs. surface [C/N] abundance of post-FDU stars below the RGB bump. Top right: helium abundance; surface [C/N] abundance of post-FDU stars below the RGB bump vs. average mass of the MSTO stars. For low values of Y, there is no RGB bump at log(Age) = 9.6 [years]. Middle left: convective overshoot mixing efficiency in the hydrogen core; surface [C/N] abundance of RC stars vs. $B-V$ color at the MSTO. Middle right: metallicity; average mass of the MSTO stars vs. $B-V$ color at the MSTO. Bottom left: mass loss; surface [C/N] abundance of post-FDU stars below the RGB bump vs. average mass difference between the RGB and RC stars. Bottom right: thermohaline mixing; surface [C/N] abundance of post-FDU stars below the bump vs. surface [C/N] abundance of RC stars. The blue error bar represents a typical observational uncertainty (see Section 2 for an in-depth overview of different observational data sets).

gle and constrain the parameters under consideration. For this exercise, we investigate three open clusters, NGC6819, M67, and NGC6791. We chose these systems for several reasons. First, all three clusters have been studied extensively and therefore represent the some of the best-case scenarios. All three clusters have been observed by the *Kepler* mission either as part of the original campaign (NGC6819 and NGC6791) or the repurposed *K2* mission (M67). They have all been observed in several photomet-

ric bands, targeted by the APOGEE spectroscopic survey (Holtzman et al. 2015), and they are known to harbor one or more DEBs. Second, we do not have to worry about non-solar-scaled abundances in open clusters (but see Linden et al. 2017 regarding NGC6791) unlike in globular clusters (Bedin et al. 2004; Piotto et al. 2007). However, it is possible to model globular clusters in this context as well (see Dotter et al. 2015 where the authors created tailored stellar interior and atmosphere models for NGC6752 taking into account the individual abundances). Third, these three clusters form a sequence in age and thus allow for model comparison in different stellar mass regimes. We note that NGC6791 is noticeably more metal-rich compared to the other two clusters. The main conclusion of this section is that although there is currently a rich data set for these clusters, they are not sufficiently accurate nor precise to allow for disentangling of the key uncertain parameters.

4.4.1 NGC6819

NGC6819 is a solar-metallicity, intermediate-age (2 Gyr), richly populated open cluster (Yang et al. 2013; Anthony-Twarog et al. 2014; Lee-Brown et al. 2015). As the youngest system in our sample, its MSTO stars are massive enough to have convective cores, giving rise to a distinctive MSTO morphology called the Henyey hook.

Figure 4.8 shows the multi-panel plot summary of NGC6819. The panels are analogous to those presented in Figures 4.1 through 4.6. The photometry comes from several sources: BVI (Ak et al. 2016), VI (Yang et al. 2013) from the WIYN Open Cluster Study (WOCS; Mathieu 2000), and JHK_s (Hole et al. 2009). The black isochrone corresponds to an example "fit" to the data using the MIST isochrone. We started with literature values of reddening, distance, age, metallicity, all of which have non-negligible dispersion, and chose "best-fit" values by eye for purely illustrative purposes. Here, the MIST models assume $\mu = 13.09$, $\log(\mathrm{Age})$ [yr] $= 9.92$, [Fe/H] $= 0.29$, and $A_V = 0.49$.

The mass and radius measurements of the two EB systems, WOCS 24009 (Auner 665; KIC 5023948)

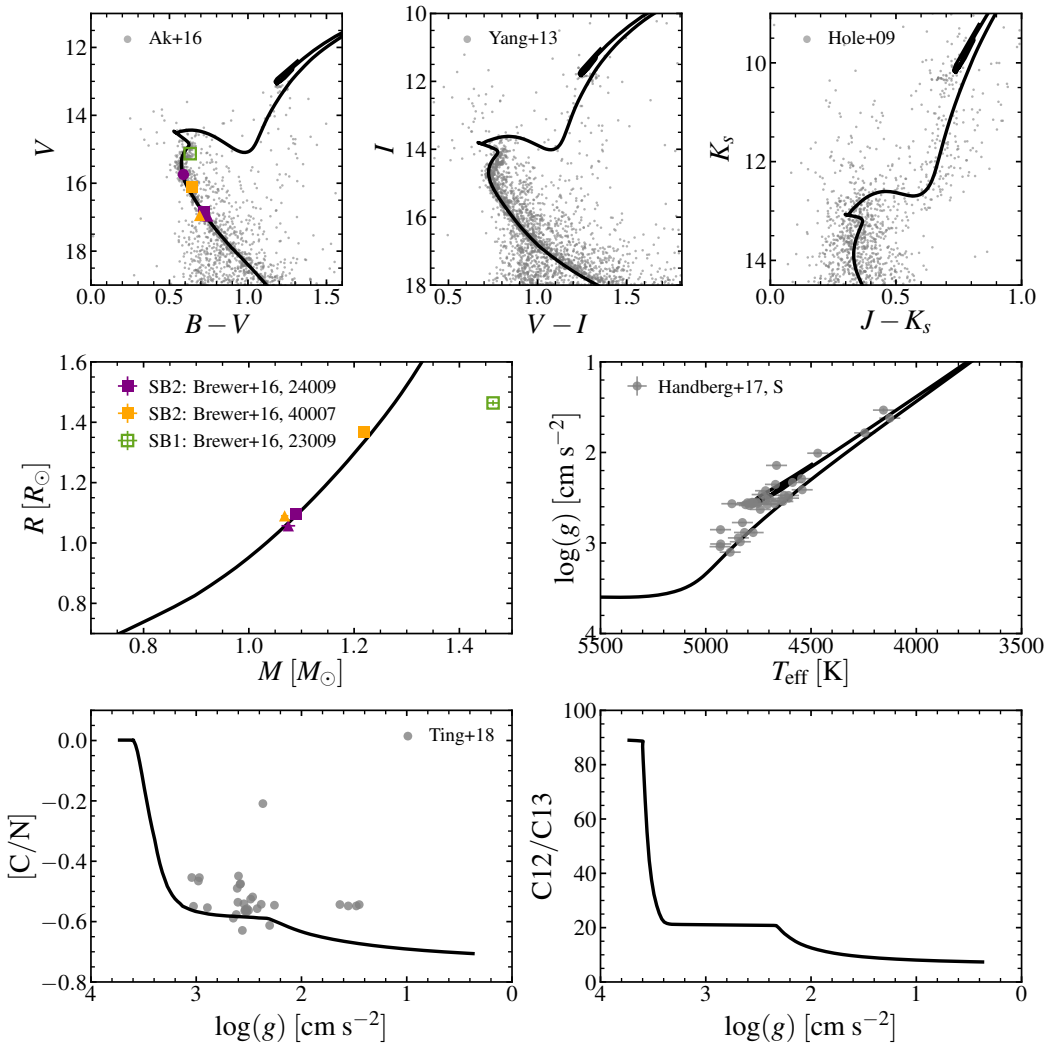


Figure 4.8: NGC6819, a solar-metallicity, intermediate-age (2 Gyr) open cluster. The top three panels show literature photometry from Ak et al. (2016), Yang et al. (2013), and Hole et al. (2009) with the MIST models. The MIST CMDs assume $\mu = 11.8$, log(Age) [yr] $= 9.35$, [Fe/H] $= -0.04$, and $A_V = 0.6$. The left panel in the middle row shows stellar parameters measured from DEB (Brewer et al. 2016) with the MIST mass-radius relation. The open and closed symbols indicate that the system is a single- (SB1) and double-lined (SB2) spectroscopic binary system, respectively. When available, the individual EB components are also shown in the CMDs, where the square, triangle, and circle symbols correspond to the primary, secondary, and tertiary components, respectively. The right panel shows the asteroseismic $\log g$ of single stars inferred from the scaling relations (Handberg et al. 2017) with the effective temperatures from the Casagrande & VandenBerg (2014) color-temperature relations. The bottom left panel shows the comparison between predicted surface [C/N] abundances with the measured abundances, shown as gray circles. The surface abundances are obtained by reanalyzing the publicly-available APOGEE DR14 spectra (Holtzman et al. 2015; SDSS Collaboration et al. 2016) with *the Payne* (Ting et al. 2018). The measurement of $^{12}C/^{13}C$ in the right panel is currently being explored.

and WOCS 40007 (KIC 5113053), are derived from a combination of *Kepler* and ground-based photometry and spectroscopy (Brewer et al. 2016). In fact, each one belongs to its own triple system: WOCS 24009

is a triple-lined system where the brightest, non-eclipsing component is orbiting a short-period binary system and WOCS 40007 is a double-lined system. There is a third EB system WOCS 23009 (Hole et al. 2009; Sandquist et al. 2013), but it is a single-lined EB and thus the inferred parameters are less certain. Nevertheless, we include the parameters of the primary in our comparison, but in open symbols to reflect its lower fidelity. When available, the individual EB components are also shown in the CMDs, where the square, triangle, and circle symbols correspond to the primary, secondary, and tertiary components, respectively.

Moving on to the right panel, we show the asteroseismic $\log g$ and $T_{\rm eff}$ for single stars from Handberg et al. (2017). The authors used a variation of the classic scaling relations that are recast to include bolometric luminosities. The bolometric corrections and color-temperature relations that are required to estimate L and $T_{\rm eff}$ come from Casagrande & VandenBerg (2014). They utilize V (Milliman et al. 2014) and Ks (Cutri et al. 2003) photometry and assume a nominal reddening value of $E(B-V) = 0.15$ and [Fe/H]=0.02$\pm$0.10. We adopt a $T_{\rm eff}$ uncertainty of 50 K following the authors' estimates. Overall, the asteroseismic $\log g$ and $T_{\rm eff}$ are in good agreement with the MIST model predictions, in particular the RC magnitude and the RGB $T_{\rm eff}$.

Finally, the last row shows the comparison between predicted surface [C/N] abundances with measured the observed abundances, shown as gray circles. The surface abundances are obtained by reanalyzing the publicly-available APOGEE DR14 spectra (Holtzman et al. 2015; SDSS Collaboration et al. 2016) with *the Payne* (Ting et al. 2018). Here we only briefly describe *the Payne* since the details of the methodology are presented in Ting et al. (2018). *The Payne* utilizes the idea of generative models; it fits the variations in normalized flux with respect to stellar labels (stellar parameters and elemental abundances) with a flexible functional form approximated with neural networks. The neural networks are trained on the ATLAS12/SYNTHE model spectra (Kurucz 1970; Kurucz & Avrett 1981; Kurucz 1993) and the observed spectra are fit via full-spectral fitting. The formal uncertainties for *the Payne* are very small (< 0.01 dex),

but the true uncertainties are usually dominated by model systematics. The abundance spreads measured in open clusters, which are presumed to be chemically homogeneous, imply a precision of ≈ 0.03 dex (Ting et al. 2018). *The Payne* [C/N] abundances fall slightly above the MIST prediction (≈ 0.1 dex), suggesting a slight preference for an older age and/or lower metallicity (see Figure 4.1). The full-spectral fitting approach in principle allows for the measurement of $^{12}C/^{13}C$, which is currently being explored.

4.4.2 M67

M67 is a nearby solar-metallicity, intermediate-age (4 Gyr) open cluster (Taylor 2007; Sarajedini et al. 2009; Önehag et al. 2014). One of the reasons it is so well studied is that its MSTO mass is very close to the transition mass above and below which stars burn hydrogen convectively and radiatively in their cores. Its Henyey hook is frequently used to calibrate the efficiency of convective overshoot mixing in low mass stars (e.g., VandenBerg et al. 2006; Magic et al. 2010; Bressan et al. 2012; Choi et al. 2016).

Figure 4.9 shows the multi-panel plot summary of M67. The MIST models assume $\mu = 9.62$, $\log(\text{Age})\ [\text{yr}] = 9.63$, $[\text{Fe/H}] = -0.03$, and $A_V = 0.15$. The optical and near-infrared photometry comes from Yadav et al. (2008) and Sarajedini et al. (2009), respectively. Only a subset of the stars with membership probability $> 20\%$ is plotted. An additional proper motion selected sample of likely single-star members from Sandquist (2004) is overplotted for comparison.

The left panel in the middle row compares the MIST mass-radius relation with two independent mass and radius determinations of HV Cnc. HV Cnc was initially reported to be a single-lined binary (Mathieu et al. 1990), but detections of a weak secondary and a possible tertiary component were reported in subsequent works (Melo et al. 2001; Sandquist & Shetrone 2003). Sandquist & Shetrone (2003) analyzed VI photometry and radial velocity data and found a third non-binary component in the spectra, though its association with the HV Cnc system is still uncertain. They deconvolved the photometry of the three stars to yield the parameters of the two binary components, shown in yellow. The primary is hotter than the ma-

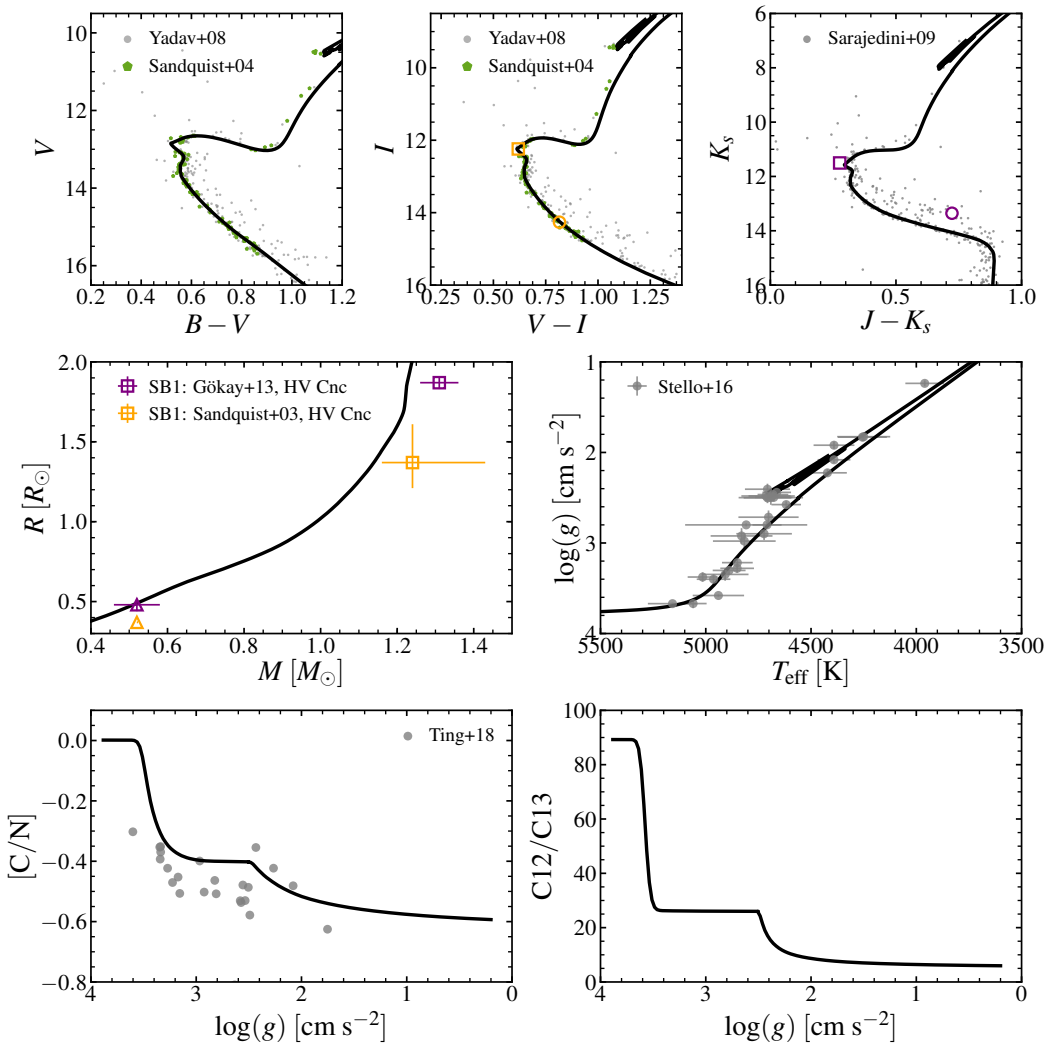


Figure 4.9: Same as Figure 4.8 except now for M67, a solar-metallicity and solar-age (4 Gyr) open cluster. The top three panels show literature photometry from Yadav et al. (2008), Sandquist (2004), and Sarajedini et al. (2009) with the MIST models. The Sandquist (2004) is a sample of likely single star members selected based on their proper motions. The MIST CMDs assume $\mu = 9.62$, $\log(\mathrm{Age})$ [yr] $= 9.63$, [Fe/H] $= -0.03$, and $A_V = 0.15$. The left panel in the middle row shows two measurements of the stellar parameters of HV Cnc (Sandquist & Shetrone 2003; Gökay et al. 2013) with the MIST mass-radius relation. The open symbols indicate that the system is a single-lined (SB1) spectroscopic binary system. When available, the individual EB components are also shown in the CMDs, where the square, triangle, and circle symbols correspond to the primary, secondary, and tertiary components, respectively. The right panel shows the asteroseismic $\log g$ inferred from the scaling relations (Stello et al. 2016) with the effective temperatures from the Casagrande & VandenBerg (2014) color-temperature relations. The surface abundances are obtained by reanalyzing the publicly-available APOGEE DR14 spectra (Holtzman et al. 2015; SDSS Collaboration et al. 2016) with *the Payne* (Ting et al. 2018). The measurement of $^{12}\mathrm{C}/^{13}\mathrm{C}$ in the right panel is currently being explored.

jority of the cluster MSTO stars, which suggests that it is either a blue straggler or undergoing the overall contraction phase along the Henyey hook. Gökay et al. (2013) provided an updated set of parameters by

adding in the *JHKs* photometry, confirming the spectroscopic detection of a third component. They combined the radial velocity solution of the primary with the mass ratio inferred from the light curves in order to obtain the full solution of the binary system, shown in purple points. Again, we use open symbols to indicate that HV Cnc is a single-lined binary system. When available, the individual EB components are also shown in the CMDs, where the square, triangle, and circle symbols correspond to the primary, secondary, and tertiary components, respectively.

The right panel shows the asteroseismic $\log g$ from the analysis of the *K2* photometry (Stello et al. 2016). The authors computed $T_{\rm eff}$ using the optical and 2MASS photometry with the color-temperature relations from Casagrande et al. (2010), assuming $[{\rm Fe/H}] = 0$ and $E(B-V) = 0.03$. Their $T_{\rm eff}$ uncertainties were estimated by the scatter in the $T_{\rm eff}$ inferred from different combinations of the photometric systems, plus an additional 20 K to account for the $T_{\rm eff}$ zero-point uncertainty. Overall, the data are in excellent agreement with the model predictions including the SGB-RGB morphology and the RC magnitude.

Finally, we plot the [C/N] and $^{12}{\rm C}/^{13}{\rm C}$ surface abundance evolution on the RGB. *The Payne* [C/N] abundances are shown as gray circles for comparison. The spectroscopic [C/N] abundances fall ≈ 0.1 dex below the MIST prediction, suggesting a weak preference for a younger age and/or higher metallicity (see Figure 4.1). Measurement of $^{12}{\rm C}/^{13}{\rm C}$ from the APOGEE spectra is currently being explored.

4.4.3 NGC6791

NGC6791 is an exceptionally old (8 Gyr) and metal-rich ([Fe/H]≈0.3–0.5) open cluster (e.g., Stetson et al. 2003; Gratton et al. 2004; Carney et al. 2005; King et al. 2005; Origlia et al. 2006; Linden et al. 2017). It is also well-known for its puzzling double white dwarf cooling sequence, both of which imply cluster ages that are nominally inconsistent with the MSTO age (Bedin et al. 2005, 2008a but see also García-Berro et al. 2010). Several explanations have been put forth, including the presence of a secondary population of massive helium WDs (Hansen 2005; Kalirai et al. 2007) and WD binaries (Bedin et al.

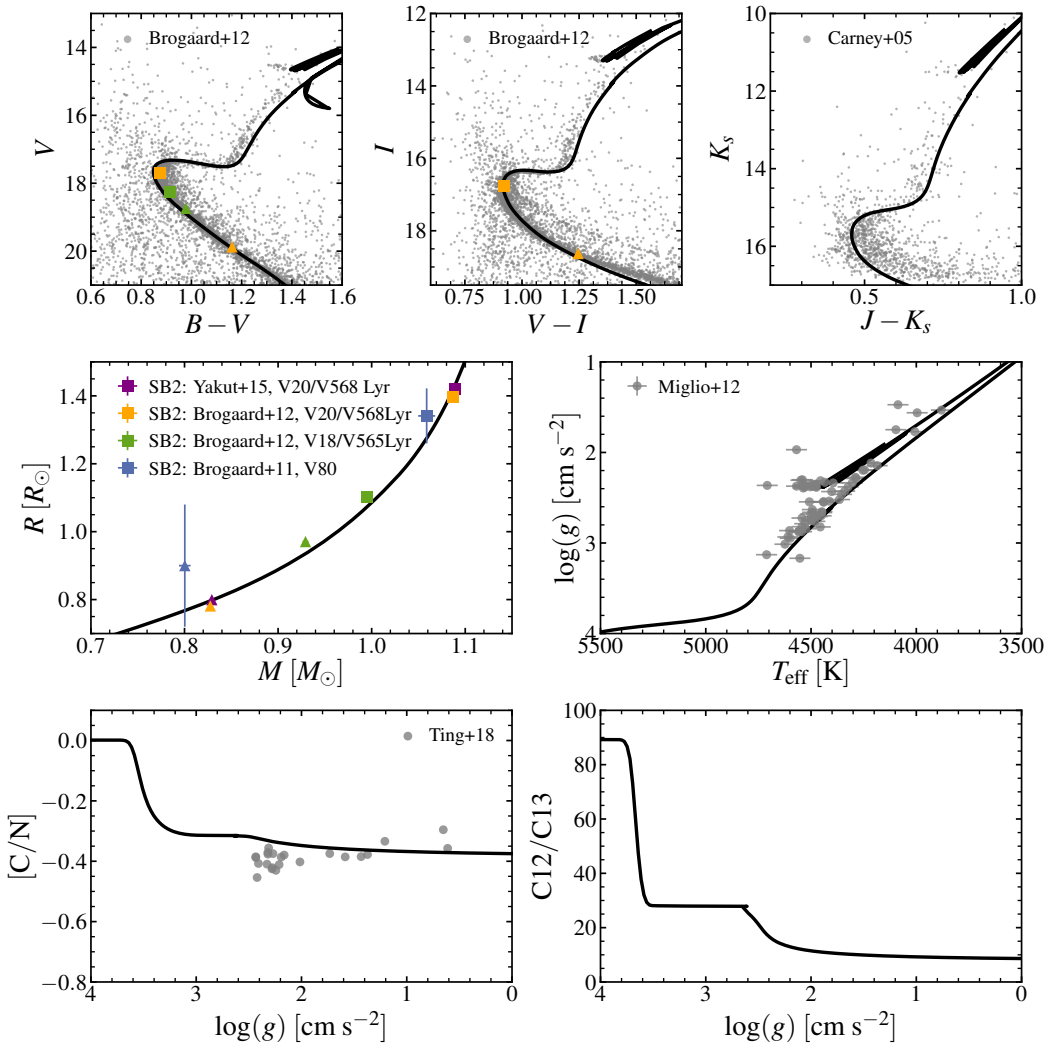


Figure 4.10: Same as Figure 4.8 except now for NGC6791, a metal-rich ([Fe/H] $\approx +0.3$) and old (8 Gyr) open cluster. The top three panels show literature photometry from Brogaard et al. (2012) and Carney et al. (2005) with the MIST models. The MIST CMDs assume $\mu = 13.09$, log(Age) [yr] $= 9.92$, [Fe/H] $= 0.29$, and $A_V = 0.49$. The left panel in the middle row compares the mass and radius measurements of three DEB systems (Brogaard et al. 2011, 2012; Yakut et al. 2015) with the MIST mass-radius relation. The closed symbols indicate that the system is a double-lined (SB2) spectroscopic binary system. When available, the individual EB components are also shown in the CMDs, where the square and triangle symbols correspond to the primary and secondary, respectively. The right panel shows the asteroseismic $\log g$ inferred from the scaling relations (Miglio et al. 2012) with the effective temperatures from the Ramírez & Meléndez (2005) color-temperature relations. The surface abundances are obtained by reanalyzing the publicly-available APOGEE DR14 spectra (Holtzman et al. 2015; SDSS Collaboration et al. 2016) with *the Payne* (Ting et al. 2018). The measurement of $^{12}C/^{13}C$ in the right panel is currently being explored.

2008b).

Figure 4.10 shows the multi-panel plot summary of NGC6791. Here, the MIST models assume $\mu = 13.09$, log(Age) [yr] $= 9.92$, [Fe/H] $= 0.29$, and $A_V = 0.49$. The *BVI* photometry comes from Bro-

gaard et al. (2012) which includes differential reddening corrections to the Stetson et al. (2003) photometry. There is also a rich *HST*/WFC3 dataset of largely medium- and narrow-band imaging obtained as part of a campaign to calibrate photometric metallicities (Ross et al. 2014). Overall, there is moderate tension between the model-predicted and observed RGB colors and $T_{\rm eff}$ (approximately 0.03 dex in $B-V$ and $V-I$ and 50 K, respectively), which may point to interesting model deficiencies (e.g., $\alpha_{\rm MLT}$ variation; Bonaca et al. 2012; Tayar et al. 2017 but see also Salaris et al. 2018; Choi et al., submitted), and/or poorly-"fit" cluster parameters, but we do not conclusively attribute the discrepancy to any one source at this time.

In the middle row, we compare the mass-radius measurements of three systems, V18, V20, and V80, with the MIST model predictions. Brogaard et al. (2012) updated the analysis for V18 and V20 from Brogaard et al. (2011) using a new photometric reduction procedure and an improved analysis of the V20 secondary: the contribution to the light curve from the third component in V20 was accounted for using four "twin stars" that were identified in a much higher-resolution *HST*/ACS image. According to Brogaard et al. (2011), photometric and radius measurements of V80 are very uncertain due to magnetic activity possibly induced by its close-in orbit. Nevertheless, all three systems are double-lined binaries: there are mass measurements for all three systems and radius measurements for V18 and V20 to within 1%. Additionally, there is an updated measurement for V20 from Yakut et al. (2015) where the authors utilized very precise *Kepler* light curves to obtain more accurate estimates of the stellar parameters. When available, the individual EB components are also shown in the CMDs, where the square and triangle symbols correspond to the primary and secondary, respectively.

In the next panel, we plot the asteroseismic $\log g$ measurements from Miglio et al. (2012). The authors adopted effective temperatures calculated from the Ramírez & Meléndez (2005) color-temperature relation in $V-K$ assuming $[{\rm Fe/H}] = +0.3$ and $E(B-V) = 0.16 \pm 0.02$. Following Hekker et al. (2011), they assume an uncertainty of 50 K, though they caution that systematic uncertainties due to color-temperature calibrations and reddening could result in a number closer to $\sim$ 110 K. We adopt 50 K for computing un-

certainties in $\log g$.

In the last row, we plot the [C/N] and $^{12}C/^{13}C$ surface abundance evolution on the RGB. For comparison, *the Payne* [C/N] abundances are shown as gray circles. Finally, we plot the [C/N] and $^{12}C/^{13}C$ surface abundance evolution on the RGB. *The Payne* [C/N] abundances are shown as gray circles for comparison, which are generally in good agreement with the MIST prediction. Measurement of $^{12}C/^{13}C$ from the APOGEE spectra is currently being explored.

4.5 What We Can Expect From Gaia

In addition to obtaining μas astrometry and proper motions for a billion Milky Way stars, the *Gaia* mission will also deliver high-precision photometry consisting of both broadband G and blue/red (B/R) spectrophotometry (Jordi et al. 2010). Together, they will yield homogeneous, proper motion-cleaned photometry of clusters with well-determined distances. In this section, we illustrate what we might expect from *Gaia* photometry using M67 as a fiducial case.

In Figure 4.11, we show example CMDs representative of M67, where each of the six panels shows a series of MIST models illustrating the effects of uncertain parameters. The gray error bars represent the end-of-mission (assuming 70 visits to each field) photometric standard errors estimated according to a performance model made available by the *Gaia* mission.* For display purposes, we inflate the errors in each band by a factor of 10. We emphasize that these errors are representative of *relative* photometric precision only, because the *absolute* photometric accuracy is still dominated by the photometric zero-point uncertainty. The photometric zero-point measurement is tied to the 1% calibration of Vega's spectra (Carrasco et al. 2016), which ultimately yields ≈ 0.014 mag absolute photometric uncertainty in color, shown as black error bars (0.01 mag added in quadrature). However, these uncertain model parameters change the CMD morphology in qualitatively distinct ways, and thus should be separable with high quality mod-

*https://www.cosmos.esa.int/web/gaia/science-performance

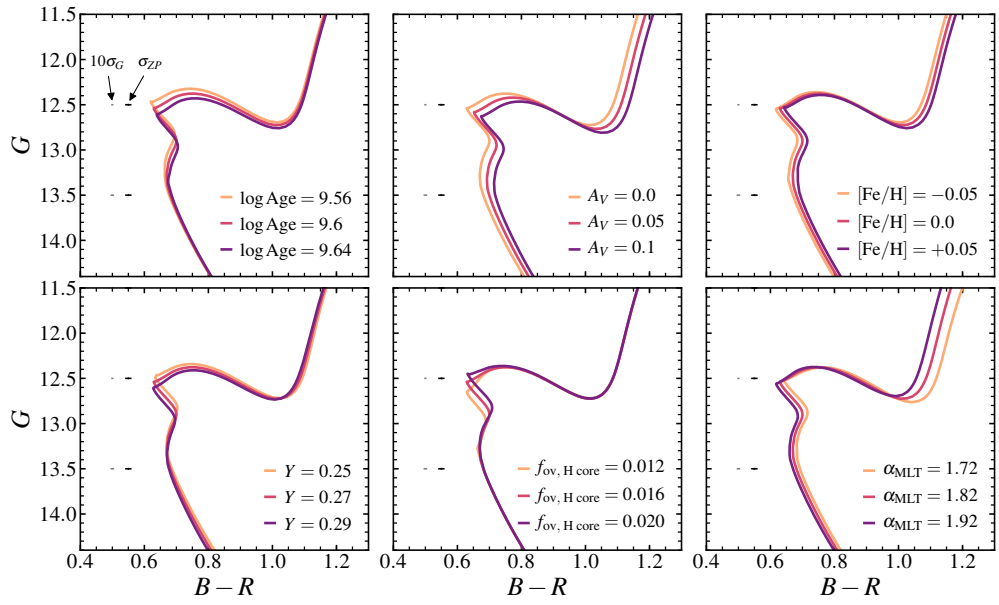


Figure 4.11: MIST isochrones that illustrate the effects of uncertain parameters on various parts of the *Gaia* CMD. A distance modulus of $\mu = 9.7$ is applied to all models and extinction is not included unless noted otherwise. The log Age, [Fe/H], initial helium abundance, convective overshoot efficiency in the hydrogen-burning core, and mixing length α are held fixed to 9.6, 0.0, 0.2703, 0.016, and 1.82 unless noted otherwise. While these parameters indeed have only a subtle influence on the CMD morphology, they change the CMD in unique ways and thus should be separable with high quality models, data, and fitting tools. What these panels do not explicitly show is the effect of these parameters on the lifetimes. The representative *Gaia* end-of-mission median-straylight photometric standard errors assuming 70 visits per field are shown in gray. For display purposes, we multiply the uncertainties in each band by a factor of 10. We also show the absolute photometric accuracy due to zero-point uncertainty (≈ 0.014 mag) in black. Top left: varying the stellar age. Top middle: varying the amount of reddening assuming the $R_V = 3.1$ reddening law from Cardelli et al. (1989). Top right: varying the metallicity. Bottom left: varying the initial helium abundance. Bottom middle: varying the convective overshoot mixing in the hydrogen core. Bottom right: varying the mixing length α_{MLT}.

els, data, and fitting tools even in the presence of zero-point uncertainties. What these panels do not explicitly show is the effect of these parameters on the lifetimes—this information is encoded in the density distribution or number ratios of stars in various parts of the CMD. The subtle differences illustrated in Figure 4.11 are difficult to distinguish using traditional techniques, e.g., fitting empirical MS ridgelines, but we will soon be able to leverage the exquisite *Gaia* photometry, proper motions, and parallax, in combination with a diverse dataset including spectroscopy and asteroseismology. These data sets will place very stringent constraints on the models in Figures 4.8, 4.9, and 4.10, which show isochrones that were "fit" by eye for illustrative purposes. A future direction in this area includes a quantitative and objective determination of the best likelihood parameters (e.g., MATCH, Dolphin 2002; BASE9, von Hippel et al. 2006;

MINESweeper, Cargile et al., in prep.).

4.6 Summary

In this work, we provided an overview of the currently available and future data sets that can be leveraged simultaneously to both improve our constraints on the uncertain stellar model parameters and to infer the properties of open clusters. We first explored the effects of key parameters—age, metallicity, helium content, mixing length parameter, convective boundary mixing efficiency in hydrogen and helium cores, thermohaline mixing efficiency, and mass loss efficiency—on the various observational diagnostics. Next, we identified pairs of observables that are sensitive to each parameter of interest and stellar age, taking into account the observational feasibility. The key plot that summarizes the results is shown in Figure 4.7.

There are several important caveats. At this level of scrutiny, photometric zero-points and differential reddening may well dominate the observational uncertainties. However, the former induces an overall shift in the CMD while the key parameters considered in this work shape the CMD morphologies in qualitatively distinct ways, and thus the two should be separable. On the theoretical modeling side, a proper treatment of the detailed abundance patterns (for example, see Dotter et al. 2015 where the authors analyzed NGC6752 using self-consistent stellar interior and atmosphere models computed according to the detailed spectroscopic abundances), the effects of atomic diffusion on the surface abundances (Dotter et al. 2017), and the surface boundary conditions (e.g., Salaris & Cassisi 1996; Chabrier & Baraffe 1997; VandenBerg et al. 2008; Choi et al., submitted) may be important.

We also evaluated the current status of the various observational data sets using three well-studied open clusters—NGC6819, M67, and NGC6791—as case studies. The main takeaway (see Figures 4.8, 4.9, and 4.10) is that we find no obvious discrepancies between the existing data and the MIST models in almost all comparisons, although more precise observations are required to reveal any interesting potential discrepancies. Upcoming *Gaia* parallax measurements will remove distance as a source of uncertainty

and the accompanying *Gaia* photometry (*B*, *R*, and *G*) and proper motion memberships will immensely improve the quality of the CMDs (see Figure 4.11). CMDs contain a tremendous amount of information, and thus the combination of exquisite photometry, flexible and robust stellar models, and objective fitting tools will allow us to measure stellar ages and disentangle the effects of key stellar model parameters in the near future.

ACKNOWLEDGMENTS

We thank Lars Bildsten, Benjamin D. Johnson, and Guillermo Torres for helpful discussions. We also thank Bill Paxton and the rest of the MESA community who have made this project possible.

5

The Assembly Histories of Quiescent Galaxies Since $z = 0.7$ From Absorption Line Spectroscopy

We present results from modeling the optical spectra of a large sample of quiescent galaxies between $0.1 < z < 0.7$ *from the Sloan Digital Sky Survey (SDSS) and the AGN and Galaxy Evolution Survey (AGES). We examine how the stellar ages and abundance patterns of galaxies evolve over time as a function of stellar mass from* $10^{9.6}$–$10^{11.8}$ $M_{\odot}$. *Galaxy spectra are stacked in bins of mass and redshift, and modeled over a wavelength range from* 4000 Å *to* 5500 Å. *Full spectrum stellar population synthesis modeling provides estimates of the age and the abundances of the elements Fe, Mg, C, N, and Ca. We find negligible evolution in elemental abundances at fixed stellar mass over roughly* 7 Gyr *of cosmic time. In addition, the increase in stellar ages with time for massive galaxies is consistent with passive evolution since* $z = 0.7$. *Taken together, these results favor a scenario in which the inner* ~ 0.3–3 $R_{\rm e}$ *of massive quiescent galaxies have been passively evolving over the last half of cosmic time. Interestingly, the derived stellar ages are considerably younger than the age of the universe at all epochs, consistent with an* equivalent *single-burst star formation epoch of* $z \lesssim 1.5$. *These young stellar population ages coupled with the existence of massive quiescent galaxies at* $z > 1$ *indicate the inhomogeneous nature of the* $z \lesssim 0.7$ *quiescent population. The data also permit the addition of newly-quenched galaxies at masses below* $\sim 10^{10.5}$ $M_{\odot}$ *at* $z < 0.7$. *Additionally, we analyze very deep Keck DEIMOS spectra of the two brightest quiescent galaxies in a cluster at* $z = 0.83$. *There is tentative evidence that these galaxies are older than their counterparts in low-density environments. In Section 5.6, we demonstrate that our full spectrum modeling technique allows for accurate and reliable modeling of galaxy spectra to low S/N (*$\sim 20\,\text{Å}^{-1}$*) and/or low spectral resolution (*$R \sim 500$*).*

5.1 INTRODUCTION

Considerable progress has been made over the last several decades toward understanding the formation and assembly histories of galaxies. On the observational front, two complementary techniques are widely used. Lookback studies aim to study the evolution of galaxies in a statistical manner by comparing snapshots of the galaxy population at different cosmic epochs. This technique has been powered by major spectroscopic surveys such as the Sloan Digital Sky Survey (SDSS; York et al. 2000), the 2dF Galaxy Redshift Survey (2dFGRS; Colless et al. 2001), the VIMOS VLT Deep Survey (VVDS; Le Fèvre et al. 2004, 2005), the PRIsm MUlti-object Survey (PRIMUS; Coil et al. 2011), the Deep Extragalactic Evolutionary Probe 2 (DEEP2) survey (Newman et al. 2013), and the AGN and Galaxy Evolution Survey (AGES; Kochanek et al. 2012), among many others. In addition, targeted surveys out to $z \sim 1$ have provided many insights into the assembly histories of galaxies (e.g., van Dokkum & Franx 1996; Rusin & Kochanek 2005; Treu et al. 2005; Holden et al. 2010; Jørgensen & Chiboucas 2013). In contrast, in the archaeological approach, one infers past evolution through detailed studies of $z \sim 0$ galaxies and their stellar populations. This method of extrapolating back in time is enabled by high quality data of nearby galaxies.

One of the most basic probes of galaxy formation and evolution enabled by large-scale redshift surveys is the time evolution of galaxy luminosity and stellar mass functions. At $z \gtrsim 2$, star-forming galaxies dominate quiescent galaxies in number at all stellar masses, but the mass density of quiescent galaxies has increased by almost an order of magnitude between $z \sim 2$ and today (e.g., Bell et al. 2004; Blanton 2006; Brown et al. 2007; Faber et al. 2007; Cirasuolo et al. 2007; Arnouts et al. 2007; Cappellari et al. 2009; Ilbert et al. 2010; Whitaker et al. 2010; van de Sande et al. 2011; Brammer et al. 2011; Domínguez Sánchez et al. 2011). While the quiescent population has been on a global rise, there is strong evidence that this process is mass-dependent. Between $z \sim 2$ and $z \sim 1$, the space density of massive galaxies has been observed to increase rapidly (Arnouts et al. 2007; Cirasuolo et al. 2007; Ilbert et al. 2010; Nicol et al. 2011; Bram-

mer et al. 2011). By $z \sim 1$, massive galaxies are mostly assembled, and they appear to passively evolve to $z \sim 0$ (e.g., Bundy et al. 2006; Renzini 2006; Cirasuolo et al. 2007; Vergani et al. 2008; Marchesini et al. 2009; Banerji et al. 2010; Moustakas et al. 2013; Muzzin et al. 2013). Thus the rapid evolution in the mass and luminosity functions of quiescent galaxies at late times has mostly been attributed to the rise in low- and intermediate-mass quiescent galaxies, although the details are still under active debate (e.g., Cimatti et al. 2006; Scarlata et al. 2007; Brown et al. 2007; Stewart et al. 2009; Ilbert et al. 2010; Robaina et al. 2010; Whitaker et al. 2010; Eliche-Moral et al. 2010; Pozzetti et al. 2010; Brammer et al. 2011; Skelton et al. 2012; Moustakas et al. 2013). However, mass and luminosity functions by necessity depend on the ability to accurately measure global photometry of extended sources. In particular, accurate photometry accounting for diffuse light at large radius is notoriously difficult even at $z = 0$ (Bernardi et al. 2013), and it only becomes more challenging at higher redshifts due to the $(1+z)^4$ decrease in surface brightness.

There has been a tremendous effort in the past decade to study the outskirts of massive quiescent galaxies as a function of cosmic time. Both size evolution studies using deep imaging and dynamical studies have shown that the sizes of massive galaxies have increased by a factor of 2–4 from $z \sim 2$ to the present (Daddi et al. 2005; Trujillo et al. 2006; van Dokkum et al. 2008; van der Wel et al. 2008; Cimatti et al. 2008; Bezanson et al. 2009; Damjanov et al. 2009; Williams et al. 2010; Cassata et al. 2010; van Dokkum et al. 2010; López-Sanjuan et al. 2012; McLure et al. 2013; Belli et al. 2013). The inner regions ($r \lesssim 5$ kpc) of massive galaxies have apparently undergone very little mass growth, but mass out to ~ 75 kpc has increased by a factor of four since $z \sim 2$ (e.g., van Dokkum et al. 2010). The main channel for size and mass growth is likely dominated by minor mergers, though in-situ star formation and major mergers are also thought to play a role. A simple scaling argument based on the virial theorem explains the dramatic size growth during minor mergers, where the radius increases quadratically with mass instead of linearly as in major mergers (Naab et al. 2009). Observations showing that the oldest and most massive galaxies at high redshift are smaller by a factor of ~ 5 compared to low-redshift galaxies of comparable

mass (e.g., Daddi et al. 2005; Onodera et al. 2012) further corroborate the "inside-out growth" of massive galaxies. Simulations support this notion that galaxy formation occurs in two phases: compact cores are thought to form rapidly at $z \gtrsim 2$ from star formation triggered by infalling cold gas, followed by a slower growth in both mass and size over a longer period of time through the accretion of satellites (e.g., Naab et al. 2007; Kereš et al. 2009; Naab et al. 2009; Hopkins et al. 2009; Dekel et al. 2009; Lackner et al. 2012; Hilz et al. 2013). This is still a controversial field, however, with some groups proposing other modes of size growth, e.g., baryonic mass loss leading to the "puffing up" of galaxies (e.g., Fan et al. 2010). Others invoke progenitor bias, arguing that the new galaxies entering the quiescent population are inherently larger in size (e.g., Carollo et al. 2013), and some groups even find evidence for a lack of size evolution (e.g., Mancini et al. 2010; Stott et al. 2011).

Stellar population analysis offers yet another way of probing the evolution of galaxies (see Walcher et al. 2011, Conroy 2013 for recent reviews). The most popular technique for analyzing properties of old stellar populations in quiescent galaxies, such as age, metallicity, and abundance patterns, is to measure and model several key absorption features using the Lick/IDS index system (Burstein et al. 1984; Worthey et al. 1994). Based on this approach, stellar populations in massive quiescent galaxies are found to be old and enhanced in α elements compared to the Milky Way disk stars (e.g., Worthey et al. 1994). Moreover, numerous independent groups have found strong positive correlations with velocity dispersion for age, total metallicity, and the ratio of α elements to Fe—almost ubiquitously represented by [Mg/Fe] in the literature—but almost no trend for [Fe/H] (Trager et al. 1998; Thomas et al. 2005; Graves et al. 2007; Schiavon 2007; Smith et al. 2009; Zhu et al. 2010; Johansson et al. 2012; Conroy et al. 2014; Worthey et al. 2014). The total metallicity is an important diagnostic for galaxy formation and evolution because it is sensitive to the depth of the potential well in which their stellar populations formed (e.g., supernovae-driven winds can efficiently remove metals from shallow potential wells; Larson 1974). On the other hand, [α/Fe] is sensitive to the timescale of star formation: massive stars expel α elements into their interstellar envi-

ronments on million-year timescales, while Type Ia supernovae enrich the star-forming gas with Fe on billion-year timescales (e.g., Tinsley 1979). By measuring the relative abundances of α elements and Fe in stellar populations, the time and the rate at which stars formed in their host galaxies can be inferred (e.g., Thomas et al. 1999).

More recently, several groups have begun modeling the full optical spectrum of galaxies. First used to measure star formation histories and metallicities (Heavens et al. 2000; Cid Fernandes et al. 2005; Ocvirk et al. 2006; Tojeiro et al. 2009), this technique was further developed by Walcher et al. (2009) and Conroy & van Dokkum (2012) to include variable elemental abundances. The present work can be viewed as the high-redshift extension of Conroy et al. (2014), which focused on full spectrum modeling of high-quality SDSS spectra of $z \sim 0$ quiescent galaxies to derive their ages and detailed abundance patterns. In this work, we use a hybrid approach of combining lookback and archaeological studies to carry out detailed stellar population analysis at progressively higher redshifts. For the first time, we derive accurate ages and abundance measurements for a large mass-complete sample of galaxies from $z \sim 0.1$ to $z \sim 0.7$, and examine how their stellar population properties evolve over time as a function of stellar mass. As we demonstrate, powerful constraints can be placed on the assembly histories of galaxies from the time evolution of their stellar population properties.

The paper is organized as follows: Section 5.2 gives an overview of the data sets and the sample selection process, and Section 5.3 presents background information on our models and the full spectrum fitting technique. The main science results are introduced in Section 5.4, which we discuss and interpret in detail in Section 5.5. Next, we present the results of various systematic tests to explore the robustness of our analysis in Section 5.6, then we conclude with a summary in 5.7. All wavelengths in this paper are quoted in vacuum. Where necessary, we assume a Chabrier IMF (Chabrier 2003) for the stellar mass range 0.1–100 $M_{\odot}$ unless noted otherwise, and ΛCDM cosmology, with $H_0 = 70$ km s^{-1} Mpc^{-1}, $\Omega_{\rm m} = 0.3$, and $\Omega_{\Lambda} = 0.7$.

5.2 DATA

In this work we primarily utilize two large spectroscopic surveys to select samples of quiescent galaxies. At intermediate redshift we rely on the AGN and Galaxy Evolution Survey (AGES; Kochanek et al. 2012), while at low redshift we use a large sample of galaxies selected from the Sloan Digital Sky Survey (SDSS; York et al. 2000). In this section we provide brief overviews of the surveys, data, and sample selection process.

5.2.1 SDSS

Our low-redshift sample of galaxies is selected from the SDSS Data Release 7 (DR7; Abazajian et al. 2009). This dataset includes *ugriz* photometry for 357 million objects over 11,663 deg^2, and optical spectroscopy for roughly 930,000 galaxies over 9380 deg^2. We choose 427,536 galaxies observed as part of the main galaxy survey (Strauss et al. 2002) with $14.5 < r < 17.6$ and $0.05 < z < 0.2$ from the SDSS/DR7 New York University Value Added Galaxy Catalog (NYU/VAGC; Blanton et al. 2005).*

Following Moustakas et al. (2013), broadband photometry from the ultraviolet (UV) to the rest-frame near-infrared is assembled for this sample. Specifically, we obtain near- and far-UV photometry from the *Galaxy Evolution Explorer* (*GALEX*; Martin et al. 2005) *GALEX* Release 6 (GR6), optical *ugriz* photometry from the SDSS, and *Wide-field Infrared Survey Explorer* (*WISE*; Wright et al. 2010) [3.4] and [4.6] photometry from the *WISE* All-Sky Data Release. We make every effort to ensure that our photometry captures as much of the total light of the galaxy in each band as possible; in particular, the SDSS `model` magnitudes are used to measure the optical colors of each galaxy, scaled by the *r*-band `cmodel` magnitude, which provides the most reliable estimate of the integrated (total) galaxy flux irrespective of galaxy type (Bernardi et al. 2010; Blanton et al. 2011). Finally, the stellar velocity dispersions measured by the SDSS pipeline and distributed as part of the NYU/VAGC are adopted in this work.

*http://sdss.physics.nyu.edu/vagc

We use `iSEDfit` (Moustakas et al. 2013), a Bayesian SED modeling code, to derive the stellar masses and star formation rates for the galaxies in our sample. The Flexible Stellar Population Synthesis models (FSPS, v2.4; Conroy et al. 2009, 2010) and a Chabrier (2003) IMF over the mass range 0.1–100 $M_{\odot}$ are adopted. The Bayesian priors used to fit the photometry are similar to those adopted in Moustakas et al. (2013), but "delayed" star formation histories of the form $\mathrm{SFR}(t) \propto t\exp(-t/\tau)$ with a uniform prior on τ in the range $0.1 - 5$ Gyr are assumed instead of simple exponentially declining star formation histories. We also include nebular emission lines whose strength is tied self-consistently to the number of hydrogen-ionizing photons in the SED of the composite stellar population. In this paper, M refers to the stellar mass resulting from SED-fitting.

From the parent sample, we make the following initial cuts: $100 < \sigma$ (km s^{-1}) < 350, $0.07 < z < 0.09$, and $10.4 < \log(M/M_{\odot}) < 11.8$. The velocity dispersion cut is used to remove objects that are unlikely to be bona fide quiescent galaxies, whereas the redshift selection is a trade-off between overlapping with AGES redshift and reaching a sufficiently low stellar mass limit. The lower mass limit is chosen such that the sample is complete down to that limiting mass. Next, we use specific star formation rate (sSFR) to define the quiescent sample. When viewed in the sSFR versus stellar mass plane, the remaining sample separates into two groups, one that makes up the star-forming main sequence and another that lies below consisting of a quiescent subpopulation. The left panel in Figure 5.1 shows a subset of the data, where the two distinct clouds can be clearly seen. To obtain the quiescence cut, the sample is divided into three mass bins—$10.4 < \log(M/M_{\odot}) < 11.45$ in bin widths of 0.35*—and histograms of sSFR values are constructed. The resulting distributions are clearly bimodal, and we locate the valley and the sSFR value at which it occurs. Next, we perform a linear least-squares fit to these three sSFR values. This line is used to separate the quiescent population from the star-forming main sequence. The resulting quiescence cut is shown as a dashed line in Figure 5.1. The redshift interval for this particular sample is narrow enough that we do not

*The highest mass bin is excluded due to its insufficient number of galaxies for the construction of a well-sampled histogram, which is necessary to cleanly locate the bimodality minimum.

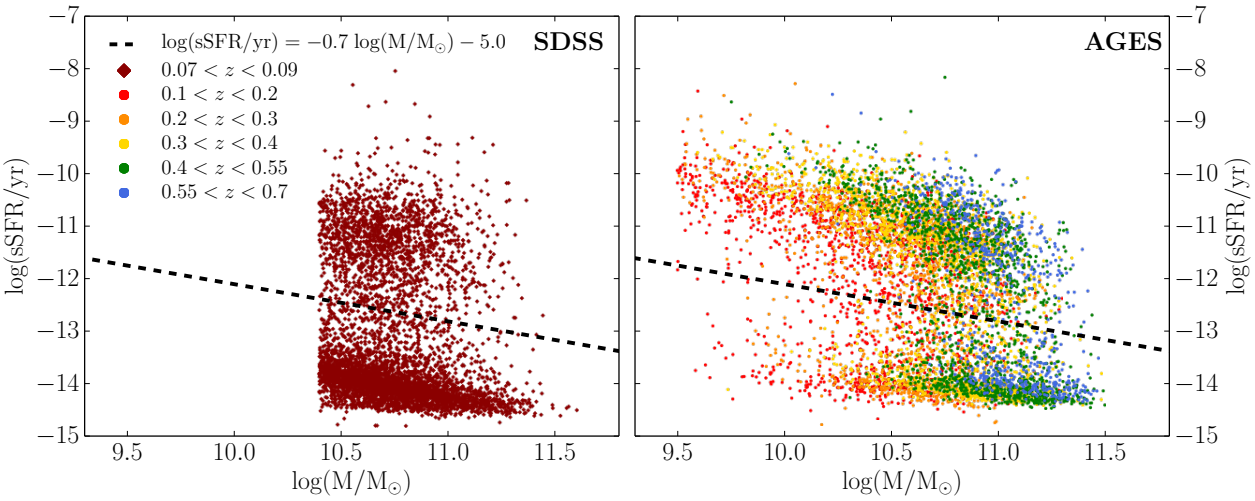


Figure 5.1: *Left panel*: specific star formation rate (sSFR) as a function of stellar mass for a subset of the SDSS sample. A random subset is shown for display purposes. Both the quiescent cloud and the star-forming main sequence can be seen. We locate the minimum of the bimodal distribution in three mass slices and perform a linear least-squares fit to those points. The resulting quiescence threshold is shown as a dashed line. We discard all galaxies above this quiescence cut to obtain a sample of quiescent galaxies. *Right panel*: sSFR as a function of stellar mass for the entire AGES sample. The black dashed line corresponds to the quiescence cut determined from the SDSS sample. Only those that fall below the sSFR threshold are included in our quiescent sample. We use a quiescence cut that is constant with redshift because there is no evidence for evolution in the location of the green valley.

need to consider a cut that evolves with redshift. The final quiescent SDSS sample is shown in Figure 5.2.

Finally, we divide the remaining ∼37,000 objects into four bins in mass with log-uniform spacing, ranging from $10^{10.4}\ M_\odot$ to $10^{11.8}\ M_\odot$. In order to stack spectra with different continuum shapes and normalizations as well as varying degrees of smoothness due to velocity broadening, we divide each spectrum through by an $n = 6$ polynomial to continuum-normalize, then convolve with a Gaussian kernel to achieve an effective dispersion of 350 km s^{-1}, the highest σ in our entire sample. The goal of the polynomial division is to remove the broad continuum shape while preserving the integrity of the individual absorption features. We have tested the effects of varying the polynomial order and have found that n between 4 and 7 satisfactorily eliminates the broadband shape without significantly affecting the absorption features. The systematic effects of smoothing with a Gaussian kernel are explored in Section 5.6.0.2.

Continuum-normalized and smoothed spectra are then coadded with weights provided by the flux uncertainty at each pixel ($w_\lambda = 1/{\sigma_\lambda}^2$). Each galaxy contributes almost equally to the stack, but a luminous galaxy has smaller Poisson error at every pixel and thus more weight in the stack. As discussed in

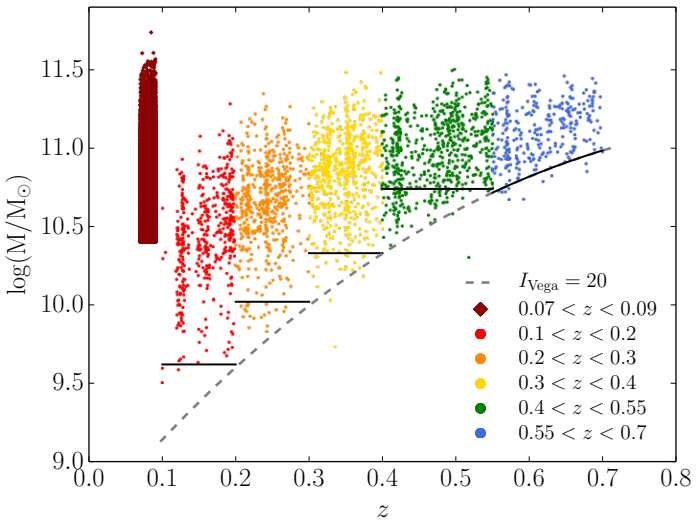


Figure 5.2: Stellar mass as a function of redshift for the quiescent galaxy sample. A subset of the $0.07 < z < 0.09$ SDSS sample is shown in maroon diamonds and the entire AGES sample is shown in colored circles. The black lines show the mass cuts applied to each color-coded redshift bin and the dashed gray line corresponds to $I_{\rm Vega}$=20 estimated from a photometric redshift sample (Brodwin et al. 2006, 2013). Our sample is complete in mass in each redshift bin. For $0.55 < z < 0.7$, all objects above the dashed line are included in order to sample a greater range in stellar mass. Of the resulting three mass bins in this redshift interval, the lowest mass bin is thus technically incomplete. The vertical streaks in the AGES data arise due to the imprints of large scale structure on the relatively small volume covered by the survey.

Section 5.5, this weighted stacking scheme does not introduce a significant bias toward a small subset of the sample. In other words, the resulting stacks are not dominated by a few bright, young galaxies. The effects of stacking are investigated in more detail in Section 5.6.0.3, but in summary, the best-fit parameter measured from the stacked spectrum and the weighted average of best-fit parameters from fitting individual spectra agree to within 0.05 dex. Additionally, this weighting scheme serves to mask out bad regions in the spectrum by ensuring zero or very weak contribution from spurious counts with large measurement uncertainties. We fit the stacked spectrum in the rest-frame wavelength range 4000 – 5500 Å only in order to ensure identical wavelength coverage across all redshifts for both this low-redshift SDSS sample and the higher redshift AGES sample (see Section 5.2.2).

5.2.2 AGES

AGES obtained optical spectroscopy for approximately $18,000$ galaxies over 7.7 deg^2 of the NOAO Deep Wide-Field Survey (NDWFS) Boötes field (Jannuzi & Dey 1999; Kochanek et al. 2012). The survey used the Hectospec instrument (Fabricant et al. 2005) on the MMT to obtain 3700 – 9200 Åspectroscopy at a spectral resolution of 6 Å($R \approx 1000$), and achieved a spectroscopic completeness of approximately 90% (Kochanek et al. 2012; Cool et al. 2012). The median redshift of the galaxies in the survey is $\langle z \rangle \approx 0.3$, spanning the range $0 \lesssim z \lesssim 0.8$. From the full spectroscopic dataset, we select a statistically complete sample of $10,839$ galaxies with well-calibrated spectrophotometry, $15 < I_{\rm Vega} < 20$, and $0.05 < z < 0.75$.

Following Moustakas et al. (2011), 12 bands of photometry are assembled for this sample, including near- and far-UV photometry from *GALEX*/GR6, u-band photometry from the LBT/LBC (Bian et al. 2013), $B_{\rm W}RIz$ optical photometry from the NDWFS third data release and zBoötes survey (Jannuzi & Dey 1999; Cool 2007), near-infrared JHK photometry from a NOAO Extremely Wide-Field Infrared Imager (NEWFIRM; Autry et al. 2003) survey* of the Boötes field, and [3.6] and [4.5] photometry from the *Spitzer* Deep Wide-Field Survey (SDWFS; Ashby et al. 2009). Accurate galaxy colors are measured within a $4''$ diameter aperture from PSF-matched imaging using a custom code, and tied to the I-band MAG_AUTO magnitude measured using `SExtractor` (Bertin & Arnouts 1996). Additional details regarding the photometry can be found in Brown et al. (2007) and Moustakas et al. (2011). In particular, using simulated galaxies inserted into the NDWFS I-band imaging, Brown et al. (2007) showed that MAG_AUTO yields the total galaxy flux within $\approx 5\%$ for galaxies brighter than $I_{\rm Vega} = 20$ over a wide range of apparent size and galaxy type (i.e., surface brightness profile). Finally, the velocity dispersions for this sample are measured as described in Moustakas et al. (2010, 2011) using a modified version of the PPXF continuum-fitting code (Cappellari & Emsellem 2004).

Stellar masses and SFRs for AGES are determined by fitting the photometry using `iSEDfit` (see

*`http://archive.noao.edu/nsa/NEWFIRM_NDWFS.html`

Section 5.2.1). After removing galaxies with poorly constrained velocity dispersions ($\lesssim 6\%$ of the quiescent sample*), the following cuts are applied—$100 < \sigma$ (km s^{-1}) < 350 and $9.5 < \log(M/M_{\odot}) < 11.5$—leaving approximately 7000 galaxies. Finally, we select a sample of quiescent galaxies adopting the same sSFR($\log M$) cut derived from the SDSS sample (see the right panel in Figure 5.1). The quiescence cut used here is constant with redshift because there is no evidence for evolution in location of the green valley, i.e., the minimum in the sSFR bimodality.

Since the AGES sample covers a large redshift range, we further partition the data in redshift with the bin divisions at 0.1, 0.2, 0.3, 0.4, 0.55, and 0.7. These uneven redshift slices are meant to reflect roughly constant intervals in time of 1 Gyr.

To ensure that the redshift bins are complete in mass, we compute the limiting stellar mass corresponding to $I_{\rm Vega} = 20$ using a different, larger photometric redshift sample to compare against our spectroscopic dataset. We utilize the sample from Brodwin et al. (2013), which updated the photometric redshifts from Brodwin et al. (2006) with deeper *Spitzer* photometry. The photometric redshifts for the 4.5 μm selected galaxy sample in the ~ 10 deg^2 SDWFS (Ashby et al. 2009) are measured from multi-wavelength photometry combining the deep *Spitzer* mid-IR photometry with optical photometry from the NDWFS (Jannuzi & Dey 1999) and NIR photometry from the FLAMINGOS Extragalactic Survey (FLAMEX; Elston et al. 2006). The stellar masses and SFR are estimated from `iSEDfit`, and quiescent galaxies are selected using a bimodality cut similar to the one applied to the fiducial SDSS and AGES sample. Next, the typical stellar mass corresponding to $I_{\rm Vega} = 20$ is calculated via linear least-squares fitting of stellar mass versus $I_{\rm Vega}$ in narrow redshift intervals. The resulting mass limit is used as a guideline to apply completeness cuts to the AGES quiescent galaxy sample, leaving approximately 2400 objects in the final sample. However, for $0.55 < z < 0.7$, all objects above the $I_{\rm Vega} = 20$ limit are included in order to sample a greater range in stellar mass. Of the resulting three mass bins in this redshift interval, the lowest mass bin is thus

*These objects preferentially have low S/N but are uniformly distributed in $U - V$ color within each mass–redshift bin. The omission of these objects from the stacks is thus unlikely to significantly bias the results.

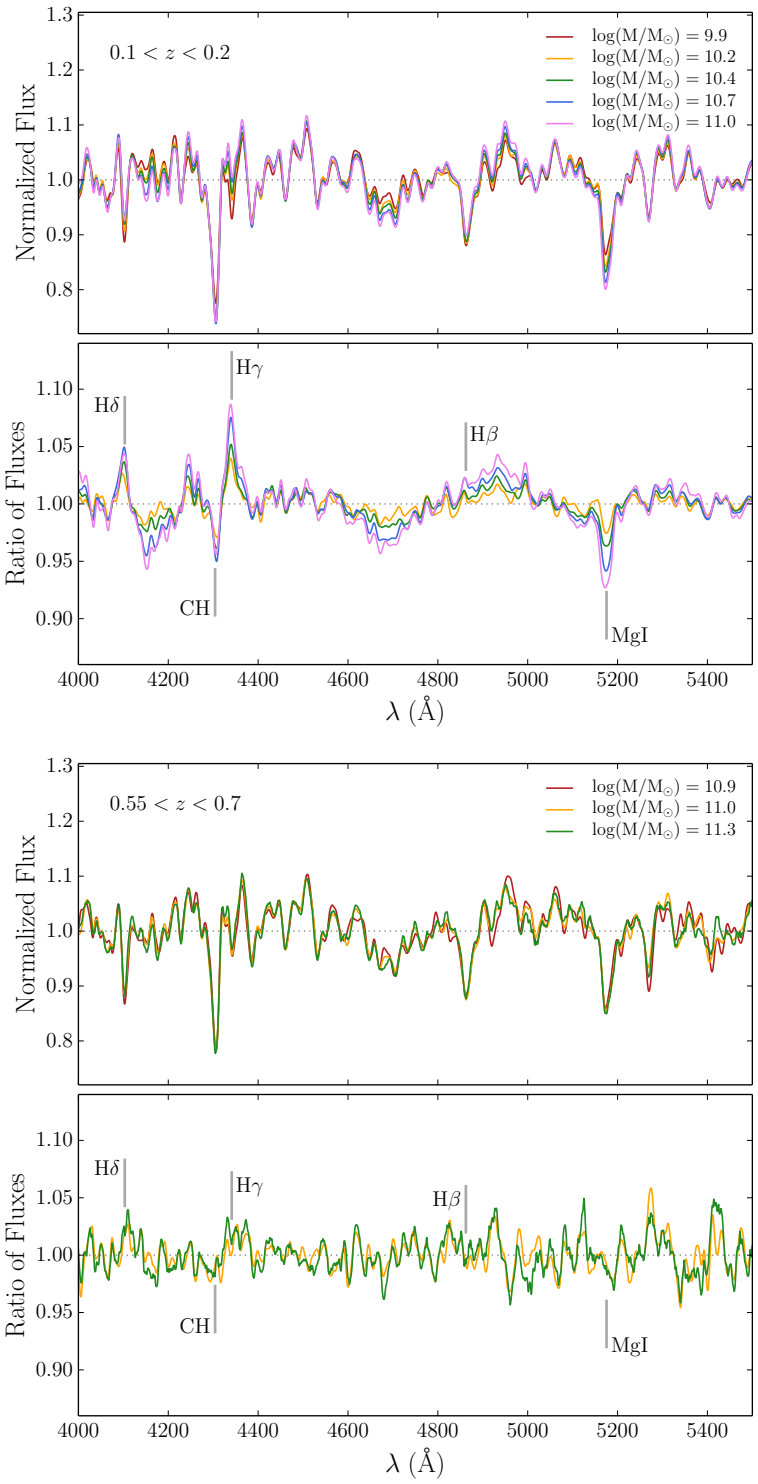


Figure 5.3: Continuum-normalized stacked spectra of AGES quiescent galaxies. Stacked spectra for the lowest and highest redshift intervals are shown in the top panels. The lower panels show the ratio of the fluxes to the flux in the lowest mass bin in each redshift interval using the same color scheme as in their respective top panels. The displayed stellar masses are median values of individual galaxies in each respective bin.

incomplete and biased toward the lower limit of the redshift bin.

Figure 5.2 shows stellar mass as a function of redshift after the quiescence cut has been applied, with the AGES data points shown in colored circles and the black lines demarcating the mass cuts. The dashed gray line shows the $I_{\rm Vega} = 20$ limit from the photometric redshift sample. The vertical streaks, especially prominent in the $0.1 < z < 0.2$ slice, are a consequence of sampling a relatively small volume of the large scale structure: the survey cone happened to intersect three overdense regions within which the galaxies in our sample are clustered.

We divide each redshift interval into six mass bins, continuum-divide, smooth the spectra to an effective velocity dispersion of 350 km s^{-1}, and stack the spectra. See Section 5.2.1 for more detail on this stacking process. We do not bin our spectra in velocity dispersion because a given velocity dispersion bin is incomplete in mass at the highest redshifts. There are tens to hundreds of objects in each mass–redshift bin, but one of them—corresponding to $0.2 < z < 0.3$ and $11.2 < \log(M/M_{\odot}) < 11.5$—contains only five objects. More details regarding the stacked spectra can be found in Table 5.1.

In Figure 5.3 we show the stacked AGES spectra in several mass bins for both the lowest and the highest redshift intervals to highlight the differences in their spectral features. The bottom panels show the ratio of the fluxes to the flux in the lowest mass bin in each redshift interval. The typical S/N for the low- and high-redshift stacked spectra are $\sim$ 100–200 Å^{-1} and $\sim$ 50 Å^{-1}, respectively. While differences are fairly modest overall, variations in the strengths of absorption features such as Hδ at 4103 Å, CH at 4300 Å, Hγ at 4341 Å, Hβ at 4862 Å, and MgI at 5175 Å are clearly noticeable.

5.2.3 KECK DEIMOS

In addition to the two survey data sets, we also analyze DEIMOS (Faber et al. 2003) spectra of the two brightest quiescent galaxies in the magnitude-limited survey of cluster MS 1054-03 at $z = 0.83$ (Holden et al. 2010). They were observed in 2 hr exposure intervals using the 600 line mm^{-1} grating for a total

integration time of 20 hr to achieve a S/N $\approx$ 30 Å^{-1} at 5000 Å. Additional details about the two objects, 7415 and w5756, can be found in Table A1 in Holden et al. (2010). These spectra are fit individually from 4000 Åto 5440 Åafter continuum-normalization.

5.3 Model Fitting

The main analysis tool for our work was developed by Conroy & van Dokkum (2012) and subsequently updated in Conroy et al. (2014). The technique involves full spectrum fitting of optical-NIR spectra (3500 Å – 2.4 μm with $R \sim 2000$) of quiescent galaxies. It is an alternative method to the traditional technique of modeling the Lick/IDS indices (Burstein et al. 1984; Worthey et al. 1994; Trager et al. 1998; Thomas et al. 2005; Schiavon 2007). A defining feature of this code is that it fits the entire continuum-normalized spectrum. The main advantage of this technique is that since all of the absorption features are fit simultaneously, there is more information available to better constrain the fit, resulting in a reliable measurement of the stellar population parameters even at low S/N (see Section 5.6.0.1). This implies that for a fixed S/N per Å, the age-metallicity degeneracy (Worthey et al. 1994) is less pronounced when fitting the full spectrum (see also Sánchez-Blázquez et al. 2011).

As described in Conroy & van Dokkum (2012) and Conroy et al. (2014), the model follows standard stellar population synthesis techniques by making use of stellar isochrones and empirical stellar spectral libraries to fit the wavelength range 0.35–2.4 μm. Since the stars used to construct the spectral libraries have solar abundance patterns and are roughly $Z \sim Z_{\odot}$, necessary adjustments must be made to account for α-enhancements and super-solar metallicities observed in quiescent galaxies. To achieve this task, the code makes use of response functions constructed using a large grid of model stellar atmospheres and spectra computed with the ATLAS12 package (Kurucz 1970, 1993), ported to Linux by Sbordone et al. (2004). These response functions (see, e.g., Figure 2, 3, 4 in Conroy et al. 2014) are derived for each element as a function of wavelength, which are then used to modify the template model galaxy spectrum. The model

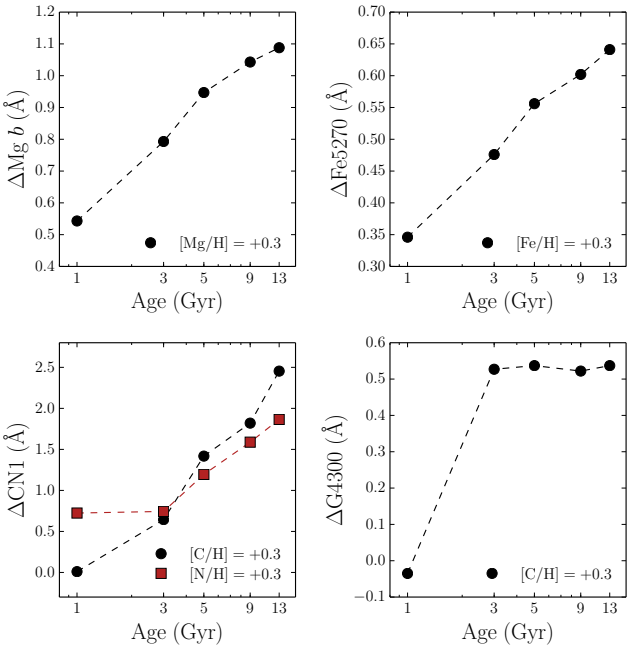


Figure 5.4: Change in Lick indices as a function of age due to a 0.3 dex increase in various elements. These panels highlight the importance of using age-dependent response functions when modeling the spectra of quiescent galaxies. The G4300 index measures the strength of the CH band at 4300 Å. Note that the indices shown here are for illustrative purposes only. In our main analysis we fit models to the full optical spectra.

first presented in Conroy & van Dokkum (2012) and subsequently updated in Conroy et al. (2014) has since been updated to include younger populations. Whereas the first generation model ranged from 3–13.5 Gyr in age, the model is now capable of fitting populations as young as 1 Gyr. We note that the stellar isochrones are not recomputed for different elemental mixtures in the model. To account for a shift in effective temperature of the isochrone due to changes in the abundance patterns, Conroy & van Dokkum (2012) included $\Delta T_{\rm eff}$ as an additional parameter in the fit. In the 'simple' version of the code used in the present work, we do not include $\Delta T_{\rm eff}$. This is not expected to cause an appreciable systematic effect (Conroy & van Dokkum 2012), though this will be tested in future work. We also note that this assumption is standard in the modeling of old stellar populations (Thomas et al. 2005; Schiavon 2007).

An additional improvement to the model since Conroy et al. (2014) is the inclusion of time-dependent response functions. Originally, the response functions were constructed only for a 13 Gyr isochrone. Given the nature of this current work, however, we have deemed it important to consider the response functions

at younger ages (1, 3, 5, and 9 Gyr). For demonstrative purposes, we show the change in Lick indices due to a 0.3 dex increase in various elemental abundances as a function time in Figure 5.4.* All indices are quoted as equivalent widths with units of Å (for detail on index measurements, see Worthey et al. 1994). The indices become less sensitive to changes in abundances at young ages (see also Lee et al. 2009). Changes in elemental abundances not only influence the absorption features themselves but the continuum as well. These new response functions will be described in detail in future work.

Exploration of parameter space is achieved using a Markov Chain Monte Carlo (MCMC) algorithm, which yields error estimates on the fit parameters derived from the full posterior distributions, i.e., by marginalizing over the other parameters. These errors are statistical only. A typical systematic uncertainty of $\pm$ 0.05 dex should be assumed in addition to the statistical errors (see Section 5.6 and also Conroy et al. 2014). The original MCMC algorithm originally used in Conroy & van Dokkum (2012) has since been replaced with `emcee`, an implementation of the affine-invariant ensemble sampler for MCMC (Foreman-Mackey et al. 2013).† The main advantage of `emcee` is that there are only one to two hand-tuned parameters, a dramatic decrease compared to $\sim N^2$ required for a traditional MCMC algorithm sampling a N-dimensional parameter space.

The spectrum fitting code is run in 'simple' mode, which measures 10 stellar population parameters—simple stellar population (SSP)-equivalent age,‡ [Fe/H], [Mg/Fe], [O/Fe], [C/Fe], [N/Fe], [Na/Fe], [Si/Fe], [Ca/Fe], and [Ti/Fe]—in addition to redshift and velocity dispersion over the wavelength range 4000 – 5500 Å. Since we are not fitting wavelengths redward of 5500 Å, which harbor dwarf-sensitive features, IMF parameters are not explored in the fit and a Kroupa IMF (Kroupa 2001) is enforced.§ Additionally,

*Note that no attempt was made to place these indices on the standard Lick/IDS index zero point scale. The indices are measured on spectra broadened to 100 km s^{-1}.

†`http://dan.iel.fm/emcee`

‡We note that light-weighted and SSP-equivalent ages are distinct concepts. Light-weighted age is obtained by integrating over SFR(t) weighted by luminosity, whereas SSP-equivalent age specifically assumes a single burst. SSP-equivalent ages are generally younger than light-weighted ages, and both are younger than mass-weighted ages. See also Trager et al. (2000), Serra & Trager (2007), and Trager & Somerville (2009).

§The difference between stellar masses computed assuming a Kroupa and Chabrier IMF is < 0.05 dex.

[Na/Fe] is set to track [Mg/Fe] because the spectral range we fit does not contain Na-sensitive features, but this assumption has little consequence in our fits. We tested the effects of changing the reddest limit in the wavelength range we fit (varying from 5300 Å to 5800 Å) and found that the resulting parameters vary comfortably within their 1σ errors. We refer the reader to Section 5.6 for more details regarding additional systematic tests.

5.4 Results

We now present our main science results from modeling the spectra of $z = 0.1 - 0.8$ quiescent galaxies. We first review the $z = 0.1 - 0.7$ AGES and SDSS data together, then introduce the Keck DEIMOS $z = 0.83$ cluster data.

5.4.1 Stellar Population Parameters of Quiescent Galaxies from AGES and SDSS Spectra

We begin by showing representative SDSS and AGES spectra and best-fit models in Figures 5.5 and 5.6. The continuum-normalized fluxes are shown in black while the models are plotted in red in the top panels.* By eye, the models are excellent fits to these high S/N stacked spectra. The bottom panels show the percent fractional residuals between the best-fit model and data in black and the flux uncertainties as the gray shaded region. In Figure 5.5, the fit is worse than is formally allowed by the uncertainties in the SDSS data, but the S/N is extremely high, which imposes strong demands on the model. In Figure 5.6, the residuals are comfortably within the data uncertainties. The displayed $\log M$ values are the median values of individual galaxies in each respective bin, while the S/N is the median calculated in the wavelength range 4000 – 5500 Å.

In Figure 5.7 we compare the residuals for AGES and SDSS stacked spectra. The top panel shows a

*We note that the intrinsic variation due to spectral features is $\sim$ 5%–10%, so the residuals with rms of $\sim$ 0.5%–1% correspond to a factor of $\sim$ 10 improvement in the quality of the fit over a straight line.

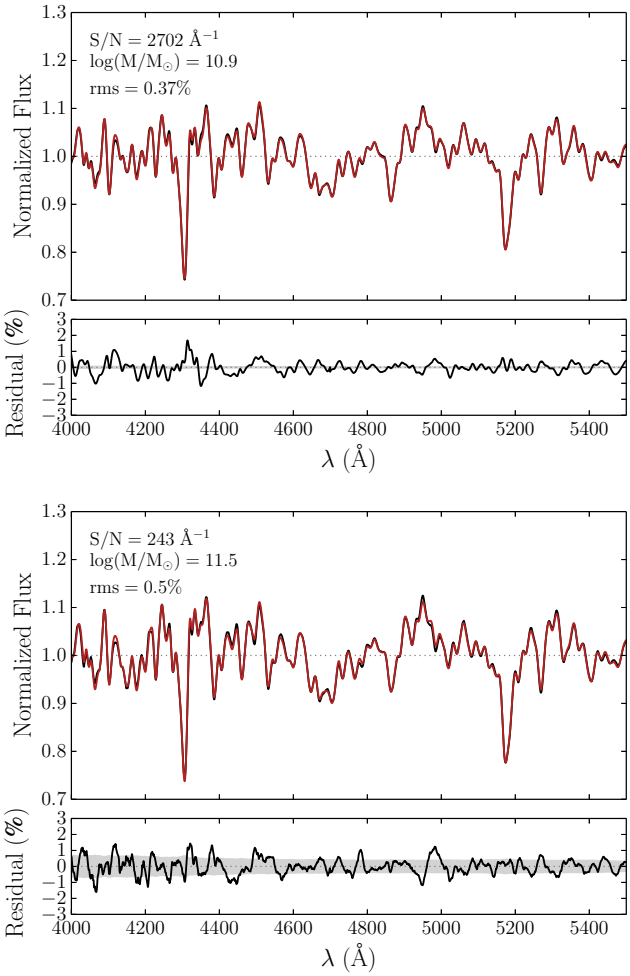


Figure 5.5: Representative comparison between SDSS stacked spectra and the corresponding best-fit models, displayed in black and red, respectively. The flux has been continuum-normalized by a high-order polynomial. The bottom panel shows the fractional residuals in the models in black and the flux uncertainties as the gray shaded region. The residual is formally larger than is allowed by the uncertainties in the data, but the stacked data are of exquisite quality, which imposes very strong demands on the model. The displayed stellar masses are median values of individual galaxies in each respective bin, while the S/N is the median calculated in the wavelength range 4000 – 5500 Å.

comparison between SDSS and AGES $0.1 < z < 0.2$ and $0.3 < z < 0.4$ bins, with median masses around $\log(M/M_\odot) \sim 11$. The residuals are very well-behaved, demonstrating that any coherent behavior between these residuals is due to the model and not dominated by differences in the data, such as the sampled redshift range, reduction pipeline, or sample selection criteria. The size of the fluctuations is comparable despite the wide range in the median S/N values, implying that the residuals eventually hit a floor even when fitting exquisite high S/N spectra. The bottom panel shows a comparison between different AGES mass–redshift bins with median S/N around 120 Å^{-1}. The residuals show no systematic trend with mass

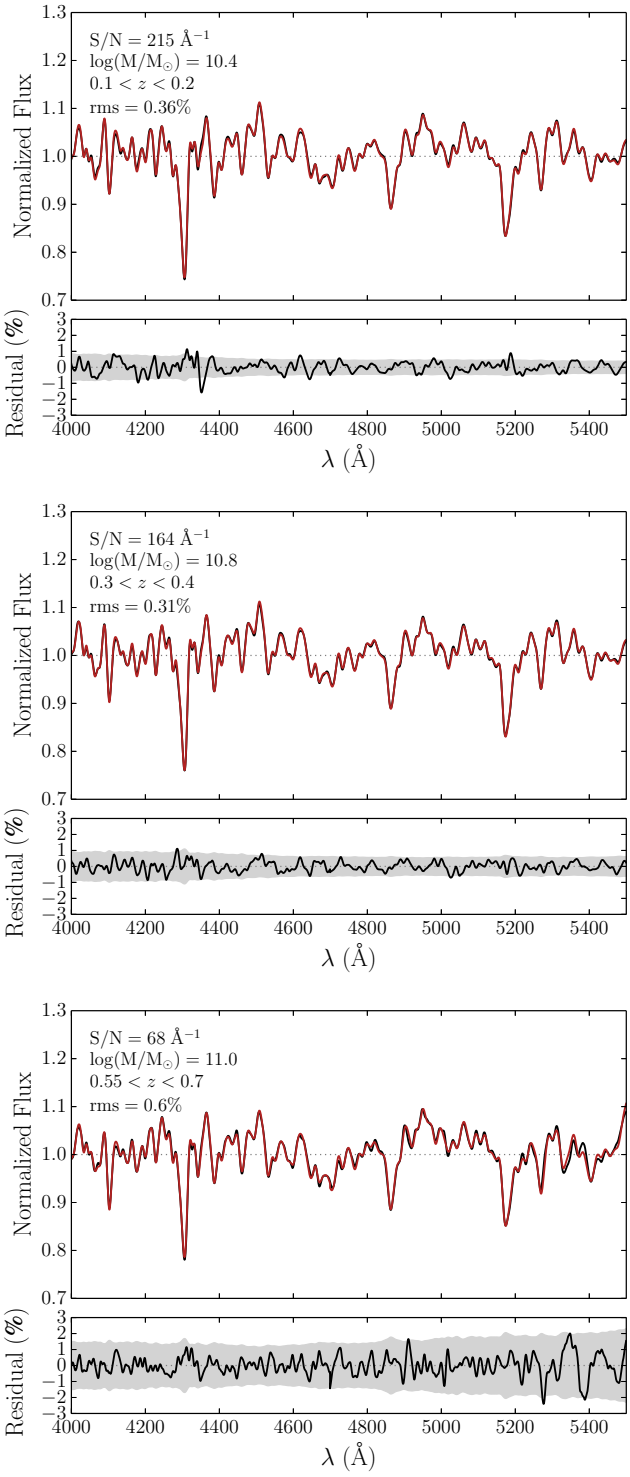


Figure 5.6: The same as Figure 5.5, now for AGES stacked spectra.

or redshift, confirming the findings of Conroy et al. (2014) that both high-mass galaxies with α-enhanced abundance patterns and low-mass galaxies with roughly solar-abundance patterns are well-described by

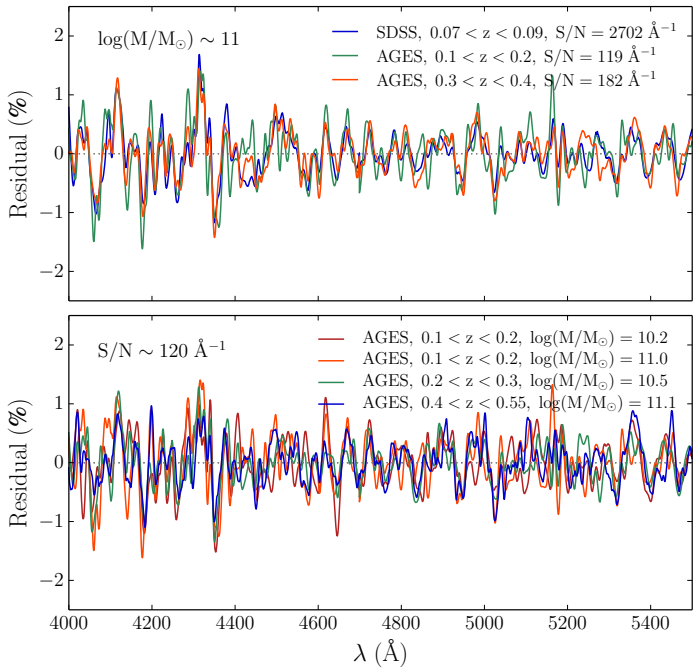


Figure 5.7: Residuals between the data and best-fit models for AGES and SDSS stacked spectra. *Top panel:* a comparison between SDSS and AGES $0.1 < z < 0.2$ and $0.3 < z < 0.4$ bins, with median masses around $\log(M/M_{\odot}) \sim 11$, showing that the residuals are very well-behaved. This demonstrates that any coherent behavior between these residuals is due to the model and not dominated by differences in the data, such as the sampled redshift range, reduction pipeline, or sample selection criteria. *Bottom panel:* a comparison between different AGES mass–redshift bins with median S/N around 120 Å^{-1}. The residuals show no systematic trend with mass or redshift, confirming the findings of Conroy et al. (2014) that both high-mass galaxies with α-enhanced abundance patterns and low-mass galaxies with roughly solar-abundance patterns are well-described by our model.

our model. In other words, the residuals are present even in the low-mass stacks where the abundance ratios are roughly solar, suggesting that the theoretical templates are not a major sources of the systematic residuals.

Now we present the main science results of this work. In Figure 5.8 we display the resulting best-fit SSP-equivalent age and abundance measurements from full spectrum fitting of AGES and SDSS stacked spectra as a function of stellar mass. The SDSS and AGES data are shown in maroon diamonds and red, orange, yellow, green, and blue circles, respectively. The stellar masses were estimated from broadband UV, optical, NIR, and mid-IR SEDs with the `iSEDfit` modeling code (see Sections 5.2.1 and 5.2.2). The displayed mass for each bin corresponds to the median stellar mass of the samples within that bin. Although other elemental abundance ratios—[O/Fe], [Na/Fe], [Si/Fe], and [Ti/Fe]—are included in the fit, the effects

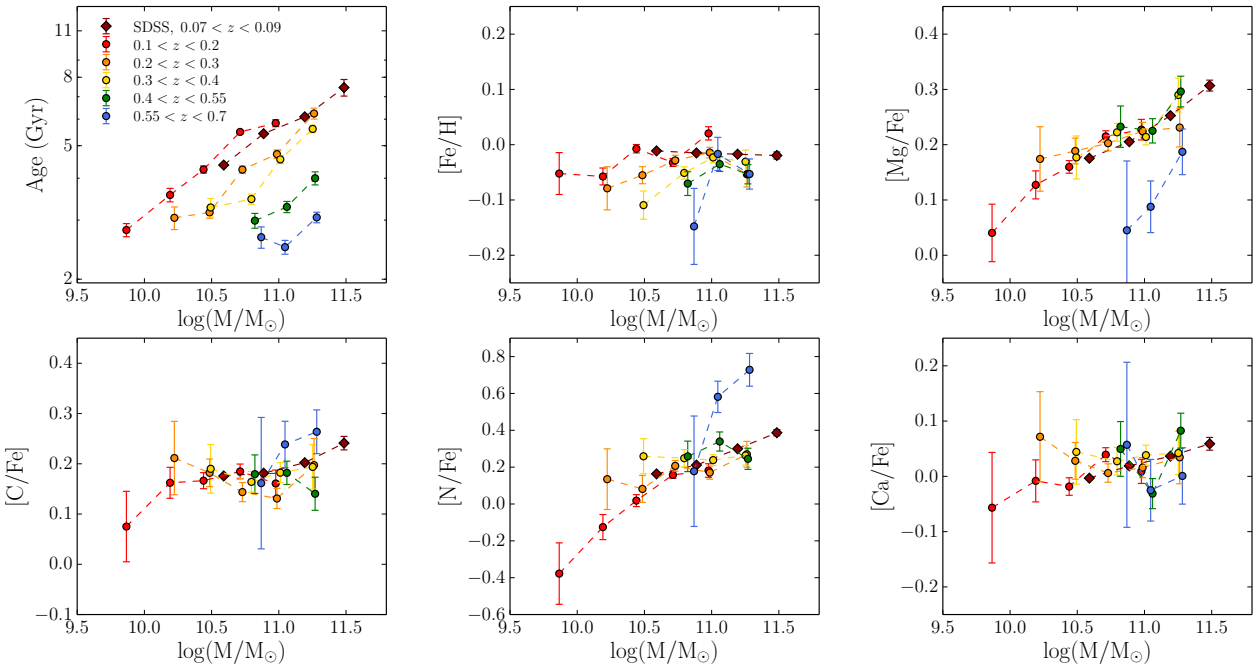


Figure 5.8: Best-fit stellar population parameters shown as a function of stellar mass for SDSS (maroon diamonds) and AGES (red, orange, yellow, green, and blue circles) data. The mass values correspond to the median stellar mass of the samples within each bin. The lowest mass bins are absent at higher redshifts because the parent sample is magnitude-limited and thus does not include distant low-mass galaxies. The error estimates are statistical only and come directly from the Markov Chain Monte Carlo spectrum-fitting algorithm. Note the change in y-axis scale between panels. Overall, the abundance patterns show no evidence for evolution with redshift at fixed stellar mass over the last half of cosmic time.

of these elements on the spectra are smaller than the other elements, so they are not discussed in this paper. As previously mentioned, Na is set to track Mg, and the response functions for O, Si, and Ti require data at other wavelengths for robust results and/or are generally weaker than the others, requiring higher S/N spectra (Conroy et al. 2014). The results are summarized in Table 5.1.

There is good agreement between SDSS and AGES data at $z \sim 0.1$. This implies that the spectroscopic pipelines and other aspects of the data reduction for both surveys contribute minimally to the error budget. Additionally, the difference in spectroscopic fiber size (SDSS fiber is twice as large as the Hectospec fiber for AGES) appears to have little effect, which means that there are no discernible radial gradients between 0.3 and 0.7 R_e. Lastly, as we demonstrate in Section 5.6.0.1, we do not expect the differences in S/N to systematically affect the AGES results relative to the high-S/N SDSS results.

The well-known trend of the most massive galaxies harboring the oldest stellar populations is evident

Table 5.1: Results from Modeling Quiescent Galaxy Spectra .

z	$\log M$ ($M_\odot$)	$R_{\rm fiber}/R_{\rm e}$	$N_{\rm obj}$	S/N (Å^{-1})	Age (Gyr)	[Fe/H]	[C/Fe]	[N/Fe]	[Mg/Fe]	[Ca/Fe]
SDSS										
0.07–0.09	10.6	1.11	19356	2457	4.38 ± 0.01	$-0.01 \pm 0.00^*$	$0.18 \pm 0.00^*$	$0.16 \pm 0.00^*$	$0.18 \pm 0.00^*$	$0.00 \pm 0.00^*$
	10.9	0.76	14189	2702	5.43 ± 0.01	$-0.01 \pm 0.00^*$	$0.18 \pm 0.00^*$	$0.21 \pm 0.00^*$	$0.21 \pm 0.00^*$	$0.02 \pm 0.00^*$
	11.2	0.51	3059	1554	6.10 ± 0.01	$-0.02 \pm 0.00^*$	$0.20 \pm 0.00^*$	$0.30 \pm 0.00^*$	$0.25 \pm 0.00^*$	$0.04 \pm 0.00^*$
	11.5	0.35	62	243	7.45 ± 0.42	-0.02 ± 0.01	0.24 ± 0.01	0.39 ± 0.02	0.31 ± 0.01	0.06 ± 0.01
AGES										
0.1–0.2	9.9	2.97	41	54	2.80 ± 0.13	-0.05 ± 0.04	0.08 ± 0.07	-0.38 ± 0.17	0.04 ± 0.05	-0.06 ± 0.10
	10.2	2.02	83	111	3.57 ± 0.17	-0.06 ± 0.02	0.16 ± 0.03	-0.13 ± 0.07	0.13 ± 0.03	-0.01 ± 0.04
	10.4	1.56	192	215	4.25 ± 0.10	-0.01 ± 0.01	0.17 ± 0.02	0.02 ± 0.03	0.16 ± 0.01	-0.02 ± 0.02
	10.7	1.06	126	228	5.50 ± 0.06	-0.03 ± 0.01	0.18 ± 0.01	0.16 ± 0.02	0.21 ± 0.01	0.04 ± 0.01
	11.0	0.72	23	119	5.84 ± 0.14	0.02 ± 0.01	0.16 ± 0.03	0.18 ± 0.04	0.23 ± 0.02	0.01 ± 0.02
0.2–0.3	10.2	2.95	34	47	3.05 ± 0.24	-0.08 ± 0.04	0.21 ± 0.07	0.13 ± 0.16	0.17 ± 0.06	0.07 ± 0.08
	10.5	2.0	147	121	3.16 ± 0.12	-0.06 ± 0.02	0.18 ± 0.03	0.08 ± 0.07	0.19 ± 0.02	0.03 ± 0.03
	10.7	1.55	253	196	4.24 ± 0.11	-0.03 ± 0.01	0.14 ± 0.02	0.21 ± 0.03	0.20 ± 0.01	0.01 ± 0.02
	11.0	1.05	88	154	4.72 ± 0.14	-0.01 ± 0.01	0.13 ± 0.02	0.17 ± 0.04	0.22 ± 0.02	0.02 ± 0.02
	11.3	0.71	5	58	6.24 ± 0.23	-0.05 ± 0.02	0.20 ± 0.05	0.27 ± 0.07	0.23 ± 0.04	0.03 ± 0.05
0.3–0.4	10.5	2.6	88	72	3.27 ± 0.21	-0.11 ± 0.03	0.19 ± 0.05	0.26 ± 0.10	0.18 ± 0.04	0.04 ± 0.06
	10.8	1.76	260	164	3.47 ± 0.12	-0.05 ± 0.01	0.16 ± 0.02	0.25 ± 0.05	0.22 ± 0.02	0.03 ± 0.03
	11.0	1.36	254	182	4.55 ± 0.13	-0.02 ± 0.01	0.18 ± 0.02	0.24 ± 0.03	0.21 ± 0.01	0.04 ± 0.02
	11.3	0.93	45	85	5.61 ± 0.15	-0.03 ± 0.02	0.19 ± 0.04	0.26 ± 0.05	0.29 ± 0.03	0.04 ± 0.04
0.4–0.55	10.8	2.31	144	75	2.99 ± 0.15	-0.07 ± 0.02	0.18 ± 0.04	0.26 ± 0.08	0.23 ± 0.04	0.05 ± 0.05
	11.1	1.57	285	123	3.28 ± 0.13	-0.04 ± 0.01	0.18 ± 0.02	0.34 ± 0.05	0.23 ± 0.02	-0.03 ± 0.03
	11.3	1.21	122	89	4.00 ± 0.18	-0.05 ± 0.02	0.14 ± 0.03	0.25 ± 0.06	0.30 ± 0.03	0.08 ± 0.03
0.55–0.7	10.9	2.49	24	24	2.67 ± 0.20	-0.15 ± 0.07	0.16 ± 0.13	0.18 ± 0.30	0.05 ± 0.13	0.06 ± 0.15
	11.0	2.18	153	68	2.49 ± 0.12	-0.02 ± 0.03	0.24 ± 0.05	0.58 ± 0.09	0.09 ± 0.05	-0.03 ± 0.06
	11.3	1.48	109	67	3.06 ± 0.11	-0.05 ± 0.03	0.26 ± 0.04	0.73 ± 0.09	0.19 ± 0.04	0.00 ± 0.05
Keck										s
0.83	10.9	...	1	24	5.68 ± 0.28	0.06 ± 0.04	-0.32 ± 0.08	-0.54 ± 0.21	0.31 ± 0.07	-0.23 ± 0.08
0.83	11.1	...	1	27	5.16 ± 0.30	-0.03 ± 0.04	0.06 ± 0.12	-0.23 ± 0.24	0.35 ± 0.08	-0.01 ± 0.07

Notes. Stellar masses are medians within the mass-redshift bins and they assume a Chabrier 2003 IMF. $R_{\rm fiber}/R_{\rm e}$ is estimated using the mass-size relation from Shen et al. 2003 and applying a redshift scaling from Williams et al. 2010 (See Section 5.5.3). Signal to noise is the median between 4000 – 5500 Å. Ages are SSP-equivalent ages. The quoted errors are statistical only, and systematic errors are estimated to be $\lesssim 0.05$ dex (see Section 5.6 and also Conroy et al. 2014). Statistical uncertainties smaller than 0.01 dex are marked with *.

in Figure 5.8. As expected, the age increases with decreasing redshift at a fixed mass. There is no strong evidence for the variation of [Fe/H] with either mass or redshift. Overall, [Fe/H] is very slightly sub-solar, and it varies by $\lesssim 0.05$ dex over the full mass and redshift range. We find a positive trend between [Mg/Fe] and mass, but no evidence of evolution with redshift.

However, [Mg/Fe] abundances for the two lowest mass bins in the highest redshift interval (blue points in top right panel of Figure 5.8) noticeably deviate from the main trend, albeit with large error bars. Mg abundance measurements rely on the Mg *b* feature at ~ 5175 Å, which corresponds to 8000 – 8800 Å in the observed frame for $0.55 < z < 0.7$. The Mg *b* feature at these high redshifts unfortunately falls in

the spectral region affected by atmospheric absorption as well as sky emission features. In particular, there is an H_2O band spanning the wavelength interval 8000 – 8400 Å (Pallé et al. 2009). Between $z = 0.545$ and $z = 0.627$, the Mg *b* absorption feature is redshifted to wavelengths that overlap this atmospheric absorption feature. Since contamination affects continuum-normalization as well as the shape of the Mg *b* feature, we have carried out a test where we selected narrow redshift intervals that avoid the H_2O band, stacked the spectra, and remeasured the Mg abundances. The resulting Mg abundances were consistent with the original results and remained low. We have performed an additional test by stacking a subset of spectra with median S/N > 5 Å^{-1} per galaxy (the highest 50% S/N in the redshift bin). The resulting Mg abundances were again consistent with the original results. As abundance ratios are generally expected to remain constant or decrease, but not increase, with time (see Figure 5.12), we remain skeptical regarding the Mg abundances at these high redshifts. A definitive resolution will require more and deeper spectra, and very careful attention to the sky subtraction and telluric corrections.

Similar to Mg, N and C also increase with mass, though the slope for C is modest and the scatter is larger compared to that of N. However, as in the case of [Fe/H], there is no redshift evolution in these trends. Although formally an α element, Ca tracks Fe and is close to solar. The interpretation is that a significant fraction of observed Ca originates from Type Ia SNe along with the iron-peak elements, rather than from massive stars (Nomoto et al. 1984). *In summary, there is no compelling evidence for redshift evolution in the abundances of quiescent galaxies at a fixed stellar mass*.

Figure 5.9 offers another way of examining the age evolution of quiescent galaxies by showing the evolution with redshift of galaxies at fixed stellar mass. Each set of colored symbols shows a single mass bin from the AGES sample for the three highest mass bins. Lower mass bins are not shown because they do not span a wide range in redshift. The age corresponds to the SSP-equivalent age of the representative galaxy in each mass–redshift bin. The black curves represent the evolution of light-weighted age from FSPS, v2.4 (Conroy et al. 2009, 2010) models with different star formation histories of the form SFR$(t) \propto$

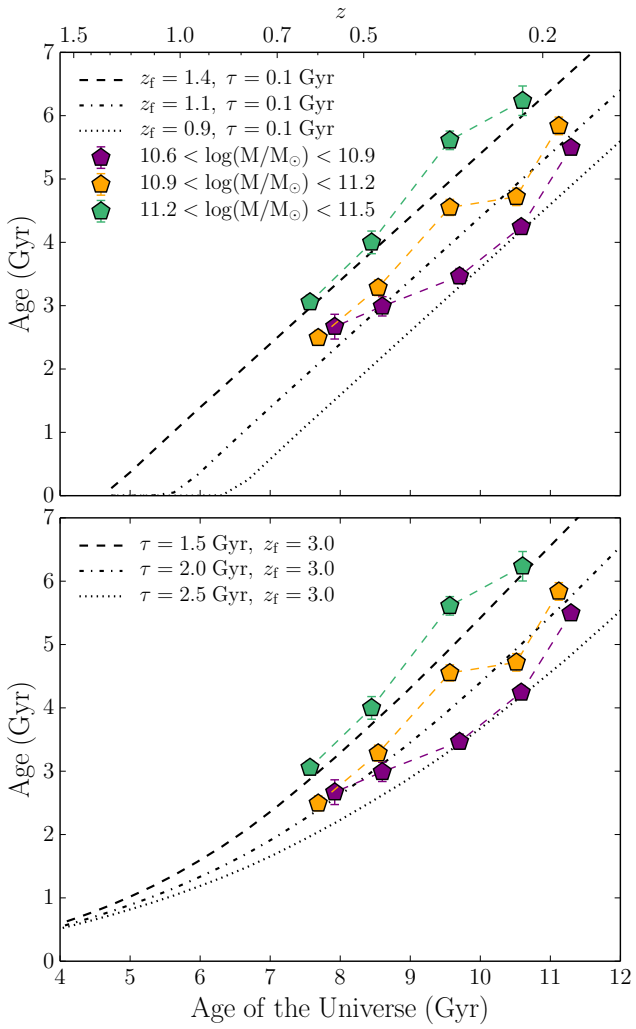


Figure 5.9: *Top panel:* age evolution of AGES galaxies for the three highest mass bins. Lower mass bins are not shown because they do not span a wide range in redshift. Each set of colored pentagons corresponds to a single mass bin. The age corresponds to the SSP-equivalent age of the representative galaxy in the mass–redshift bin. The three curves represent the evolution of light-weighted age of models with different star formation histories of the form $\mathrm{SFR}(t) \propto \exp(-t/\tau)$. The tracks correspond to passive evolution following a burst ($\tau = 0.1$ Gyr) at different formation redshifts, z_f. *Bottom panel:* the same as the top panel, but now for the same formation redshift, $z_f = 3.0$, and varying τ. The age evolution of the most massive galaxies is consistent with passive evolution while there is evidence for a shallower age evolution for the lower mass galaxies shown in this figure. This suggests that the age evolution of the lower mass galaxies is diluted, or slowed down, by the addition of newly-quenched, young galaxies.

$\exp(-t/\tau)$. These are solar-metallicity and dust-free models, and the light-weighted ages are measured at 5000 Å. In the top panel, the tracks correspond to passive evolution following a burst ($\tau = 0.1$ Gyr) at three different formation redshifts, z_f. In the bottom panel, the models have the same $z_f = 3$ but different τ. If $z_f = 2$ is assumed instead, the equivalent track corresponds to a value of τ that is smaller by 0.5 Gyr. The extended star formation histories associated with a large τ value are conceptually equivalent to differ-

ent galaxies in the considered sample undergoing star formation with different starting and ending times, thus implying the inhomogeneous nature of the $z < 1$ quiescent population. Regardless of the details of the adopted star formation histories, massive galaxies in our sample appear to be passively evolving for over half of cosmic time, though more data at $z \gtrsim 1$ will be required to differentiate between the different models. More specifically, the age evolution of the highest-mass galaxies is strongly consistent with passive evolution while there is evidence for a shallower age evolution for the lower mass galaxies shown in this figure. This suggests that the age evolution of these lower mass galaxies is diluted, or slowed down, by the addition of newly-quenched, young galaxies. At even lower masses ($\lesssim 10^{10.5}\ M_{\odot}$), the data do not span a large enough range in redshift to make definitive statements.

5.4.2 Stellar Population Parameters of Quiescent Galaxies in a z=0.83 Galaxy Cluster from Keck DEIMOS Spectra

In addition to the stacked spectra of SDSS and AGES galaxies, we also fit spectra of two individual galaxies (7415 and w5756) in the cluster MS 1054-03 at $z = 0.83$. Figure 5.10 shows the data and the best-fit model. The continuum-normalized fluxes are shown in black while the models are plotted in red in the top panels. The model and data flux have been smoothed by a 3-point boxcar for display purposes only. The bottom panels show the percent fractional residuals between the best-fit models and data in black and the flux uncertainties as the gray shaded region. The region around 4200 Å is masked out and not fit due to the location of the atmospheric *A*-band in the observed frame, and the $\sim$ 5100 Å region is also masked out due to the presence of strong sky OH emission lines. Overall, the quality of the fit is very good and the residuals are consistent with the flux uncertainties.

The resulting best-fit parameters are displayed in magenta symbols in Figure 5.11 along with the SDSS and AGES points shown in gray. The stellar masses of the galaxies come from combining the reported *r*-band magnitudes from Holden et al. (2010) and M/L output from modeling the spectra. Both

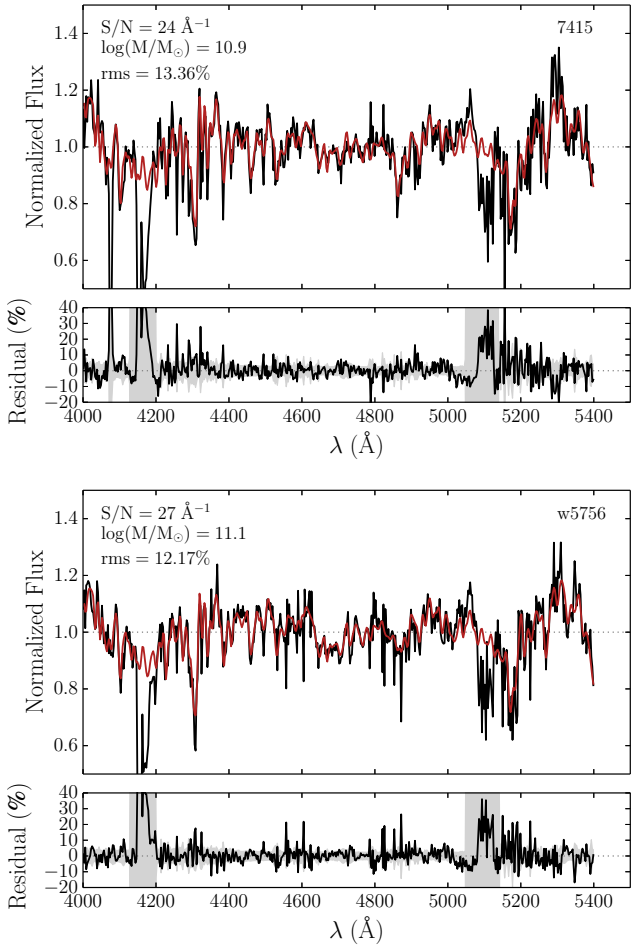


Figure 5.10: Same as Figure 5.5, now for Keck DEIMOS spectra of the two brightest quiescent galaxies in the $z = 0.83$ cluster MS 1054-03 from Holden et al. (2010). The data and model spectra have been smoothed for display purposes only.

galaxies are older than expected from the AGES results but still consistent with the age of the universe at that epoch. At $z = 0.83$, the universe is approximately 6.5 Gyr old, and the galaxies are measured to be approximately 5 Gyr in age. We note that previous studies of the M/L ratios of massive quiescent galaxies did not find large differences between galaxies in low- and high-density environments (e.g. van Dokkum & van der Marel 2007). This may be caused by a difference in selection criteria: many studies of the M/L ratios of galaxies in low-density environments selected objects by color and morphology rather than SFR (see, e.g., van der Wel et al. 2005). The abundances of these cluster galaxies are broadly consistent with the AGES and SDSS trends. However, [C/Fe] and [Ca/Fe] for 7415 and [N/Fe] for both objects are low, though this may be due to the influence of the *A*-band which is partially polluting the CN feature.

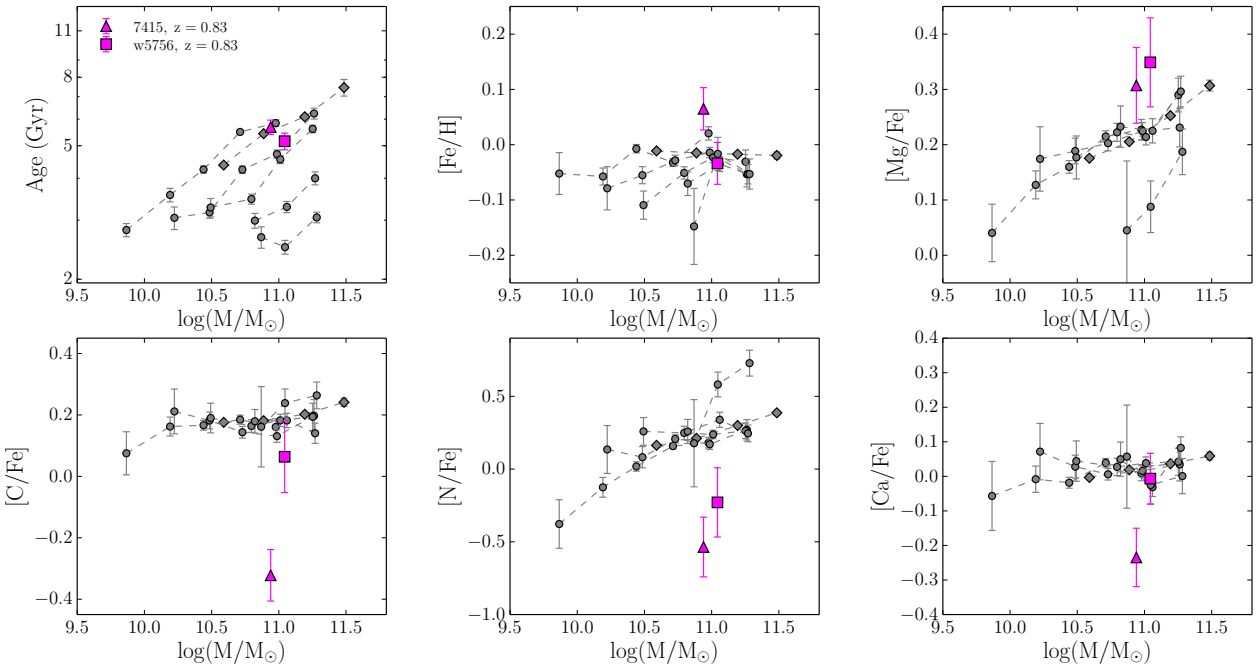


Figure 5.11: Same as Figure 5.8, but now including the two $z = 0.83$ cluster galaxies. The AGES and SDSS data are shown in gray symbols for comparison.

These results serve as interesting and sobering test cases for modeling stellar populations of galaxies at progressively higher redshifts. Although our models work well at low S/N on idealized test cases (see Section 5.6.0.1), the reliable measurement of stellar population parameters also requires clean rest-frame optical spectra. As evidenced here and also in the previous section for the AGES spectra at $0.55 < z < 0.7$, obtaining high-quality spectra becomes very challenging at these redshifts due to the rest-frame optical becoming redshifted to the observed-frame NIR, where telluric absorption and sky emission features dominate. We therefore caution against over-interpreting the results in Section 5.6 when applied to data with strong systematic uncertainties due to sky subtraction and telluric features.

5.5 DISCUSSION

5.5.1 THE ASSEMBLY HISTORIES OF QUIESCENT GALAXIES

Our results indicate that for quiescent galaxies, there is negligible evolution in elemental abundances ($\lesssim 0.1$ dex) at fixed stellar mass over roughly 7 Gyr, and the increase in their ages with cosmic time is consistent with passive evolution since $z = 0.7$ (see Figures 5.8 and 5.9). The stellar masses from SED-fitting nominally represent the total stellar mass. However, since our stellar population analysis is based on spectra obtained with a $1\farcs5$ fiber, the measured parameters are sensitive to stellar populations in the inner regions of galaxies directly probed by the fiber. There are two effects at play: the angular size of galaxies of fixed physical size increases with decreasing redshift and galaxies undergo intrinsic size growth with decreasing redshift. The implications of fiber aperture bias are investigated in Section 5.5.3, where we demonstrate that this has a negligible effect on our conclusions. The conclusion from that section is that we are probing the evolution of the inner ~ 0.3–$3\ R_{\rm e}$ of massive quiescent galaxies.

We compare the main results shown in Figure 5.8 with simple conceptual models in an attempt to interpret the trends in the context of the assembly histories of galaxies. We consider four scenarios, graphically represented in Figure 5.12. The age and abundance ratio (e.g., [Mg/Fe]) trends with mass are well-known in the local universe. In all four panels, we consider a high-redshift population of quiescent galaxies and trace their evolution over time using their age and abundances, rather than starting with the $z = 0$ relation and extrapolating back in time. The stellar population parameters are assumed to be measured within a spectroscopic fiber which has an extent of $\sim 1\ R_{\rm e}$, unless noted otherwise. The stellar mass spans ≈ 1 dex, the age spans ≈ 0.7 dex, and the abundance ratio spans ≈ 0.3 dex in all panels. At low masses, galaxies are assumed to have solar-scaled abundance ratios.

It should be noted that these scenarios are applicable only for $z \lesssim 1$. At the highest redshifts, these relations should break down and the [α/Fe] abundances are predicted to be super-solar at all stellar masses.

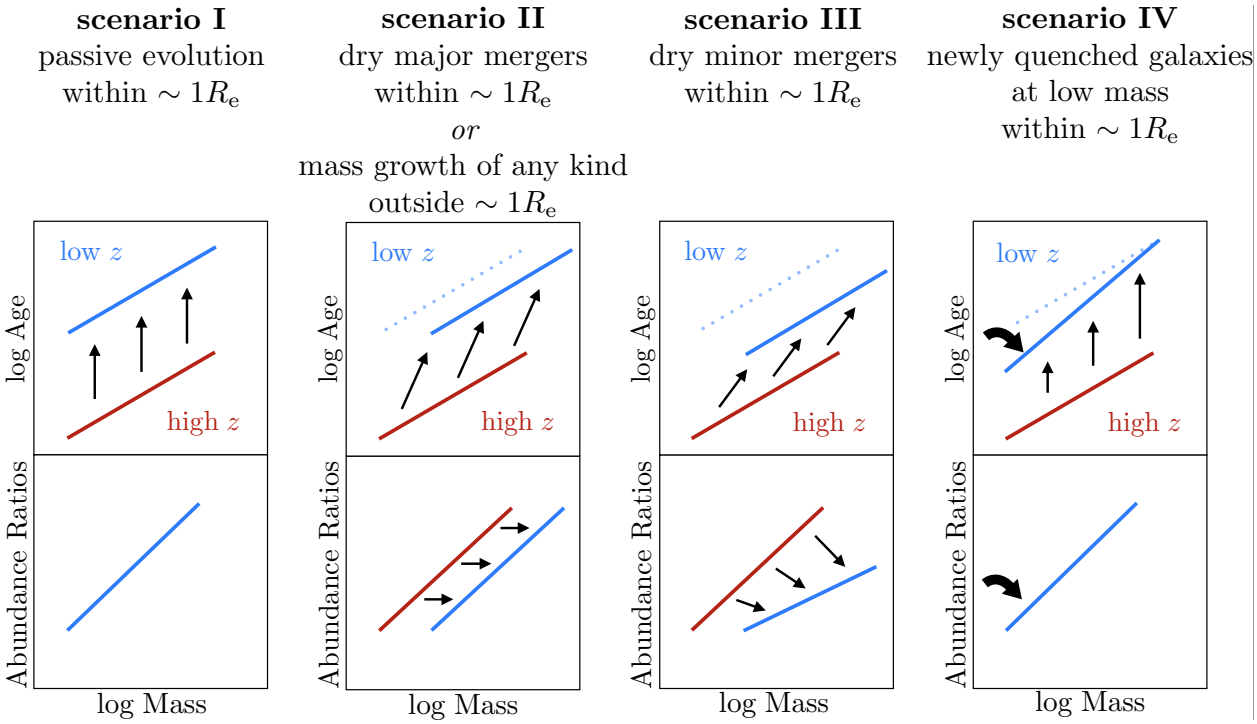


Figure 5.12: Schematic diagrams for the time evolution of age and abundance ratios (e.g., [Mg/Fe]) of quiescent galaxies as a function of their stellar mass for four scenarios. Ages and abundance ratios are assumed to be measured within a spectroscopic fiber which has an extent of $\sim 1\ R_e$, unless noted otherwise. The stellar mass spans ≈ 1 dex, the age spans ≈ 0.7 dex, and the abundance ratio spans ≈ 0.3 dex in all panels. At low masses, galaxies are assumed to have solar-scaled abundance ratios. *First panel*: passive evolution of isolated galaxies. The galaxies simply age over time, and the trend in abundance ratios remains unchanged. *Second panel*: dry major mergers (1:1) where a given galaxy doubles it mass, or mass growth of any kind occurring outside the fiber resulting in the doubling of total mass. For comparison, the low-redshift relation for passive evolution is shown as a dotted blue line. The major merger of two similar galaxies results in a more massive galaxy with stellar population properties that are unchanged. This simply moves the new galaxy to the right toward higher masses. This scenario is also equivalent to a passively evolving stellar population in the inner region accompanied by mass buildup in the outskirts. The accumulation of disrupted galaxies and/or in situ star formation at large radius leads to an increase in total stellar mass and shifts the galaxy to the right, but the spectroscopic data are insensitive to these outer regions and thus stellar population parameters remain unchanged. *Third panel*: dry minor mergers (1:10) within $\sim 1\ R_e$ where a given galaxy doubles its mass. The accretion of a lower mass galaxy "dilutes" both age and abundances, shifting the new galaxy both downward and to the right from the original relation. For an equal fractional gain in mass, the changes introduced to both age and abundance ratios are thus larger for minor mergers compared to major mergers. *Fourth panel*: introduction of newly quenched low-mass galaxies to the passive population. New galaxies are assumed to have solar-scaled abundance ratios. The massive end evolves passively with the universe, but the ages at the low-mass end are lowered due to the presence of younger stellar populations. It should be noted that these scenarios are applicable only for $z \lesssim 1$. At the highest redshifts, these relations should break down and the [α/Fe] abundances are predicted to be super-solar at all stellar masses. This is because a quenched galaxy at very high redshift, regardless of its stellar mass, has to have formed its stars on short timescales to be consistent with the very young age of the universe.

This is because a quenched galaxy at very high redshift, regardless of its stellar mass, has to have formed its stars on short timescales to be consistent with the very young age of the universe.

The first scenario shows the expected evolution of a population of isolated, passively evolving quiescent galaxies. The galaxies simply age over time, and the trend in abundance ratios remains unchanged. For the next two panels, we assume that a given galaxy doubles its total stellar mass through one or more merger events. The second panel illustrates the evolution of quiescent galaxies undergoing dry (i.e., no star formation) major mergers (1:1) or mass growth of any kind occurring outside the fiber resulting in the doubling of total mass. For comparison, the low-redshift relation for passive evolution is shown as a dotted blue line. The major merger of two similar galaxies results in a more massive galaxy with stellar population properties that are unchanged. This simply moves the new galaxy to the right toward higher masses. This scenario is also equivalent to a passively evolving stellar population in the inner region accompanied by mass buildup in the outskirts. The accumulation of disrupted galaxies and/or in-situ star formation at large radius leads to an increase in total stellar mass and shifts the galaxy to the right, but the spectroscopic data are insensitive to these outer regions and thus stellar population parameters remain unchanged. The third panel shows the evolution of quiescent galaxies undergoing dry minor mergers (1:10) within $\sim 1\ R_{\rm e}$. The accretion of a lower mass galaxy "dilutes" both age and abundances, shifting the new galaxy both downward and to the right from the original relation. For an equal fractional gain in mass (i.e., a factor of two in this case), the changes introduced to both age and abundance ratios are thus more severe for minor mergers compared to major mergers. The fourth scenario is a passive evolution model that includes the addition of recently quenched low-mass galaxies, which are assumed to have solar-scaled abundance ratios. The massive end evolves passively with the universe, but the ages at the low-mass end are lowered due to the presence of recently formed stellar populations. These illustrated relations are only meant to represent a simple schematic picture, since the exact relations and relative slopes depend on the details of the merger history as well as the age and abundance distributions of the new quiescent galaxies. Never-

theless, these simple models highlight the power of the measured abundances combined with the age to probe the evolution of quiescent galaxies. All scenarios produce subtle changes in age, which are difficult to reliably detect owing to the systematic uncertainties affecting stellar age measurements. However, in the abundance-mass space, the changes are more pronounced and qualitatively different, thereby enabling greater distinction between the different scenarios.

Our main result is that at fixed stellar mass, the abundance ratios at difference redshifts vary by less than 0.1 dex for most cases. This conclusion is most robust for the massive galaxies ($> 10^{10.5}\ M_{\odot}$) because there are more data spanning a large redshift range at higher masses. The lack of evolution with cosmic time in the mass-abundance ratio correlation leads us to favor scenario I. Taken at face value, these results favor a scenario in which the inner $\sim$ 0.3–3 $R_{\rm e}$ of massive quiescent galaxies have been passively evolving for the past $\sim$ 7 Gyr. As we demonstrate at the end of this section, the results are also consistent with modest mass growth between $z = 0.7$ and $z = 0.1$ in the outskirts (scenario II).

Due to the absence of lower mass galaxies at high redshifts in our sample, we cannot draw definitive conclusions about the evolution of these objects from the data. However, the young ages of these galaxies combined with their roughly solar-scaled abundances indicate that our results are consistent with the addition of new, low-mass quiescent galaxies with solar-scaled abundance ratios (see scenario IV in Figure 5.12). The addition of low-mass quiescent galaxies over time is also favored by simulations (e.g., Cen 2014) as well as independent data, such as evolution in the luminosity and mass functions, which indicate that the number of red galaxies has doubled since $z = 1$ (e.g., Faber et al. 2007; Pozzetti et al. 2010; Moustakas et al. 2013).

As demonstrated in Figure 5.9, the derived SSP-equivalent ages are considerably younger than the age of the universe at all epochs, suggesting an *equivalent* single-burst star formation epoch of $z_{\rm f} \lesssim 1.5$. We stress that $z_{\rm f}$ is a representative parameter, and not suggestive of the *actual* formation epoch. The real SFH is likely more complex and extended in time, but it is a common point of comparison to represent

complex SFHs with an SSP-equivalent, or effective single-burst, epoch (e.g., Treu et al. 2005; van Dokkum & van der Marel 2007). In other words, this result should not be interpreted as the galaxies in each mass–redshift bin having uniformly formed their stars in a single burst at $z_f \lesssim 1.5$. Instead, the low value of z_f implies that our results are inconsistent with all of the stars in the galaxies in our sample having formed at very high redshifts (see also the discussion in Schiavon et al. 2006). The addition of newly quenched galaxies at $z_f \gtrsim 1$ (van Dokkum & Franx 2001) naturally explains the young ages of galaxies in our sample, and is supported by both simulations and observations (e.g., Whitaker et al. 2010; Eliche-Moral et al. 2010; Prieto et al. 2013; Cen 2014; Marchesini et al. 2014). In order to be consistent with the apparent passive evolution since $z = 0.7$, young quiescent galaxies cannot be entering the sample in large numbers at these late times at the highest masses.

The inhomogeneous nature of the $z < 0.7$ quiescent population suggests that there may be variations in the ages of galaxies within a given mass–redshift bin (see also Whitaker et al. 2010). We have tried performing unweighted stacking to ensure that a few bright, young galaxies, which are given more weight during the stacking procedure due to their smaller flux errors, are not driving the ages to low values. The resulting best-fit ages as well as the abundances agree with results from weighted stacking to within 1σ errors, thereby demonstrating that this is a negligible effect. In addition, there is no correlation between S/N and $U - V$ color of individual galaxies within each mass–redshift bin, indicating that there is no obvious bias against the reddest galaxies, i.e., the reddest galaxies are equally likely to have large weights in the stacks as the bluest galaxies in the sample. As discussed in Section 5.6.0.3, the best-fit parameter measured from the stacked spectrum and the weighted average of best-fit parameters from fitting individual spectra agree to within 0.05 dex. Moreover, the unweighted average of the best-fit ages resulting from fitting individual galaxies agrees with the weighted average age to within 1 Gyr. Thus we conclude that these low ages are representative of the galaxies in the sample, though it should be noted that these are still SSP-equivalent ages.

Our results are also consistent with the conclusions from size evolution studies (Daddi et al. 2005; Trujillo et al. 2006; van Dokkum et al. 2008; van der Wel et al. 2008; Cimatti et al. 2008; Bezanson et al. 2009; Damjanov et al. 2009; Williams et al. 2010; Cassata et al. 2010; van Dokkum et al. 2010; López-Sanjuan et al. 2012; McLure et al. 2013; Belli et al. 2013). For example, van Dokkum et al. (2010) found that stellar mass in the central regions (inner 5 kpc) has remained roughly constant with redshift, while the outer regions (out to $\sim$ 75 kpc) of massive quiescent galaxies have been gradually building up over the last 10 Gyr. In other words, stellar populations have been passively evolving in the centers of massive quiescent galaxies, undisturbed by bursts of star formation or merger activities, while the outskirts have been evolving overtime. Mass and size growth is thought to occur mostly via minor mergers, although in-situ star formation may contribute $\sim$ 20% to the total mass buildup (van Dokkum et al. 2010).

As previously discussed, stellar masses quoted in this work nominally represent the total stellar mass. As noted above, the size growth of massive galaxies suggests that they are growing in total mass as well. However, the amount of mass growth from $z = 0.7$ to $z = 0.1$ is not dramatic, amounting to $\lesssim$ 30% or $\lesssim$ 0.15 dex (van Dokkum et al. 2010), which is comparable to the uncertainties in our stellar mass estimates. Moreover, since the adopted mass bins for creating stacked spectra are $\gtrsim$ 0.3 dex wide, the effects of modest mass growth (e.g., 0.15 dex) will not be discernible in the present work. In other words, our main results taken at face value favor a passively evolving stellar population since $z = 0.7$, but they are also consistent with modest mass growth in the outskirts over time.

5.5.2 Comparisons to Previous Work

Our results broadly agree with previous work on stellar populations in quiescent galaxies at low redshift (e.g., Trager et al. 2000; Saglia et al. 2002; Cenarro et al. 2003; Eisenstein et al. 2003; Thomas et al. 2003; Worthey 2004; Thomas et al. 2005; Sánchez-Blázquez et al. 2006a; Graves et al. 2007; Schiavon 2007; Graves & Schiavon 2008; Matković et al. 2009; Smith et al. 2009; Zhu et al. 2010; Johansson et al.

2012; Worthey et al. 2014; Conroy et al. 2014). The primary conclusions from low-redshift studies, including our own, is that more massive galaxies are older, more metal-rich, and have enhanced abundance ratios in the elements Mg, C, and N compared to lower mass galaxies.

Owing to the demanding S/N requirements, there have been relatively few studies* of stellar abundances patterns at $z \gtrsim 0.1$. Kelson et al. (2006) examined 19 cluster elliptical and lenticular galaxies at $z = 0.33$ and measured the age and abundance ratios using eight blue Lick/IDS indices. Interestingly, while they found that total metallicity and [N/Fe] are tightly correlated with velocity dispersion, they did not find significant variations in age, [α/Fe], nor [C/Fe] with velocity dispersion.

Sánchez-Blázquez et al. (2009) analyzed stacked spectra of 215 red-sequence galaxies in cluster and group environments from $z \sim 0.75$ to 0.45 using Lick/IDS indices. The authors confirmed that massive galaxies have $Z \sim Z_{\odot}$ and are enhanced in α-elements. Additionally age variation was found to be consistent with passive evolution, all in agreement with the present work. They concluded that massive galaxies formed their stars at high redshift and passively evolved with time, while lower mass galaxies experienced longer star formation episodes and thus have constant luminosity-weighted ages over the redshift range considered. Also in qualitative agreement with our results, they demonstrated that the total metallicity and [α/Fe] as a function of velocity dispersion (or mass) are constant with time.

Schiavon et al. (2006) went beyond the cluster environment and pushed to even higher redshifts, analyzing Keck DEIMOS spectra of $0.7 \leq z \leq 0.9$ red field galaxies. Their stellar population synthesis modeling showed that $z \sim 0.9$ galaxies have mean light-weighted ages of only 1 Gyr. The authors concluded that either individual galaxies are experiencing low-level star formation (i.e., "frosting") or galaxies with younger stars are continually being added to the quiescent population. Interestingly, the time elapsed be-

*During the refereeing process, we became aware of Gallazzi et al. (2014), who analyzed optical spectra of $\sim$ 70 star-forming and quiescent galaxies in the redshift range $0.65 \geq z \geq 0.75$ and obtained relations between light-weighted stellar age, stellar mass, and stellar metallicity for both the total galaxy population and for star-forming and quiescent galaxies separately. The authors concluded that both the metallicity and age evolutions of the quiescent galaxies at $z = 0.7$ are consistent with passive evolution, in excellent agreement with our results.

tween $z \sim 0.9$ and $z \sim 0.7$ is roughly 1 Gyr, and we estimate the youngest $z \sim 0.7$ AGES galaxies to be approximately 2–3 Gyr in age. It is thus plausible that the $z \sim 0.9$ quiescent galaxies from Schiavon et al. (2006) are progenitors of the $z \sim 0.7$ galaxies in our sample.

Recently, Jørgensen & Chiboucas (2013) analyzed the stellar populations of quiescent galaxies in three galaxy clusters at $z = 0.54$, 0.83, and 0.89, and inferred that while the evolution in the fundamental plane is consistent with passive evolution, the variations in total metallicity and [α/Fe] with redshift appear to be inconsistent with a passive evolution scenario in the redshift interval considered. Their velocity dispersion-line indices scaling relations indicate that the blue metal lines are stronger than expected for passive evolution.

At least some of the discrepancies between conclusions of previous work and our favored interpretation can be attributed to differences in the analysis (e.g., different stellar population synthesis models) and sample selection. The present work selects quiescent galaxies based on sSFR estimated from SED-fitting, but other options for quiescence selection include various combinations of morphological, emission line, S/N, and/or color cuts. In contrast to our quiescent sample which was selected to be mass-complete, most previous high-redshift studies specifically targeted group and cluster environments (of the four discussed above, only Schiavon et al. 2006 examined field galaxies) due to the efficiency of obtaining many simultaneous spectra with current generation multi-object spectrographs. Typically a few groups or clusters were analyzed at a time, rendering the task of connecting the results to the global quiescent galaxy population difficult as the results can be affected by small-number statistics. These factors make a straightforward and detailed comparison between our results and previous work very challenging.

The role of environment on stellar population properties at fixed stellar mass is a subject of ongoing debate in the literature (Sánchez-Blázquez et al. 2003; Eisenstein et al. 2003; Thomas et al. 2005; Sánchez-Blázquez et al. 2006a; Trager et al. 2008; Toloba et al. 2009; Zhu et al. 2010; Thomas et al. 2010; Johansson et al. 2012). In the present work, we have found that the Keck DEIMOS sample consisting of

two bright quiescent galaxies in a $z = 0.83$ cluster are older compared to the average quiescent galaxy at $z = 0.7$, but their ages are consistent with the age of the universe at $z = 0.83$. The results hint at the impact of environment on stellar populations of galaxies, but larger samples will be required to verify these tantalizing trends.

5.5.3 Radial Gradients and Fiber Size

An important effect that needs to be considered is the fraction of the galaxy observed as a function of both the fiber size and the redshift of the galaxy. The Hectospec instrument on the MMT has a fiber that subtends $1\farcs5$ on the sky, whereas the SDSS spectroscopic fiber has a diameter of $3''$ For reference, $1\farcs5$ corresponds to 2.8 kpc and 10.7 kpc at $z = 0.1$ and 0.7, respectively. There are two effects that need to be considered. First, the angular extent of a galaxy of fixed physical size is larger at smaller redshift. Second, quiescent galaxies are believed to have been growing in both size and mass over the last $\sim$10 Gyr (e.g., Naab et al. 2009; van Dokkum et al. 2010). This implies that we are sampling different fractions of the galaxy at different redshifts, both due to the varying angular diameter distance and to the intrinsic growth of the galaxy with redshift. In the presence of radial gradients, this could introduce a bias (with respect to the global properties of the galaxy) in the inferred stellar population parameters.

Spatially resolved observations of galaxies at low redshift have enabled radial gradient measurements of various stellar population parameters (e.g., Gorgas et al. 1990; Sánchez-Blázquez et al. 2007; Baes et al. 2007; Brough et al. 2007; Rawle et al. 2010; Spolaor et al. 2010; Loubser & Sánchez-Blázquez 2012; La Barbera et al. 2012; Greene et al. 2013). Greene et al. (2013) measured the radial gradients of a sample of 33 massive quiescent galaxies and found a modest negative gradient in [Fe/H] and a strong radial decline in [C/Fe], but almost constant [Mg/Fe], [N/Fe], and [Ca/Fe] out to 2.5 R_e. Additionally, the age gradient was measured to be very weak or nonexistent. Similarly, Spolaor et al. (2010) inferred almost no radial gradient in age and [α/Fe] but a weak negative gradient in [Z/H] from a sample of 37 massive quiescent

galaxies. From these local studies it thus appears unlikely that our age and [α/Fe] measurements are biased by the sampling radius of the fiber, but we cannot immediately rule out the possibility that our [Fe/H] and [C/Fe] measurements are affected by radial gradients.

We carry out simple simulations to quantitatively assess this possibility. We investigate [Fe/H] only, but similar conclusions can be drawn for [C/Fe]. We adopt a metallicity gradient from Spolaor et al. (2010), corresponding roughly to $\nabla_{[\mathrm{Fe/H}]} \equiv \Delta[\mathrm{Fe/H}]/\Delta\log(R/R_\mathrm{e}) = -0.23$ dex decade^{-1} over the range 0.5 R_e–2.5 R_e, assuming that [Z/H] $\propto$ [Fe/H]. The metallicity profile $[\mathrm{Fe/H}](r)$ is convolved with an $n = 4$ Sersic profile $I(r)$ to obtain a light-weighted average metallicity within a given radius, $\langle[\mathrm{Fe/H}](r)\rangle$. The effects of seeing ($\approx 1\farcs5$ for AGES, which is comparable to the diameter of the fiber) is ignored because while light is scattered out of the fiber, light from larger radius is also scattered inward. Thus light captured by the fiber is actually sampled from a larger radius, on average, thereby effectively reducing the magnitude of aperture bias. Here we define f_origin, the fraction of light originating from outside the fiber radius that is scattered into the fiber, i.e., $f_\mathrm{origin} = 0$ in the absence of seeing. In the high-z limit where the fiber size and seeing are larger than the effective radius, suppose by a fiducial factor of three, $f_\mathrm{origin} \approx 0.1$. In the low-$z$ limit where the effective radius is roughly three times larger than both the fiber and the seeing, $f_\mathrm{origin} \approx 0.3$, which is non-negligible. In the calculations below we do not include the effects of seeing because it provides the worst-case scenario for bias effects.

The bias introduced as a result of observing within an aperture of radius r is calculated following Moustakas et al. (2011):

$$\Delta\langle[\mathrm{Fe/H}](r)\rangle = \langle[\mathrm{Fe/H}](r)\rangle - \langle[\mathrm{Fe/H}]_\infty\rangle \,, \tag{5.1}$$

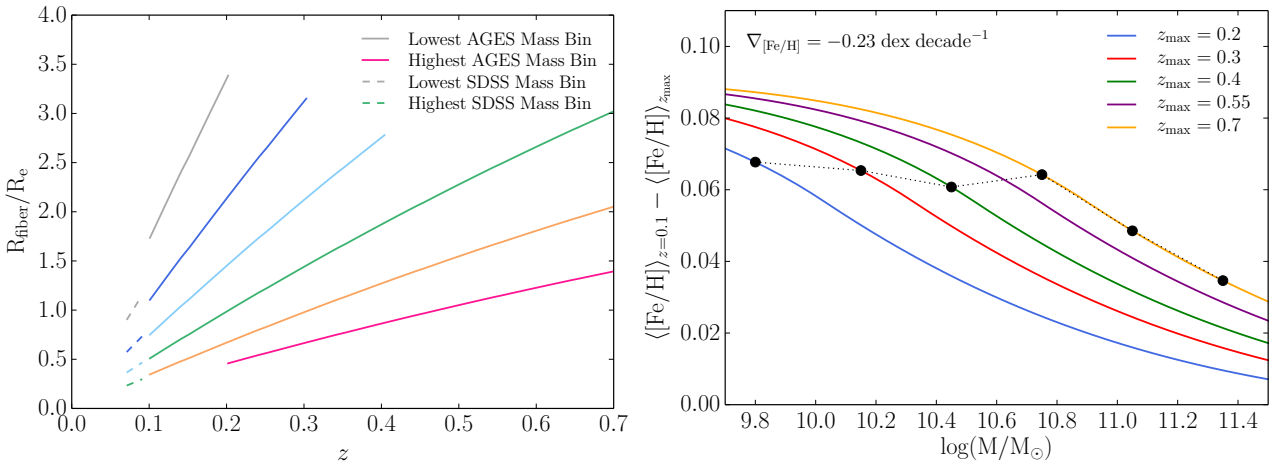


Figure 5.13: *Top panel:* the ratio of fiber radius to the effective radius as a function of redshift. The effective radius is computed by assuming a mass-size relation at $z \sim 0$ from SDSS data (Shen et al. 2003) and applying a redshift evolution scaling $R_e \propto (1+z)^{-1}$ (e.g., Williams et al. 2010). Each curve spans the entire redshift range sampled by the data in each mass bin. The dashed and solid lines correspond to SDSS and AGES data, respectively. The mass bins increase from top to bottom (gray to pink). The mid-bin values for each mass interval are $\log(M/M_\odot) = 9.80$, 10.15, 10.45, 10.75, 11.05, and 11.35 for AGES, and $\log(M/M_\odot) = 10.58$, 10.93, 11.28, and 11.63 for SDSS. *Bottom panel:* the differences in inferred [Fe/H] between $z = 0.1$ and five different values of z ranging from 0.2 to 0.7, shown in different colored curves for a metallicity gradient of $\nabla_{[Fe/H]} \equiv \Delta[Fe/H]/\Delta\log(R/R_e) = -0.23$ dex decade^{-1}. The black circles represent the maximum aperture bias between the lowest and highest redshift bins within each AGES stellar mass bin.

where

$$\langle[Fe/H](r)\rangle = \frac{\int_0^r [Fe/H](r')I(r')r'dr'}{\int_0^r I(r')r'dr'}, \tag{5.2}$$

and $\langle[Fe/H]_\infty\rangle$ is the same quantity integrated out to ∞. For $\nabla_{[Fe/H]} = -0.23$ dex decade^{-1}, the bias introduced is relatively modest, corresponding to ≈ 0.08 dex and ≈ 0.05 dex when probing 0.5 R_e and 2 R_e, respectively. When the gradient is twice as strong, akin to that found by Greene et al. (2013), the resulting bias is roughly doubled.

The goal of this section is to investigate how much apparent evolution in [Fe/H] in our sample could be due to the effects of aperture bias. We estimate the average sizes of our quiescent galaxies as a function of redshift (direct size estimates are unfortunately not available for individual galaxies) to determine the fraction of the galaxy probed by the spectroscopic fiber as a function of redshift. To do this we assume

a mass-size relation at $z \sim 0$ from SDSS data (Shen et al. 2003) and apply a redshift evolution scaling $R_e \propto (1+z)^{-1}$ (e.g., Williams et al. 2010). The top panel of Figure 5.13 shows the ratio of fiber radius to the effective radius as a function of redshift. Next, we compute the differences in inferred [Fe/H] between $z = 0.1$ and five different values of z ranging from 0.2 to 0.7 purely due to the sampled fraction of the galaxy evolving with redshift, shown as different colored curves in the bottom panel of Figure 5.13. The black circles represent the maximum aperture bias between the lowest and highest redshift bins within each AGES stellar mass bin. At lower masses, an apparent evolution of ≈ 0.06 dex is induced due to the evolving aperture bias, implying that for an intrinsically unevolving population, we would observe [Fe/H] to increase by ≈ 0.06 dex with time in the redshift range probed (e.g., from $z = 0.4$ to $z = 0.1$ for the third lowest mass bin). Apparent evolution is the strongest for low-mass galaxies, and the effect becomes weaker with increasing mass.

If radial gradients in [Fe/H] are present in our sample at the level we have assumed for this test, then this apparent evolution can masquerade as a true intrinsic evolution in stellar population parameters purely as a consequence of probing different fractions of the galaxy. However this is a small effect, amounting to at most $\lesssim 0.06$ dex in our sample (or $\lesssim 0.1$ dex in the more extreme case where the gradient is twice as strong for our sample of quiescent galaxies). Moreover, if we account for the effects of seeing, the magnitude of the bias would be even smaller. In comparison, the observed variation in the stellar population parameters as a function of redshift is $\lesssim 0.1$ dex (see Figure 5.8). Thus we conclude that aperture bias has a minor effect on the interpretation of our results.

5.6 Quantifying Systematic Uncertainties

In this section we carry out several systematic tests to explore the robustness of our analysis tools and methods. First we explore how our full spectrum fitting model behaves at low S/N. Next we examine the effect of smoothing the spectra to higher effective velocity dispersions. Lastly, we compare the distribu-

tions of resulting parameters measured from individual spectra against the results derived from a stacked spectrum. In summary, these systematic tests show that both the age and abundance measurements are generally very robust, resulting in systematic uncertainties of $\lesssim 0.05$ dex in most cases.

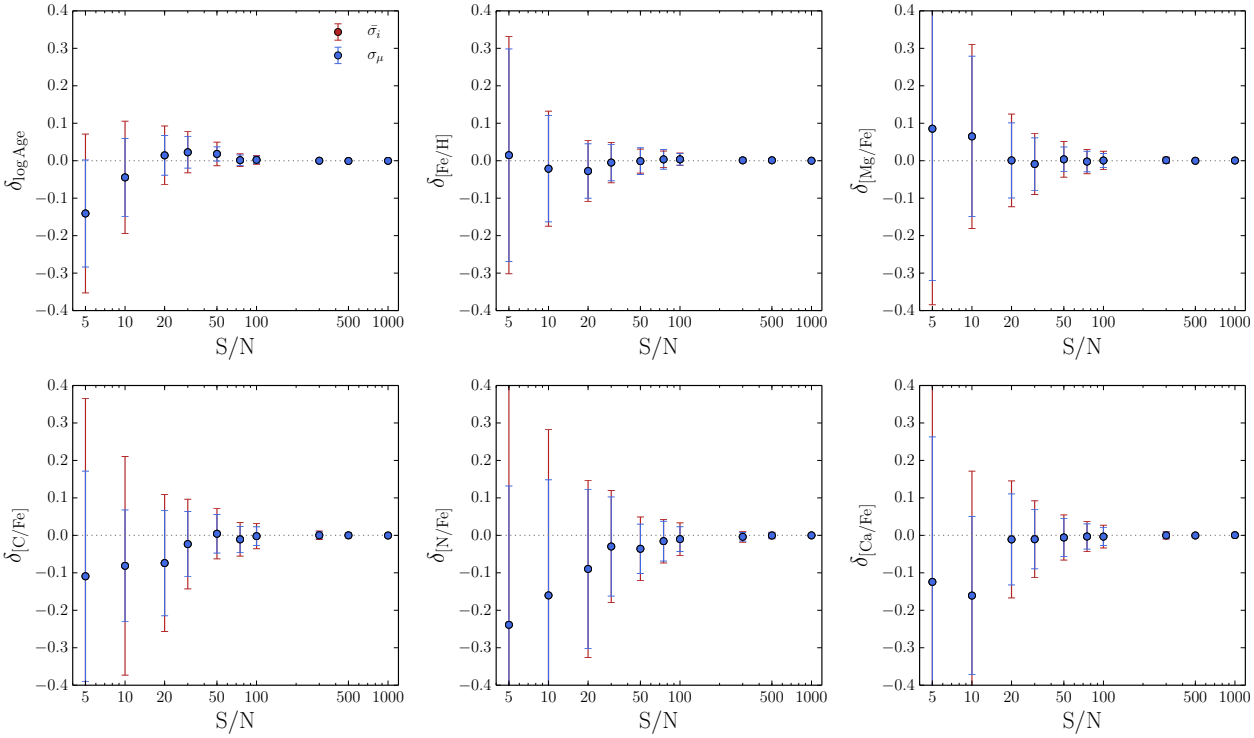


Figure 5.14: Difference between parameters measured from artificially degraded spectra and the original high-quality SDSS stacked spectrum. We construct 50 realizations at each S/N. The different colored symbols represent two independent error estimates, where the red is the average of the 50 errors measured by the fitting code and the blue corresponds to the 1σ scatter of the 50 measured parameters. Age and [Fe/H] are accurately recovered without significant systematic offsets down to S/N ≈ 10 Å^{-1}. [Mg/Fe] and [Ca/Fe], on the other hand, require S/N ≈ 20 Å^{-1}, and [C/Fe] and [N/Fe] demand S/N ≈ 30 Å^{-1}.

5.6.0.1 Parameters as a Function of S/N

To test the ability of our models to recover parameters at low S/N, we have artificially degraded high S/N spectra, fit them with our models, and compared the derived fits to the results at high S/N. We select a S/N > 1000 Å^{-1} SDSS stack corresponding to the second highest mass bin to carry out this test. Since the model spectra utilized in the fitting code are constructed from solar-scaled empirical stellar spectral library, we purposefully use the a high-mass bin (second highest rather than the highest due to its sufficiently high

S/N) to test whether or not we can successfully recover non-solar abundance measurements. The S/N at 5000 Å in the original spectrum is used as the reference value in the following test. We construct 50 realizations for each S/N value, and compute the difference between the resulting parameter and the best-fit parameter from fitting the high S/N template spectrum. The results are shown in Figure 5.14. The different colored symbols represent two independent error estimates, where the red is the average of the statistical errors for the 50 trials as output by the fitting code, and the blue corresponds to the 1σ scatter in the best-fit parameters for the 50 trials.

There are two remarkable features of this figure. First, the age and [Fe/H] are accurately recovered without significant systematic offsets down to S/N ≈ 10 Å^{-1}. [Mg/Fe] and [Ca/Fe], on the other hand, require S/N ≈ 20 Å^{-1}, and [C/Fe] and [N/Fe] demand S/N ≈ 30 Å^{-1}. Second, the two uncertainty estimates are broadly comparable, though the errors estimated by the spectrum fitting code may be conservative.

We discuss two caveats regarding the results. First, the results generally become biased toward the mean of the prior at low S/N. In the limit of S/N $= 0$ Å^{-1}, the fit is unconstrained and the resulting best-fit parameter is trivially the mean of the prior regardless of its true value, with the width of the prior as the uncertainty. Thus the conclusions here are appropriate for the sample in this paper, and should be treated with caution when applied to low S/N spectra of galaxies with unusually extreme stellar population properties. Second, as discussed in Section 5.4.2, we also urge caution with data containing strong systematic uncertainties due to sky subtraction and telluric features. The reliable measurement of stellar population parameters not only hinges on robust models but also on clean rest-frame optical spectra.

Figure 5.15 shows the uncertainty on the parameters as a function of S/N per Angstrom. The solid green line is the theoretical expectation $\sigma = (\mathrm{S/N})^{-1}$, and the dashed line labeled J12 is the S/N relation measured in the g-band from Johansson et al. (2012). This relation comes from fitting models to 25 standard Lick absorption line indices measured from SDSS quiescent galaxy spectra. The yellow points are error estimates from fitting a representative sample of individual AGES spectra, and the red symbols are

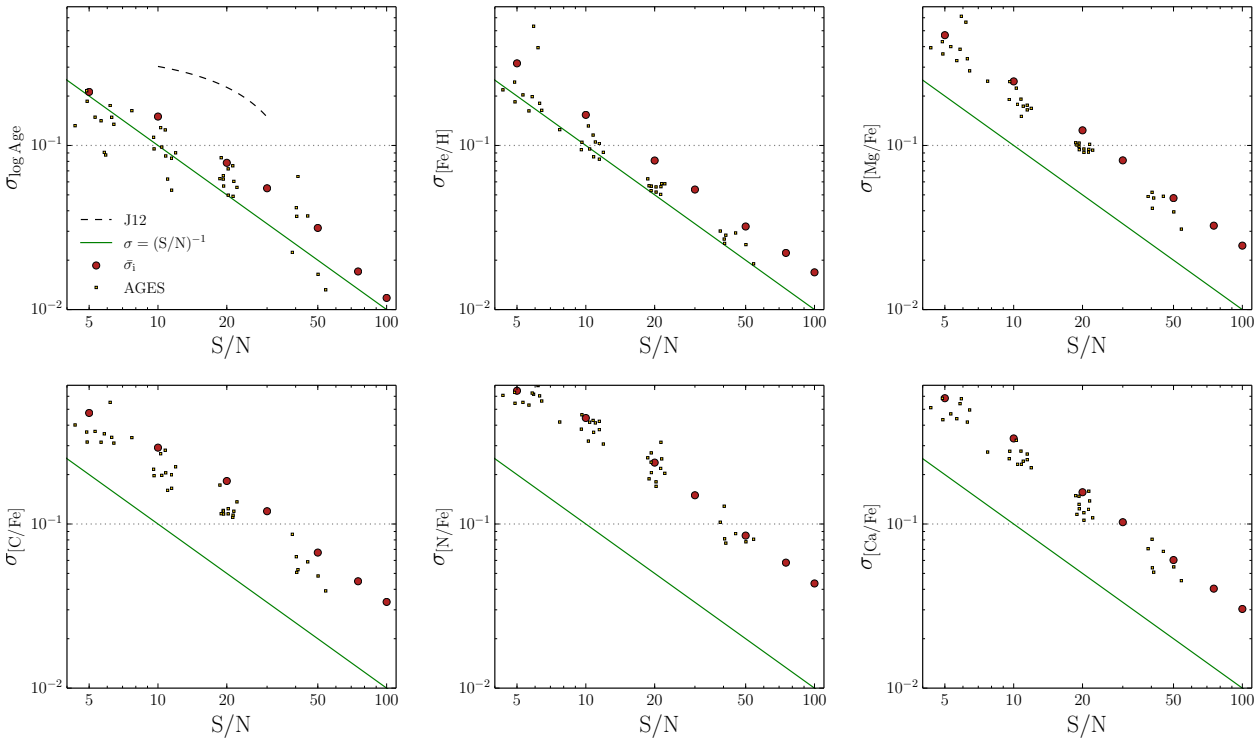


Figure 5.15: Uncertainty on the parameters as a function of S/N per Angstrom. The solid green line is the theoretical expectation, and the dashed line labeled J12 is the S/N relation from Johansson et al. (2012) derived from fitting Lick indices to the spectra. The yellow points are errors on the best-fit parameters from individual AGES spectra, and the red symbols are the average of the 50 errors measured by the fitting code (the same red error bars from Figure 5.14). Comparison in this figure between the simulated Gaussian noise result and the real AGES data shows that our assumption of ideal, uncorrelated noise for the former is a reasonable approximation. In addition, the errors are well-behaved and scale as expected. Age and [Fe/H] are reliably measured to ≈ 0.1 dex errors at S/N ≈ 10 Å^{-1}, while [Mg/Fe] and [Ca/Fe] are reliably measured to ≈ 0.1 dex errors at S/N ≈ 20 Å^{-1}. [C/Fe] and [N/Fe], on the other hand, require S/N $\approx$ 30–50 Å^{-1} for ≈ 0.1 dex errors.

the average of the 50 errors measured by the fitting code (the same red error bars from Figure 5.14). Comparison in this figure between the simulated Gaussian noise result and the real AGES data shows that our assumption of ideal, uncorrelated noise for the former is a reasonable approximation. The derived errors are well-behaved and scale as expected, though the errors are larger probably due to degeneracies. Age and [Fe/H] are reliably measured to ≈ 0.1 dex errors at S/N ≈ 10 Å^{-1}, while [Mg/Fe] and [Ca/Fe] are reliably measured to ≈ 0.1 dex errors at S/N ≈ 20 Å^{-1}. [C/Fe] and [N/Fe], on the other hand, require S/N $\approx$ 30–50 Å^{-1} for ≈ 0.1 dex errors. It is important to note, however, that these errors are statistical only.

5.6.0.2 PARAMETERS AS A FUNCTION OF VELOCITY DISPERSION

Now we turn our attention to exploring systematics arising due to the Doppler broadening of the spectra. To make our test spectra, we divide individual SDSS spectra into two groups ($\sigma < 150$ km s^{-1} and $\sigma \geq 250$ km s^{-1}). Spectra in each group are smoothed to $\sigma = 150$ km s^{-1} and $\sigma = 350$ km s^{-1}, continuum-divided, and stacked to create the template spectra. Next, each template spectrum is convolved with a Gaussian kernel whose width is chosen such that $\sigma^2_{\rm target} = \sigma^2_{\rm kernel} + \sigma^2_{\rm original}$. This convolution increases the effective velocity dispersion of the spectrum. The difference between the parameters measured from these smoothed spectra and the original unsmoothed spectrum is shown in Figure 5.16. The vertical dotted line marks $\sigma = 350$ km s^{-1}, the effective velocity dispersion to which we broaden our science spectra for the stacking procedure. When $\sigma < 150$ km s^{-1} spectra are smoothed to 350 km s^{-1}, there is almost no bias for [Mg/Fe], [C/Fe], and [Ca/Fe]. On the other hand, only a modest systematic offset of $\lesssim 0.05$ dex is introduced at 350 km s^{-1} for age, [Fe/H], and [N/Fe]. Moreover, there appears to be relatively small bias introduced in smoothing spectra even up to ~ 1000 km s^{-1}, which is quite remarkable. A velocity dispersion of 1000 km s^{-1} corresponds to a resolution of $R \sim 130$. Grism spectra often achieve resolving powers of ~ 100, suggesting that we may be able to recover reliable abundance patterns even from such low resolution data.

5.6.0.3 THE EFFECTS OF STACKING SPECTRA

As described in Sections 5.2.1 and 5.2.2, we bin the individual spectra by mass and redshift, smooth them to an effective velocity dispersion of $\sigma = 350$ km s^{-1}, and stack the spectra together. The objective is to test whether the stacked spectrum produces results that are consistent with fitting individual, unsmoothed spectra in each bin and then averaging the individual best-fit parameters. To carry out this test, we use the highest-mass SDSS bin for computational feasibility since it contains 62 objects rather than

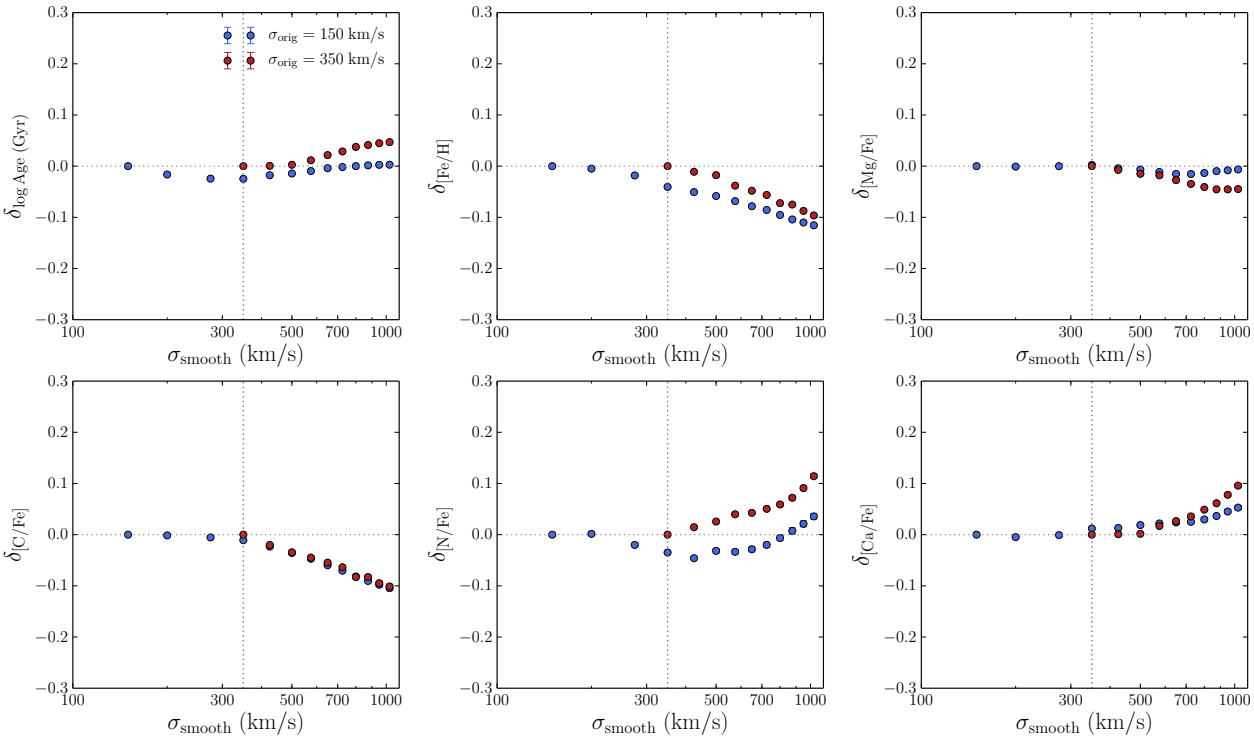


Figure 5.16: Difference between parameters measured from artificially broadened spectra and the original unsmoothed SDSS stacked spectra. The vertical dotted line denotes $\sigma = 350$ km s^{-1}, the effective velocity dispersion to which we smooth all of our science spectra. When $\sigma < 150$ km s^{-1} spectra are smoothed to 350 km s^{-1}, there is almost no bias for [Mg/Fe], [C/Fe], and [Ca/Fe]. On the other hand, only a modest systematic offset of $\lesssim 0.05$ dex is introduced at 350 km s^{-1} for age, [Fe/H], and [N/Fe]. In addition, there are only modest offsets ($\lesssim 0.1$ dex) when the spectra are smoothed to $\sigma = 1000$ km s^{-1}.

$\sim 3000 - 20000$ as in other bins. Histograms of parameters measured from fitting individual spectra are shown in Figure 5.17. The green and red lines correspond, respectively, to the best-fit parameter measured from the stacked spectrum and the weighted average of the distribution. Their corresponding uncertainties are shown as shaded regions. If there were no systematic effects introduced during the stacking process, then we would expect the green and the red lines to overlap to within the uncertainties. The two quantities are in excellent agreement to within 0.05 dex. Weighted average and unweighted average are also comparable to within ≈ 0.05 dex. This test demonstrates that analyzing stacked spectra is essentially equivalent to analyzing individually each spectrum that contributed to the stack.

For the abundances, the width of the distribution is comparable to the measurement uncertainties for the individual galaxies, implying that there is no evidence for an abundance spread within the bin. For

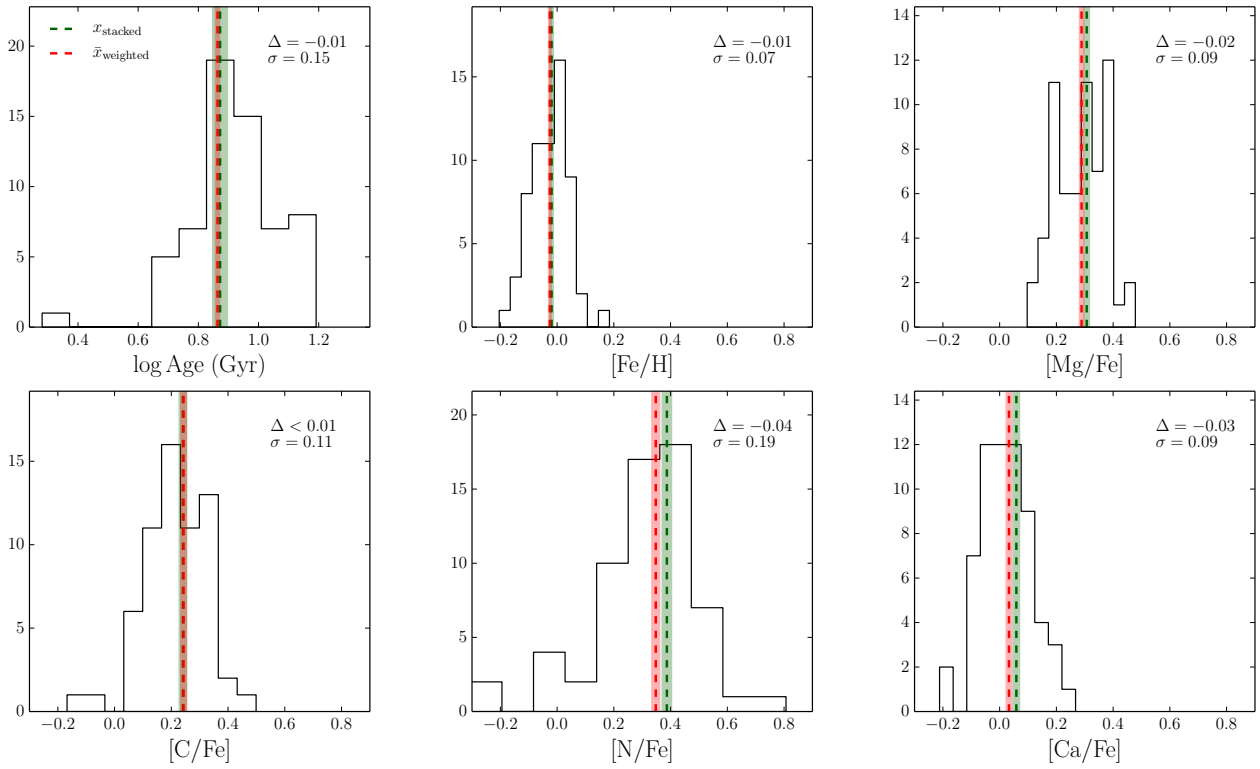


Figure 5.17: Histograms of parameters measured from individual SDSS spectra in the highest mass bin. The green and red lines correspond, respectively, to the best-fit parameter measured from the stacked spectrum and the weighted average of the distribution. Their corresponding uncertainties are shown as shaded regions. The difference between the two quantities and the standard deviation of the distribution are displayed in the top right corner of each panel. The median of each distribution tracks the weighted average very closely, and is thus not displayed. The green and red lines are in excellent agreement, which means that no significant biases are introduced when analyzing stacked spectra.

the ages, on the other hand, the measurement uncertainties can only account for approximately half of the width of the distribution. Thus there must be an intrinsic variation in the ages of the galaxies within this sample. A more stringent version of the test would involve greater variations within the bin. Exploration of parameter variations within stellar mass bins will be the subject of future work.

5.7 Summary

In this paper we measured SSP-equivalent ages and detailed abundance patterns of quiescent galaxies using stacked SDSS and AGES spectra and individual spectra of two brightest $z = 0.83$ cluster galaxies from Holden et al. (2010). The main sample spans a redshift interval of $0.1 < z < 0.7$ and a stellar mass

range from $10^{9.6}$ to $10^{11.8}$ $M_{\odot}$. We selected quiescent galaxies based on their star formation rates estimated from SED-fitting. The AGES sample of quiescent galaxies were divided into five redshift intervals each spanning roughly 1 Gyr in cosmic time and further divided into mass bins. The mass bins were chosen such that the sample was complete in stellar mass at each redshift. The stacked spectra were fit using a full spectrum modeling MCMC code developed by Conroy & van Dokkum (2012). We also carried out a variety of systematic tests to examine the robustness of the modeling code. We now summarize our main results.

1. We confirm earlier results of stellar population modeling of quiescent galaxies at low redshift. Massive galaxies harbor old stellar populations with roughly solar [Fe/H] abundances and enhanced [Mg/Fe], [C/Fe], and [N/Fe] abundance ratios. Adopting [Mg/Fe] as a star-formation timescale indicator, massive galaxies seem to form their stars on shorter timescales compared to lower mass galaxies.

2. There is negligible evolution in the abundances of Fe, Mg, C, N, and Ca at fixed stellar mass over roughly 7 Gyr of cosmic time, and the evolution of the stellar ages of massive galaxies is consistent with passive evolution since $z = 0.7$. The 0.1 dex or smaller variation in abundance ratios (e.g., [Fe/H], [Mg/Fe], [Ca/Fe]) as a function of stellar mass from $z = 0.1$ to $z = 0.7$ puts a stringent constraint on the assembly histories of galaxies over the redshift interval considered. Our results support the passive evolution of the inner $\sim$ 0.3–3 $R_{\rm e}$ of massive quiescent galaxies ($M > 10^{10.5}$ $M_{\odot}$) over the last $\sim$ 7 Gyr. At lower masses our results are also consistent with the addition of younger, newly quenched galaxies over time.

3. The derived SSP-equivalent ages are considerably younger than the age of the universe at all epochs, consistent with an *equivalent* single-burst star formation epoch of $z_{\rm f} \lesssim 1.5$. The addition of newly quenched galaxies at $z_{\rm f} \gtrsim 1.5$ naturally explains the young ages of galaxies in our sample. These young stellar population ages coupled with the existence of massive quiescent galaxies at $z > 1$ indicate the inhomogeneous nature of the $z \lesssim 0.7$ quiescent population. In order to be consistent with the apparent passive evolution since $z = 0.7$, young quiescent galaxies cannot be entering the sample at these late times at the highest masses.

4. There is tentative evidence that galaxies in cluster environments are older than galaxies inhabiting low-density environments. We hesitate to draw any strong conclusions, however, due to the small sample size as well as the possibility of contamination from atmospheric absorption and sky emission features imparting systematic effects on our spectral modeling results. This stresses the importance of obtaining deeper spectra with careful attention to telluric corrections and sky subtractions in addition to the development of tools capable of modeling low S/N spectra of these high-redshift galaxies.

5. The full spectrum fitting approach allows reliable and accurate abundance measurements, including age, Fe, Mg, C, N, and Ca, down to low S/N. The ability to accurately measure detailed abundance patterns in low S/N spectra with reliable uncertainty estimates opens the possibility to engage in detailed stellar population analysis at high redshift and in the low surface brightness outskirts of nearby galaxies.

ACKNOWLEDGMENTS

We thank the referee for a prompt and constructive report. We also thank Tomer Tal for useful discussions and assistance with investigating the effects of radial gradients and Dan Foreman-Mackey for providing a custom Fortran implementation of `emcee`. JC acknowledges support from the National Science Foundation Graduate Research Fellowship Program. CC acknowledges support from NASA grant NNX13AI46G, NSF grant AST-1313280, and the Alfred P. Sloan and Packard Foundations. MJIB acknowledges financial support from the Australian Research Council (FT100100280) and the Monash Research Accelerator Program (MRA).

This research has made use of observations obtained at the MMT Observatory, a joint facility of the University of Arizona and the Smithsonian Institution, and at the W.M. Keck Observatory, which is operated as a scientific partnership among the California Institute of Technology, the University of California and the National Aeronautics and Space Administration. W.M. Keck Observatory was made possible by the generous financial support of the W.M. Keck Foundation. Funding for the SDSS and SDSS-II has been provided by the Alfred P. Sloan Foundation, the Participating Institutions, the National Science Foundation, the U.S. Department of Energy, the National Aeronautics and Space Administration, the Japanese Monbukagakusho, the Max Planck Society, and the Higher Education Funding Council for England. The SDSS Web site is http://www.sdss.org/. The SDSS is managed by the Astrophysical Research Consortium for the Participating Institutions. The Participating Institutions are the American Museum of Natural History, Astrophysical Institute Potsdam, University of Basel, University of Cambridge, Case Western Reserve Uni-

versity, University of Chicago, Drexel University, Fermilab, the Institute for Advanced Study, the Japan Participation Group, Johns Hopkins University, the Joint Institute for Nuclear Astrophysics, the Kavli Institute for Particle Astrophysics and Cosmology, the Korean Scientist Group, the Chinese Academy of Sciences (LAMOST), Los Alamos National Laboratory, the Max-Planck-Institute for Astronomy (MPIA), the Max-Planck-Institute for Astrophysics (MPA), New Mexico State University, Ohio State University, University of Pittsburgh, University of Portsmouth, Princeton University, the United States Naval Observatory, and the University of Washington.

6

THE EVOLUTION AND PROPERTIES OF ROTATING MASSIVE STAR POPULATIONS

We investigate the integrated properties of massive ($> 10\ M_{\odot}$), rotating, single-star stellar populations for a variety of initial rotation rates ($v/v_{\rm crit} = 0.0, 0.2, 0.4, 0.5,$ and 0.6). We couple the new MESA Isochrone and Stellar Tracks (MIST) models to the Flexible Stellar Population Synthesis (FSPS) package, extending the stellar population synthesis models to include the contributions from very massive stars ($> 100\ M_{\odot}$), which can be significant in the first ~ 4 Myr after a starburst. These models predict ionizing luminosities that are consistent with recent observations of young nuclear star clusters. We also construct composite stellar populations assuming a distribution of initial rotation rates. Even in low-metallicity environments where rotation has a significant effect on the evolution of massive stars, we find that stellar population models require a significant contribution from fast-rotating ($v/v_{\rm crit} > 0.4$) stars in order to sustain the production of ionizing photons beyond a few Myr following a starburst. These results have potentially important implications for cosmic reionization by massive stars and the interpretation of nebular emission lines in high-redshift star-forming galaxies.

6.1 Introduction

Massive stars, though rare in number, are energetically dominant across a wide range of environments spanning star cluster to extragalactic scales. Stellar feedback from young, massive stars in H II regions and star-forming galaxies is a crucial yet poorly understood process. Broadly speaking, stellar feedback refers to the deposition of energy, momentum, mass, and nuclear-burning products via channels that include type I and type II supernovae (SNe), stellar radiation, and winds (e.g., Murray et al. 2010; Hopkins et al. 2011). These processes influence the state of the interstellar medium (e.g., McKee & Ostriker 1977), thereby regulating star formation (e.g., Williams & McKee 1997; Mac Low & Klessen 2004; McKee & Ostriker 2007) and driving both turbulence and galactic-scale outflows (e.g., Dekel & Silk 1986; Martin 1999; de Avillez & Breitschwerdt 2004; Joung & Mac Low 2006; Oppenheimer & Davé 2006; Agertz et al. 2009; Tamburro et al. 2009; Hopkins et al. 2012; Creasey et al. 2013).

Observations of star-forming giant molecular clouds (GMCs) have suggested that early feedback processes disperse the dense gas well before the first SNe explode, which may increase the overall efficiency of feedback and reduce the star formation efficiency (e.g., Evans et al. 2009; Krumholz et al. 2012). Proposed mechanisms of this early feedback include the destruction of the dense molecular regions by expanding H II bubbles (e.g., Whitworth 1979; Matzner 2002; Walch et al. 2012; Lopez et al. 2014) and radiation pressure (e.g., Murray et al. 2005; Krumholz & Matzner 2009). The complex interplay between the properties of young stellar populations and the dissolution of their birth gas has significant implications for the number of photons that are able to leak out of the host galaxies (e.g., Dove & Shull 1994; Gnedin 2000; Ma et al. 2015) and drive cosmic reionization (e.g., Haardt & Madau 1996).

The influence of stellar feedback in a galactic context has been explored by many groups, both analytically and in simulations (e.g., Haehnelt 1995; Murray et al. 2005; Nath & Silk 2009; Murray et al. 2011; Hopkins et al. 2011, 2012; Agertz et al. 2013; Ma et al. 2015; Muratov et al. 2015; Fierlinger et al. 2016).

Prescriptions for the time-dependent momentum and energy deposition of stellar populations require stellar population synthesis (SPS) models such as Starburst99 (SB99; Leitherer et al. 1999; Vázquez & Leitherer 2005; Leitherer et al. 2010, 2014), which in turn rely on stellar evolution models, e.g., the Geneva models (Ekström et al. 2012; Georgy et al. 2013) and realistic stellar spectra, especially in the EUV. Stellar population models that include the effects of stellar rotation lead to an overall increase in feedback efficiency (Levesque et al. 2012; Leitherer et al. 2014) because rotation makes stars hotter, brighter, and longer-lived (e.g., Maeder & Meynet 2000). In other words, rotating stellar populations have higher bolometric luminosities and sustain harder radiation fields (i.e., more ionizing photons) over a longer period of time compared to non-rotating stellar populations.

Binary interaction is another important and complex aspect of massive star evolution. A large fraction of O- and B-type stars are found in binary or higher multiplicity systems, and an estimated $\gtrsim 70\%$ of O-type stars are believed to undergo mass exchange, a third of which likely end up in a binary merger product (e.g., Chini et al. 2012; Sana et al. 2012, 2013; de Mink et al. 2014; but see also Kobulnicky et al. 2014, where the authors found that the multiplicity fraction is closer to $\sim 55\%$ for orbital periods less than 5000 days, and that it likely depends on the orbital period and separation). Broadly speaking, binarity and rotation have similar effects on stellar evolution. This is a fortunate aspect since large grids of stellar evolution models generally account for only one of these effects due to the sheer size of the parameter space that would otherwise need to be explored (see Song et al. 2016 for a recent example that accounts for tidal interactions in a binary system of rotating stars). We focus on single star models with rotation in this work and we compare with predictions from the Binary Population and Spectral Synthesis model (BPASS; Eldridge & Stanway 2009).

In this work, we investigate two features of single massive stars in the context of SPS modeling. First, we explore the contribution from very massive stars (VMSs) to the integrated stellar population properties by extending the initial mass function (IMF) upper mass limit from the fiducial value of 100 $M_{\odot}$ to

300 $M_{\odot}$. Recent observations of star clusters have suggested the need to include VMSs in models (e.g., Crowther et al. 2016; Smith et al. 2016), though a top-heavy IMF has also been proposed (e.g., Turner et al. 2015).

Second, we explore the effects of rotation over a range of rotation rates. We build on the previous work by Levesque et al. (2012), who investigated the effect of stellar rotation on the resulting stellar population properties. Their conclusions were based on a single rotation value (surface velocity set to 40% of the critical, or break-up, velocity, $v/v_{\rm crit} = 0.4$), though the authors also considered a composite population by weighting 30% non-rotating and 70% rotating stellar populations. We also investigate the effects of stellar populations harboring a range of rotations rates, which is supported by observations (Huang et al. 2010), and explore their significance in the context of cosmic reionization. One of the distributions considered in this work includes a tail of fast-rotators with $v/v_{\rm crit} > 0.4$, which may be of binary origin (Ramírez-Agudelo et al. 2013).

Both VMSs and a distribution of rotation rates have interesting implications in light of recent observational and theoretical work. Smith et al. (2016) advocated for VMSs in lieu of rapid rotators to resolve the discrepancy between photometric and spectroscopic ages inferred for a young stellar population in NGC 5253. The authors reasoned that large numbers of rapid rotators, though able to explain the observed nitrogen enhancement and ionizing flux, are in tension with the moderate rotational velocities reported in a recent survey of single O-type stars in 30 Doradus (Ramírez-Agudelo et al. 2013). We explore whether a combination of moderate rotation rates and VMSs can provide a solution to this problem. Furthermore, Steidel et al. (2014) analyzed rest-frame optical spectra of $z \sim 2$–3 star-forming galaxies and found that their position in the "Baldwin, Phillips, and Terlevich" (BPT) diagram—a nebular emission line diagnostic first introduced in Baldwin et al. (1981)—is offset relative to their $z = 0$ counterparts. The authors concluded that this shift could be explained by a harder stellar ionizing radiation field ($T_{\rm blackbody} =$ 50000–60000 K), higher ionization parameter, and nitrogen-enhanced nebular gas, suggesting rapid stellar

rotation or binaries to explain these observations. In subsequent work, Steidel et al. (2016) found that the BPASS binary star models can self-consistently explain the observed line ratios. This, together with the finding that binary models can sufficiently boost the escape fraction of ionizing photons, $f_{\rm esc}$, to explain cosmic reionization (Ma et al. 2016b), are based on a unique feature of binary models: the ability to sustain sufficiently long-lived ($\gtrsim$ 5 Myr) far-UV stellar radiation field. We investigate whether this can be explained by rotating stellar populations, particularly those with contributions from fast-rotators.

The paper is organized as follows. In Sections 6.2 and 6.3, we describe the MESA Isochrones and Stellar Tracks (MIST) and Flexible Stellar Population Synthesis (FSPS) models. Next, in Section 6.4, we present the results from stellar population modeling, including an investigation of the effects of VMSs, metallicity, and rotation distributions. In Section 6.5, we discuss the implications of our models in the context of the cosmic reionization and high-redshift star-forming galaxies. We conclude with a summary in Section 6.6.

6.2 MIST Models

In this section we provide a brief overview of the MIST models, focussing on the details that are most salient to the evolution of massive, rotating stars. For a comprehensive description and summary, the reader is referred to Section 3 and Table 1 in Choi et al. (2016).

6.2.1 Modules for Experiments in Stellar Astrophysics (MESA)

The stellar evolutionary tracks are computed using MESA,* an open-source stellar evolution package (Paxton et al. 2011, 2013, 2015). MESAstar, its 1D stellar evolution module, solves the fully coupled Lagrangian equations of stellar structure and composition. Some of the key advantages of MESA include its robust numerical methods, its modular structure that easily enables a user to adapt it to a wide range of

*http://mesa.sourceforge.net/

problems in stellar astrophysics, and parallelization via OpenMP. The reader is encouraged to consult the original MESA instrument papers and Section 2 in Choi et al. (2016) for more details.

6.2.2 Abundances

All of the models computed for this work are initialized with the solar-scaled abundances and $Z = Z_{\odot,\mathrm{protosolar}} = 0.0142$ from Asplund et al. (2009). The helium mass fraction, Y, is computed assuming a linear enrichment law from the primordial helium abundance $Y_\mathrm{p} = 0.249$ (Planck Collaboration et al. 2015) to the protosolar helium abundance $Y_{\odot,\mathrm{protosolar}} = 0.2703$ (Asplund et al. 2009), where $\Delta Y/\Delta Z = 1.5$.

Although [Fe/H] ranges from -4.0 to 0.5 in the full set of grids published on the MIST website,* we focus on the range $-2.0 \leq [\mathrm{Fe/H}] \leq 0.0$ in this work.

6.2.3 Rotation

The effects of rotation appear in MESA stellar evolution calculations in three main ways. First, rotation decreases the gravitational acceleration g via the centrifugal force, which in turn affects the stellar structure, making the star appear more extended and cooler near the equator. Second, rotation can promote extra mixing in the interior, providing a boost to the transport of chemicals and angular momentum. As a result, the helium fraction—and hence the mean molecular weight μ—is increased in the surface layers and more fuel can be introduced to the convective core, resulting in a hotter, brighter, and more long-lived star. MESA adopts the common approach of treating the chemical and angular momentum transport in a diffusion approximation (Endal & Sofia 1978; Zahn 1983; Pinsonneault et al. 1989; Heger et al. 2000 but see also Maeder & Meynet 2000; Eggenberger et al. 2008; Potter et al. 2012). Third, rotation enhances mass loss (e.g., Heger et al. 2000; Brott et al. 2011a; Potter et al. 2012). MESA adopts the formulation from Langer (1998), where the mass loss rate $\dot{M}$ is multiplied by a factor that increases

*http://waps.cfa.harvard.edu/MIST/

dramatically as the surface angular velocity Ω approaches critical, or break-up, angular velocity, $\Omega_{\rm crit} = [(1-(L/L_{\rm Edd}))(GM/R^3)]^{0.5}$.* Because $\Omega_{\rm crit}$ depends on the ratio of the bolometric luminosity to the Eddington luminosity, $L/L_{\rm Edd}$, massive stars near the Eddington limit can experience a sizable increase in their mass loss rates even with small amount of rotation, resulting in a prompt removal of their surface hydrogen layer (e.g., Maeder & Meynet 2000; Choi et al. 2016).

Models are initialized following solid-body rotation near the zero-age main sequence (ZAMS), similar to the approach adopted by many other stellar evolution codes (Pinsonneault et al. 1989; Heger et al. 2000; Eggenberger et al. 2008). We compute models with $v/v_{\rm crit} = 0.0$, 0.2, 0.4, 0.5, and 0.6 at ZAMS, where $v/v_{\rm crit}$ corresponds to the ratio of the stellar rotation velocity to the critical rotation velocity at the surface and $v_{\rm crit} = [(1-(L/L_{\rm Edd}))(GM/R)]^{0.5}$.

6.2.4 MIXING

Convective mixing of elements is treated as a time-dependent diffusive process with the diffusion coefficient provided by the mixing length formalism of Henyey et al. (1965) and assuming $\alpha_{\rm MLT} = 1.82$ obtained from the solar calibration (Choi et al. 2016). Convectively unstable zones are identified according to the Ledoux criterion, which is similar to the Schwarzschild criterion but also includes composition effects. The effects of convective overshoot mixing beyond the fiducial Ledoux boundary are taken into account following Freytag et al. (1996) and Herwig (2000), which assumes that the diffusion coefficient decays exponentially with distance from the convective boundary. A free parameter that controls the efficiency of this extra mixing in the core, $f_{\rm ov} = 0.016$, is empirically calibrated to reproduce the main-sequence turnoff (MSTO) morphology in M67 (Choi et al. 2016, but see also Magic et al. 2010). Semiconvection and thermohaline mixing are also included, where we adopt the efficiency parameters $\alpha_{\rm sc} = 0.1$ and $\alpha_{\rm th} = 666$.

*Note that this expression assumes that the surface brightness is uniform over the stellar surface. Maeder & Meynet (2000) worked out an alternative expression that takes into account gravity darkening effects, but the difference is small unless $L/L_{\rm Edd}$ is much larger than ~ 0.65.

Finally, we account for five rotationally induced instabilities that lead to chemical and angular momentum transport, namely the dynamical shear instability, secular shear instability, Solberg-Høiland instability, Eddington-Sweet circulation, and Goldreich-Schubert-Fricke instability (Heger et al. 2000; Paxton et al. 2013). We do not include mixing due to internal magnetic fields generated by a Tayler-Spruit dynamo (Spruit 2002).

6.2.5 Mass Loss

In hot stars, mass loss is driven by the momentum transfer from ultraviolet photons to metal ions in the atmosphere (Lucy & Solomon 1970; Castor et al. 1975) and is therefore metallicity-dependent. Mass loss in massive stars is separated into three categories in the MIST model calculations. For stars with $T_{\rm eff} > 1.1 \times 10^4$ K and surface hydrogen mass fraction $X_{\rm surf} > 0.4$, we adopt the mass loss prescription from Vink et al. (2000, 2001). If the star loses a considerable amount of its outer hydrogen layer ($X_{\rm surf} < 0.4$) and becomes a Wolf-Rayet (WR) star, we use the wind prescription of Nugis & Lamers (2000) instead. Lastly, we use the de Jager et al. (1988) prescription for all stars that have effective temperatures below 10^4 K, including red supergiant (RSG) stars. As discussed in 6.2.3, mass loss is enhanced in rotating models by a factor that depends on the rotation rate and the Eddington ratio.

6.2.6 Tracks and Isochrones

We compute MIST isochrones for five rotation rates—$v/v_{\rm crit} = 0.0, 0.2, 0.4, 0.5$, and 0.6—for each metallicity. The stellar evolutionary tracks ranging from 0.1 to 300 $M_\odot$ are computed by MESA and processed into isochrones following the procedure outlined in Dotter (2016). We modified the mass sampling in the isochrones in this work compared to that in the standard MIST grids to ensure that fast evolutionary phases at early times are particularly well-represented. Figures 6.1 and 6.2 show 1, 3, 5, and 10 Myr isochrones at $[{\rm Fe/H}] = -1.0$ and 0.0, respectively. We omit $v/v_{\rm crit} = 0.5$ from these figures for display

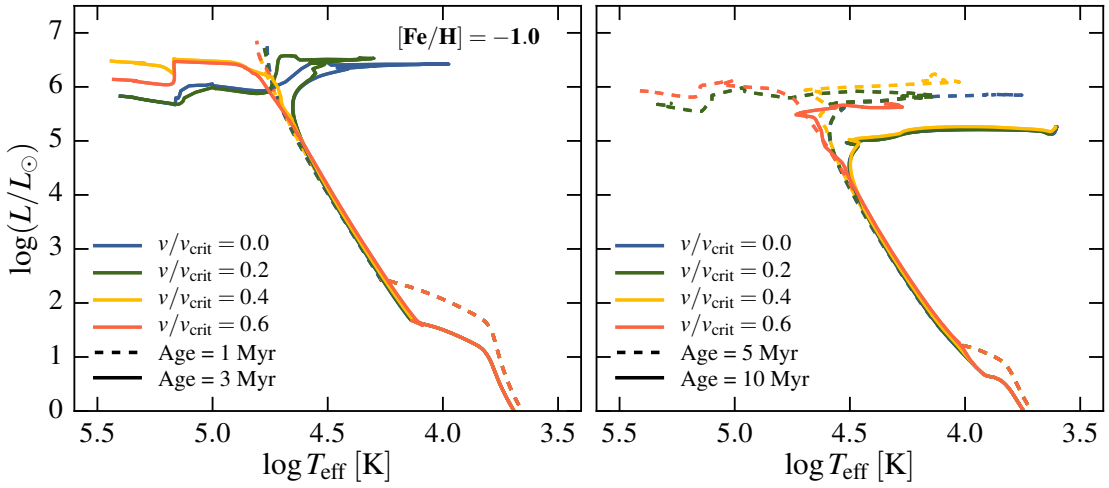


Figure 6.1: $[\mathrm{Fe/H}] = -1.0$ isochrones as a function of age and rotation. The four colors correspond to four different values of the initial rotation rates, represented in units of the critical rotation rate. Fast rotation generally leads to hotter, brighter, and more long-lived stars. Left: 1 and 3 Myr. Right: 5 and 10 Myr.

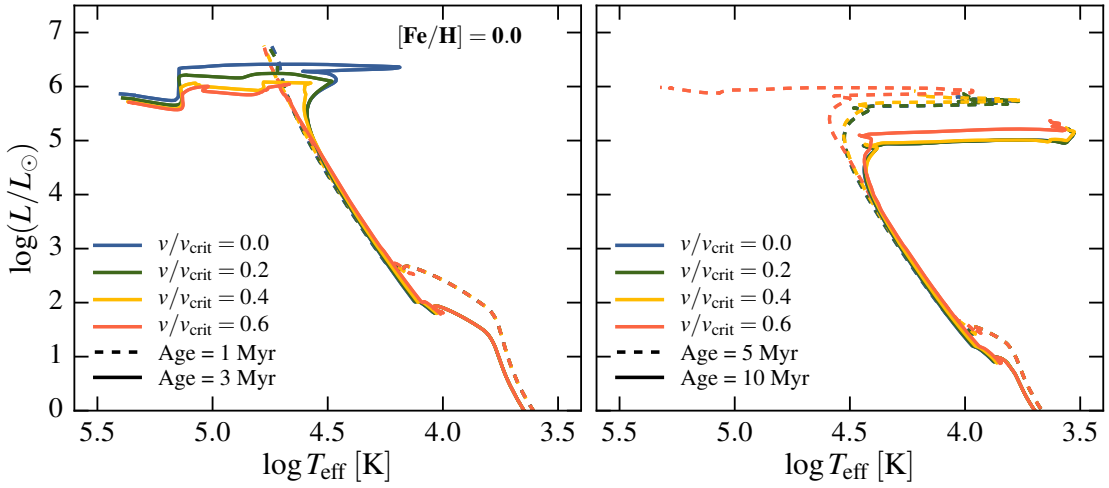


Figure 6.2: Same as Figure 6.1 except now showing $[\mathrm{Fe/H}] = 0.0$.

purposes. There are several notable features. First, the rotating models tend to be hotter and more luminous overall. Second, WR stars from very massive progenitors appear between 1 Myr and 5 Myr, particularly for $v/v_{\mathrm{crit}} > 0.2$. Third, some isochrones, e.g., $v/v_{\mathrm{crit}} = 0.6$ at $[\mathrm{Fe/H}] = -1.0$, show signatures of quasi-chemically homogeneous evolution (QCHE; Maeder 1987; Langer 1992). QCHE occurs in massive, fast-rotating stars where the mixing timescale becomes shorter than or comparable to the nuclear burning timescale. In this scenario, nuclear burning products—mostly helium—from the core are mixed into the

outer layers and a large fraction of the star undergoes nuclear fusion as fresh fuel is channeled into the core. Overall, the star becomes hotter due to the reduced mean opacity, and brighter and more long-lived due to enhanced mixing in the core (see Figures 5, 6, and 7 in Brott et al. 2011a for examples). QCHE occurs more readily at low metallicity due to the reduced angular momentum loss via stellar winds (Yoon & Langer 2005; Woosley & Heger 2006) and the more compact stellar structure resulting in a decreased mixing timescale ($\tau \sim R^2/D$, where R is the radius of the star and D is the diffusion coefficient for mixing). To verify that both processes indeed contribute, we performed a simple test where we ran a total of eight 60 $M_\odot$ models, with and without rotation, with and without mass loss, at solar and one-tenth-solar metallicities. We found that even in the absence of mass loss, i.e., no angular momentum loss, the MS lifetime enhancement due to rotation was still larger for the low metallicity model ($\sim 20\%$) compared to the solar metallicity model ($\sim 10\%$), which suggests that the compactness of the star at low metallicity is indeed an important effect. In the rotating case, there was a small ($\lesssim 5\%$) enhancement in the MS lifetime for the models without any mass loss compared to those with mass loss. An extensive study examining the relative importance of the two effects as a function of metallicity, rotation rate, mass, etc. is beyond the scope of this paper, but would be worth exploring further.

In Figures 6.3 and 6.4 we compare the $v/v_{\rm crit} = 0.0$ and 0.4 MIST isochrones with the non-rotating and rotating Geneva isochrones, zooming in around the MSTO for clarity. In detail, there are clear morphological differences between the MIST and Geneva isochrones, but both their evolution with time and their modifications due to rotation are qualitatively similar. A notable difference is the magnitude of the effect of rotation on the MS lifetimes and the trajectory in the HR diagram at $t \gtrsim 5$ Myr; rotating Geneva models are much brighter than the non-rotating models compared to their MIST counterparts.

In order to investigate the effect of rotation on the MS lifetimes of massive stars in more detail, we plot the MS lifetime–initial mass relations in Figure 6.5. The black dotted and dot-dashed lines correspond to the non-rotating and rotating Geneva (Ekström et al. 2012; Georgy et al. 2013) evolutionary tracks for

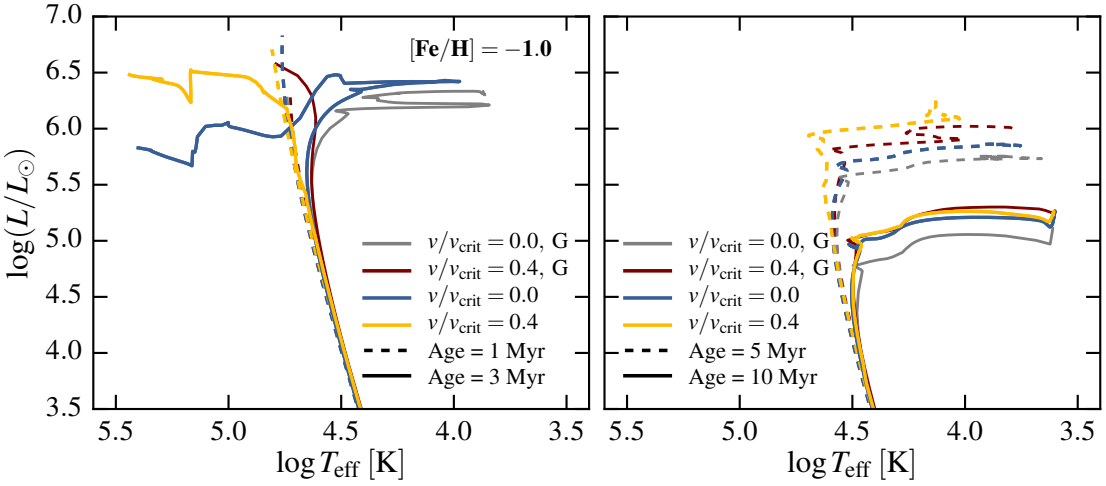


Figure 6.3: Same as Figure 6.1 except now zooming in near the MSTO. Isochrones for the Geneva rotating and non-rotating models are also included for comparison. For MIST, we only show the $v/v_{\rm crit} = 0.0$ and 0.4 isochrones for display purposes.

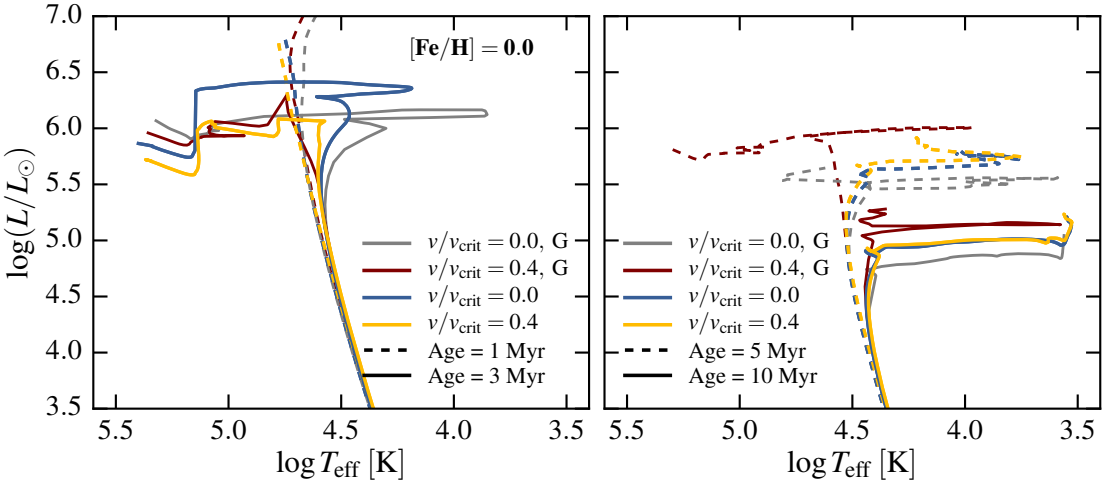


Figure 6.4: Same as Figure 6.3 except now showing [Fe/H] = 0.0.

$Z = 0.002$ ([Fe/H] $= -0.86$ assuming their adopted $Z_\odot = 0.014$) and $Z = 0.014$. At a fixed initial mass, a higher rotation rate lengthens the MS lifetime due to more efficient rotational mixing. Note that these plots demonstrate that the MS lifetime boost at a fixed initial mass is larger in the Geneva models compared to that in the MIST models (see also Figure 20 in Choi et al. 2016), suggesting that rotational mixing may be more efficient in the former. The MS lifetime flattens out at the high mass end since $t \propto L/M$ and luminosity becomes a shallower function of mass: for $L \propto M^\alpha$, we find $\alpha \sim 4$ for $M \lesssim 10\,M_\odot$ and $\alpha \sim 1.5$ for

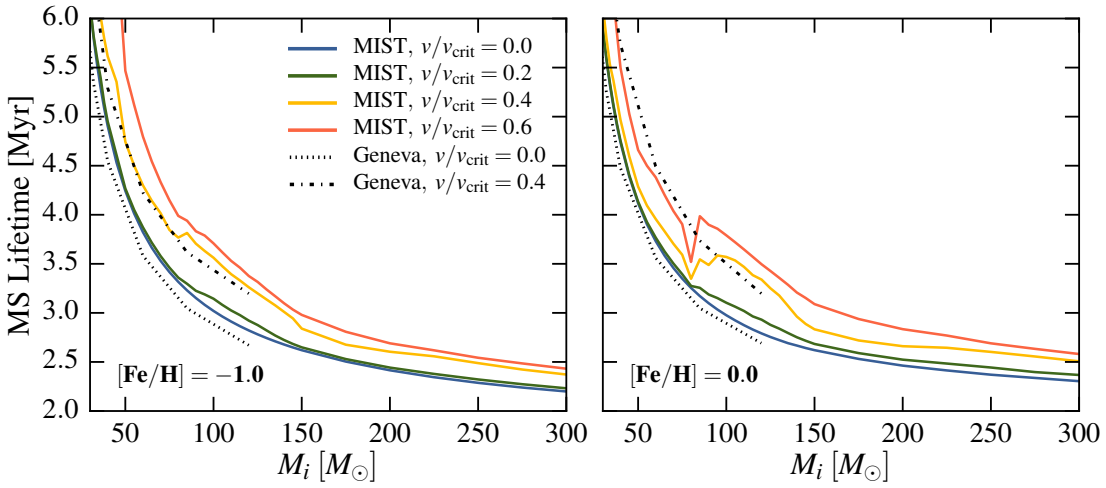


Figure 6.5: Left: MS lifetimes as a function of initial mass for four different values of initial rotation rates at [Fe/H] = −1.0. The black curves represent MS lifetimes for the Geneva (Ekström et al. 2012; Georgy et al. 2013) evolutionary tracks at $Z = 0.002$ ([Fe/H] = −0.86 assuming their adopted $Z_\odot = 0.014$). Right: same as the left panel except now showing [Fe/H] = 0.0.

$M \gtrsim 100\ M_\odot$. At solar metallicity, there is an interesting non-monotonic behavior around 80 $M_\odot$. Rapidly rotating stars with masses greater than 80 $M_\odot$ begin to evolve more vertically and blueward in the HR diagram during the MS.* Due to their high luminosities and temperatures and therefore heavy mass loss, they quickly shed their H-rich envelopes and become WR stars. As they continue to lose significant mass due to heavy WR winds, they effectively "reset" as lower-mass stars, which prolongs their MS lifetimes. In other words, the MS lifetime–initial mass relation systematically shifts upward to another branch beyond 80 $M_\odot$.

6.3 Stellar Population Synthesis Models

6.3.1 Flexible Stellar Population Synthesis

Models of simple stellar populations (SSPs) in this work are computed using the Flexible Stellar Population Synthesis package (FSPS; Conroy et al. 2009, 2010). The primary stellar spectral library consists of the MILES empirical library (Sánchez-Blázquez et al. 2006c; Falcón-Barroso et al. 2011), which is sup-

*Although quasi-chemically homogeneous evolution appears more readily in low-metallicity environments, they may also occur in metal-rich systems. See Martins et al. (2013) for more details.

plemented with the CMFGEN WR spectra (available for both WN and WC subtypes) from Smith et al. (2002) and the WM-Basic (Pauldrach 2012) hot star spectra (J.J. Eldridge, priv. comm.). We identify WR stars in the isochrones using the definition adopted by the Geneva group (Meynet & Maeder 2003; Georgy et al. 2012): $T_{\rm eff} > 10^4$ K and the surface hydrogen mass fraction $X_{\rm surf} < 0.3$. These stars are further categorized into WN and WC subtypes according to their surface compositions: stars with surface C/N number ratio > 1 and ≤ 1 are labeled as WC and WN, respectively. Note that this type of theoretically-motivated classification based on the average surface abundances is not directly equivalent to the classification scheme adopted by observers who rely on the spectroscopic detection of emission lines (e.g., van der Hucht (2001); see Groh et al. (2014) for a detailed discussion on bridging this gap for massive stars by coupling the stellar interior evolution models to the atmosphere models). The WM-Basic models are applied for MS stars with $T_{\rm eff} > 2.5 \times 10^4$ K.

For all subsequent analyses, we simulate a population of total mass $10^6\ M_\odot$ following an instantaneous burst of star formation. All integrated quantities are computed following the Kroupa 2001 initial mass function (IMF), assuming that the IMF is fully sampled. The IMF lower and upper mass limits are set to 0.08 $M_\odot$ and 300 $M_\odot$, respectively (see Section 6.4.4 for a discussion). Stochastic IMF sampling effects are likely to have a bearing on real stellar populations, especially in low-mass systems (e.g., Cerviño et al. 2000, 2001; da Silva et al. 2012, 2014). We revisit this point briefly in Section 6.3.2.

As discussed in Maeder (1990), assigning a spectrum to a WR star in the isochrone is a non-trivial task due to the high optical depth of its wind. As a result, the effective photosphere—the $\tau = 2/3$ surface—has a radius larger than the hydrostatic radius reported in the stellar evolutionary track, and the inferred temperature from observations, $T_{\rm eff,\,WR}$, is cooler than the temperature from stellar evolution calculations, T_*. We follow the standard approach adopted by Maeder (1990) and Smith et al. (2002), where $T_{\rm eff,\,WR}$ is

estimated via a weighted sum of T_* and $T_{\text{eff, wind}}$. $T_{\text{eff, wind}}$ is computed by assuming a velocity law:

$$v(r) = v_\infty \left(1 - \frac{R}{r}\right)^2 \quad , \tag{6.1}$$

where v_∞ is the terminal velocity, set to 3×10^8 cm s^{-1}.

Starting with the definition of optical depth $d\tau = -\kappa\rho \; dr$ and integrating inward to $\tau = 2/3$, the effective photosphere is obtained

$$R_{\text{eff, WR}} = R_* + \frac{3\kappa|\dot{M}|}{8\pi v_\infty} \quad . \tag{6.2}$$

Since L is constant, it is trivial to compute $T_{\text{eff, WR}}$ in terms of $R_{\text{eff, WR}}$, R_*, and T_*. Then the temperature used to retrieve the spectrum for a WR star with T_* is $0.6T_* + 0.4T_{\text{eff, WR}}$. Smith et al. (2002) chose this weighting scheme to reproduce the range of observed temperatures of the Galactic and LMC WR population. In principle, the weighting factors should be re-derived for this work given the differences in the underlying stellar evolutionary models adopted in Smith et al. (2002) (Meynet et al. 1994 tracks) and MIST. However, the objective here is a simple assessment of the uncertainties introduced due to the ill-defined WR temperatures. We revisit this point in Section 6.4.2.

6.3.2 IMF Stochasticity

We evaluate the assumption that the IMF is smoothly sampled for this work. A key concern regarding IMF stochasticity in the context of SPS modeling is that many quantities of interest, e.g., ionizing flux, are dominated by a very small number of the most massive stars, a subpopulation that is also the rarest and thus most prone to sampling effects. Thus two stellar populations that are otherwise completely identical in parameter space (e.g., metallicity, total mass, age) may appear quite different depending on the stellar mass distribution. Figure 6.6, which shows the fractional flux contribution from stars in different mass

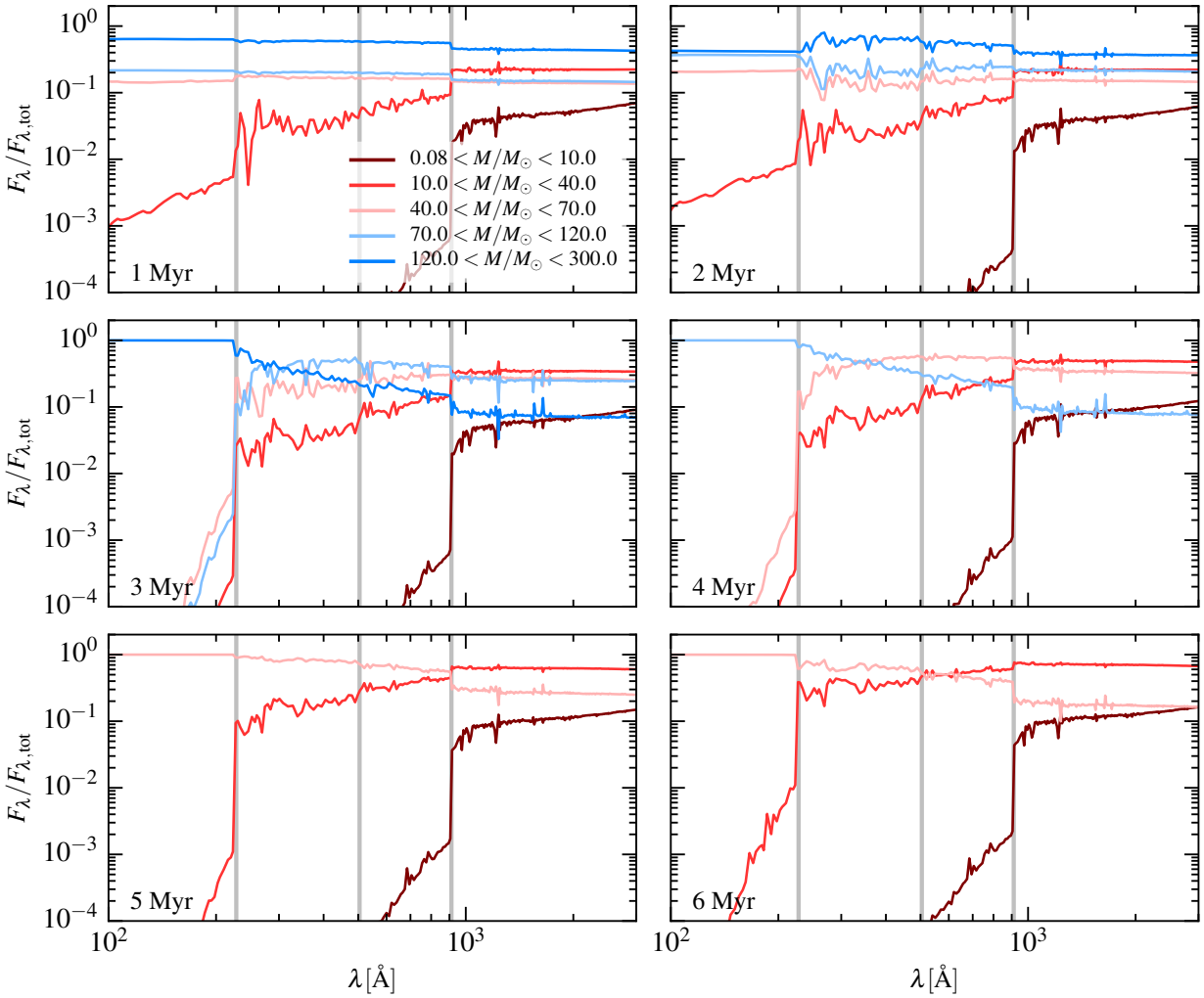


Figure 6.6: Fractional flux contribution to the total ultraviolet flux from stars in different mass ranges for a single-burst population with $v/v_{\mathrm{crit}} = 0.6$ at $[\mathrm{Fe/H}] = -1.0$ over 1–6 Myr. The three grey vertical lines mark the wavelengths below which photons can ionize hydrogen, singly ionize helium, and doubly ionize helium (912 Å, 504 Å, and 228 Å).

ranges, provides a sense of how much variation there may be in spectral energy distributions (SEDs) due to the IMF sampling effects.

There are alternative approaches to SPS modeling (e.g., Barbaro & Bertelli 1977; Cerviño et al. 2000; Villaverde et al. 2010; Eldridge 2012; da Silva et al. 2012, 2014) that simulate the IMF stochastic sampling effects. Cerviño et al. (2002) constructed a statistical formalism to quantify the uncertainties due to IMF sampling errors and applied their results to model a starburst population from birth to 20 Myr. Overall, they found that a minimum total stellar mass of $10^5\ M_\odot$ is necessary to ensure a relative dispersion of less

than 10% in hydrogen and helium ionizing flux, though during the "WR phase" (between 2 and 5 Myr), this threshold mass is increased to $10^6\ M_\odot$.

Since we are operating under the assumption that the total stellar mass of the cluster modeled in our work is $10^6\ M_\odot$, random IMF sampling effects are likely unimportant for our conclusions. However, the exact value of this critical cluster mass depends on the adopted IMF (e.g., functional form, lower and upper mass limits). The conclusions from Cerviño et al. (2002) were based on a Salpeter 1955 IMF over the mass range 2–120 $M_\odot$. Even though the increased mass range (0.08–300 $M_\odot$) in our work would push the threshold total mass upward, an ensemble of such clusters in e.g., a starburst galaxy, should collectively smear out the sampling effects (see e.g., Cerviño et al. 2000; Eldridge 2012).

6.4 Stellar Population Properties

6.4.1 Spectral Energy Distributions (SEDs)

Figures 6.7 and 6.8 show SEDs from 1 to 20 Myr for $[\mathrm{Fe/H}] = -1.0$ and 0.0, respectively. The colored curves represent four different initial rotation rates for FSPS+MIST, while the gray and black curves show the BPASS v2.0* (Stanway et al. 2016) and SB99+Geneva (Leitherer et al. 2014) predictions† for comparison where available. The $v/v_{\mathrm{crit}} = 0.5$ FSPS+MIST model is excluded for clarity. The three blue vertical lines mark the wavelengths of photons capable of ionizing hydrogen, singly ionizing helium, and doubly ionizing helium (912 Å, 504 Å, and 228 Å). For clarity, we do not include the BPASS single star or SB99+Geneva non-rotating models, but they are in broad agreement with the FSPS+MIST non-rotating models.

The FSPS+MIST model predicts a harder spectrum compared to the SB99+Geneva model, partially due to differences in the underlying isochrones. Moreover, the FSPS+MIST model presented here is slightly

*IMF slopes of -1.30 for $0.1 < M_i/M_\odot < 0.5$ and -2.35 for $0.5 < M_i/M_\odot < 300$.
†IMF slopes of -1.3 for $0.1 < M_i/M_\odot < 0.5$ and -2.3 for $0.5 < M_i/M_\odot < 100$.

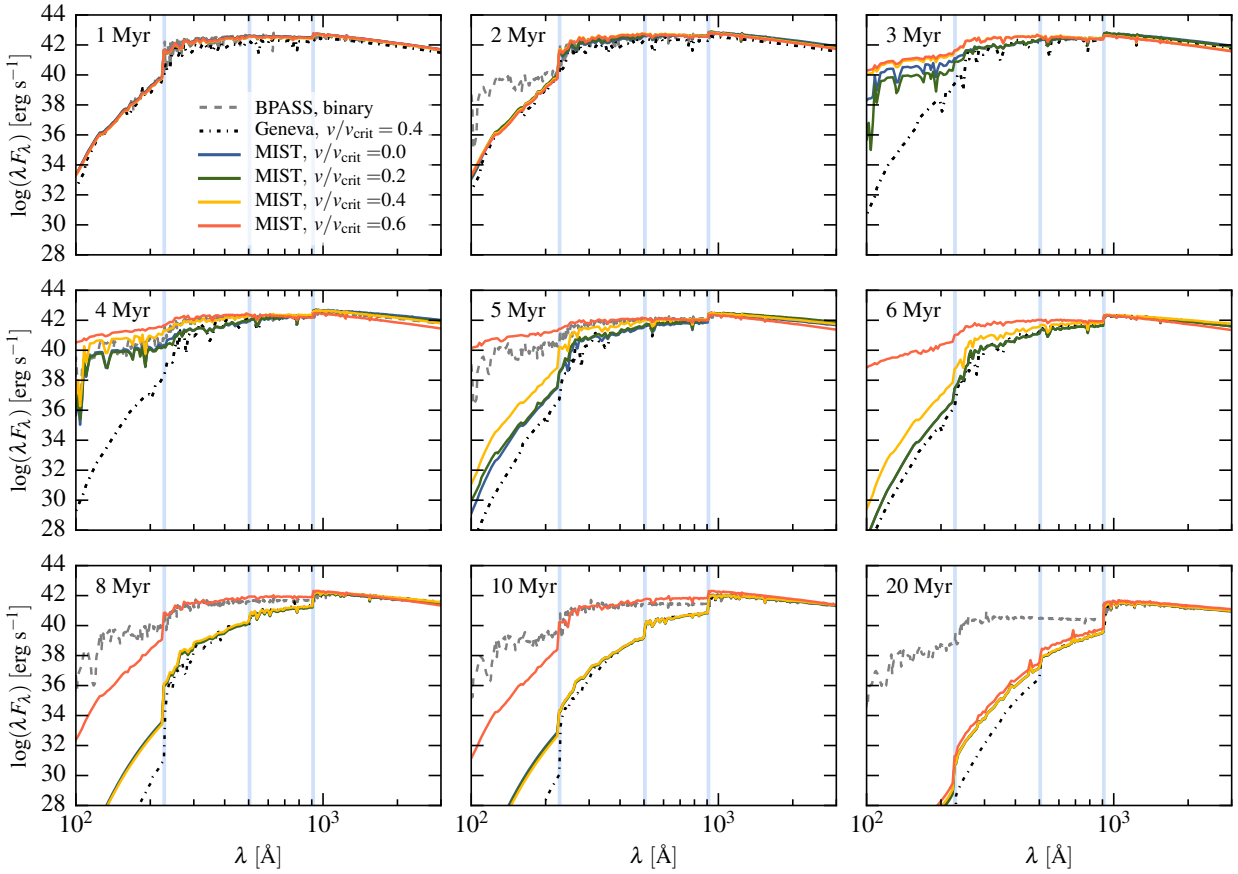


Figure 6.7: Time evolution of SED model predictions for a single-burst, $10^6\ M_\odot$ stellar population at [Fe/H] $= -1.0$. There are four initial rotation rates considered for FSPS+MIST, a binary-star model from BPASS, and a rotating model from SB99+Geneva. The $v/v_{\rm crit} = 0.5$ model is excluded for clarity. Note that BPASS is not shown in every panel. The three blue vertical lines mark the wavelengths of photons able to ionize hydrogen, singly ionize helium, and doubly ionize helium (912 Å, 504 Å, and 228 Å). The FSPS+MIST and BPASS models assume an IMF upper mass limit of 300 $M_\odot$ while the SB99+Geneva model assumes 100 $M_\odot$. Only the $v/v_{\rm crit} = 0.6$ and binary models are capable of producing significant EUV flux for ≥ 5 Myr and only the binary model can produce substantial EUV flux beyond 10 Myr.

more metal-poor than the SB99+Geneva model. The large discrepancy at 3 Myr is due to the lack of stars more massive than 300 $M_\odot$ in the SB99+Geneva models.* With the exception of $v/v_{\rm crit} = 0.6$, the FSPS+MIST models cease to produce an appreciable amount of photons blueward of 228 Å beyond ~ 6 Myr, while the BPASS binary models continue to output significant EUV flux even at very late times (20 Myr). This can be understood by recalling that single star models rely exclusively on the most massive stars to produce

*The Geneva group has published stellar evolutionary tracks of VMSs (120 to 500 $M_\odot$) at solar, LMC, and SMC metallicities (Yusof et al. 2013), but the corresponding isochrones are not incorporated into SB99 at the time of writing.

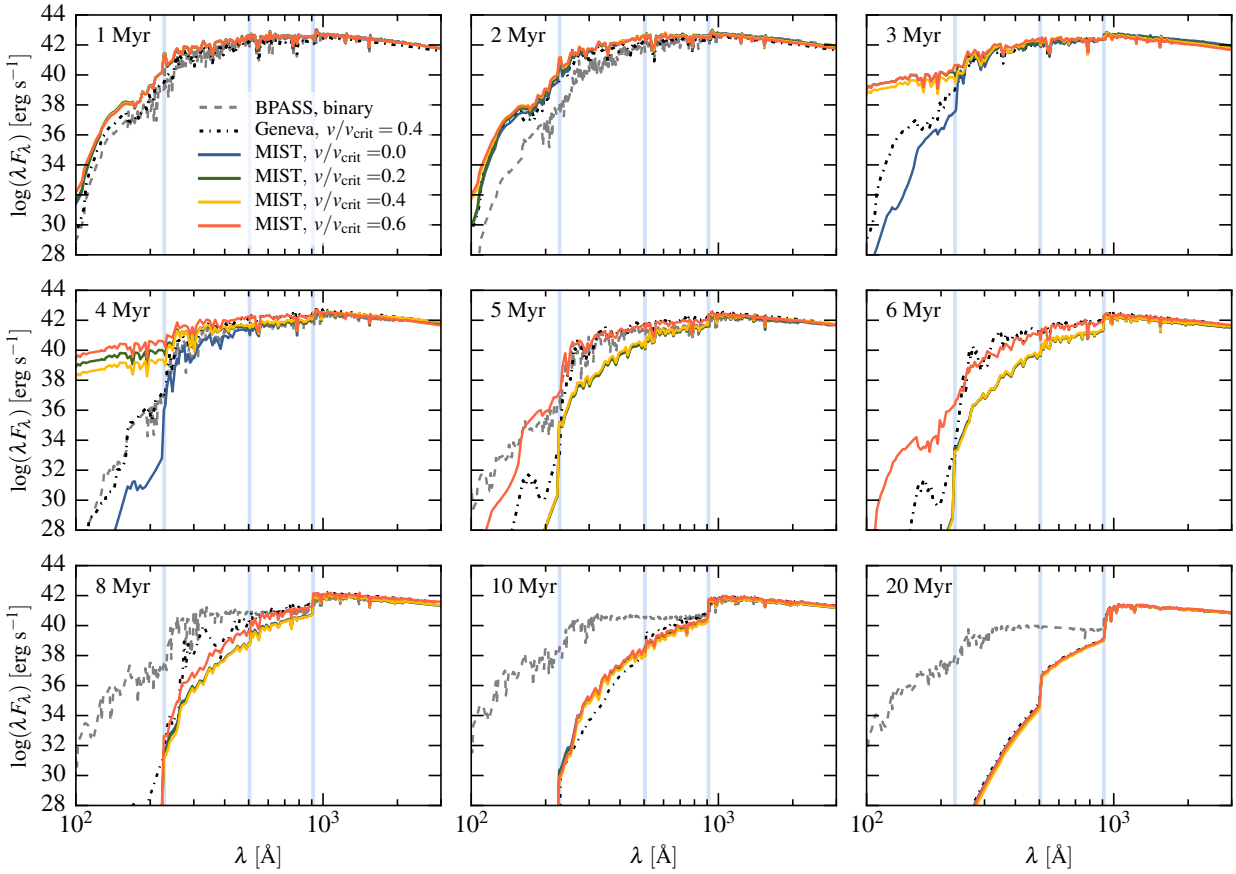


Figure 6.8: Same as Figure 6.7 except now showing [Fe/H] = 0.0.

ionizing photons. As a result, the principle ionizing sources vanish once the most massive stars disappear after the first few Myrs. In contrast, binary interactions and mergers can persist even after the most massive stars disappear, so binary models are capable of generating ionizing photons at late times.

6.4.2 Ionizing Photons

Starting from the SEDs as a function of age, $F_\lambda(t)$, we can compute the time evolution of the ionizing photon luminosity, $Q(t)$. Figures 6.9 and 6.10 show $Q(t)$ from 1 to 30 Myr for a $10^6\ M_\odot$ population at [Fe/H] $= -1.0$ and 0.0. The top, middle, and bottom panels show photons with wavelengths below 912 Å, 504 Å, and 228 Å, respectively. We also show the BPASS binary and SB99+Geneva rotating model predictions for comparison. Note that the metallicities are not perfectly matched: for BPASS and SB99+Geneva,

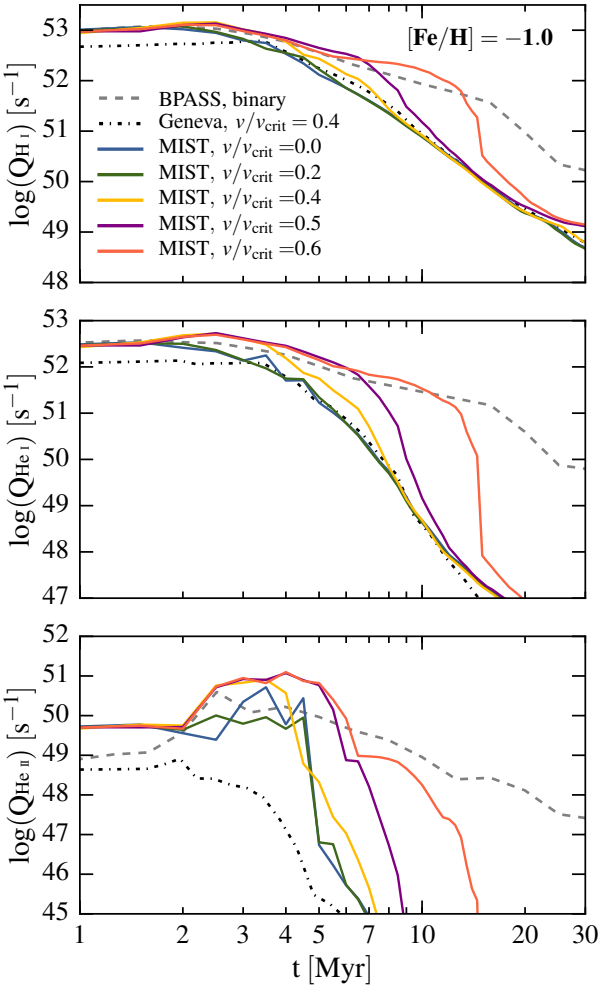


Figure 6.9: Time evolution of the ionizing photon luminosity from the FSPS+MIST, BPASS, and SB99+Geneva models for a $10^6\ M_\odot$ single-burst stellar population at $[\mathrm{Fe/H}] = -1.0$. The FSPS+MIST and BPASS models assume an IMF upper mass limit of 300 $M_\odot$ while the SB99+Geneva model assumes 100 $M_\odot$, which explains the discrepancy at the earliest ages. Non-rotating and moderately rotating models predict a steep decline in the ionizing luminosity with time. Top: photons capable of ionizing hydrogen. Middle: photons capable of singly ionizing helium. Bottom: photons capable of doubly ionizing helium.

$Z = 0.002$ and 0.001 for Figure 6.9 and $Z = 0.014$ and 0.02 for Figure 6.10.

All of the models produce comparable hydrogen-ionizing photon output rates until $\sim$ 3 Myr. Note that Q is systematically offset in the SB99+Geneva model at very early times due to the lack of stars more massive than 300 $M_\odot$. The discrepancies between different models become more pronounced at higher energies: for photons blueward of 228 Å, the differences are substantial as early as 2 Myr. This is because Q becomes much more sensitive to the shape of the SED at progressively shorter wavelengths, where the pre-

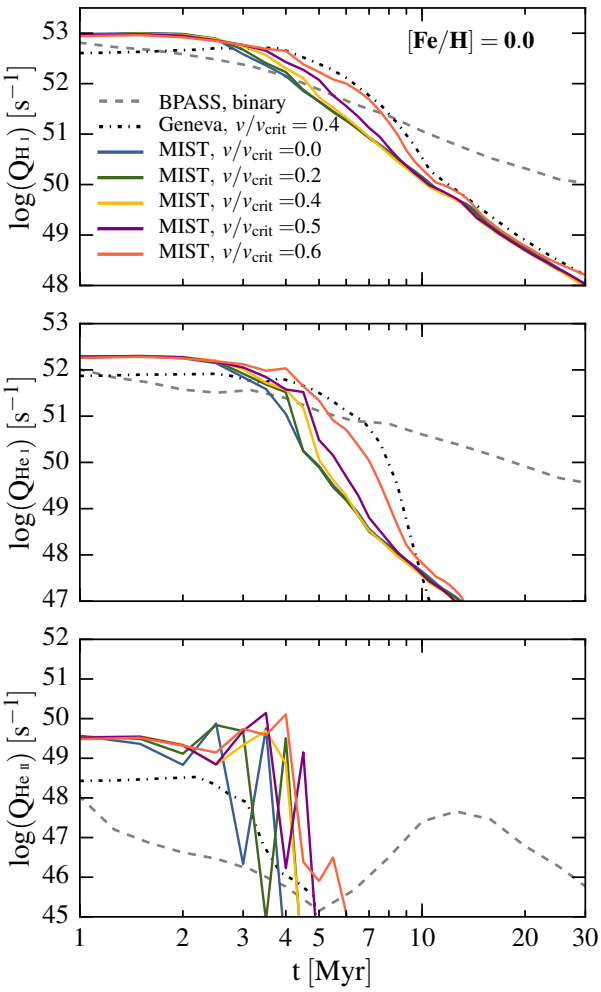


Figure 6.10: Same as Figure 6.9 except now showing [Fe/H] = 0.0.

dictions are sensitive to fast evolving stars and details of hot star SEDs. Overall, the SB99+Geneva models produce the softest radiation field (see also Figures 6.7 and 6.8). The FSPS+MIST models produce copious amounts of helium-ionizing photons after 2 Myr when the WR stars begin to appear, which is several orders of magnitude larger than the SB99+Geneva models. Again, the binary effects are responsible for the prolonged production of ionizing photons at very late times.

As described in Section 6.3.1, assigning an appropriate spectrum to a WR star in the isochrone is a nontrivial task due to the high optical depth of the WR wind beyond the standard hydrostatic surface computed by stellar evolutionary codes. We tested the effect of modifying the WR temperature according

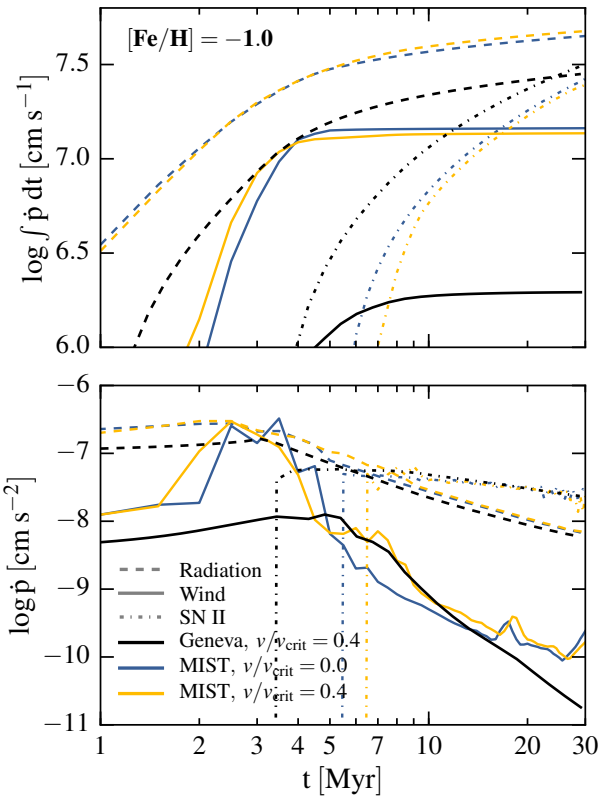


Figure 6.11: Top: cumulative specific momentum injected via radiation, wind, and type II supernovae for a single-burst stellar population at $[\mathrm{Fe/H}] = -1.0$. We compare $v/v_{\mathrm{crit}} = 0.0$ (blue) and 0.4 (yellow) FSPS+MIST model predictions with that from SB99+Geneva, which is shown as a black curve. We assume a $\tau_{\mathrm{IR}} = 1$ for simplicity. Bottom: instantaneous specific momentum. The FSPS+MIST models assume an IMF upper mass limit of 300 $M_{\odot}$ while the SB99+Geneva model assumes 100 $M_{\odot}$. This differences largely explains the offset between the two models at very early times.

to the Smith et al. (2002) weighting scheme, which is the default choice in SB99. Consistent with what Levesque et al. (2012) found, the difference is negligible for the hydrogen ionizing luminosity but becomes more pronounced for harder photons, which may explain the large discrepancy between the SB99+Geneva and FSPS+MIST predictions for helium-ionizing photons. Since this pertains to WR stars only, any variation due to the choice of WR temperatures disappears after $\sim$ 5–6 Myr. We proceed with our default WR T_{eff} assignment, but emphasize that the choice of this weighting scheme (or the lack thereof) will introduce some variation to the predicted output of the most energetic photons.

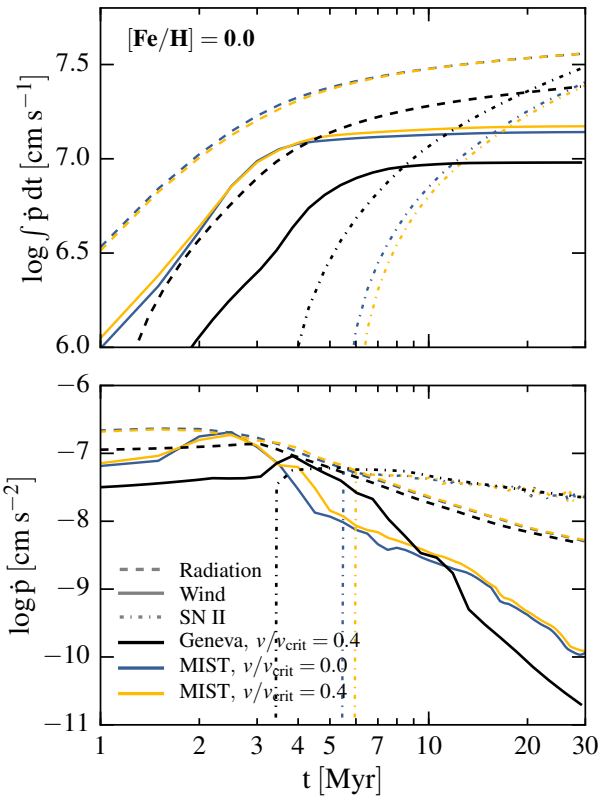


Figure 6.12: Same as Figure 6.11 except now showing [Fe/H] = 0.0.

6.4.3 Momentum Output

Here we consider the momentum output from massive stars. Figures 6.11 and 6.12 show the cumulative (top) and instantaneous (bottom) specific momentum injected in radiation, wind, and type II supernovae. Momentum injected via radiation is computed as follows:

$$\frac{dp_{\rm rad}}{dt} = (1+\tau_{\rm IR})\frac{L_{\rm bol}(t)}{c} \quad , \tag{6.3}$$

where $\tau_{\rm IR}$ is the infrared optical depth. In detail there is also a factor of $(1-\exp(-\tau_{\rm UV/optical}))$, but given the large optical depth of UV/optical photons, it reduces to a factor of order unity (e.g., Agertz et al. 2013). The $\tau_{\rm IR}$ term accounts for multiple absorption and re-radiation of the infrared photons in a very optically thick medium. Its preferred fiducial value is still under debate (e.g., Murray et al. 2010; Andrews & Thomp-

son 2011; Hopkins et al. 2011; Krumholz & Thompson 2012). For simplicity, we assume $\tau_{\rm IR} = 1$ in order to isolate the effect of SPS models alone, but empirical relations between $\tau_{\rm IR}$ and cluster mass (see e.g., Figure 3 in Agertz et al. 2013) suggest that $\tau_{\rm IR}$ can be as large as ~ 100 for a $10^6\ M_\odot$ cluster.

The momentum injection rate from a stellar wind is obtained using the mass loss rate and the wind speed:

$$\frac{dp_{\rm wind}}{dt} = \dot{M} v_{\rm wind} \ , \tag{6.4}$$

The wind speed is estimated using the relation adopted in SB99 (Leitherer et al. 1992), which is comparable to the escape speed from the stellar photosphere:

$$\begin{aligned} \log(v_{\rm wind})\ [{\rm km\ s^{-1}}] = 1.23 - 0.30\log(L/L_\odot) \\ +0.55\log(M/M_\odot) + 0.64\log(T_{\rm eff}\ [K]) \\ +0.13\log(Z/Z_\odot) \ . \end{aligned} \tag{6.5}$$

Finally, the momentum deposition per type II SN (SNII) event is

$$p_{\rm SNII} = \frac{2E_{\rm SNII}}{v_{\rm SNII}} \ , \tag{6.6}$$

where we assume that a typical SNII explosion outputs 10^{51} erg of kinetic energy (thermalization via shocks) and the ejecta are launched at $v_{\rm SNII} = 3 \times 10^8$ cm s^{-1} (Dale 2015). Moreover, we assume that only stars with initial masses between 8 $M_\odot$ and 40 $M_\odot$ terminate their lives as typical SNII and stars more massive than 40 $M_\odot$ directly collapse to a black hole (Fryer 1999, but see also e.g., Sukhbold & Woosley 2014). The corresponding momentum injection rate is

$$\frac{dp_{\rm SNII}}{dt} = p_{\rm SNII} \frac{dN_{\rm SNII}}{dt} \ , \tag{6.7}$$

where the supernovae rate is obtained by integrating the IMF weight over the most massive star still alive in the previous and current time steps divided by the time interval.

We compare FSPS+MIST to SB99+Geneva, which is a popular choice for stellar population model in many galaxy simulations that attempt to include the effects of stellar feedback (e.g., Hopkins et al. 2014; Agertz & Kravtsov 2015). We use the SB99 outputs directly for the wind momentum and SNII rates, but we compute ourselves the radiation momentum using the bolometric luminosity reported by SB99 along with Equation 6.3, and convert the SNII rates to the SNII momentum injection rate using Equations 6.6 and 6.7. The first SN explosion occurs at an earlier time in the SB99+Geneva model because their rate calculation assumes that all stars above 8 $M_{\odot}$ explode as SNII. For the FSPS+MIST model, the onset of SNII is delayed at higher rotation rates due to the increased lifetimes (see also Figure 6.5). Radiative momentum is generally dominant, though this may be an underestimate since we set the $\tau_{\rm IR}$ enhancement factor to unity. At a fixed rotation rate, the metal-poor population ($[{\rm Fe/H}] = -1.0$) outputs more radiative momentum compared to the metal-rich population, because metal-poor stars tend to be hotter and brighter.

6.4.4 The Effects of Very Massive Stars

The IMF dictates how frequently stars within a certain mass range occur in nature. Understanding the origin of and quantifying the high-mass IMF slope and the cutoff mass (and their dependence on environmental factors such as metallicity) are active areas of research (e.g., Krumholz et al. 2011; Kroupa et al. 2013; Hopkins 2013; Andrews et al. 2013; Narayanan & Davé 2013; Dib 2014; Weisz et al. 2015). There are ongoing efforts to constrain these properties, but it is a difficult task due to their short lifetimes, rare numbers, and stochastic sampling effects.

Here we investigate the importance of VMSs ($M > 100\ M_{\odot}$) in SPS modeling by comparing two otherwise identical models with different cutoff masses. The default option in SB99, a widely-used SPS package that is commonly paired with the Geneva stellar evolutionary models (Ekström et al. 2012; Georgy

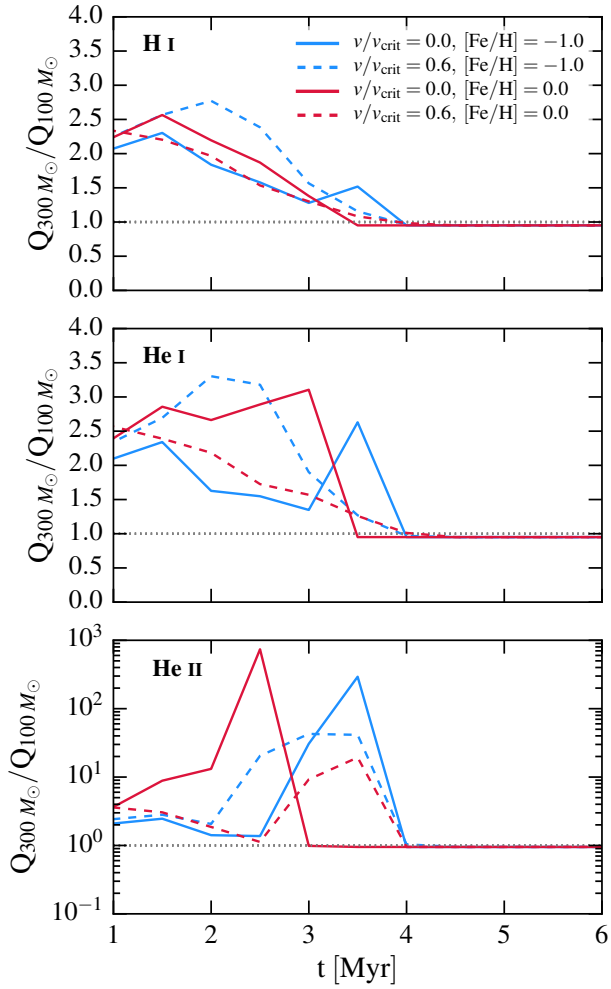


Figure 6.13: The ratio of the number of ionizing photons in the FSPS+MIST models with the IMF mass cutoff at 300 $M_\odot$ and 100 $M_\odot$ for two initial rotation rates and two metallicities. As expected, the ratio is essentially unity beyond ~ 4 Myr, by which time stars more massive than 100 $M_\odot$ have disappeared. In detail, it is slightly less than unity due to the IMF weights. Top: photons capable of ionizing hydrogen. Middle: photons capable of singly ionizing helium. Bottom: photons capable of doubly ionizing helium. Note the vastly different y-axis range compared to the top two panels.

et al. 2013; Yusof et al. 2013), accounts for stars with initial masses up to 100 $M_\odot$, though the underlying Geneva models are available up to 500 $M_\odot$. The BPASS models are available with the upper mass limit set to either 100 $M_\odot$ or 300 $M_\odot$. In a recent observational work, Smith et al. (2016) found that VMSs, rather than less massive but very fast-rotating stars, are necessary to simultaneously explain the large ionizing flux and spectral emission line features observed in the nuclear star clusters in a blue compact dwarf galaxy NGC 5253. They stressed the need for SPS models to include stars more massive than 100 $M_\odot$ in order

to correctly predict the properties of young massive star clusters, including those residing in high-redshift star-forming galaxies.

Since the MIST model grid ranges from 0.1 to 300 $M_{\odot}$, we are able to examine the contribution from VMSs to the SED, more specifically the ionizing luminosity over time. Recall from Figure 6.6 that the most massive stars contribute significantly to the flux blueward of 228 Å at 1 and 2 Myr, and completely dominate at 3 Myr. Beyond 3 Myr, they contribute zero flux because they have all but disappeared.

Figure 6.13 shows the ratio of ionizing luminosity emitted by stellar populations with IMF cutoffs at 300 and 100 $M_{\odot}$. For simplicity, we show only the $v/v_{\rm crit} = 0.0$ and 0.6 models. Similarly, Figure 6.14 shows the ratio of the total bolometric luminosity and momentum output. As expected, the ratio is nearly unity beyond $\sim$ 4 Myr, by which time stars more massive than 100 $M_{\odot}$ have disappeared. In detail, it is slightly less than unity due to the IMF weights. Moreover, note that the ratio of the momentum injection from supernovae is unity at all times because we assume that only stars less massive than 40 $M_{\odot}$ end their lives as SNII. These plots confirm what could be gleaned from Figure 6.6; the inclusion of VMSs can have an important effect on the integrated stellar population properties at very early times. Interestingly, this amounts to a factor of a few difference in some cases, e.g., hydrogen ionizing flux, bolometric luminosity, and radiative momentum output, whereas there can be an order of magnitude or more difference in the hardest EUV photon flux and wind momentum output. The dramatic difference in the helium ionizing photon luminosity can be understood by examining the contribution to the flux blueward of 228 Å in Figure 6.6; the large peak between 2 and 4 Myr is directly linked to the inclusion (or exclusion) of massive stars completely stripped of their hydrogen envelope.

These results are in broad agreement with those reported by Smith et al. (2016), who investigated the discrepancy in ages inferred from SED-fitting ($\sim$ 1 Myr; Calzetti et al. 2015) and WR spectroscopic features (3–5 Myr; Turner et al. 2015) of two nuclear star clusters in NGC 5253. They concluded that VMSs can explain the observed WR-like spectroscopic features, bringing the two age estimates into agreement

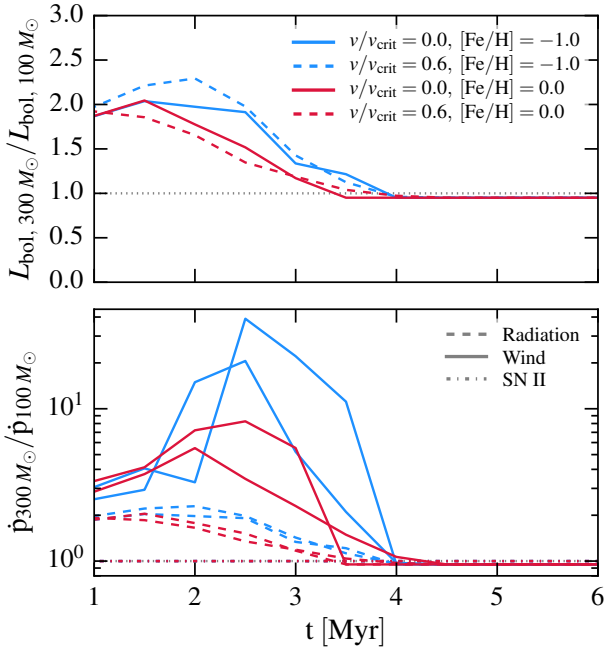


Figure 6.14: Top: the ratio of the bolometric luminosities in the FSPS+MIST models with the IMF mass cutoff at 300 $M_\odot$ and 100 $M_\odot$ for two initial rotation rates and two metallicities. Bottom: the same as the top panel except now showing the ratio of the instantaneous momentum injection.

(1–2 Myr) without needing to invoke older ages or extreme rotators. We separately computed the ionizing photon luminosity of a $v/v_{\rm crit} = 0.4$, $[{\rm Fe/H}] = -0.50$ (the metallicity of NGC 5253 is 35% of the solar value assuming the Asplund et al. 2009 solar oxygen abundance; Monreal-Ibero et al. 2012) stellar population both with and without stars more massive than 100 $M_\odot$. Following Smith et al. (2016), we assumed a total stellar mass of 3.3×10^5 $M_\odot$ for the two clusters and compared the ionizing flux at 2 and 4 Myr to the observed value of 2.2×10^{52} s^{-1} for the central 5 pc. When we set the IMF upper limit at 100 $M_\odot$, we obtain 1.7×10^{52} s^{-1} and 1.0×10^{52} s^{-1} at 2 and 4 Myr, respectively. Importantly, the maximum value of the ionizing flux attained by a population excluding VMSs is only $\sim 1.9 \times 10^{52}$ s^{-1}. We confirm the Smith et al. (2016) result that models that do not account for VMSs underpredict the ionizing flux. However, when we extend the upper mass limit to 300 $M_\odot$, we obtain 4.0×10^{52} s^{-1} (maximum) and 0.9×10^{52} s^{-1} at 2 and 4 Myr. The conclusions do not change qualitatively when we instead consider a non-rotating stellar population. However, some rotational mixing resulting from a moderate rotation is necessary in order

to match the observed factor of ~ 3 enhancement in the nebular nitrogen abundance reported by Smith et al. (2016). Both the excess and the enrichment timescale for nitrogen in the MIST rotating model are in agreement with the Köhler et al. (2015) evolutionary model, which was demonstrated in Smith et al. (2016) to be capable of producing the level of enrichment observed in the clusters.

The main conclusion here is that for most integrated quantities of interest, such as the hydrogen ionizing luminosity, increasing the IMF upper mass cutoff to 300 $M_{\odot}$ results in a factor of a few increase at very early times ($t \lesssim 3$ Myr; see also Stanway et al. 2016). This difference may still have important observational consequences, as discussed in Smith et al. (2016). For other quantities, such as the production of the most extreme EUV photons, the difference can be as large as several orders of magnitude, though these quantities are more sensitive to the underlying models of VMSs, which still have large uncertainties.

6.4.5 The Effects of Metallicity

Although we focus on $[\mathrm{Fe/H}] = -1.0$ and 0.0 stellar populations in this work to enable a roughly equal comparison across different models,* it is important to explore the effects of metallicity over a broader range. Metal-poor populations are particularly worth investigating since the effect of rotation on stellar population properties becomes more significant at lower metallicities. Moreover, as we will discuss in Section 6.5, high-redshift galaxies believed to be the principle sources of ionizing photons have stellar metallicities of $\log(Z/Z_{\odot}) \lesssim -2$ at $z = 6$ (e.g., Ma et al. 2016a).

Figure 6.15 illustrates the effect of metallicity on the ionizing photon production. In the top panel, we show the total number of hydrogen ionizing photons produced by 10 Myr. The different colors correspond to rotating stellar populations at different metallicities. As expected, the ionizing photon production is more efficient in low metallicity environments. For comparison, the equivalent point for the lowest metallicity BPASS binary model available ($Z = 0.001$) is shown in black. We note that for the BPASS model,

*As a reminder, we compare with SB99+Geneva models at $Z = 0.002$ and $Z = 0.014$ and BPASS models at $Z = 0.001$, and $Z = 0.020$.

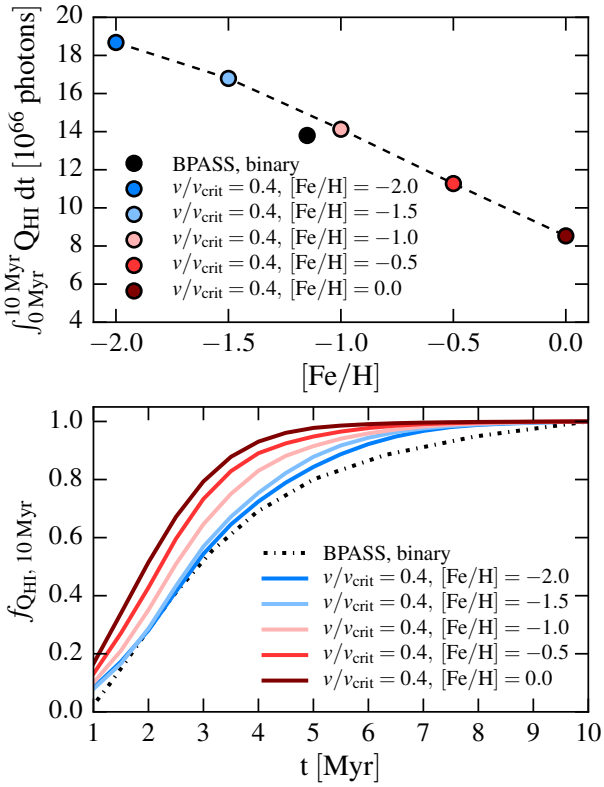


Figure 6.15: Top: the total number of hydrogen ionizing photons produced by 10 Myr. The different colors correspond to rotating stellar populations at different metallicities. As expected, the ionizing photon production is more efficient in low metallicity environments. For comparison, the equivalent point for the lowest metallicity BPASS binary model available ($Z = 0.001$) is shown in black. For the BPASS model, integrating out to 30 Myr instead of 10 Myr makes a $\sim 10\%$ difference in the total number of photons. Bottom: the fraction of total hydrogen-ionizing photons emitted by 10 Myr for the same set of models. The decrease in ionizing photon production with time is more gradual at lower metallicities.

integrating out to 30 Myr instead of 10 Myr makes a $\sim 10\%$ difference in the total number of photons. The bottom panel shows the fraction of total hydrogen-ionizing photons emitted by 10 Myr for the same set of models. The decrease in ionizing photon production with time is more gradual at lower metallicities. We revisit these points in Section 6.5.

6.4.6 The Effects of a Rotation Distribution

Observations of massive stars in Galactic and local group clusters show a distribution of rotation rates (e.g., Penny 1996; Huang et al. 2010; Ramírez-Agudelo et al. 2013), which may hold important clues for shedding light on their formation processes (e.g., Zinnecker & Yorke 2007). A distribution of rotation rates

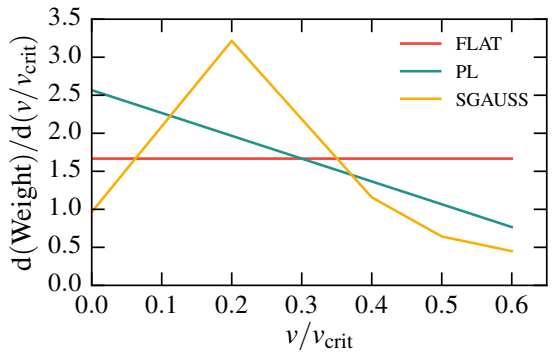


Figure 6.16: A schematic diagram showing the three types of rotational probably distribution functions explored in this work. "FLAT" represents a simple case of a flat distribution. "PL" is a simple power law that decreases with the rotation rate. "SGAUSS" is meant to approximate a skewed Gaussian distribution centered at $v/v_{\rm crit} = 0.2$.

is interesting in the context of this work for the simple reason that it would introduce *a range of lifetimes, and therefore a range of MSTO masses at a fixed age*. For example, by the time the dense GMC is sufficiently dispersed, allowing for ionizing photons to escape, the most massive slowly rotating stars will have already died, perhaps as SNe. However, the most massive rapidly rotating stars will still be present and producing copious quantities of ionizing photons.

For this work, recall that we computed MIST isochrones at five different rotation rates—$v/v_{\rm crit} = 0.0, 0.2, 0.4, 0.5$, and 0.6—for each metallicity. From these, we create three composite populations by combining SSPs with different $v/v_{\rm crit}$ according to the probability distribution functions (PDFs) shown in Figure 6.16. "FLAT" represents a simple case of a flat distribution. "PL" is a simple power law that decreases with the rotation rate. "SGAUSS" approximates a skewed Gaussian distribution centered at $v/v_{\rm crit} = 0.2$, which is supposed to mimic the observed distribution of O-type stars in the 30 Doradus region of the Large Magellanic Cloud (Ramírez-Agudelo et al. 2013). We simplify our approach by assuming that the rotation distribution is mass-independent over the mass range of interest ($M > 20\ M_{\odot}$). This is an acceptable assumption for two reasons. First, the rotation rate measurements of stars more massive than $M \sim 40\ M_{\odot}$ are scarce—for instance, $< 20\%$ of the Ramírez-Agudelo et al. 2013 sample was estimated to have masses above $40\ M_{\odot}$—so their rotation rates, let alone their mass-dependence, are still relatively uncertain. Sec-

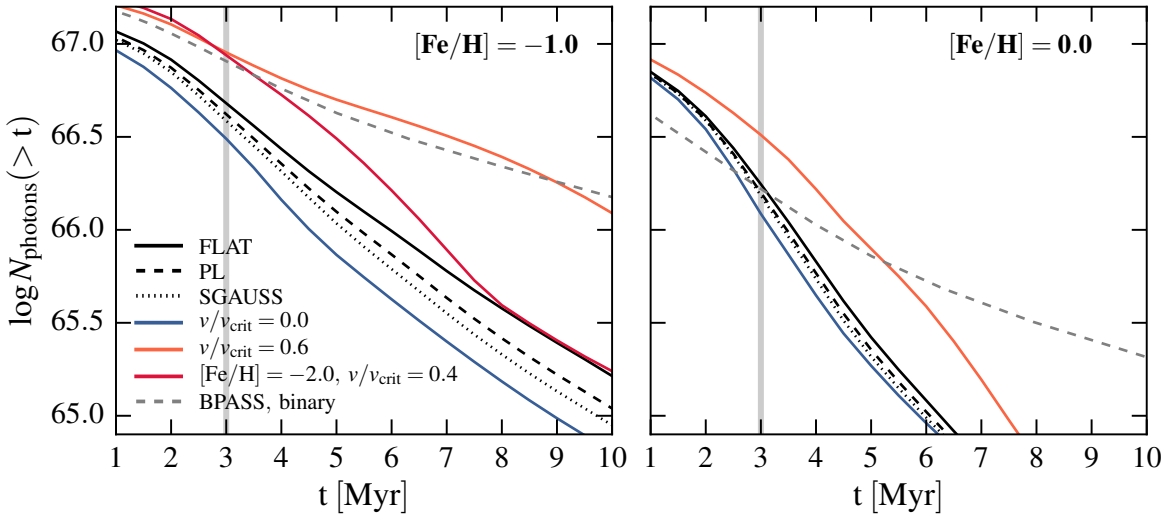


Figure 6.17: The total number of hydrogen-ionizing photons emitted between time t and 30 Myr. Blue and orange curves correspond to the $v/v_{\rm crit} = 0.0$ and 0.6 models at $[{\rm Fe/H}] = -1.0$ (left) and 0.0 (right). "FLAT" represents a simple case of a flat distribution, "PL" corresponds to a power law that decreases with the rotation rate, and "SGAUSS" approximates a skewed Gaussian distribution centered at $v/v_{\rm crit} = 0.2$. The BPASS model assumes an IMF cutoff of 300 $M_\odot$ for $Z = 0.001$ (left) and $Z = 0.014$(right). In the left panel, we also show the $v/v_{\rm crit} = 0.4$ model at $[{\rm Fe/H}] = -2.0$ for comparison. The gray vertical line marks roughly when GMCs begin to disperse (Ma et al. 2015), yielding order unity escape fraction of ionizing photons.

ond, the observed rotation rates do not necessarily represent the rotation rates at birth: processes such as stellar winds, magnetic braking, and binary interactions modify the surface rotation rates, and the angular momentum is redistributed in the interior through mechanisms that are not fully understood in stars of all masses (e.g., Wolff et al. 2004; Cantiello & Langer 2010; Gallet & Bouvier 2013; Fuller et al. 2015). However, studying a select sample of young MS stars somewhat alleviates this issue (for example, Huang et al. 2010 uses a $\log g$ criterion). Further complications include macroturbulence (e.g., Penny & Gies 2009) and $\sin i$ projection effects, which make the task of inferring the initial conditions and the subsequent evolution much more complex. We attempt to mitigate some of these problems by exploring a range of rotation PDFs. Nevertheless, given these complexities, we emphasize that this is an attempt to explore the broad effects of a rotation distribution on observed quantities.

In Figure 6.17, we plot the total number of hydrogen-ionizing photons emitted from time t to 30 Myr for $[{\rm Fe/H}] = -1.0$ (left) and 0.0 (right). The blue and orange curves correspond to $v/v_{\rm crit} = 0.0$ and 0.6

single-rotation models and the gray dashed line represents the BPASS binary model, which assumes an IMF cutoff of 300 $M_{\odot}$ for $Z = 0.001$ (left) and $Z = 0.014$ (right). In the left panel, we additionally show the $v/v_{\rm crit} = 0.4$ model at $[{\rm Fe/H}] = -2.0$ for comparison. The gray vertical line marks roughly when GMCs begin to disperse, yielding order unity escape fraction of ionizing photons out of GMCs (e.g., Ma et al. 2015).

A composite population with a flat rotational distribution ("FLAT")—which has the largest contribution from $v/v_{\rm crit} = 0.6$—still has three times fewer photons in its budget compared to the fastest-rotating and binary scenarios by the time GMCs begin to disperse. The very low-metallicity case ($[{\rm Fe/H}] = -2.0$), where the rotation effects are expected to be large and therefore the fall-off in the production rate of ionizing photons is more gradual in time (Figure 6.15), has a comparable ionizing photon budget compared to the fast-rotating and binary scenarios by 3 Myr. However the number of available photons falls by an order of magnitude below that of the binary model by 8 Myr.

Interestingly, a very rapidly rotating population with $v/v_{\rm crit} = 0.6$ is able to mimic the time-dependence of ionizing luminosity in a binary population. However, observations of single O-type stars in the LMC (Ramírez-Agudelo et al. 2013) effectively rule out populations of very fast-rotating massive stars, at least in the local Universe. It is also interesting to note that the ionizing luminosity in a moderately rotating stellar population at very low metallicity can rival that of the binary model and rapidly rotating model, though the production rate also falls off steeply beyond $\sim$ 5–6 Myr.

6.5 Discussion

In this section we discuss the implications of the rotating, massive star models in two main contexts: cosmic reionization and the interpretation of high-redshift star-forming galaxies.

In our current understanding of the high-redshift universe, cosmic reionization was largely driven by high energy photons leaking out from star-forming galaxies (e.g., Madau et al. 1999; Haardt & Madau

2012). The escape fraction of these ionizing photons, $f_{\rm esc}$, required to explain the observed ionization state of the $z = 6$ intergalactic medium exceeds 10% (e.g., Finkelstein et al. 2012; Robertson et al. 2013; Gnedin & Kaurov 2014), well above the values inferred from their lower redshift analogs (e.g., Iwata et al. 2009; Boutsia et al. 2011; Siana et al. 2010; Leitet et al. 2013). Galaxy simulations have produced a wide range of predicted $f_{\rm esc}$ (e.g., Gnedin et al. 2008; Razoumov & Sommer-Larsen 2010; Wise et al. 2014). In particular, a recent suite of simulations from the Feedback in Realistic Environment (FIRE) project produced a time-averaged $f_{\rm esc}$ of only $\lesssim 5\%$ (Ma et al. 2015). Since the production of ionizing photons is dominated by young massive stellar populations embedded in optically-thick natal environments, $f_{\rm esc}$ from these simulations depends sensitively on the complex connection between the properties of the underlying stellar population model* and the mechanisms that disrupt the GMCs (e.g., Murray et al. 2010). In their follow-up work, Ma et al. (2016b) found that replacing the underlying stellar population model with one that includes binary effects (BPASS) in their post-processing radiative transfer calculations can boost $f_{\rm esc}$ significantly due to its ability to sustain ionizing photon production at late times, well after the disruption of the GMCs. As emphasized by the authors, the key difference between the fiducial single star models and the binary models is the time-dependence of the ionizing photon production. Other mechanisms have also been proposed to increase the escape fraction of ionizing radiation, including runaway massive stars (Conroy & Kratter 2012; Kimm & Cen 2014).

In Section 6.4.6, we explored the same concept by considering low metallicities and velocity distributions as means to prolong the ionizing photon production. Together, Figures 6.15 and 6.17 demonstrate that stellar populations in sufficiently low-metallicity environments (e.g., high redshift) require only moderate rotation rates in order to produce significant ionizing photons. Moreover, at the time of order unity escape fraction (~ 3 Myr), the ionizing photon budget can rival that of a binary population or a fast-rotating but slightly more metal-rich population. However, it is very challenging to prolong the emission of ioniz-

*The FIRE simulations use SB99 with the "Padova+Asymptotic Giant Branch" option (Bressan et al. 1993; Fagotto et al. 1994a,b; Girardi et al. 2000).

ing photons by an amount required to reproduce the relatively large values of f_{esc} implied by the cosmic reionization models (Ma et al. 2016b), and we conclude that binary interactions may indeed play a critical role. Detailed numerical simulations using these low-metallicity rotating stellar population models are required to address this point more quantitatively.

Rotating massive stars have also been considered in the context of high-redshift star-forming galaxies. Recently, Steidel et al. (2014) have found that the locus of $z \sim 2$–3 star-forming galaxies is offset relative to their $z = 0$ counterparts in the BPT diagram (Baldwin et al. 1981), an empirical diagnostic for probing the physical conditions and ionizing sources of nebular gas. The authors concluded that this shift could be explained by a harder stellar ionizing radiation field ($T_{\rm blackbody} = 50000$–$60000$ K), higher ionization parameter (the ratio of the number densities of hydrogen ionizing photons to hydrogen atoms in a H II region), and nitrogen-enhanced nebular gas, all of which could be explained by rapid rotation or binaries. In subsequent work, Steidel et al. (2016) found that the BPASS binary models are able to generate sufficiently hard ionizing radiation fields to reproduce the various observed line ratios, while the Geneva+SB99 cannot self-consistently explain the observations at any gas-phase metallicity or ionization parameter. Figure 6.7 shows that the FSPS+MIST models predict EUV flux that falls right in between the two models considered in Steidel et al. (2016). A more detailed comparison between the emission line predictions for the FSPS+MIST, Geneva+SB99, and BPASS models will be carried out in Byler et al. (2017, submitted).

6.6 Summary

In this work we explored the integrated properties of massive, rotating single-star stellar populations in both metal-rich and metal-poor environments. Our main conclusions are as follows:

1. We confirm that rotation leads to longer MS lifetimes and brighter and hotter stars. We also find that the magnitude of the effects is non-linear with the rotation rate. In particular, the $v/v_{\rm crit} = 0.5$ and 0.6 models show a significant enhancement in the ionizing luminosity due to the blueward evolution of massive stars in the HR diagram at ages greater than 3 Myr. A comparison of the predicted MS lifetimes for the Geneva (Ekström et al. 2012; Georgy et al. 2013; Yusof et al. 2013) and MIST

(Dotter 2016; Choi et al. 2016) stellar evolutionary tracks demonstrates that the MS lifetime boost at a fixed mass is larger in the Geneva models compared to that in the MIST models, which suggests that rotational mixing may be more efficient in the former.

2. Rotation effects become more significant at lower metallicities as the star becomes more compact and angular momentum loss due to winds becomes less important. We found that the $[\mathrm{Fe/H}] = -2.0$ population produces twice as many photons as the $[\mathrm{Fe/H}] = 0.0$ population by 10 Myr. From comparisons among models ranging from $[\mathrm{Fe/H}] = 0.0$ to -2.0, we conclude that rotation leads to a more gradual decline in ionizing luminosity with time at low metallicities. As demonstrated in Ma et al. (2016b), this time-dependence has interesting ramifications for the escape fraction of ionizing photons, which in turn could impact high redshift, metal-poor galaxies at the time of cosmic reionization.

3. The contribution from VMSs ($\geq 100\ M_{\odot}$) is significant for a short period of time ($t \lesssim 4$ Myr), increasing the ionizing luminosity by a factor of a few (H I) to a few orders of magnitude (He II). Although the cumulative effect is small in most cases, taking VMSs into account in SPS modeling may be important for understanding a number of recent observations, including the ages and ionizing photon budget in nuclear star clusters (Smith et al. 2016).

4. We explored composite stellar populations with three different rotation PDFs to investigate whether a small number of fast rotators can lead to a significant boost in the ionizing photon luminosity at late times ($\sim$ 10 Myr) compared to a non-rotating population. We find that the effect is small, amounting to a factor of two or smaller for a skewed distribution peaking at low v/v_{crit} and a factor of ~ 3 for the extreme case of a flat PDF. Numerical simulations are required to assess whether or not this effect is important for the disruption of GMCs and/or the escape of ionizing radiation from galaxies.

ACKNOWLEDGMENTS

We thank J.J. Eldridge, Mason Ng, and Georgie Taylor for sharing with us their unpublished WM-Basic models. We thank Matteo Cantiello, Aaron Dotter, and Daniel Weisz for useful comments and suggestions that have improved the manuscript. We also thank Bill Paxton and the rest of the MESA community who have made this project possible. C.C. acknowledges support from NASA grant NNX13AI46G, NSF grant AST- 1313280, and the Packard Foundation.

7

CONCLUSIONS

7.1 SUMMARY

In this thesis, I explored the connection between stars and galaxies in a series of chapters that fall into one of two broad themes.

In the first half of this work, I discussed the construction of new stellar evolution models and explored the implications of several model uncertainties, beginning with the introduction of the MIST models in Chapter 2. The goal of this project was to create an extensive stellar evolution database computed within a single, self-consistent framework using MESA, a state-of-the-art 1D stellar evolution code. I generated models with solar-scaled abundance ratios covering a wide range of ages ($5 \leq \log(\mathrm{Age})\ [\mathrm{yr}] \leq 10.3$), masses ($0.1 \leq M/M_{\odot} \leq 300$), and metallicities ($-4.0 \leq [\mathrm{Z/H}] \leq 0.5$) that are continuously evolved from the pre-main sequence to the advanced evolutionary phases such as the white dwarf cooling sequence and the end of carbon burning, depending on the initial mass. I provided an overview of key ingredients describing stellar physics and presented an exhaustive set of comparisons against observations and other models widely used in the literature. In Chapter 3, I investigated the importance of surface boundary conditions in stellar evolution calculations on the effective temperatures of red giant stars, which has important consequences for inferring stellar ages from isochrones and placing constraints on the mixing length pa-

rameter, $\alpha_{\rm MLT}$. I found that even though the models under consideration can reproduce the properties of the Sun (as a result of solar-calibration), both the type of boundary condition and the location at which it is applied to the interior model yield ≈ 100 K, metallicity- and $\log g$-dependent changes to the effective temperature distribution along the red giant branch. Next, in Chapter 4, I explored the effects of several important model uncertainties on the typical observations of star clusters, such as the surface abundances on the red giant branch and the main sequence turn off colors in CMDs, with the goal of accurately inferring stellar ages in the *Gaia* era. I expect that high quality photometry, parallax distances, and cluster memberships from *Gaia* will be immensely useful for disentangling the subtle but qualitatively distinct ways that these model and stellar parameters shape the CMD morphologies.

In the second half, I showcased two examples that highlight the star-galaxy connection. In Chapter 5, I inferred the assembly histories of quiescent galaxies using their stellar populations as tracers. I modeled the SDSS and AGES optical spectra of a large sample of quiescent galaxies between $0.1 < z < 0.7$ to measure stellar ages and the abundances of Fe, Mg, C, N, and Ca. I concluded that there is negligible evolution in the elemental abundances at fixed stellar mass over the last ~ 7 Gyr and that the increase in stellar ages with time for massive galaxies is consistent with passive evolution since $z = 0.7$. These results provide strong support for the passive evolution scenario in the inner regions of massive quiescent galaxies over the last half of cosmic time. Finally, in Chapter 6, I investigated the impact of stellar rotation on the SEDs of young, massive stellar populations and examined the implications for cosmic reionization by massive stars and the interpretation of nebular emission lines in high-redshift star-forming galaxies. I coupled the MIST isochrones, computed for several initial rotation rates, with the Flexible Stellar Population Synthesis package to generate model SEDs and predict the ionizing photon production as a function of time. I found that even in low-metallicity environments where rotation has a significant effect on the evolution of massive stars, a substantial contribution from fast-rotating (initial rotation rate $> 40\%$ of critical rotation rate) stars is required to sustain the production of ionizing photons beyond a few Myr following a starburst.

7.2 Future Work

In the following sections, I discuss ongoing work in two areas.

7.2.1 Stellar Evolution Models with Non-solar-scaled Abundances

The first MIST paper and data release (v1.0) focused exclusively on stellar evolutionary tracks and isochrones computed with solar-scaled abundances. My collaborators and I are currently working on MIST v2.0 that features non-solar-scaled abundances (Dotter et al., in prep.), and these new models will be applied to systems that are known to harbor stellar populations with non-solar-scaled, e.g., α-enhanced, abundances, such as globular clusters (e.g., Cohen 1978; Pilachowski et al. 1980; Gratton & Ortolani 1989) and massive elliptical galaxies (e.g., Graves & Schiavon 2008; Thomas et al. 2010; Johansson et al. 2012; Worthey et al. 2014; Conroy et al. 2014).

We computed the new MESA evolutionary tracks according to the original MIST framework but with several updates, two of which I discuss here. First, to ensure self-consistency, we implemented new tables of low- and high-temperature opacities (AESOPUS, Marigo & Aringer 2009; OPAL, Iglesias & Rogers 1996), surface boundary conditions from the ATLAS12 (Kurucz 1970, 1993) models atmospheres, and bolometric corrections from the SYNTHE/C3K (Conroy et al., submitted.) synthetic stellar spectra, all assuming non-solar-scaled mixtures. Second, we incorporated updates to white dwarf physics that have been introduced in MESA since the publication of MIST v1.0. Now we account for the gravitational settling of ^{22}Ne isotopes, which may be a significant source of heating during the late cooling phase prior to the crystallization in the interior (e.g., Isern et al. 1991; Bildsten & Hall 2001; García-Berro et al. 2008). As a result, the white dwarf cooling phase can be delayed by a few tenths to a few Gyr depending on the mass and metallicity, which has interesting ramifications for white dwarf luminosity functions and age-dating clusters with their white dwarf populations (García-Berro et al. 2010).

As with the first MIST paper, we plan to perform extensive calibrations and comparisons with observations and some of the most widely-used existing models in the literature. The new models will also enable several exciting and novel techniques, such as the simultaneous fitting of the main sequence turn off and the white dwarf cooling sequence in globular clusters. In the next section, I will highlight one example application of the new non-solar-scaled isochrones in stellar population synthesis.

7.2.2 The Effect of Non-solar-scaled Abundances on Galaxy SEDs

The current generation of SPS models has enabled measurements of stellar ages and metallicities, and the simultaneously prediction of UV through IR broadband data for many types of galaxies (Conroy 2013). However, there is one relatively under-developed area: non-solar-scaled elemental abundances (but see also Coelho et al. 2007; Walcher et al. 2009; Vazdekis et al. 2015). In particular, there is a general lack of consistency between the spectral libraries and isochrones—in terms of the physical assumptions and the composition—that are coupled together in SPS models, and this may play a key role in resolving a long-standing problem in the field. First noted in Eisenstein et al. 2001, the model SEDs of solar metallicity, old simple stellar populations are far too red compared to the observed SEDs of luminous red galaxies, also known as LRGs.

Several theories have been put forth, including a "frosting" of young stars and/or metal-poor stars as well as a variable IMF (e.g., Maraston et al. 2009; Conroy et al. 2010; Ricciardelli et al. 2012). But the impact of non-solar-scaled abundance patterns on e.g., broadband SEDs and absorptions features, has only recently started to be explored in depth (Vazdekis et al. 2015), even though LRGs have been known to contain primarily old, low-mass stars (e.g., Graves & Schiavon 2008; Thomas et al. 2010; Johansson et al. 2012; Worthey et al. 2014; Conroy et al. 2014).

Relaxing the solar-scaled assumption affects both the isochrones and stellar spectra. Increasing the α abundance at fixed total metallicity makes the isochrones hotter and decreases the main sequence lifetimes

(Dotter et al. 2007) due to the decreased overall opacity (heavier iron-peak elements are being replaced by oxygen). However, the individual α elements influence the physical properties of a star in distinct ways: for example, oxygen makes the main sequence turnoff hotter while neon has almost no effect. Moreover, a given element shapes the morphology of the isochrone in the HR diagram in complex ways, i.e., it is not an overall shift in $T_{\rm eff}$. Similarly, increasing the α abundance at fixed total metallicity makes the stellar spectrum bluer overall (e.g., Coelho et al. 2007), but the individual α elements change the continua and the absorption features in unique, wavelength-dependent ways (e.g., see Figures 2 and 3 in Conroy et al. 2014). I am currently investigating the importance of both the α-enhancement (in lock step) and variable abundances on the predictions of broadband colors of quiescent galaxies—while also ensuring that the detailed absorption features in the spectrum are correctly reproduced—as a possible solution to the "SED color problem."

7.3 The *Gaia* Era and Beyond

As I noted throughout the chapters and discussed in detail in Chapter 4, *Gaia* is set to revolutionize the field of stellar astrophysics and galactic archaeology. *Gaia* is the successor to the *Hipparcos* mission—launched almost 30 years ago—whose objective is to measure the positions, distances, space motions, and other physical properties of approximately one billion stars, resulting in the most extensive and precise 3D catalog of the Milky Way and beyond (Gaia Collaboration et al. 2016). *Gaia*'s microarcsecond astrometry will deliver 0.1% distances for 700,000 stars out to a few hundred parsecs, 1% distances for $>$ 20 million stars out to a few kpc, and 10% distances beyond 10 kpc.* For comparison, the *Hipparcos* mission obtained milliarcsecond astrometry of some 200,000 stars, yielding 10% distances for $\sim 21,000$ stars within 100 parsecs (Perryman et al. 1997).

Accurate distances, membership determinations, and photometry from *Gaia*, combined with exist-

*http://sci.esa.int/gaia/31398-stellar-astrophysics/

ing panchromatic photometry and spectroscopic catalogs, will be the most stringent tests of stellar interior and atmosphere models to date. One possible extension to the work presented in Chapter 4 is a more rigorous, quantitative analysis of the effects of uncertain model parameters on the observations using the Fisher matrix formalism (Fisher 1935). This technique provides a straightforward framework to combine the constraints from inhomogeneous datasets and predict the utility of the observations for the model parameter inference (see also Angelou et al. 2017). This methodology is commonly used within the cosmology community (e.g., Albrecht et al. 2006), but in recent years it has been applied to other areas of astrophysics, including stellar spectroscopy (Ting et al. 2017) and galactic dynamics (Bonaca & Hogg 2018).

In addition to *Gaia*, next-generation observatories such as *LSST*, *JWST*, *TESS*, and *WFIRST*, and 30-meter telescope facilities such as the *ELT*, *GMT*, and *TMT*, will provide an unprecedented volume of high-quality photometric, asteroseismic, and spectroscopic data. On the stellar interior modeling side, we are taking small steps to evolve beyond the 1D framework that has defined our field for over 50 years. Using 2D and 3D simulations of important physical processes, such as convection (Brown et al. 2013; Trampedach et al. 2014; Magic et al. 2015; Arnett et al. 2015), to inform our physical intuition and to propose 1D approximations that are more accurate and better motivated is an active area of research. Although full 3D simulations of stellar evolution seem too far beyond grasp today, I am excited to see where our field takes us in the next decade.

REFERENCES

Abazajian, K. N., et al. 2009, ApJS, 182, 543

Aerts, C., Molenberghs, G., Kenward, M. G., & Neiner, C. 2014, ApJ, 781, 88

Agertz, O., & Kravtsov, A. V. 2015, ApJ, 804, 18

Agertz, O., Kravtsov, A. V., Leitner, S. N., & Gnedin, N. Y. 2013, ApJ, 770, 25

Agertz, O., Lake, G., Teyssier, R., Moore, B., Mayer, L., & Romeo, A. B. 2009, MNRAS, 392, 294

Ak, T., Bostancı, Z. F., Yontan, T., Bilir, S., Güver, T., Ak, S., Ürgüp, H., & Paunzen, E. 2016, Astrophys. Space Sci, 361, 126

Alastuey, A., & Jancovici, B. 1978, ApJ, 226, 1034

Albrecht, A., et al. 2006, ArXiv Astrophysics e-prints

Alecian, G., Michaud, G., & Tully, J. 1993, ApJ, 411, 882

Allard, F., Homeier, D., & Freytag, B. 2012, Philosophical Transactions of the Royal Society of London Series A, 370, 2765

Alonso, A., Arribas, S., & Martinez-Roger, C. 1996, A&A, 313, 873

An, D., et al. 2009, ApJ, 700, 523

Anders, E., & Grevesse, N. 1989, Geochimica et Cosmochimica Acta, 53, 197

Andersen, J. 1991, The Astronomy and Astrophysics Review, 3, 91

Andrews, B. H., & Thompson, T. A. 2011, ApJ, 727, 97

Andrews, J. E., et al. 2013, ApJ, 767, 51

Angelou, G. C., Bellinger, E. P., Hekker, S., & Basu, S. 2017, ApJ, 839, 116

Angelou, G. C., D'Orazi, V., Constantino, T. N., Church, R. P., Stancliffe, R. J., & Lattanzio, J. C. 2015, MNRAS, 450, 2423

Angulo, C., et al. 1999, Nuclear Physics A, 656, 3

Anthony-Twarog, B. J., Deliyannis, C. P., & Twarog, B. A. 2014, AJ, 148, 51

Antia, H. M., & Basu, S. 2005, ApJL, 620, L129

Arentoft, T., Brogaard, K., Jessen-Hansen, J., Silva Aguirre, V., Kjeldsen, H., Mosumgaard, J. R., & Sandquist, E. L. 2017, ApJ, 838, 115

Aringer, B., Girardi, L., Nowotny, W., Marigo, P., & Lederer, M. T. 2009, A&A, 503, 913

Arnett, W. D., Meakin, C., Viallet, M., Campbell, S. W., Lattanzio, J. C., & Mocák, M. 2015, ApJ, 809, 30

Arnouts, S., et al. 2007, A&A, 476, 137

Ashby, M. L. N., et al. 2009, ApJ, 701, 428

Asplund, M., Grevesse, N., & Sauval, A. J. 2005, in Astronomical Society of the Pacific Conference Series, Vol. 336, Cosmic Abundances as Records of Stellar Evolution and Nucleosynthesis, ed. T. G. Barnes, III & F. N. Bash, 25

Asplund, M., Grevesse, N., Sauval, A. J., Allende Prieto, C., & Kiselman, D. 2004, A&A, 417, 751

Asplund, M., Grevesse, N., Sauval, A. J., & Scott, P. 2009, ARA&A, 47, 481

Autry, R. G., et al. 2003, in Society of Photo-Optical Instrumentation Engineers (SPIE) Conference Series, Vol. 4841, Instrument Design and Performance for Optical/Infrared Ground-based Telescopes, ed. M. Iye & A. F. M. Moorwood, 525–539

Baes, M., Sil'chenko, O. K., Moiseev, A. V., & Manakova, E. A. 2007, A&A, 467, 991

Baglin, A., Auvergne, M., Barge, P., Deleuil, M., Catala, C., Michel, E., Weiss, W., & COROT Team. 2006, in ESA Special Publication, Vol. 1306, ESA Special Publication, ed. M. Fridlund, A. Baglin, J. Lochard, & L. Conroy, 33

Bahcall, J. N., Basu, S., Pinsonneault, M., & Serenelli, A. M. 2005a, ApJ, 618, 1049

Bahcall, J. N., Basu, S., & Serenelli, A. M. 2005b, ApJ, 631, 1281

Bahcall, J. N., Serenelli, A. M., & Basu, S. 2006, ApJS, 165, 400

Bailey, J. E., et al. 2015, Nature, 517, 5659

Baldwin, J. A., Phillips, M. M., & Terlevich, R. 1981, PASP, 93, 5

Banerji, M., Ferreras, I., Abdalla, F. B., Hewett, P., & Lahav, O. 2010, MNRAS, 402, 2264

Baraffe, I., Chabrier, G., Allard, F., & Hauschildt, P. H. 1995, ApJL, 446, L35

—. 1997, A&A, 327, 1054

—. 1998, A&A, 337, 403

Baraffe, I., Chabrier, G., Barman, T. S., Allard, F., & Hauschildt, P. H. 2003, A&A, 402, 701

Baraffe, I., Chabrier, G., & Gallardo, J. 2009, ApJL, 702, L27

Baraffe, I., Homeier, D., Allard, F., & Chabrier, G. 2015, A&A, 577, A42

Barbaro, C., & Bertelli, C. 1977, A&A, 54, 243

Bastian, N., & Lardo, C. 2017, ArXiv e-prints

Basu, S., & Antia, H. M. 2004, ApJL, 606, L85

Bedding, T. R., et al. 2010, ApJL, 713, L176

Bedin, L. R., King, I. R., Anderson, J., Piotto, G., Salaris, M., Cassisi, S., & Serenelli, A. 2008a, ApJ, 678, 1279

Bedin, L. R., Piotto, G., Anderson, J., Cassisi, S., King, I. R., Momany, Y., & Carraro, G. 2004, ApJL, 605, L125

Bedin, L. R., Salaris, M., Piotto, G., Cassisi, S., Milone, A. P., Anderson, J., & King, I. R. 2008b, ApJL, 679, L29

Bedin, L. R., Salaris, M., Piotto, G., King, I. R., Anderson, J., Cassisi, S., & Momany, Y. 2005, ApJL, 624, L45

Bell, E. F., et al. 2004, ApJ, 608, 752

Belli, S., Newman, A. B., & Ellis, R. S. 2013, ArXiv e-prints

Bernardi, M., Meert, A., Sheth, R. K., Vikram, V., Huertas-Company, M., Mei, S., & Shankar, F. 2013, MNRAS, 436, 697

Bernardi, M., Shankar, F., Hyde, J. B., Mei, S., Marulli, F., & Sheth, R. K. 2010, MNRAS, 404, 2087

Bertin, E., & Arnouts, S. 1996, A&AS, 117, 393

Bessell, M., Bloxham, G., Schmidt, B., Keller, S., Tisserand, P., & Francis, P. 2011, PASP, 123, 789

Bessell, M., & Murphy, S. 2012, PASP, 124, 140

Bessell, M. S. 2001, PASP, 113, 66

—. 2011, PASP, 123, 1442

Bessell, M. S., & Brett, J. M. 1988, PASP, 100, 1134

Bezanson, R., van Dokkum, P. G., Tal, T., Marchesini, D., Kriek, M., Franx, M., & Coppi, P. 2009, ApJ, 697, 1290

Bian, F., et al. 2013, ApJ, 774, 28

Bildsten, L., & Hall, D. M. 2001, ApJL, 549, L219

Bird, J. C., & Pinsonneault, M. H. 2011, ApJ, 733, 81

Bjorkman, J. E., & Cassinelli, J. P. 1993, ApJ, 409, 429

Blanton, M. R. 2006, ApJ, 648, 268

Blanton, M. R., Kazin, E., Muna, D., Weaver, B. A., & Price-Whelan, A. 2011, AJ, 142, 31

Blanton, M. R., et al. 2005, AJ, 129, 2562

Blöcker, T. 1995, A&A, 297, 727

Bohlin, R. C. 2014, AJ, 147, 127

Böhm, K.-H. 1963, ApJ, 138, 297

Böhm-Vitense, E. 1958, Zeitschrift für Astrophysik, 46, 108

Bonaca, A., & Hogg, D. W. 2018, ArXiv e-prints

Bonaca, A., et al. 2012, ApJL, 755, L12

Boudreault, S., Lodieu, N., Deacon, N. R., & Hambly, N. C. 2012, MNRAS, 426, 3419

Bouret, J.-C., Lanz, T., Martins, F., Marcolino, W. L. F., Hillier, D. J., Depagne, E., & Hubeny, I. 2013, A&A, 555, A1

Boutsia, K., et al. 2011, ApJ, 736, 41

Bouvier, J. 2008, A&A, 489, L53

Bovy, J., Rix, H.-W., Liu, C., Hogg, D. W., Beers, T. C., & Lee, Y. S. 2012, ApJ, 753, 148

Boyajian, T. S., et al. 2012a, ApJ, 746, 101

—. 2012b, ApJ, 757, 112

—. 2013, ApJ, 771, 40

Boyer, M. L., et al. 2011, AJ, 142, 103

Braithwaite, J. 2006, A&A, 449, 451

Braithwaite, J., & Spruit, H. C. 2004, Nat, 431, 819

Brammer, G. B., et al. 2011, ApJ, 739, 24

Brandenburg, A., & Subramanian, K. 2005, Physics Reports, 417, 1

Bressan, A., Fagotto, F., Bertelli, G., & Chiosi, C. 1993, A&AS, 100, 647

Bressan, A., Marigo, P., Girardi, L., Salasnich, B., Dal Cero, C., Rubele, S., & Nanni, A. 2012, MNRAS, 427, 127

Bressan, A. G., Chiosi, C., & Bertelli, G. 1981, A&A, 102, 25

Brewer, L. N., et al. 2016, AJ, 151, 66

Brodwin, M., et al. 2006, ApJ, 651, 791

—. 2013, ApJ, 779, 138

Brogaard, K., Bruntt, H., Grundahl, F., Clausen, J. V., Frandsen, S., Vandenberg, D. A., & Bedin, L. R. 2011, A&A, 525, A2

Brogaard, K., et al. 2012, A&A, 543, A106

Brott, I., et al. 2011a, A&A, 530, A115

—. 2011b, A&A, 530, A116

Brough, S., Proctor, R., Forbes, D. A., Couch, W. J., Collins, C. A., Burke, D. J., & Mann, R. G. 2007, MNRAS, 378, 1507

Brown, J. A., Wallerstein, G., & Zucker, D. 1997, AJ, 114, 180

Brown, J. M., Garaud, P., & Stellmach, S. 2013, ApJ, 768, 34

Brown, M. J. I., Dey, A., Jannuzi, B. T., Brand, K., Benson, A. J., Brodwin, M., Croton, D. J., & Eisenhardt, P. R. 2007, ApJ, 654, 858

Brown, T. M., Christensen-Dalsgaard, J., Dziembowski, W. A., Goode, P., Gough, D. O., & Morrow, C. A. 1989, ApJ, 343, 526

Brown, T. M., Gilliland, R. L., Noyes, R. W., & Ramsey, L. W. 1991, ApJ, 368, 599

Brown, T. M., et al. 2014, ApJ, 796, 91

Bundy, K., et al. 2006, ApJ, 651, 120

Burbidge, E. M., Burbidge, G. R., Fowler, W. A., & Hoyle, F. 1957, Reviews of Modern Physics, 29, 547

Burke, C. J., Depoy, D. L., Gaudi, B. S., & Marshall, J. L. 2003, in Astronomical Society of the Pacific Conference Series, Vol. 294, Scientific Frontiers in Research on Extrasolar Planets, ed. D. Deming & S. Seager, 379–382

Burstein, D., Faber, S. M., Gaskell, C. M., & Krumm, N. 1984, ApJ, 287, 586

Caffau, E., Ludwig, H.-G., Steffen, M., Freytag, B., & Bonifacio, P. 2011, Soar Phys., 268, 255

Caloi, V., & D'Antona, F. 2011, MNRAS, 417, 228

Calzetti, D., et al. 2015, ApJ, 811, 75

Cantiello, M., & Langer, N. 2010, A&A, 521, A9

Cantiello, M., Mankovich, C., Bildsten, L., Christensen-Dalsgaard, J., & Paxton, B. 2014, ApJ, 788, 93

Canto Martins, B. L., Lèbre, A., Palacios, A., de Laverny, P., Richard, O., Melo, C. H. F., Do Nascimento, Jr., J. D., & de Medeiros, J. R. 2011, A&A, 527, A94

Cappellari, M., & Emsellem, E. 2004, PASP, 116, 138

Cappellari, M., et al. 2009, ApJL, 704, L34

Cardelli, J. A., Clayton, G. C., & Mathis, J. S. 1989, ApJ, 345, 245

Carney, B. W., Lee, J.-W., & Dodson, B. 2005, AJ, 129, 656

Carollo, C. M., et al. 2013, ApJ, 773, 112

Carrasco, J. M., et al. 2016, A&A, 595, A7

Carrera, R., & Pancino, E. 2011, A&A, 535, A30

Carretta, E., et al. 2009, A&A, 505, 117

Casagrande, L., Flynn, C., & Bessell, M. 2008, MNRAS, 389, 585

Casagrande, L., Ramírez, I., Meléndez, J., Bessell, M., & Asplund, M. 2010, A&A, 512, A54

Casagrande, L., & VandenBerg, D. A. 2014, MNRAS, 444, 392

Cassata, P., et al. 2010, ApJL, 714, L79

Cassisi, S., Potekhin, A. Y., Pietrinferni, A., Catelan, M., & Salaris, M. 2007, ApJ, 661, 1094

Cassisi, S., & Salaris, M. 2013, Old Stellar Populations: How to Study the Fossil Record of Galaxy Formation

Castellani, V., Chieffi, A., Tornambe, A., & Pulone, L. 1985, ApJ, 296, 204

Castelli, F., Gratton, R. G., & Kurucz, R. L. 1997, A&A, 318, 841

Castelli, F., & Kurucz, R. L. 2004, ArXiv Astrophysics e-prints

Castor, J. I., Abbott, D. C., & Klein, R. I. 1975, ApJ, 195, 157

Castro, N., Fossati, L., Langer, N., Simón-Díaz, S., Schneider, F. R. N., & Izzard, R. G. 2014, A&A, 570, L13

Catalán, S., Isern, J., García-Berro, E., & Ribas, I. 2008a, MNRAS, 387, 1693

Catalán, S., Isern, J., García-Berro, E., Ribas, I., Allende Prieto, C., & Bonanos, A. Z. 2008b, A&A, 477, 213

Cen, R. 2014, ApJ, 781, 38

Cenarro, A. J., Gorgas, J., Vazdekis, A., Cardiel, N., & Peletier, R. F. 2003, MNRAS, 339, L12

Cerviño, M., Gómez-Flechoso, M. A., Castander, F. J., Schaerer, D., Mollá, M., Knödlseder, J., & Luridiana, V. 2001, A&A, 376, 422

Cerviño, M., Luridiana, V., & Castander, F. J. 2000, A&A, 360, L5

Cerviño, M., Valls-Gabaud, D., Luridiana, V., & Mas-Hesse, J. M. 2002, A&A, 381, 51

Chaboyer, B., Fenton, W. H., Nelan, J. E., Patnaude, D. J., & Simon, F. E. 2001, ApJ, 562, 521

Chaboyer, B., & Zahn, J.-P. 1992, A&A, 253, 173

Chabrier, G. 2003, PASP, 115, 763

Chabrier, G., & Baraffe, I. 1997, A&A, 327, 1039

Chabrier, G., Baraffe, I., & Plez, B. 1996, ApJL, 459, L91

Charbonneau, P., & MacGregor, K. B. 1993, ApJ, 417, 762

Charbonnel, C. 1994, A&A, 282, 811

Charbonnel, C., & Lagarde, N. 2010, A&A, 522, A10

Charbonnel, C., & Talon, S. 2005, Science, 309, 2189

Charbonnel, C., & Zahn, J.-P. 2007, A&A, 467, L15

Chen, C. H., Mamajek, E. E., Bitner, M. A., Pecaut, M., Su, K. Y. L., & Weinberger, A. J. 2011, ApJ, 738, 122

Chen, Y., Girardi, L., Bressan, A., Marigo, P., Barbieri, M., & Kong, X. 2014, MNRAS, 444, 2525

Chieffi, A., & Limongi, M. 2013, ApJ, 764, 21

Chini, R., Hoffmeister, V. H., Nasseri, A., Stahl, O., & Zinnecker, H. 2012, MNRAS, 424, 1925

Choi, J., Dotter, A., Conroy, C., Cantiello, M., Paxton, B., & Johnson, B. D. 2016, ApJ, 823, 102

Christensen-Dalsgaard, J., di Mauro, M. P., Houdek, G., & Pijpers, F. 2009, A&A, 494, 205

Chun, S.-H., Yoon, S.-C., Jung, M.-K., Kim, D. U., & Kim, J. 2018, ApJ, 853, 79

Cid Fernandes, R., Mateus, A., Sodré, L., Stasińska, G., & Gomes, J. M. 2005, MNRAS, 358, 363

Cimatti, A., Daddi, E., & Renzini, A. 2006, A&A, 453, L29

Cimatti, A., et al. 2008, A&A, 482, 21

Cirasuolo, M., et al. 2007, MNRAS, 380, 585

Claret, A., & Torres, G. 2016, A&A, 592, A15

Claver, C. F., Liebert, J., Bergeron, P., & Koester, D. 2001, ApJ, 563, 987

Coelho, P., Bruzual, G., Charlot, S., Weiss, A., Barbuy, B., & Ferguson, J. W. 2007, MNRAS, 382, 498

Cohen, J. G. 1978, ApJ, 223, 487

Cohen, M., Wheaton, W. A., & Megeath, S. T. 2003, AJ, 126, 1090

Coil, A. L., et al. 2011, ApJ, 741, 8

Colless, M., et al. 2001, MNRAS, 328, 1039

Conroy, C. 2013, ARA&A, 51, 393

Conroy, C., Graves, G. J., & van Dokkum, P. G. 2014, ApJ, 780, 33

Conroy, C., Gunn, J. E., & White, M. 2009, ApJ, 699, 486

Conroy, C., & Kratter, K. M. 2012, ApJ, 755, 123

Conroy, C., & van Dokkum, P. 2012, ApJ, 747, 69

Conroy, C., White, M., & Gunn, J. E. 2010, ApJ, 708, 58

Cool, R. J. 2007, ApJS, 169, 21

Cool, R. J., et al. 2012, ApJ, 748, 10

Correnti, M., Gennaro, M., Kalirai, J. S., Brown, T. M., & Calamida, A. 2016, ApJ, 823, 18

Corsaro, E., De Ridder, J., & García, R. A. 2015, A&A, 579, A83

Cowley, A. P., Dawson, P., & Hartwick, F. D. A. 1979, PASP, 91, 628

Cox, A. N., & Stewart, J. N. 1965, ApJS, 11, 22

—. 1970, ApJS, 19, 243

Cox, J. P. 1968, Principles of stellar structure - Vol.1: Physical principles; Vol.2: Applications to stars

Creasey, P., Theuns, T., & Bower, R. G. 2013, MNRAS, 429, 1922

Crowther, P. A., Lennon, D. J., & Walborn, N. R. 2006, A&A, 446, 279

Crowther, P. A., et al. 2016, MNRAS, 458, 624

Cummings, J. D., Kalirai, J. S., Tremblay, P.-E., & Ramirez-Ruiz, E. 2015, ApJ, 807, 90

Cunha, K., Hubeny, I., & Lanz, T. 2006, ApJL, 647, L143

Cunha, K., & Lambert, D. L. 1994, ApJ, 426, 170

Cutri, R. M., et al. 2003, 2MASS All Sky Catalog of point sources.

Cyburt, R. H., et al. 2010, ApJS, 189, 240

da Silva, R. L., Fumagalli, M., & Krumholz, M. 2012, ApJ, 745, 145

da Silva, R. L., Fumagalli, M., & Krumholz, M. R. 2014, MNRAS, 444, 3275

Daddi, E., et al. 2005, ApJ, 626, 680

Daflon, S., Cunha, K., Becker, S. R., & Smith, V. V. 2001, ApJ, 552, 309

Dalcanton, J. J., et al. 2012, ApJS, 200, 18

Dale, J. E. 2015, New Astronomy Review, 68, 1

Dalton, G., et al. 2012, in Proc. of the SPIE, Vol. 8446, Ground-based and Airborne Instrumentation for Astronomy IV, 84460P

Damjanov, I., et al. 2009, ApJ, 695, 101

D'Antona, F., & Caloi, V. 2008, MNRAS, 390, 693

D'Antona, F., & Mazzitelli, I. 1997, Mem.S.A.It., 68, 807

de Avillez, M. A., & Breitschwerdt, D. 2004, A&A, 425, 899

de Geus, E. J., de Zeeuw, P. T., & Lub, J. 1989, A&A, 216, 44

de Jager, C., Nieuwenhuijzen, H., & van der Hucht, K. A. 1988, A&AS, 72, 259

de Jong, R. S., et al. 2016, in Proc. of the SPIE, Vol. 9908, Ground-based and Airborne Instrumentation for Astronomy VI, 99081O

de Mink, S. E., Cantiello, M., Langer, N., & Pols, O. R. 2010, in American Institute of Physics Conference Series, Vol. 1314, American Institute of Physics Conference Series, ed. V. Kalogera & M. van der Sluys, 291–296

de Mink, S. E., Cantiello, M., Langer, N., Pols, O. R., Brott, I., & Yoon, S.-C. 2009, A&A, 497, 243

de Mink, S. E., Langer, N., Izzard, R. G., Sana, H., & de Koter, A. 2013, ApJ, 764, 166

de Mink, S. E., Sana, H., Langer, N., Izzard, R. G., & Schneider, F. R. N. 2014, ApJ, 782, 7

De Silva, G. M., et al. 2015, MNRAS, 449, 2604

de Zeeuw, P. T., Hoogerwerf, R., de Bruijne, J. H. J., Brown, A. G. A., & Blaauw, A. 1999, AJ, 117, 354

Dekel, A., Sari, R., & Ceverino, D. 2009, ApJ, 703, 785

Dekel, A., & Silk, J. 1986, ApJ, 303, 39

Demarque, P., & Geisler, J. E. 1963, ApJ, 137, 1102

Demarque, P., Woo, J.-H., Kim, Y.-C., & Yi, S. K. 2004, ApJS, 155, 667

Denissenkov, P. A. 2010, ApJ, 723, 563

Denissenkov, P. A., & Pinsonneault, M. 2007, ApJ, 655, 1157

Dib, S. 2014, MNRAS, 444, 1957

Dobbie, P. D., Pinfield, D. J., Napiwotzki, R., Hambly, N. C., Burleigh, M. R., Barstow, M. A., Jameson, R. F., & Hubeny, I. 2004, MNRAS, 355, L39

Doherty, C. L., Gil-Pons, P., Siess, L., Lattanzio, J. C., & Lau, H. H. B. 2015, MNRAS, 446, 2599

Dohm-Palmer, R. C., & Skillman, E. D. 2002, AJ, 123, 1433

Dolphin, A. E. 2002, MNRAS, 332, 91

Domínguez Sánchez, H., et al. 2011, MNRAS, 417, 900

Dotter, A. 2016, ApJS, 222, 8

Dotter, A., Chaboyer, B., Ferguson, J. W., Lee, H.-c., Worthey, G., Jevremović, D., & Baron, E. 2007, ApJ, 666, 403

Dotter, A., Chaboyer, B., Jevremović, D., Kostov, V., Baron, E., & Ferguson, J. W. 2008, ApJS, 178, 89

Dotter, A., Conroy, C., Cargile, P., & Asplund, M. 2017, ApJ, 840, 99

Dotter, A., Ferguson, J. W., Conroy, C., Milone, A. P., Marino, A. F., & Yong, D. 2015, MNRAS, 446, 1641

Dotter, A., Sarajedini, A., & Anderson, J. 2011, ApJ, 738, 74

Dove, J. B., & Shull, J. M. 1994, ApJ, 430, 222

Drake, J. J., & Testa, P. 2005, Nat, 436, 525

Drout, M. R., Massey, P., & Meynet, G. 2012, ApJ, 750, 97

Dupree, A. K., & Avrett, E. H. 2013, ApJL, 773, L28

Eddington, A. S. 1926, The Internal Constitution of the Stars

Eggenberger, P., Maeder, A., & Meynet, G. 2005, A&A, 440, L9

Eggenberger, P., Meynet, G., & Maeder, A. 2002, A&A, 386, 576

Eggenberger, P., Meynet, G., Maeder, A., Hirschi, R., Charbonnel, C., Talon, S., & Ekström, S. 2008, Astrophys. Space Sci, 316, 43

Eggenberger, P., Montalbán, J., & Miglio, A. 2012, A&A, 544, L4

Eggleton, P. P. 1971, MNRAS, 151, 351

Eggleton, P. P., Dearborn, D. S. P., & Lattanzio, J. C. 2006, Science, 314, 1580

—. 2008, ApJ, 677, 581

Eisenstein, D. J., et al. 2001, AJ, 122, 2267

—. 2003, ApJ, 585, 694

Ekström, S., et al. 2012, A&A, 537, A146

Eldridge, J. J. 2012, MNRAS, 422, 794

Eldridge, J. J., Izzard, R. G., & Tout, C. A. 2008, MNRAS, 384, 1109

Eldridge, J. J., & Stanway, E. R. 2009, MNRAS, 400, 1019

Eldridge, J. J., & Tout, C. A. 2004, MNRAS, 348, 201

Elias, J. H., Frogel, J. A., & Humphreys, R. M. 1985, ApJS, 57, 91

Eliche-Moral, M. C., et al. 2010, A&A, 519, A55

Elston, R. J., et al. 2006, ApJ, 639, 816

Endal, A. S., & Sofia, S. 1976, ApJ, 210, 184

—. 1978, ApJ, 220, 279

Evans, II, N. J., et al. 2009, ApJS, 181, 321

Faber, S. M., et al. 2003, in Society of Photo-Optical Instrumentation Engineers (SPIE) Conference Series, Vol. 4841, Instrument Design and Performance for Optical/Infrared Ground-based Telescopes, ed. M. Iye & A. F. M. Moorwood, 1657–1669

Faber, S. M., et al. 2007, ApJ, 665, 265

Fabricant, D., et al. 2005, PASP, 117, 1411

Fagotto, F., Bressan, A., Bertelli, G., & Chiosi, C. 1994a, A&AS, 104

—. 1994b, A&AS, 105

Falcón-Barroso, J., Sánchez-Blázquez, P., Vazdekis, A., Ricciardelli, E., Cardiel, N., Cenarro, A. J., Gorgas, J., & Peletier, R. F. 2011, A&A, 532, A95

Fan, L., Lapi, A., Bressan, A., Bernardi, M., De Zotti, G., & Danese, L. 2010, ApJ, 718, 1460

Faulkner, D. J., & Cannon, R. D. 1973, ApJ, 180, 435

Fazio, G. G., et al. 2004, ApJS, 154, 10

Feiden, G. A., & Chaboyer, B. 2012, ApJ, 757, 42

—. 2013, ApJ, 779, 183

Ferguson, J. W., Alexander, D. R., Allard, F., Barman, T., Bodnarik, J. G., Hauschildt, P. H., Heffner-Wong, A., & Tamanai, A. 2005, ApJ, 623, 585

Ferrario, L., Wickramasinghe, D., Liebert, J., & Williams, K. A. 2005, MNRAS, 361, 1131

Ferraro, F. R., Valenti, E., Straniero, O., & Origlia, L. 2006, ApJ, 642, 225

Fierlinger, K. M., Burkert, A., Ntormousi, E., Fierlinger, P., Schartmann, M., Ballone, A., Krause, M. G. H., & Diehl, R. 2016, MNRAS, 456, 710

Finkelstein, S. L., et al. 2012, ApJ, 758, 93

Fisher, R. A. 1935, Journal of the Royal Statistical Society, 98, 39

Flower, P. J. 1996, ApJ, 469, 355

Fontaine, G., Brassard, P., Green, E. M., Chayer, P., Charpinet, S., Andersen, M., & Portouw, J. 2008, A&A, 486, L39

Foreman-Mackey, D., Hogg, D. W., Lang, D., & Goodman, J. 2013, PASP, 125, 306

Francois, P., Danziger, J., Buonanno, R., & Perrin, M. N. 1997, A&A, 327, 121

Freedman, R. S., Marley, M. S., & Lodders, K. 2008, ApJS, 174, 504

Freeman, K., & Bland-Hawthorn, J. 2002, ARA&A, 40, 487

Freytag, B., Ludwig, H.-G., & Steffen, M. 1996, A&A, 313, 497

Fricke, K. J., & Kippenhahn, R. 1972, ARA&A, 10, 45

Friend, D. B., & Abbott, D. C. 1986, ApJ, 311, 701

Frogel, J. A., Mould, J., & Blanco, V. M. 1990, ApJ, 352, 96

Frommhold, L., Abel, M., Wang, F., Gustafsson, M., Li, X., & Hunt, K. 2010, Molecular Physics, 108, 2265

Fryer, C. L. 1999, ApJ, 522, 413

Fuller, J., Cantiello, M., Lecoanet, D., & Quataert, E. 2015, ApJ, 810, 101

Fynbo, H. O. U., et al. 2005, Nat, 433, 136

Gaia Collaboration et al. 2016, A&A, 595, A1

Gallazzi, A., Bell, E. F., Zibetti, S., Brinchmann, J., & Kelson, D. D. 2014, ApJ, 788, 72

Gallet, F., & Bouvier, J. 2013, A&A, 556, A36

García-Berro, E., Althaus, L. G., Córsico, A. H., & Isern, J. 2008, ApJ, 677, 473

García-Berro, E., et al. 2010, Nat, 465, 194

Gáspár, A., Rieke, G. H., Su, K. Y. L., Balog, Z., Trilling, D., Muzzerole, J., Apai, D., & Kelly, B. C. 2009, ApJ, 697, 1578

Gathier, R., Lamers, H. J. G. L. M., & Snow, T. P. 1981, ApJ, 247, 173

Gaulme, P., et al. 2016, ApJ, 832, 121

Genel, S., et al. 2014, MNRAS, 445, 175

Georgy, C., Ekström, S., Meynet, G., Massey, P., Levesque, E. M., Hirschi, R., Eggenberger, P., & Maeder, A. 2012, A&A, 542, A29

Georgy, C., et al. 2013, A&A, 558, A103

Gies, D. R., & Lambert, D. L. 1992, ApJ, 387, 673

Gilliland, R. L., et al. 2010, PASP, 122, 131

Gilmore, G., et al. 2012, The Messenger, 147, 25

Girardi, L. 1999, MNRAS, 308, 818

Girardi, L., Bertelli, G., Bressan, A., Chiosi, C., Groenewegen, M. A. T., Marigo, P., Salasnich, B., &

Weiss, A. 2002, A&A, 391, 195

Girardi, L., Bressan, A., Bertelli, G., & Chiosi, C. 2000, A&AS, 141, 371

Girardi, L., & Marigo, P. 2007, A&A, 462, 237

Girardi, L., Marigo, P., Bressan, A., & Rosenfield, P. 2013, ApJ, 777, 142

Girardi, L., et al. 2008, PASP, 120, 583

—. 2010, ApJ, 724, 1030

Glebbeek, E., Gaburov, E., de Mink, S. E., Pols, O. R., & Portegies Zwart, S. F. 2009, A&A, 497, 255

Gnedin, N. Y. 2000, ApJ, 535, 530

Gnedin, N. Y., & Kaurov, A. A. 2014, ApJ, 793, 30

Gnedin, N. Y., Kravtsov, A. V., & Chen, H.-W. 2008, ApJ, 672, 765

Gökay, G., Gürol, B., & Derman, E. 2013, AJ, 146, 123

González Hernández, J. I., & Bonifacio, P. 2009, A&A, 497, 497

Gordon, K. D., et al. 2011, AJ, 142, 102

Gorgas, J., Efstathiou, G., & Aragon Salamanca, A. 1990, MNRAS, 245, 217

Graboske, H. C., Dewitt, H. E., Grossman, A. S., & Cooper, M. S. 1973, ApJ, 181, 457

Gräfener, G., Vink, J. S., de Koter, A., & Langer, N. 2011, A&A, 535, A56

Gratton, R., Sneden, C., & Carretta, E. 2004, ARA&A, 42, 385

Gratton, R. G., Carretta, E., & Bragaglia, A. 2012, The Astronomy and Astrophysics Review, 20, 50

Gratton, R. G., & Ortolani, S. 1989, A&A, 211, 41

Gratton, R. G., Sneden, C., Carretta, E., & Bragaglia, A. 2000, A&A, 354, 169

Graves, G. J., Faber, S. M., Schiavon, R. P., & Yan, R. 2007, ApJ, 671, 243

Graves, G. J., & Schiavon, R. P. 2008, ApJS, 177, 446

Greene, J. E., Murphy, J. D., Graves, G. J., Gunn, J. E., Raskutti, S., Comerford, J. M., & Gebhardt, K. 2013, ApJ, 776, 64

Grevesse, N., & Sauval, A. J. 1998, Space Science Reviews, 85, 161

Groenewegen, M. A. T., & de Jong, T. 1993, A&A, 267, 410

Groh, J. H., Meynet, G., Ekström, S., & Georgy, C. 2014, A&A, 564, A30

Grossman, S. A., & Taam, R. E. 1996, MNRAS, 283, 1165

Gustafsson, B., Edvardsson, B., Eriksson, K., Jørgensen, U. G., Nordlund, Å., & Plez, B. 2008, A&A, 486, 951

Haardt, F., & Madau, P. 1996, ApJ, 461, 20

—. 2012, ApJ, 746, 125

Haehnelt, M. G. 1995, MNRAS, 273, 249

Handberg, R., Brogaard, K., Miglio, A., Bossini, D., Elsworth, Y., Slumstrup, D., Davies, G. R., & Chaplin, W. J. 2017, MNRAS, 472, 979

Hansen, B. M. S. 2005, ApJ, 635, 522

Harmanec, P. 1988, Bulletin of the Astronomical Institutes of Czechoslovakia, 39, 329

Harris, J., & Zaritsky, D. 2004, AJ, 127, 1531

—. 2009, AJ, 138, 1243

Harris, W. E., & Harris, G. L. H. 2002, AJ, 123, 3108

Hartwick, F. D. A. 1970, ApL, 7, 151

Hauschildt, P. H., Allard, F., & Baron, E. 1999a, ApJ, 512, 377

Hauschildt, P. H., Allard, F., Ferguson, J., Baron, E., & Alexander, D. R. 1999b, ApJ, 525, 871

Heavens, A. F., Jimenez, R., & Lahav, O. 2000, MNRAS, 317, 965

Heger, A., Langer, N., & Woosley, S. E. 2000, ApJ, 528, 368

Heger, A., & Woosley, S. E. 2002, ApJ, 567, 532

Heger, A., Woosley, S. E., & Spruit, H. C. 2005, ApJ, 626, 350

Hekker, S., Elsworth, Y., Mosser, B., Kallinger, T., Basu, S., Chaplin, W. J., & Stello, D. 2013, A&A, 556, A59

Hekker, S., et al. 2011, A&A, 530, A100

Henriques, B., Maraston, C., Monaco, P., Fontanot, F., Menci, N., De Lucia, G., & Tonini, C. 2011, MNRAS, 415, 3571

Henyey, L., Vardya, M. S., & Bodenheimer, P. 1965, ApJ, 142, 841

Henyey, L. G., Forbes, J. E., & Gould, N. L. 1964, ApJ, 139, 306

Herbig, G. H. 1962, ApJ, 135, 736

Herczeg, G. J., & Hillenbrand, L. A. 2015, ApJ, 808, 23

Herwig, F. 2000, A&A, 360, 952

—. 2004, ApJS, 155, 651

—. 2005, ARA&A, 43, 435

Herwig, F., & Austin, S. M. 2004, ApJL, 613, L73

Herwig, F., Pignatari, M., Woodward, P. R., Porter, D. H., Rockefeller, G., Fryer, C. L., Bennett, M., & Hirschi, R. 2011, ApJ, 727, 89

Hewett, P. C., Warren, S. J., Leggett, S. K., & Hodgkin, S. T. 2006, MNRAS, 367, 454

Hilz, M., Naab, T., & Ostriker, J. P. 2013, MNRAS, 429, 2924

Hirschi, R., Meynet, G., & Maeder, A. 2004, A&A, 425, 649

Holden, B. P., van der Wel, A., Kelson, D. D., Franx, M., & Illingworth, G. D. 2010, ApJ, 724, 714

Hole, K. T., Geller, A. M., Mathieu, R. D., Platais, I., Meibom, S., & Latham, D. W. 2009, AJ, 138, 159

Holtzman, J. A., Burrows, C. J., Casertano, S., Hester, J. J., Trauger, J. T., Watson, A. M., & Worthey, G. 1995, PASP, 107, 1065

Holtzman, J. A., et al. 2015, AJ, 150, 148

Hopkins, P. F. 2013, MNRAS, 433, 170

Hopkins, P. F., Bundy, K., Murray, N., Quataert, E., Lauer, T. R., & Ma, C.-P. 2009, MNRAS, 398, 898

Hopkins, P. F., Kereš, D., Oñorbe, J., Faucher-Giguère, C.-A., Quataert, E., Murray, N., & Bullock, J. S. 2014, MNRAS, 445, 581

Hopkins, P. F., Quataert, E., & Murray, N. 2011, MNRAS, 417, 950

—. 2012, MNRAS, 421, 3488

Hosokawa, T., Offner, S. S. R., & Krumholz, M. R. 2011, ApJ, 738, 140

Howell, S. B., et al. 2014, PASP, 126, 398

Hoyle, F., & Schwarzschild, M. 1955, ApJS, 2, 1

Hu, H., Tout, C. A., Glebbeek, E., & Dupret, M.-A. 2011, MNRAS, 418, 195

Huang, W., Gies, D. R., & McSwain, M. V. 2010, ApJ, 722, 605

Huber, D., et al. 2011, ApJ, 743, 143

—. 2014, ApJS, 211, 2

Humphreys, R. M. 1979, ApJS, 39, 389

Hunter, I., et al. 2007, A&A, 466, 277

—. 2008, ApJL, 676, L29

—. 2009, A&A, 496, 841

Hurley, J. R., Tout, C. A., & Pols, O. R. 2002, MNRAS, 329, 897

Iben, Jr., I. 1982, ApJ, 260, 821

—. 1983, ApJL, 275, L65

Iben, Jr., I., Kaler, J. B., Truran, J. W., & Renzini, A. 1983, ApJ, 264, 605

Iglesias, C. A., & Rogers, F. J. 1991, ApJ, 371, 408

—. 1993, ApJ, 412, 752

—. 1996, ApJ, 464, 943

Ilbert, O., et al. 2010, ApJ, 709, 644

Irwin, J. M., et al. 2011, ApJ, 742, 123

Isern, J., Hernanz, M., Mochkovitch, R., & Garcia-Berro, E. 1991, A&A, 241, L29

Itoh, N., Totsuji, H., Ichimaru, S., & Dewitt, H. E. 1979, ApJ, 234, 1079

Ivezic, Z., et al. 2008, ArXiv e-prints

Iwata, I., et al. 2009, ApJ, 692, 1287

Izzard, R. G., Dray, L. M., Karakas, A. I., Lugaro, M., & Tout, C. A. 2006, A&A, 460, 565

Jackson, R. J., & Jeffries, R. D. 2014, MNRAS, 441, 2111

Jannuzi, B. T., & Dey, A. 1999, in Astronomical Society of the Pacific Conference Series, Vol. 193, The Hy-Redshift Universe: Galaxy Formation and Evolution at High Redshift, ed. A. J. Bunker & W. J. M. van Breugel, 258

Jeffries, R. D., & Oliveira, J. M. 2005, MNRAS, 358, 13

Jiang, Y.-F., Cantiello, M., Bildsten, L., Quataert, E., & Blaes, O. 2015, ApJ, 813, 74

Jimenez, R., Bernardi, M., Haiman, Z., Panter, B., & Heavens, A. F. 2007, ApJ, 669, 947

Johansson, J., Thomas, D., & Maraston, C. 2012, MNRAS, 421, 1908

Jordi, C., et al. 2010, A&A, 523, A48

Jørgensen, B. R., & Lindegren, L. 2005, A&A, 436, 127

Jørgensen, I., & Chiboucas, K. 2013, AJ, 145, 77

Joung, M. K. R., & Mac Low, M.-M. 2006, ApJ, 653, 1266

Joyce, M., & Chaboyer, B. 2017, ArXiv e-prints

Juarez, A. J., Cargile, P. A., James, D. J., & Stassun, K. G. 2014, ApJ, 795, 143

Kaiser, N., et al. 2010, in Society of Photo-Optical Instrumentation Engineers (SPIE) Conference Series, Vol. 7733, Society of Photo-Optical Instrumentation Engineers (SPIE) Conference Series, 0

Kalirai, J. S., Bergeron, P., Hansen, B. M. S., Kelson, D. D., Reitzel, D. B., Rich, R. M., & Richer, H. B. 2007, ApJ, 671, 748

Kalirai, J. S., Hansen, B. M. S., Kelson, D. D., Reitzel, D. B., Rich, R. M., & Richer, H. B. 2008, ApJ, 676, 594

Kalirai, J. S., Marigo, P., & Tremblay, P.-E. 2014, ApJ, 782, 17

Kalirai, J. S., Saul Davis, D., Richer, H. B., Bergeron, P., Catelan, M., Hansen, B. M. S., & Rich, R. M. 2009, ApJ, 705, 408

Kallinger, T., et al. 2010a, A&A, 522, A1

—. 2010b, A&A, 509, A77

Kaluzny, J., Krzeminski, W., & Mazur, B. 1995, AJ, 110, 2206

Kamai, B. L., Vrba, F. J., Stauffer, J. R., & Stassun, K. G. 2014, AJ, 148, 30

Kawaler, S. D., Novikov, I., Srinivasan, G., Meynet, G., & Schaerer, D. 1996, Stellar Remnants

Kelson, D. D., Illingworth, G. D., Franx, M., & van Dokkum, P. G. 2006, ApJ, 653, 159

Kepler, S. O., et al. 2015, MNRAS, 446, 4078

Kereš, D., Katz, N., Fardal, M., Davé, R., & Weinberg, D. H. 2009, MNRAS, 395, 160

Kilian, J. 1992, A&A, 262, 171

Kim, Y.-C., Demarque, P., Yi, S. K., & Alexander, D. R. 2002, ApJS, 143, 499

Kimm, T., & Cen, R. 2014, ApJ, 788, 121

King, I. R., Bedin, L. R., Piotto, G., Cassisi, S., & Anderson, J. 2005, AJ, 130, 626

Kippenhahn, R. 1963, ApJ, 137, 664

Kippenhahn, R., Ruschenplatt, G., & Thomas, H.-C. 1980, A&A, 91, 175

Kippenhahn, R., & Thomas, H.-C. 1970, in IAU Colloq. 4: Stellar Rotation, ed. A. Slettebak, 20

Kippenhahn, R., Weigert, A., & Weiss, A. 2012, Stellar Structure and Evolution

Kirk, B., et al. 2016, AJ, 151, 68

Kjeldsen, H., & Bedding, T. R. 1995, A&A, 293, 87

Kleinman, S. J., et al. 2013, ApJS, 204, 5

Kobulnicky, H. A., et al. 2014, ApJS, 213, 34

Kochanek, C. S., Beacom, J. F., Kistler, M. D., Prieto, J. L., Stanek, K. Z., Thompson, T. A., & Yüksel, H. 2008, ApJ, 684, 1336

Kochanek, C. S., et al. 2012, ApJS, 200, 8

Koester, D. 2010, Mem.S.A.It., 81, 921

Köhler, K., et al. 2015, A&A, 573, A71

Kraft, R. P. 1967, ApJ, 150, 551

—. 1994, PASP, 106, 553

Kraus, A. L., Cody, A. M., Covey, K. R., Rizzuto, A. C., Mann, A. W., & Ireland, M. J. 2015, ApJ, 807, 3

Kraus, A. L., & Hillenbrand, L. A. 2007, AJ, 134, 2340

Kraus, A. L., Tucker, R. A., Thompson, M. I., Craine, E. R., & Hillenbrand, L. A. 2011, ApJ, 728, 48

Krishna Swamy, K. S. 1966, ApJ, 145, 174

Kroupa, P. 2001, MNRAS, 322, 231

Kroupa, P., Weidner, C., Pflamm-Altenburg, J., Thies, I., Dabringhausen, J., Marks, M., & Maschberger, T. 2013, The Stellar and Sub-Stellar Initial Mass Function of Simple and Composite Populations, ed. T. D. Oswalt & G. Gilmore, 115

Krumholz, M. R., Dekel, A., & McKee, C. F. 2012, ApJ, 745, 69

Krumholz, M. R., Klein, R. I., & McKee, C. F. 2011, ApJ, 740, 74

Krumholz, M. R., & Matzner, C. D. 2009, ApJ, 703, 1352

Krumholz, M. R., & Thompson, T. A. 2012, ApJ, 760, 155

Kurucz, R. L. 1970, SAO Special Report, 309

—. 1993, SYNTHE spectrum synthesis programs and line data

Kurucz, R. L., & Avrett, E. H. 1981, SAO Special Report, 391

La Barbera, F., Ferreras, I., de Carvalho, R. R., Bruzual, G., Charlot, S., Pasquali, A., & Merlin, E. 2012, MNRAS, 426, 2300

Lackner, C. N., Cen, R., Ostriker, J. P., & Joung, M. R. 2012, MNRAS, 425, 641

Lafrenière, D., Jayawardhana, R., & van Kerkwijk, M. H. 2008, ApJL, 689, L153

Lagarde, N., Robin, A. C., Reylé, C., & Nasello, G. 2017, ArXiv e-prints

Langer, N. 1991, A&A, 252, 669

—. 1992, A&A, 265, L17

—. 1998, A&A, 329, 551

—. 2012, ARA&A, 50, 107

Langer, N., El Eid, M. F., & Baraffe, I. 1989, A&A, 224, L17

Langer, N., El Eid, M. F., & Fricke, K. J. 1985, A&A, 145, 179

Langer, N., Fricke, K. J., & Sugimoto, D. 1983, A&A, 126, 207

Langer, N., & Kudritzki, R. P. 2014, A&A, 564, A52

Langer, N., & Maeder, A. 1995, A&A, 295, 685

Larson, R. B. 1974, MNRAS, 169, 229

Lattanzio, J. C. 2007, in Astronomical Society of the Pacific Conference Series, Vol. 378, Why Galaxies Care About AGB Stars: Their Importance as Actors and Probes, ed. F. Kerschbaum, C. Charbonnel, & R. F. Wing, 3

Lau, H. H. B., Stancliffe, R. J., & Tout, C. A. 2009, MNRAS, 396, 1046

Law, N. M., et al. 2009, PASP, 121, 1395

Le Fèvre, O., et al. 2004, A&A, 428, 1043

—. 2005, A&A, 439, 845

Lee, H.-c., et al. 2009, ApJ, 694, 902

Lee-Brown, D. B., Anthony-Twarog, B. J., Deliyannis, C. P., Rich, E., & Twarog, B. A. 2015, AJ, 149, 121

Leitet, E., Bergvall, N., Hayes, M., Linné, S., & Zackrisson, E. 2013, A&A, 553, A106

Leitherer, C., Ekström, S., Meynet, G., Schaerer, D., Agienko, K. B., & Levesque, E. M. 2014, ApJS, 212, 14

Leitherer, C., Ortiz Otálvaro, P. A., Bresolin, F., Kudritzki, R.-P., Lo Faro, B., Pauldrach, A. W. A., Pettini, M., & Rix, S. A. 2010, ApJS, 189, 309

Leitherer, C., Robert, C., & Drissen, L. 1992, ApJ, 401, 596

Leitherer, C., et al. 1999, ApJS, 123, 3

Levesque, E. M., Leitherer, C., Ekstrom, S., Meynet, G., & Schaerer, D. 2012, ApJ, 751, 67

Levesque, E. M., Massey, P., Olsen, K. A. G., Plez, B., Josselin, E., Maeder, A., & Meynet, G. 2005, ApJ, 628, 973

Levesque, E. M., Massey, P., Olsen, K. A. G., Plez, B., Meynet, G., & Maeder, A. 2006, ApJ, 645, 1102

Li, T., Bedding, T. R., Huber, D., Ball, W. H., Stello, D., Murphy, S. J., & Bland-Hawthorn, J. 2018, MNRAS, 475, 981

Liebert, J., Bergeron, P., & Holberg, J. B. 2005, ApJS, 156, 47

Linden, S. T., et al. 2017, ArXiv e-prints

Lodders, K., Palme, H., & Gail, H.-P. 2009, Landolt Börnstein, 44

Lodieu, N. 2013, MNRAS, 431, 3222

Lodieu, N., Hambly, N. C., Jameson, R. F., & Hodgkin, S. T. 2008, MNRAS, 383, 1385

Lopez, L. A., Krumholz, M. R., Bolatto, A. D., Prochaska, J. X., Ramirez-Ruiz, E., & Castro, D. 2014, ApJ, 795, 121

López-Sanjuan, C., et al. 2012, A&A, 548, A7

Loubser, S. I., & Sánchez-Blázquez, P. 2012, MNRAS, 425, 841

Lucy, L. B., & Solomon, P. M. 1970, ApJ, 159, 879

Ma, X., Hopkins, P. F., Faucher-Giguère, C.-A., Zolman, N., Muratov, A. L., Kereš, D., & Quataert, E. 2016a, MNRAS, 456, 2140

Ma, X., Hopkins, P. F., Kasen, D., Quataert, E., Faucher-Giguère, C.-A., Kereš, D., Murray, N., & Strom, A. 2016b, MNRAS, 459, 3614

Ma, X., Kasen, D., Hopkins, P. F., Faucher-Giguère, C.-A., Quataert, E., Kereš, D., & Murray, N. 2015, MNRAS, 453, 960

Mac Low, M.-M., & Klessen, R. S. 2004, Reviews of Modern Physics, 76, 125

MacDonald, J., & Mullan, D. J. 2012, MNRAS, 421, 3084

—. 2014, ApJ, 787, 70

Madau, P., Haardt, F., & Rees, M. J. 1999, ApJ, 514, 648

Maeder, A. 1975, A&A, 40, 303

—. 1987, A&A, 178, 159

—. 1990, A&AS, 84, 139

Maeder, A., & Conti, P. S. 1994, ARA&A, 32, 227

Maeder, A., & Meynet, G. 1994, A&A, 287, 803

—. 2000, ARA&A, 38, 143

—. 2001, A&A, 373, 555

—. 2012, Reviews of Modern Physics, 84, 25

Magic, Z., Serenelli, A., Weiss, A., & Chaboyer, B. 2010, ApJ, 718, 1378

Magic, Z., Weiss, A., & Asplund, M. 2015, A&A, 573, A89

Mancini, C., et al. 2010, MNRAS, 401, 933

Maraston, C. 2005, MNRAS, 362, 799

Maraston, C., Strömbäck, G., Thomas, D., Wake, D. A., & Nichol, R. C. 2009, MNRAS, 394, L107

Marchesini, D., van Dokkum, P. G., Förster Schreiber, N. M., Franx, M., Labbé, I., & Wuyts, S. 2009, ApJ, 701, 1765

Marchesini, D., et al. 2014, ApJ, 794, 65

Marigo, P. 2002, A&A, 387, 507

Marigo, P., & Aringer, B. 2009, A&A, 508, 1539

Marigo, P., Bressan, A., Nanni, A., Girardi, L., & Pumo, M. L. 2013, MNRAS, 434, 488

Marigo, P., & Girardi, L. 2001, A&A, 377, 132

—. 2007, A&A, 469, 239

Marigo, P., Girardi, L., & Bressan, A. 1999, A&A, 344, 123

Marigo, P., Girardi, L., Bressan, A., Groenewegen, M. A. T., Silva, L., & Granato, G. L. 2008, A&A, 482, 883

Marigo, P., Girardi, L., & Chiosi, C. 2003, A&A, 403, 225

Marín-Franch, A., et al. 2009, ApJ, 694, 1498

Martig, M., et al. 2015, MNRAS, 451, 2230

—. 2016, MNRAS, 456, 3655

Martin, C. L. 1999, ApJ, 513, 156

Martin, D. C., et al. 2005, ApJL, 619, L1

Martins, F., Depagne, E., Russeil, D., & Mahy, L. 2013, A&A, 554, A23

Masseron, T., & Gilmore, G. 2015, MNRAS, 453, 1855

Massey, P. 2002, ApJS, 141, 81

Massey, P., & Olsen, K. A. G. 2003, AJ, 126, 2867

Massey, P., Zangari, A. M., Morrell, N. I., Puls, J., DeGioia-Eastwood, K., Bresolin, F., & Kudritzki, R.-P. 2009, ApJ, 692, 618

Mathieu, R. D. 2000, in Astronomical Society of the Pacific Conference Series, Vol. 198, Stellar Clusters and Associations: Convection, Rotation, and Dynamos, ed. R. Pallavicini, G. Micela, & S. Sciortino, 517

Mathieu, R. D., Latham, D. W., & Griffin, R. F. 1990, AJ, 100, 1859

Mathur, S., et al. 2017, ApJS, 229, 30

Matković, A., Guzmán, R., Sánchez-Blázquez, P., Gorgas, J., Cardiel, N., & Gruel, N. 2009, ApJ, 691, 1862

Matzner, C. D. 2002, ApJ, 566, 302

Mauron, N., & Josselin, E. 2011, A&A, 526, A156

McConnachie, A. W., et al. 2009, Nat, 461, 66

McKee, C. F., & Ostriker, E. C. 2007, ARA&A, 45, 565

McKee, C. F., & Ostriker, J. P. 1977, ApJ, 218, 148

McLure, R. J., et al. 2013, MNRAS, 428, 1088

McQuinn, K. B. W., Skillman, E. D., Dalcanton, J. J., Dolphin, A. E., Holtzman, J., Weisz, D. R., & Williams, B. F. 2011, ApJ, 740, 48

Meixner, M., et al. 2006, AJ, 132, 2268

Melbourne, J., et al. 2012, ApJ, 748, 47

Melis, C., Reid, M. J., Mioduszewski, A. J., Stauffer, J. R., & Bower, G. C. 2014, Science, 345, 1029

Melo, C. H. F., Pasquini, L., & De Medeiros, J. R. 2001, A&A, 375, 851

Mestel, L. 1968, MNRAS, 138, 359

Mestel, L., & Weiss, N. O. 1987, MNRAS, 226, 123

Meylan, G., & Maeder, A. 1982, A&A, 108, 148

Meynet, G., Eggenberger, P., & Maeder, A. 2011, A&A, 525, L11

Meynet, G., & Maeder, A. 1997, A&A, 321, 465

—. 2000, A&A, 361, 101

—. 2003, A&A, 404, 975

—. 2005, A&A, 429, 581

Meynet, G., Maeder, A., Schaller, G., Schaerer, D., & Charbonnel, C. 1994, A&AS, 103

Michaud, G., Fontaine, G., & Beaudet, G. 1984, ApJ, 282, 206

Michaud, G., Richard, O., Richer, J., & VandenBerg, D. A. 2004, ApJ, 606, 452

Miglio, A., et al. 2012, MNRAS, 419, 2077

Mihalas, D. 1978, Stellar atmospheres /2nd edition/

Miller Bertolami, M. M. 2016, A&A, 588, A25

Milliman, K. E., Mathieu, R. D., Geller, A. M., Gosnell, N. M., Meibom, S., & Platais, I. 2014, AJ, 148, 38

Milone, A. P., et al. 2013, ApJ, 767, 120

—. 2014, MNRAS, 439, 1588

Monreal-Ibero, A., Walsh, J. R., & Vílchez, J. M. 2012, A&A, 544, A60

Montalbán, J., Kupka, F., D'Antona, F., & Schmidt, W. 2001, A&A, 370, 982

Montalbán, J., Miglio, A., Noels, A., Dupret, M.-A., Scuflaire, R., & Ventura, P. 2013, ApJ, 766, 118

Morales, J. C., Gallardo, J., Ribas, I., Jordi, C., Baraffe, I., & Chabrier, G. 2010, ApJ, 718, 502

Morales, J. C., Ribas, I., & Jordi, C. 2008, A&A, 478, 507

Morel, P., & Baglin, A. 1999, A&A, 345, 156

Morel, P., & Thévenin, F. 2002, A&A, 390, 611

Morel, T., Hubrig, S., & Briquet, M. 2008, A&A, 481, 453

Moustakas, J., Kennicutt, Jr., R. C., Tremonti, C. A., Dale, D. A., Smith, J.-D. T., & Calzetti, D. 2010, ApJS, 190, 233

Moustakas, J., et al. 2011, ArXiv e-prints

—. 2013, ApJ, 767, 50

Muratov, A. L., Kereš, D., Faucher-Giguère, C.-A., Hopkins, P. F., Quataert, E., & Murray, N. 2015, MNRAS, 454, 2691

Murray, N., Ménard, B., & Thompson, T. A. 2011, ApJ, 735, 66

Murray, N., Quataert, E., & Thompson, T. A. 2005, ApJ, 618, 569

—. 2010, ApJ, 709, 191

Muzzin, A., et al. 2013, ApJ, 777, 18

Naab, T., Johansson, P. H., & Ostriker, J. P. 2009, ApJL, 699, L178

Naab, T., Johansson, P. H., Ostriker, J. P., & Efstathiou, G. 2007, ApJ, 658, 710

Narayanan, D., & Davé, R. 2013, MNRAS, 436, 2892

Nath, B. B., & Silk, J. 2009, MNRAS, 396, L90

Ness, M., Hogg, D. W., Rix, H.-W., Martig, M., Pinsonneault, M. H., & Ho, A. Y. Q. 2016, ApJ, 823, 114

Neugent, K. F., & Massey, P. 2011, ApJ, 733, 123

Neugent, K. F., Massey, P., & Georgy, C. 2012, ApJ, 759, 11

Newman, J. A., et al. 2013, ApJS, 208, 5

Nicol, M.-H., Meisenheimer, K., Wolf, C., & Tapken, C. 2011, ApJ, 727, 51

Nieuwenhuijzen, H., & de Jager, C. 1988, A&A, 203, 355

—. 1990, A&A, 231, 134

Noël, N. E. D., Greggio, L., Renzini, A., Carollo, C. M., & Maraston, C. 2013, ApJ, 772, 58

Nomoto, K., Thielemann, F.-K., & Yokoi, K. 1984, ApJ, 286, 644

Nugis, T., & Lamers, H. J. G. L. M. 2000, A&A, 360, 227

Ocvirk, P., Pichon, C., Lançon, A., & Thiébaut, E. 2006, MNRAS, 365, 46

Önehag, A., Gustafsson, B., & Korn, A. 2014, A&A, 562, A102

Onodera, M., et al. 2012, ApJ, 755, 26

Oppenheimer, B. D., & Davé, R. 2006, MNRAS, 373, 1265

Origlia, L., Valenti, E., Rich, R. M., & Ferraro, F. R. 2006, ApJ, 646, 499

Paczyński, B. 1970, Acta Astronomica, 20, 47

Palacios, A., Charbonnel, C., Talon, S., & Siess, L. 2006, A&A, 453, 261

Palacios, A., Talon, S., Charbonnel, C., & Forestini, M. 2003, A&A, 399, 603

Pallé, E., Zapatero Osorio, M. R., Barrena, R., Montañés-Rodríguez, P., & Martín, E. L. 2009, Nat, 459, 814

Paquette, C., Pelletier, C., Fontaine, G., & Michaud, G. 1986, ApJS, 61, 177

Pauldrach, A. W. A. 2012, WM-basic: Modeling atmospheres of hot stars, Astrophysics Source Code Library

Paxton, B., Bildsten, L., Dotter, A., Herwig, F., Lesaffre, P., & Timmes, F. 2011, ApJS, 192, 3

Paxton, B., et al. 2013, ApJS, 208, 4

—. 2015, ApJS, 220, 15

—. 2018, ApJS, 234, 34

Pecaut, M. J., Mamajek, E. E., & Bubar, E. J. 2012, ApJ, 746, 154

Penny, L. R. 1996, ApJ, 463, 737

Penny, L. R., & Gies, D. R. 2009, ApJ, 700, 844

Perryman, M. A. C., et al. 1997, A&A, 323, L49

Petrovic, J., Langer, N., Yoon, S.-C., & Heger, A. 2005, A&A, 435, 247

Pietrinferni, A., Cassisi, S., Salaris, M., & Castelli, F. 2004, ApJ, 612, 168

Pilachowski, C. A., Leep, E. M., & Wallerstein, G. 1980, ApJ, 236, 508

Pinsonneault, M. 1997, ARA&A, 35, 557

Pinsonneault, M. H., Kawaler, S. D., Sofia, S., & Demarque, P. 1989, ApJ, 338, 424

Pinsonneault, M. H., et al. 2014, ApJS, 215, 19

Piotto, G., et al. 2007, ApJL, 661, L53

—. 2012, ApJ, 760, 39

Planck Collaboration et al. 2015, ArXiv e-prints

Pols, O. R., Tout, C. A., Eggleton, P. P., & Han, Z. 1995, MNRAS, 274, 964

Popper, D. M. 1967, ARA&A, 5, 85

Potekhin, A. Y., & Chabrier, G. 2010, Contributions to Plasma Physics, 50, 82

Potter, A. T., Tout, C. A., & Eldridge, J. J. 2012, MNRAS, 419, 748

Pozzetti, L., et al. 2010, A&A, 523, A13

Prada Moroni, P. G., & Straniero, O. 2002, ApJ, 581, 585

Preibisch, T., Brown, A. G. A., Bridges, T., Guenther, E., & Zinnecker, H. 2002, AJ, 124, 404

Preibisch, T., & Zinnecker, H. 1999, AJ, 117, 2381

Prieto, M., et al. 2013, MNRAS, 428, 999

Przybilla, N., Firnstein, M., Nieva, M. F., Meynet, G., & Maeder, A. 2010, A&A, 517, A38

Pulone, L., De Marchi, G., Paresce, F., & Allard, F. 1998, ApJL, 492, L41

Ramírez, I., & Meléndez, J. 2005, ApJ, 626, 465

Ramírez-Agudelo, O. H., et al. 2013, A&A, 560, A29

Rauscher, T., Heger, A., Hoffman, R. D., & Woosley, S. E. 2002, ApJ, 576, 323

Rawle, T. D., Smith, R. J., & Lucey, J. R. 2010, MNRAS, 401, 852

Razoumov, A. O., & Sommer-Larsen, J. 2010, ApJ, 710, 1239

Recio-Blanco, A., et al. 2016, A&A, 585, A93

Reese, D. R., et al. 2016, A&A, 592, A14

Reimers, D. 1975, Circumstellar envelopes and mass loss of red giant stars, ed. B. Baschek, W. H. Kegel, & G. Traving, 229–256

Renzini, A. 2006, ARA&A, 44, 141

Renzini, A., & Fusi Pecci, F. 1988, ARA&A, 26, 199

Rhodes, Jr., E. J., Kosovichev, A. G., Schou, J., Scherrer, P. H., & Reiter, J. 1997, Soar Phys., 175, 287

Ricciardelli, E., Vazdekis, A., Cenarro, A. J., & Falcón-Barroso, J. 2012, MNRAS, 424, 172

Richard, O., Vauclair, S., Charbonnel, C., & Dziembowski, W. A. 1996, A&A, 312, 1000

Rivero González, J. G., Puls, J., Najarro, F., & Brott, I. 2012, A&A, 537, A79

Rix, H.-W., & Bovy, J. 2013, The Astronomy and Astrophysics Review, 21, 61

Robaina, A. R., Bell, E. F., van der Wel, A., Somerville, R. S., Skelton, R. E., McIntosh, D. H., Meisenheimer, K., & Wolf, C. 2010, ApJ, 719, 844

Robertson, B. E., et al. 2013, ApJ, 768, 71

Rogers, F. J., & Nayfonov, A. 2002, ApJ, 576, 1064

Romero, A. D., Campos, F., & Kepler, S. O. 2015, MNRAS, 450, 3708

Rosen, A. L., Krumholz, M. R., & Ramirez-Ruiz, E. 2012, ApJ, 748, 97

Rosenfield, P., et al. 2014, ApJ, 790, 22

Ross, T. L., Holtzman, J. A., Anthony-Twarog, B. J., Bond, H. E., Twarog, B., Saha, A., & Walker, A. 2014, AJ, 147, 4

Roxburgh, I. W. 1978, A&A, 65, 281

Rüdiger, G., Gellert, M., Spada, F., & Tereshin, I. 2015, A&A, 573, A80

Rusin, D., & Kochanek, C. S. 2005, ApJ, 623, 666

Russell, H. N. 1912, ApJ, 36

Saglia, R. P., Maraston, C., Thomas, D., Bender, R., & Colless, M. 2002, ApJL, 579, L13

Salaris, M., & Cassisi, S. 1996, A&A, 305, 858

—. 2015, A&A, 577, A60

Salaris, M., Cassisi, S., Schiavon, R. P., & Pietrinferni, A. 2018, ArXiv e-prints

Salaris, M., Cassisi, S., & Weiss, A. 2002, PASP, 114, 375

Salaris, M., Groenewegen, M. A. T., & Weiss, A. 2000, A&A, 355, 299

Salpeter, E. E. 1955, ApJ, 121, 161

Sana, H., et al. 2012, Science, 337, 444

—. 2013, A&A, 550, A107

Sánchez-Blázquez, P., Forbes, D. A., Strader, J., Brodie, J., & Proctor, R. 2007, MNRAS, 377, 759

Sánchez-Blázquez, P., Gorgas, J., Cardiel, N., Cenarro, J., & González, J. J. 2003, ApJL, 590, L91

Sánchez-Blázquez, P., Gorgas, J., Cardiel, N., & González, J. J. 2006a, A&A, 457, 787

Sánchez-Blázquez, P., Ocvirk, P., Gibson, B. K., Pérez, I., & Peletier, R. F. 2011, MNRAS, 415, 709

Sánchez-Blázquez, P., et al. 2006b, MNRAS, 371, 703

—. 2006c, MNRAS, 371, 703

—. 2009, A&A, 499, 47

Sanders, N. E., Caldwell, N., McDowell, J., & Harding, P. 2012, ApJ, 758, 133

Sandquist, E. L. 2004, MNRAS, 347, 101

Sandquist, E. L., & Shetrone, M. D. 2003, AJ, 126, 2954

Sandquist, E. L., et al. 2013, ApJ, 762, 58

Sarajedini, A., Dotter, A., & Kirkpatrick, A. 2009, ApJ, 698, 1872

Saumon, D., Chabrier, G., & van Horn, H. M. 1995, ApJS, 99, 713

Sbordone, L., Bonifacio, P., Castelli, F., & Kurucz, R. L. 2004, Memorie della Societa Astronomica Italiana Supplementi, 5, 93

Scarlata, C., et al. 2007, ApJS, 172, 494

Schaller, G., Schaerer, D., Meynet, G., & Maeder, A. 1992, A&AS, 96, 269

Schiavon, R. P. 2007, ApJS, 171, 146

Schiavon, R. P., et al. 2006, ApJL, 651, L93

Schoenberner, D. 1979, A&A, 79, 108

Schwarzschild, M. 1958, Structure and evolution of the stars.

Schwarzschild, M., & Härm, R. 1962, ApJ, 136, 158

—. 1965, ApJ, 142, 855

SDSS Collaboration et al. 2016, ArXiv e-prints

Searle, S. C., Prinja, R. K., Massa, D., & Ryans, R. 2008, A&A, 481, 777

Seaton, M. J. 2005, MNRAS, 362, L1

Serenelli, A. M., Basu, S., Ferguson, J. W., & Asplund, M. 2009, ApJL, 705, L123

Serra, P., & Trager, S. C. 2007, MNRAS, 374, 769

Sestito, P., & Randich, S. 2005, A&A, 442, 615

Sharma, S., Stello, D., Bland-Hawthorn, J., Huber, D., & Bedding, T. R. 2016, ApJ, 822, 15

Shaviv, G., & Salpeter, E. E. 1973, ApJ, 184, 191

Shen, S., Mo, H. J., White, S. D. M., Blanton, M. R., Kauffmann, G., Voges, W., Brinkmann, J., & Csabai, I. 2003, MNRAS, 343, 978

Siana, B., et al. 2010, ApJ, 723, 241

Siess, L. 2009, A&A, 497, 463

Siess, L., Dufour, E., & Forestini, M. 2000, A&A, 358, 593

Silva Aguirre, V., Ballot, J., Serenelli, A. M., & Weiss, A. 2011, A&A, 529, A63

Skelton, R. E., Bell, E. F., & Somerville, R. S. 2012, ApJ, 753, 44

Slesnick, C. L., Hillenbrand, L. A., & Carpenter, J. M. 2008, ApJ, 688, 377

Smartt, S. J. 2009, ARA&A, 47, 63

Smiljanic, R., et al. 2014, A&A, 570, A122

Smith, L. J., Crowther, P. A., Calzetti, D., & Sidoli, F. 2016, ApJ, 823, 38

Smith, L. J., Norris, R. P. F., & Crowther, P. A. 2002, MNRAS, 337, 1309

Smith, N. 2014, ARA&A, 52, 487

Smith, N., & Owocki, S. P. 2006, ApJL, 645, L45

Smith, R. J., Lucey, J. R., Hudson, M. J., & Bridges, T. J. 2009, MNRAS, 398, 119

Soderblom, D. R., Laskar, T., Valenti, J. A., Stauffer, J. R., & Rebull, L. M. 2009, AJ, 138, 1292

Soderblom, D. R., Nelan, E., Benedict, G. F., McArthur, B., Ramirez, I., Spiesman, W., & Jones, B. F. 2005, AJ, 129, 1616

Söderlind, G., & Wang, L. 2006, Journal of Computational and Applied Mathematics, 185, 244 , special Issue: International Workshop on the Technological Aspects of Mathematics

Somers, G., & Pinsonneault, M. H. 2014, ApJ, 790, 72

Song, H. F., Meynet, G., Maeder, A., Ekström, S., & Eggenberger, P. 2016, A&A, 585, A120

Song, I., Zuckerman, B., & Bessell, M. S. 2012, AJ, 144, 8

Southworth, J. 2015, in Astronomical Society of the Pacific Conference Series, Vol. 496, Living Together: Planets, Host Stars and Binaries, ed. S. M. Rucinski, G. Torres, & M. Zejda, 164

Spada, F., Demarque, P., Kim, Y.-C., & Sills, A. 2013, ApJ, 776, 87

Spolaor, M., Kobayashi, C., Forbes, D. A., Couch, W. J., & Hau, G. K. T. 2010, MNRAS, 408, 272

Spruit, H. C. 2002, A&A, 381, 923

—. 2013, A&A, 552, A76

Spruit, H. C., & Weiss, A. 1986, A&A, 166, 167

Stancliffe, R. J. 2010, MNRAS, 403, 505

Stancliffe, R. J., Dearborn, D. S. P., Lattanzio, J. C., Heap, S. A., & Campbell, S. W. 2011, ApJ, 742, 121

Stancliffe, R. J., Glebbeek, E., Izzard, R. G., & Pols, O. R. 2007, A&A, 464, L57

Stanway, E. R., Eldridge, J. J., & Becker, G. D. 2016, MNRAS, 456, 485

Stauffer, J. R., Jones, B. F., Backman, D., Hartmann, L. W., Barrado y Navascués, D., Pinsonneault, M. H., Terndrup, D. M., & Muench, A. A. 2003, AJ, 126, 833

Stauffer, J. R., et al. 2007, ApJS, 172, 663

Steidel, C. C., Strom, A. L., Pettini, M., Rudie, G. C., Reddy, N. A., & Trainor, R. F. 2016, ApJ, 826, 159

Steidel, C. C., et al. 2014, ApJ, 795, 165

Steinmetz, M., et al. 2006, AJ, 132, 1645

Stello, D., Bruntt, H., Preston, H., & Buzasi, D. 2008, ApJL, 674, L53

Stello, D., et al. 2013, ApJL, 765, L41

—. 2016, ApJ, 832, 133

Stetson, P. B., Bruntt, H., & Grundahl, F. 2003, PASP, 115, 413

Stewart, K. R., Bullock, J. S., Wechsler, R. H., & Maller, A. H. 2009, ApJ, 702, 307

Stothers, R., & Chin, C.-W. 1975, ApJ, 198, 407

Stothers, R., & Simon, N. R. 1969, ApJ, 157, 673

Stothers, R. B., & Chin, C.-W. 1991, ApJL, 381, L67

Stott, J. P., Collins, C. A., Burke, C., Hamilton-Morris, V., & Smith, G. P. 2011, MNRAS, 414, 445

Strauss, M. A., et al. 2002, AJ, 124, 1810

Strittmatter, P. A. 1969, ARA&A, 7, 665

Suijs, M. P. L., Langer, N., Poelarends, A.-J., Yoon, S.-C., Heger, A., & Herwig, F. 2008, A&A, 481, L87

Sukhbold, T., & Woosley, S. E. 2014, ApJ, 783, 10

Sweigart, A. V., & Mengel, J. G. 1979, ApJ, 229, 624

Takeda, Y., & Takada-Hidai, M. 2000, PASJ, 52, 113

Talon, S., & Charbonnel, C. 2005, A&A, 440, 981

Tamburro, D., Rix, H.-W., Leroy, A. K., Mac Low, M.-M., Walter, F., Kennicutt, R. C., Brinks, E., & de Blok, W. J. G. 2009, AJ, 137, 4424

Tang, J., Bressan, A., Rosenfield, P., Slemer, A., Marigo, P., Girardi, L., & Bianchi, L. 2014, MNRAS, 445, 4287

Tang, J., Bressan, A., Slemer, A., Marigo, P., Girardi, L., Bianchi, L., Rosenfield, P., & Momany, Y. 2016, MNRAS, 455, 3393

Tassoul, J.-L. 1978, Theory of rotating stars

Tayar, J., et al. 2017, ApJ, 840, 17

Taylor, B. J. 2006, AJ, 132, 2453

—. 2007, AJ, 133, 370

Thomas, D., Greggio, L., & Bender, R. 1999, MNRAS, 302, 537

Thomas, D., Maraston, C., & Bender, R. 2003, MNRAS, 343, 279

Thomas, D., Maraston, C., Bender, R., & Mendes de Oliveira, C. 2005, ApJ, 621, 673

Thomas, D., Maraston, C., Schawinski, K., Sarzi, M., & Silk, J. 2010, MNRAS, 404, 1775

Thomas, H.-C. 1967, Zeitschrift für Astrophysik, 67, 420

Thoul, A. A., Bahcall, J. N., & Loeb, A. 1994, ApJ, 421, 828

Timmes, F. X., & Swesty, F. D. 2000, ApJS, 126, 501

Ting, Y.-S., Conroy, C., Rix, H.-W., & Cargile, P. 2017, ApJ, 843, 32

—. 2018, ArXiv e-prints

Tinsley, B. M. 1979, ApJ, 229, 1046

Tognelli, E., Prada Moroni, P. G., & Degl'Innocenti, S. 2011, A&A, 533, A109

Tojeiro, R., Wilkins, S., Heavens, A. F., Panter, B., & Jimenez, R. 2009, ApJS, 185, 1

Toloba, E., Sánchez-Blázquez, P., Gorgas, J., & Gibson, B. K. 2009, ApJL, 691, L95

Tolstoy, E., Hill, V., & Tosi, M. 2009, ARA&A, 47, 371

Tonry, J. L., et al. 2012, ApJ, 750, 99

Torres, G. 2013, Astronomische Nachrichten, 334, 4

Torres, G., Andersen, J., & Giménez, A. 2010, The Astronomy and Astrophysics Review, 18, 67

Torres, G., Fischer, D. A., Sozzetti, A., Buchhave, L. A., Winn, J. N., Holman, M. J., & Carter, J. A. 2012, ApJ, 757, 161

Torres, G., Ruíz-Rodríguez, D., Badenas, M., Prato, L., Schaefer, G. H., Wasserman, L. H., Mathieu, R. D., & Latham, D. W. 2013, ApJ, 773, 40

Townsend, R. H. D., & Teitler, S. A. 2013, MNRAS, 435, 3406

Trager, S. C., Faber, S. M., & Dressler, A. 2008, MNRAS, 386, 715

Trager, S. C., Faber, S. M., Worthey, G., & González, J. J. 2000, AJ, 120, 165

Trager, S. C., & Somerville, R. S. 2009, MNRAS, 395, 608

Trager, S. C., Worthey, G., Faber, S. M., Burstein, D., & Gonzalez, J. J. 1998, ApJS, 116, 1

Trampedach, R. 2007, in American Institute of Physics Conference Series, Vol. 948, Unsolved Problems in Stellar Physics: A Conference in Honor of Douglas Gough, ed. R. J. Stancliffe, G. Houdek, R. G. Martin, & C. A. Tout, 141–148

Trampedach, R., Stein, R. F., Christensen-Dalsgaard, J., Nordlund, Å., & Asplund, M. 2014, MNRAS, 445, 4366

Traxler, A., Garaud, P., & Stellmach, S. 2011, ApJL, 728, L29

Treu, T., et al. 2005, ApJ, 633, 174

Trujillo, I., et al. 2006, ApJ, 650, 18

Trundle, C., Dufton, P. L., Lennon, D. J., Smartt, S. J., & Urbaneja, M. A. 2002, A&A, 395, 519

Turcotte, S., Richer, J., & Michaud, G. 1998, ApJ, 504, 559

Turner, J. L., Beck, S. C., Benford, D. J., Consiglio, S. M., Ho, P. T. P., Kovács, A., Meier, D. S., & Zhao, J.-H. 2015, Nat, 519, 331

ud-Doula, A., & Owocki, S. P. 2002, ApJ, 576, 413

Ulrich, R. K. 1972, ApJ, 172, 165

—. 1986, ApJL, 306, L37

Unno, W. 1957, ApJ, 126, 259

van de Sande, J., et al. 2011, ApJL, 736, L9

van den Bergh, S. 1968, Journal of the Royal Astronomical Society of Canada, 62, 145

van der Hucht, K. A. 2001, NewAR, 45, 135

van der Wel, A., Franx, M., van Dokkum, P. G., Rix, H.-W., Illingworth, G. D., & Rosati, P. 2005, ApJ, 631, 145

van der Wel, A., Holden, B. P., Zirm, A. W., Franx, M., Rettura, A., Illingworth, G. D., & Ford, H. C. 2008, ApJ, 688, 48

van Dokkum, P. G., & Franx, M. 1996, MNRAS, 281, 985

—. 2001, ApJ, 553, 90

van Dokkum, P. G., & van der Marel, R. P. 2007, ApJ, 655, 30

van Dokkum, P. G., et al. 2008, ApJL, 677, L5

—. 2010, ApJ, 709, 1018

van Saders, J. L., & Pinsonneault, M. H. 2012, ApJ, 751, 98

VandenBerg, D. A., Bergbusch, P. A., & Dowler, P. D. 2006, ApJS, 162, 375

VandenBerg, D. A., Edvardsson, B., Eriksson, K., & Gustafsson, B. 2008, ApJ, 675, 746

Vardya, M. S. 1985, ApJ, 299, 255

Varenne, O., & Monier, R. 1999, A&A, 351, 247

Vassiliadis, E., & Wood, P. R. 1993, ApJ, 413, 641

—. 1994, ApJS, 92, 125

Vauclair, S. 1983, in Saas-Fee Advanced Course 13: Astrophysical Processes in Upper Main Sequence Stars, ed. A. N. Cox, S. Vauclair, & J. P. Zahn, 167

Vazdekis, A., et al. 2015, MNRAS, 449, 1177

Vázquez, G. A., & Leitherer, C. 2005, ApJ, 621, 695

Venn, K. A., McCarthy, J. K., Lennon, D. J., Przybilla, N., Kudritzki, R. P., & Lemke, M. 2000, ApJ, 541, 610

Vergani, D., et al. 2008, A&A, 487, 89

Vernazza, J. E., Avrett, E. H., & Loeser, R. 1981, ApJS, 45, 635

Viani, L. S., Basu, S., Chaplin, W. J., Davies, G. R., & Elsworth, Y. 2017, ArXiv e-prints

Viani, L. S., Basu, S., Joel Ong J., M., Bonaca, A., & Chaplin, W. J. 2018, ApJ, 858, 28

Villamariz, M. R., & Herrero, A. 2005, A&A, 442, 263

Villamariz, M. R., Herrero, A., Becker, S. R., & Butler, K. 2002, A&A, 388, 940

Villanova, S., Geisler, D., Carraro, G., Moni Bidin, C., & Muñoz, C. 2013, ApJ, 778, 186

Villaume, A., Conroy, C., & Johnson, B. D. 2015, ApJ, 806, 82

Villaverde, M., Cerviño, M., & Luridiana, V. 2010, A&A, 522, A49

Vink, J. S., & de Koter, A. 2005, A&A, 442, 587

Vink, J. S., de Koter, A., & Lamers, H. J. G. L. M. 2000, A&A, 362, 295

—. 2001, A&A, 369, 574

Vink, J. S., Muijres, L. E., Anthonisse, B., de Koter, A., Gräfener, G., & Langer, N. 2011, A&A, 531, A132

von Hippel, T., Jefferys, W. H., Scott, J., Stein, N., Winget, D. E., De Gennaro, S., Dam, A., & Jeffery, E. 2006, ApJ, 645, 1436

Wachlin, F. C., Miller Bertolami, M. M., & Althaus, L. G. 2011, A&A, 533, A139

Wachlin, F. C., Vauclair, S., & Althaus, L. G. 2014, A&A, 570, A58

Wagenhuber, J., & Groenewegen, M. A. T. 1998, A&A, 340, 183

Walch, S. K., Whitworth, A. P., Bisbas, T., Wünsch, R., & Hubber, D. 2012, MNRAS, 427, 625

Walcher, C. J., Coelho, P., Gallazzi, A., & Charlot, S. 2009, MNRAS, 398, L44

Walcher, J., Groves, B., Budavári, T., & Dale, D. 2011, Astrophys. Space Sci, 331, 1

Walker, M. F. 1964, AJ, 69, 744

Wang, P. F., et al. 2014, ApJ, 784, 57

Weber, E. J., & Davis, Jr., L. 1967, ApJ, 148, 217

Weidemann, V. 1977, A&A, 59, 411

—. 2000, A&A, 363, 647

Weiss, A., & Ferguson, J. W. 2009, A&A, 508, 1343

Weiss, A., & Schlattl, H. 2008, Astrophys. Space Sci, 316, 99

Weisz, D. R., et al. 2011, ApJ, 739, 5

—. 2015, ApJ, 806, 198

Wheeler, J. C., Kagan, D., & Chatzopoulos, E. 2015, ApJ, 799, 85

Whitaker, K. E., et al. 2010, ApJ, 719, 1715

White, T. R., Bedding, T. R., Stello, D., Christensen-Dalsgaard, J., Huber, D., & Kjeldsen, H. 2011, ApJ, 743, 161

Whitworth, A. 1979, MNRAS, 186, 59

Williams, J. P., & McKee, C. F. 1997, ApJ, 476, 166

Williams, K. A., & Bolte, M. 2007, AJ, 133, 1490

Williams, K. A., Bolte, M., & Koester, D. 2009, ApJ, 693, 355

Williams, R. J., Quadri, R. F., Franx, M., van Dokkum, P., Toft, S., Kriek, M., & Labbé, I. 2010, ApJ, 713, 738

Willson, L. A. 2000, ARA&A, 38, 573

Wise, J. H., Demchenko, V. G., Halicek, M. T., Norman, M. L., Turk, M. J., Abel, T., & Smith, B. D. 2014, MNRAS, 442, 2560

Wolff, S., & Simon, T. 1997, PASP, 109, 759

Wolff, S. C., Strom, S. E., & Hillenbrand, L. A. 2004, ApJ, 601, 979

Wood, T. S., Garaud, P., & Stellmach, S. 2013, ApJ, 768, 157

Woodward, P. R., Herwig, F., & Lin, P.-H. 2015, ApJ, 798, 49

Woosley, S. E., & Heger, A. 2006, ApJ, 637, 914

Worthey, G. 2004, AJ, 128, 2826

Worthey, G., Faber, S. M., Gonzalez, J. J., & Burstein, D. 1994, ApJS, 94, 687

Worthey, G., Tang, B., & Serven, J. 2014, ApJ, 783, 20

Wright, E. L., et al. 2010, AJ, 140, 1868

Wu, X. S., Alexeeva, S., Mashonkina, L., Wang, L., Zhao, G., & Grupp, F. 2015, A&A, 577, A134

Yadav, R. K. S., et al. 2008, A&A, 484, 609

Yakut, K., Eggleton, P. P., Kalomeni, B., Tout, C. A., & Eldridge, J. J. 2015, MNRAS, 453, 2937

Yang, S.-C., Sarajedini, A., Deliyannis, C. P., Sarrazine, A. R., Kim, S. C., & Kyeong, J. 2013, ApJ, 762, 3

Yi, S., Demarque, P., Kim, Y.-C., Lee, Y.-W., Ree, C. H., Lejeune, T., & Barnes, S. 2001, ApJS, 136, 417

Yi, S. K., Kim, Y.-C., & Demarque, P. 2003, ApJS, 144, 259

Yoon, S.-C., & Cantiello, M. 2010, ApJL, 717, L62

Yoon, S.-C., & Langer, N. 2005, A&A, 443, 643

Yoon, S.-C., Langer, N., & Norman, C. 2006, A&A, 460, 199

York, D. G., et al. 2000, AJ, 120, 1579

Young, P. A., & Arnett, D. 2005, ApJ, 618, 908

Yurchenko, S. N., Barber, R. J., & Tennyson, J. 2011, MNRAS, 413, 1828

Yusof, N., et al. 2013, MNRAS, 433, 1114

Zahn, J.-P. 1983, in Saas-Fee Advanced Course 13: Astrophysical Processes in Upper Main Sequence Stars, ed. A. N. Cox, S. Vauclair, & J. P. Zahn, 253

Zahn, J.-P. 1992, A&A, 265, 115

Zahn, J.-P., Brun, A. S., & Mathis, S. 2007, A&A, 474, 145

Zaritsky, D., Harris, J., Thompson, I. B., Grebel, E. K., & Massey, P. 2002, AJ, 123, 855

Zasowski, G., et al. 2013, AJ, 146, 81

Zhang, F., Li, L., Han, Z., Zhuang, Y., & Kang, X. 2013, MNRAS, 428, 3390

Zhao, J. K., Oswalt, T. D., Willson, L. A., Wang, Q., & Zhao, G. 2012, ApJ, 746, 144

Zhu, G., Blanton, M. R., & Moustakas, J. 2010, ApJ, 722, 491

Zinnecker, H., & Yorke, H. W. 2007, ARA&A, 45, 481

Zurita, A., & Bresolin, F. 2012, MNRAS, 427, 1463